

論文 / 著書情報  
Article / Book Information

題目(和文)	
Title(English)	Solid state properties of organic conductors with magnetic moments
著者(和文)	山浦淳一
Author(English)	Junichi Yamaura
出典(和文)	学位:博士(理学), 学位授与機関:東京工業大学, 報告番号:甲第3401号, 授与年月日:1997年3月26日, 学位の種別:課程博士, 審査員:
Citation(English)	Degree:Doctor (Science), Conferring organization: Tokyo Institute of Technology, Report number:甲第3401号, Conferred date:1997/3/26, Degree Type:Course doctor, Examiner:
学位種別(和文)	博士論文
Type(English)	Doctoral Thesis

# **Solid State Properties of Organic Conductors with Magnetic Moments**

A Thesis Submitted to Tokyo Institute of Technology  
for the Degree of Doctor of Science (Hakushi(Rigaku))

by. Jun-Ichi Yamaura

Department of Chemistry, Faculty of Science,  
Tokyo Institute of Technology

January, 1997

## Acknowledgements

I would like to express my sincere thanks to Professor Toshiaki Enoki for his encouragement, valuable suggestions and fruitful discussions in the present work.

The author is sincerely grateful to Associate Professor Kazuya Suzuki at Yokohama National University for his continuous advice and discussion, and specially thankful to Dr. Akira Miyazaki, Dr. Hirohiko Sato and Mr. Naoki Yoneyama for excellent discussions and helpful suggestions to the experiments.

The author wishes to express thanks to Professor Gunzi Saito, Associate Professor Hideki Yamochi at Kyoto University for providing organic donors and fruitful discussion. The author wishes grateful to Associate Professor Yohji Misaki at Kyoto University and Professor Reizo Kato at The Institute for Solid State Physics, University of Tokyo for providing organic donors. The author would like to wish to thank Professor Takehiko Mori at Tokyo Institute of Technology for providing organic donors and the programs of band calculation.

The author thanks to Keizo Murata in Osaka City University for the fruitful advice of designing the high pressure clamp cell for the measurement of the magnetic susceptibility, and are indebted to Yohko Kaizu for the electronic structure calculation based on DV- $X\alpha$  method.

The author is grateful to Professor Yuji Ohashi, Technical Assistant Yoshii Sakai for collaborating on the X-ray structure analysis at room temperature. The author appreciates Professor Y. Nogami and Mr. Masashi Watanabe at Okayama University for the discussion of the low temperature X-ray result. He is grateful to Professor Toshihiro Takahashi, Mr. Ryota Tsuchiya and Mr. Satoshi Yoshizaki at Gakushuin University for the discussion of  $^1\text{H}$ -NMR results.

The author would like to thank Professor Youichi Murakami and Dr. Hajime Kawata at the Photon Factory (KEK) for collaborating X-ray on measurement under high pressure on Beam Line 4C (under proposal No. 96-G094), and grateful to Professor Yasuhiko Fujii at The Institute for Solid State Physics, University of Tokyo for offering a diamond anvil cell.

The author wishes to express his gratitude to Professor Nobuo Mouri at The Institute for Solid State Physics, University of Tokyo and lecturer Hiroki Takahashi at Nohon University for the collaborating on the high pressure resistivity measurement. He thanks Professor Seiichi Kagoshima in University of Tokyo to use the monochromatic Laue Photograph measurement, and grateful to Professor Yotaka Nishio in Toho University for their kind suggestion on the construction of the specific heat capacity calorimeter by the relaxation method.

The author would like to express their gratitude to Professor Naoto Nagaosa and Hidetoshi Fukuyama at the University of Tokyo for fruitful discussion. He would like to express his sincere thank to Professor Seiji Miyashita at Osaka University, and Professor Hiroyuki Shiba and Professor Hidetoshi Nishimori at Tokyo Institute of Technology for fruitful discussion. The author is grateful to Dr. Nobuo Suzuki at Tohoku University for the quantum Monte Carlo simulation of the distorted triangular lattice.

The author would like to thank all the members of the Professor Enoki's group for their helpful advice and suggestion.

## Publication Lists

contributed to this thesis

1. K. Suzuki, J. Yamaura, N. Sugiyasu, T. Enoki and G. Saito, "Phase Transition and Magnetic Properties of Organic Conductor (BEDT-TTF)<sub>6</sub>Cu<sub>2</sub>Br<sub>6</sub> with Mixed Valence Cu ions", *Synth. Met.*, **55-57** (1993) 2191-2197.
2. T. Enoki, J. Yamaura, N. Sugiyasu, K. Suzuki and G. Saito, "Solid State Properties of Charge Transfer Complexes of TTF Derivatives with 3d-Transition Metal Halides", *Mol. Cryst. Liq. Cryst.*, **223** (1993) 325-334.
3. T. Enoki, J. Yamaura, N. Sugiyasu, Y. Nakano and K. Suzuki, "Organic Conductors based on TTF Derivatives with Transition Metal Magnetic ions", *New Functionality Materials*, ed. by T. Tsumura, M. Doyama and M. Seno (Elsevier, 1993) Vol. C, p.509-513.
4. R. Tsuchiya, S. Yoshizaki, T. Nakamura, T. Takahashi, J. Yamaura, K. Suzuki, T. Enoki and G. Saito, "<sup>1</sup>H-NMR Study of Magnetic Anomaly in (BEDT-TTF)<sub>3</sub>CuBr<sub>4</sub>", *Synth. Met.*, **70** (1995) 967-968.
5. J. Yamaura, K. Suzuki, Y. Kaizu, T. Enoki, K. Murata and G. Saito, "Magnetic Properties of Organic Conductor (BEDT-TTF)<sub>3</sub>CuBr<sub>4</sub>", *J. Phys. Soc. Jpn.*, **65** (1996) 2645-2654.
6. T. Enoki, M. Enomoto, M. Enomoto, K. Yamaguchi, N. Yoneyama, J. Yamaura, A. Miyazaki and G. Saito, "Molecular Magnets based on TTF-Type Charge Transfer Complexes", *Mol. Cryst. Liq. Cryst.*, **285** (1996) 19-26.
7. M. Watanabe, Y. Nogami, K. Oshima, J. Yamaura, T. Enoki and G. Saito, "Low Temperature Structures of (BEDT-TTF)<sub>3</sub>CuBr<sub>4</sub>", to be published in *Synth. Met.* (1997).
8. M. Watanabe, Y. Nogami, K. Oshima, J. Yamaura, T. Enoki and G. Saito, "Structural Phase Transition in (BEDT-TTF)<sub>3</sub>CuBr<sub>4</sub> AT 60K", *Solid State Commun.*, **100** (1996) 755-758.

9. J. Yamaura, A. Miyazaki, T. Enoki and G. Saito, "Crystal Structure and Magnetic Properties of Organic Antiferromagnet  $(C_1TET-TTF)_2Br$ ", Phys. Rev. ,**B55** (1997) 3649-3655.

related papers

1. T. Kawamoto, T. Mori, J. Yamaura, T. Enoki, Y. Misaki, T. Yamabe, H. Mori and S. Tanaka, "High Pressure Conductivity of Radical-Cation Salts of BDT-TTP", to be published in Synth. Met. (1997).

# Contents

<b>1</b>	<b>Introduction</b>	<b>3</b>
1.1	Organic Conductors . . . . .	4
1.1.1	Outline of Organic Conductors . . . . .	4
1.1.2	Feature of Conducting Mechanism . . . . .	8
1.2	Mott-Hubbard system . . . . .	11
1.3	Low-Dimensional Magnetism . . . . .	15
1.4	Magnetic Interactions . . . . .	19
1.5	Organic Conductors with Localized Magnetic Moments . . . . .	22
1.5.1	$\pi$ - $d$ systems . . . . .	22
1.5.2	Mott-Hubbard systems . . . . .	26
1.6	Aim of Thesis . . . . .	35
<b>2</b>	<b>Development of Organic Conductors having <math>\pi - d</math> interaction</b>	<b>37</b>
2.1	Introduction . . . . .	38
2.2	Experimental . . . . .	48
2.3	Results and Discussion . . . . .	53
2.4	Summary . . . . .	66
<b>3</b>	<b>Solid State Properties of (BEDT-TTF)<sub>3</sub>CuBr<sub>4</sub></b>	<b>68</b>
3.1	Introduction . . . . .	69
3.2	Structural Properties . . . . .	69
3.2.1	Experimental . . . . .	70
3.2.2	Experimental Results . . . . .	74

3.2.3	Discussion . . . . .	97
3.3	Electronic Properties . . . . .	102
3.3.1	Experimental . . . . .	102
3.3.2	Experimental Results . . . . .	105
3.3.3	Discussion . . . . .	117
3.4	Magnetic and Thermal Properties of (BEDT-TTF) <sub>3</sub> CuBr <sub>4</sub> . . . . .	121
3.4.1	Experimental Details . . . . .	121
3.4.2	Experimental Results . . . . .	137
3.4.3	Discussion . . . . .	165
3.5	Summary of (BEDT-TTF) <sub>3</sub> CuBr <sub>4</sub> . . . . .	176
<b>4</b>	<b>Solid State Properties of (C<sub>1</sub>TET-TTF)<sub>2</sub>Br</b>	<b>178</b>
4.1	Introduction . . . . .	179
4.2	Experimental . . . . .	180
4.3	Experimental Results . . . . .	183
4.4	Discussion . . . . .	197
4.5	Summary . . . . .	201
<b>5</b>	<b>General Conclusion</b>	<b>202</b>



# **Chapter 1**

## **Introduction**

In general, the conduction mechanisms of the organic charge transfer complexes are characterized as the conduction of  $\pi$ -electrons in the low-dimensional space and with the strong electron-electron correlation. These features cause a large variety of the instabilities of the electrical conduction. In addition to the ordinary instabilities, an interesting of my thesis is to investigate the magnetic interactions in organic molecular conductors associated with the correlation between the conduction  $\pi$ -electron and the inorganic counter ion with the localized magnetic moment. On the basis of the interest, I investigated (BEDT-TTF)<sub>3</sub>CuBr<sub>4</sub> in detail, and synthesized new class of the cation radical salts having the magnetic interactions. The other is related to the organic magnetic insulators in view of the low-dimensional magnetism. In this connection, I studied (C<sub>1</sub>TET-TTF)<sub>2</sub>Br in detail.

In this chapter, I introduce general features of the organic conductors in the first section. Secondly, I reveal the Mott-Hubbard system strongly related to the electron-electron correlation in organic conductor. Thirdly, I present the low-dimensional magnetism because the structure of the organic cation radical salts tend to have the low-dimensional structures. Next, I describe the magnetic interactions expected in the organic conductors with the localized magnetic moments. Finally, I review the interesting organic molecular conductors with the localized magnetic moments.

## 1.1 Organic Conductors

### 1.1.1 Outline of Organic Conductors

In this section, I describe the outline of organic conductors in view of the discovery and developments of organic metals, feature of physics and introduction to the magnetic interactions.

In early 1910's, McCoy and Moore [1, 2] suggested that organic solids might exhibit metallic electrical conductivities on the basis of theoretical prediction. After about 40 years from the first theoretical suggestion, the experimental study of organic charge transfer complexes reported by Akamatsu, Inokuchi and Matsunaga [3]

in 1950's made a breakthrough in the development of organic conductors. The next important step was brought about by Ferraris et al. [4] who discovered the first true organic metal TTF-TCNQ (see Fig. 1.1) in 1973. And then, on the basis of the development of organic metals having started often the discovery of TTF-TCNQ, Bechgaard et al. found superconductivity in the quasi-one dimensional salts  $(\text{TMTSF})_2\text{X}$  (X:monovalent anions) under high pressure [5]. Now, more than 20 superconductors of BEDT-TTF salts [6]–[8] have been found mainly in TTF type donors such as TMTSF, BEDT-TTF, BEDT-TSF (see Fig. 1.1). In particular, recently the superconducting complexes are interested in the relation to near the Mott boundary [9]–[12].

Nowadays, the field of organic conductors whose progress has been bringing about the development of a large variety of conductors with different structures and electronic states provides important problems to solid state physicists and physical chemists. According to the basis of the solid state physics, the organic conductors can be characterized as low-dimensional  $\pi$ -electron systems generated by the stacking of  $\pi$ -conjugated molecules with flat shape. In the system, the variety of the electronic instabilities, such as the charge density wave and spin density wave, appear at low temperature, are expected to be caused by the competition between the transfer integral, on-site Coulomb interaction and electron phonon interaction.

In addition to these interests on the low-dimensional conducting system and the correlation among the transfer integral, on-site Coulomb interaction and electron-phonon interaction, the introduction of localized  $d$ -electrons in the charge transfer complexes provide new aspects of the above conducting systems in organic charge transfer complexes. Namely, the localized  $d$ -electrons play a role of magnetism and are expected to bring about similar phenomena to the  $s$ - $d$  interaction in ordinary transition metal magnets. Here, the magnitude of the transfer integral  $t$  is considerably small in comparison with that of the Coulomb interaction  $U$  in the charge transfer complexes. Therefore, the localized  $d$ -electrons in the low-dimensional charge transfer complexes will cooperate to cause new types of electronic insta-

bility different from the ordinary metal magnets or the existing instability in charge transfer complexes. Actually, " $\pi$ - $d$ " interactions as mentioned above give features of electronic and magnetic instability in organic molecular conductors with organic counterparts such as BEDT-TTF, BEDT-TSF, DCNQI's [13]–[17].

Another interest of my thesis is the study of magnetism on the organic molecules. Some organic conductors exist in the Mott insulating regime through the competition among the transfer integral and the on-site Coulomb interaction [18]–[22], and show the interesting magnetic properties with localized magnetic moments of  $\pi$ -electron origin. The complexes belonging to the Mott insulator regime remain not so well understood, although they are expected to give a novel class of molecule-based low-dimensional magnets. Consequently, the investigations are expected to reveal new interesting features of the magnetism among the organic magnetic insulators.

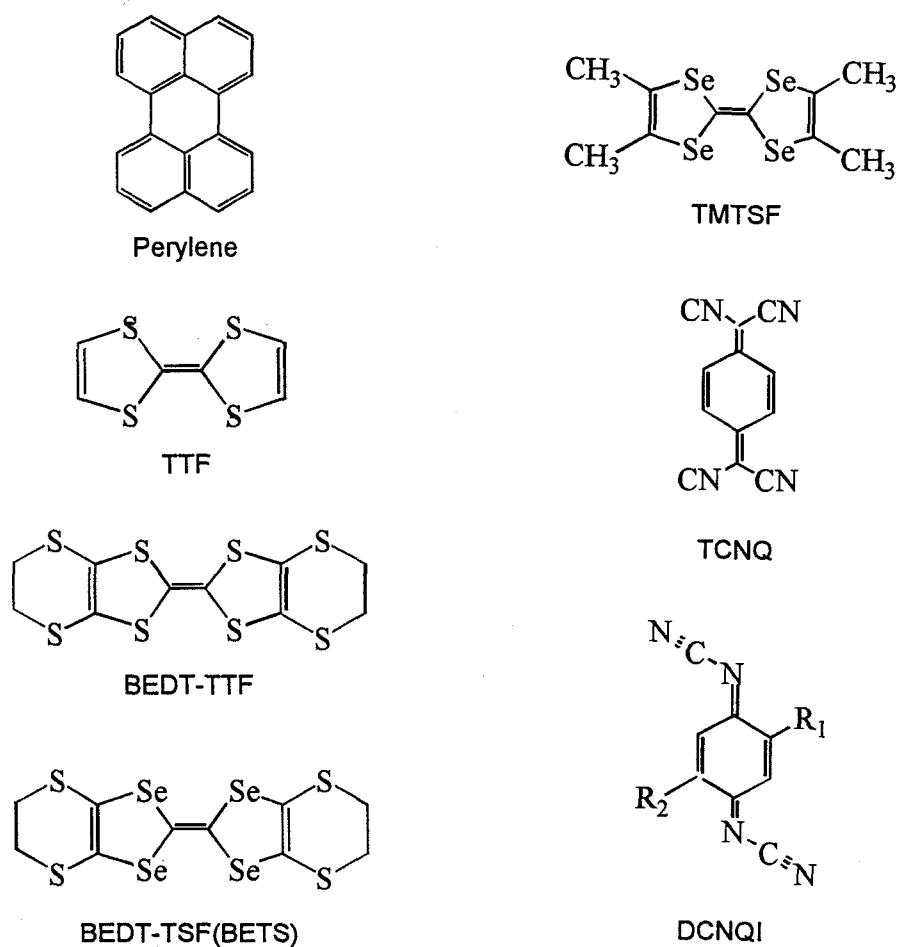


Figure 1.1: Molecular structures of perylene, TTF (tetrathiafulvalene), TMTST (tetramethyltetraselenafulvalene), BEDT-TTF (bis(ethylenedithio) tetrathiafulvalene), TCNQ (7,7,8,8-tetracyano- *p*-quinodimethane), BEDT-TSF (bis(ethylenedithio) tetraselenafulvalene), DMe-DCNQI (2,5-dimethyl- *N,N'*-dicyanoquinonediimine).

### 1.1.2 Feature of Conducting Mechanism

In this section, we discuss the mechanism of the generation of conduction electrons in organic charge transfer complexes, and then, describe the features of electrical properties in terms of the several band filling states.

According to the simple molecular orbital theory, Mulliken's concept of interaction between the charge-transfer and no-bonding structures is considered to correspond to the interaction between the highest occupied molecular orbital (HOMO) of an electron donor having closed shell and the lowest unoccupied molecular orbital (LUMO) of an electron acceptor having open shell as shown in Fig. 1.2. In Fig. 1.2, one electron in the HOMO level is transferred to the LUMO level by the charge transfer interaction, where the charge transfer salt is composed of the upper two conduction levels mainly dominated by the donor orbitals and the lower non-conduction level mainly dominated by the acceptor orbitals. When we employ the inorganic counter ions for the acceptor parts, the conduction bands are mainly described by the donor orbitals, and it contributes the conduction mechanism. Most of organic cation radical salts have these type of the conduction mechanism.

On the basis of the above conduction level, we describe electronic properties in what follows. The conducting properties are described in terms of the degree of the band filling on the conduction band, where three kinds of conducting features are considered mainly for the cation radical salts composed of the organic donors and the inorganic acceptors. The characteristics of degree of the band filling are given in the completely band filling, partially filled band and half-filled band, where the schematic band filling structures are represented in Fig. 1.3.

First, we consider the completely filled band structure as shown in Fig. 1.3 (a). In the band structure, the conduction electron is transferred to excited level beyond the band gap. The typical value of the band gap ranges the value of 0.1-1 eV in ordinary cation radical salts, while, that of the transfer integral is given to be 0.1-0.3 eV. Consequently, the conduction behavior usually shows the semiconductive

type with the activation energy derived from the band gap.

Secondly, we consider the partially filled band structure as shown in Fig. 1.3 (b). In the band structure, the electron transfer to the next molecule do not cause the energy loss of the electronic state of the conduction electron. Consequently, in this band filling, the conduction behavior shows the metallic type.

Thirdly, we present the half-filled band structure as shown in Fig. 1.3 (c). In this band filling, the transfer integral  $t$  to the next molecule overcome the loss of the transfer energy because the difference between the two-electron state and the two-hole state on a molecule cause to raise the energy of the electronic transfer, where the raise of the energy is defined by the on-site Coulomb energy  $U$ . In usual organic conductors, the transfer integral ranges the value of 0.1-0.3 eV, while, the on-site Coulomb energy  $U$  is given to be about 1 eV. Thus, it is difficult that the electron transfer energy  $t$  overcome the on-site Coulomb energy  $U$  in usual organic cation radical salts, resulting in the semiconductive behavior with an activation energy. In addition, the organic salts in the insulating state have the localized moments on the organic donor molecules. As this feature of the half-filled band gives an attractive affect in the organic conductors, we describe the detailed features of the half-filled band structure, as called Mott-Hubbard system, in the next section.

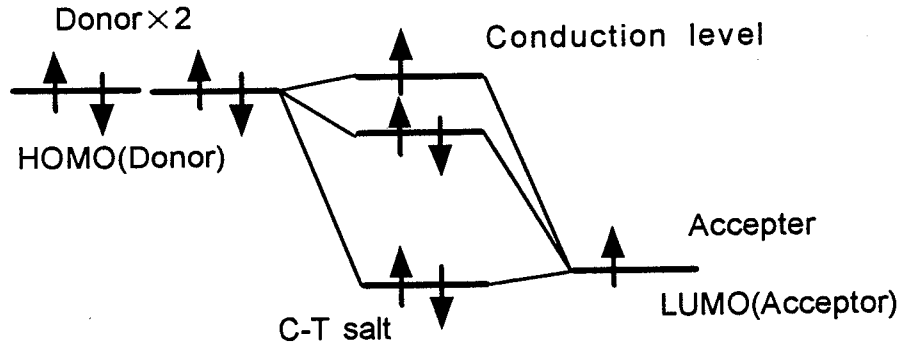


Figure 1.2: Charge-transfer(C-T) interaction between donor and acceptor in a complex with the donor-to-acceptor ratio of 2/1.

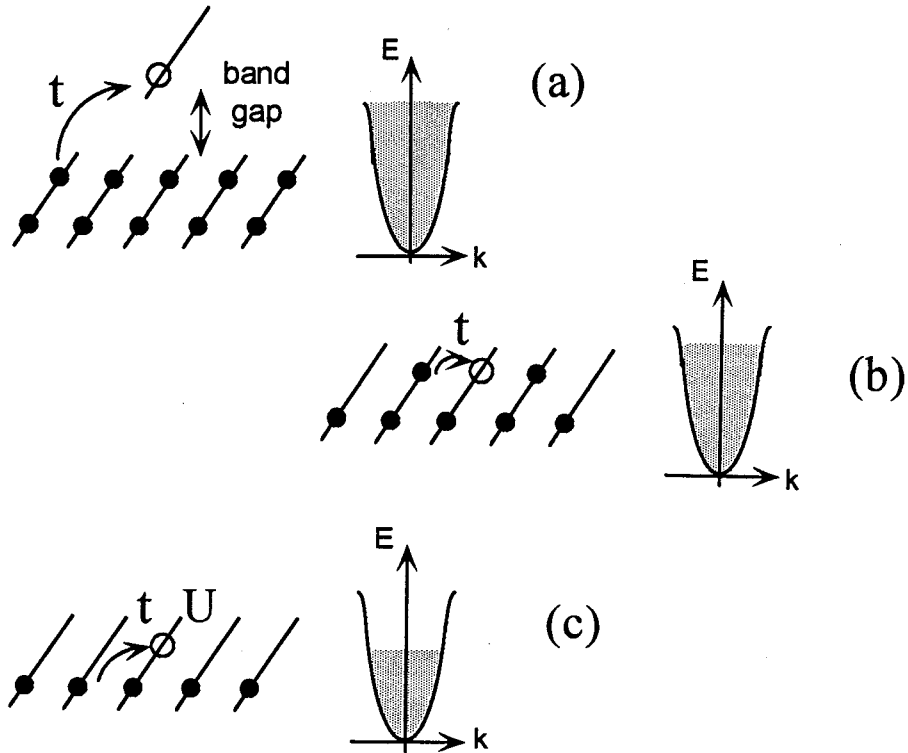


Figure 1.3: The three cases of the band filling, where  $t$  and  $U$  are transfer integral and on-site Coulomb interaction. (a) Completely filled band. (b) Partially filled band. (c) Half-filled band. The solid circle is the electron site. The open circle is the transfer site of the electron.



## 1.2 Mott-Hubbard system

In ordinary organic charge transfer complexes, the on-site Coulomb repulsion  $U$  ranges typically  $U \sim 1$  eV, while the transfer integral  $t$  is in the range of  $t \sim 0.1-0.3$  eV, so that the competition between  $U$  and  $t$  causes a metal-insulator transition (Mott transition) in the complexes with half-filled band structure based on the one-electron approximation without the consideration for Coulomb interaction. Actually, many of organic charge transfer complexes characterized as half-filled band structures show interesting conductive and magnetic properties originating from the strong electron-electron correlation. Thus, I give a summary of Mott-Hubbard system.

For understanding the feature of the half-filled band with the competition between the transfer integral and the on-site Coulomb interaction, I introduce the simplified Hamiltonian as called Hubbard Hamiltonian [23],

$$\mathcal{H} = - \sum_{i,j} t_{ij} a_{i\sigma} a_{j\sigma}^\dagger + U \sum_i n_{i\uparrow} n_{i\downarrow}. \quad (1.1)$$

Here,  $U$  is the on-site Coulomb repulsion defined by  $U = \langle e^2 / \alpha r_{12} \rangle$  ( $\alpha$ : polarizability,  $r_{12}$ : the distance between two electrons when they are at the same molecule),  $t_{ij}$  is the transfer integral between two sites  $i$  and  $j$  which is equal to  $W/2z$  ( $W$ : band width,  $z$ : coordination number).  $a_{i\sigma}^\dagger$  and  $a_{j\sigma}$  are a creation operator and an annihilation operator with spin state  $\sigma$  for site  $i$  and  $j$ , respectively. In this model, the competition between  $U$  and  $t$  influences the conductive and magnetic properties especially for the complexes with the half-filled band structure.

In the range of  $U \gg W$ , the band structure with the consideration for Coulomb interaction is split into upper and lower bands as shown in Fig. 1.4, where the lower band is completely filled by electrons. This is called a Mott insulator, in which the conductive and the magnetic properties are described in terms of semiconductive behavior having localized magnetic moments. And, the magnetism is described by antiferromagnetic Heisenberg model with the magnetic exchange interaction  $J = -2t_{ij}^2/U$ .

In the range of  $U \sim W$ , the interesting property is caused by the competition

between  $U$  and  $t$ . Namely, with increasing the band width  $W$  from the insulator side ( $U > W$ ), a metal-insulator transition appears at  $U \simeq W$  when the split bands by Coulomb energy  $U$  overlap, where the transition is called as "Mott transition" or "Mott-Hubbard transition".

In  $U \ll W$ , the band structure is described by a simple metal. However, on the metallic side near this transition ( $U \leq W$ ), the material in this range shows the interesting conductive and magnetic behavior. That is, the temperature dependence of the conductivity is different from that of normal metal and the magnetic susceptibility indicates the enhanced Pauli paramagnetism generated by the strong electron correlation.

Actually, the interesting features in view of the ratio  $W/U$  appear in the phase diagram of  $V_2O_3$  [24, 25] as shown in Fig. 1.5, which is situated around the boundary of the Mott-Hubbard regime. In  $V_2O_3$ , the amount of the doping of Cr or Ti for pure  $V_2O_3$  (chemical pressure) can corresponds to the external pressure (physical pressure). The applying the chemical or physical pressure changes the parameter  $W/U$  with changing the band width. In the high temperature and the low pressure side of the phase diagram, the material shows the insulator behavior and the localized paramagnetism which is called as the Mott insulator. The increasing the pressure from the Mott insulator side cause the insulator-metal transition (Mott transition) and stabilize the metallic state in the high pressure side. Meanwhile, the lowering the temperature in the insulator or metal phase brings about the transition to the antiferromagnetic insulator phase where the localized spins are aligned antiparallely. As mentioned above, the competition between the transfer integral and the on-site Coulomb interaction shows interesting features in the electronic and the magnetic properties.

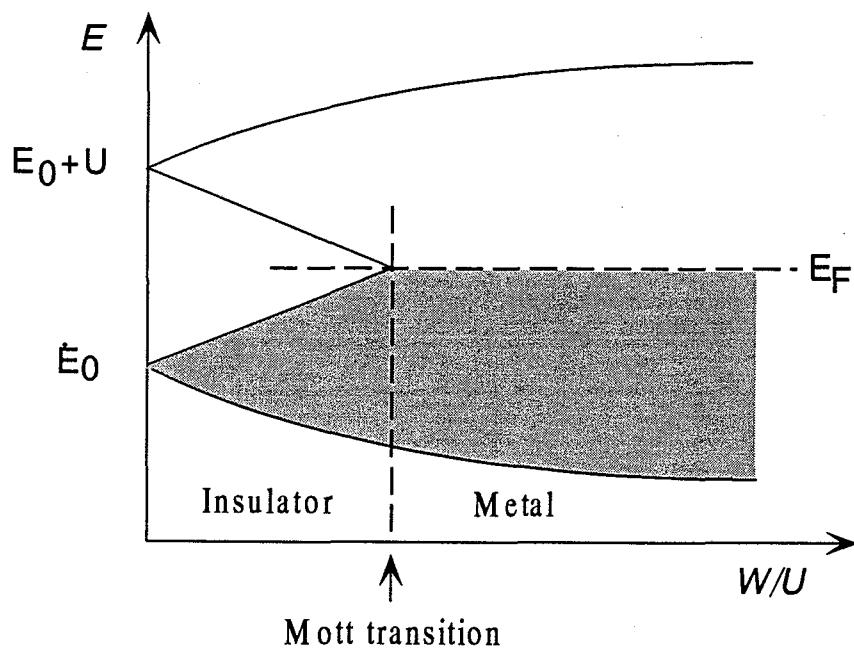


Figure 1.4: Schematic picture of the half-filled band described in terms of the on-site Coulomb  $U$  and the band width  $W$ . The hatched area is filled by the electrons.  $E_0$  is defined as the conduction level. The increasing the parameter  $W/U$  cause the Mott transition at  $W/U \sim 1$  originating from the overlap of the split bands.

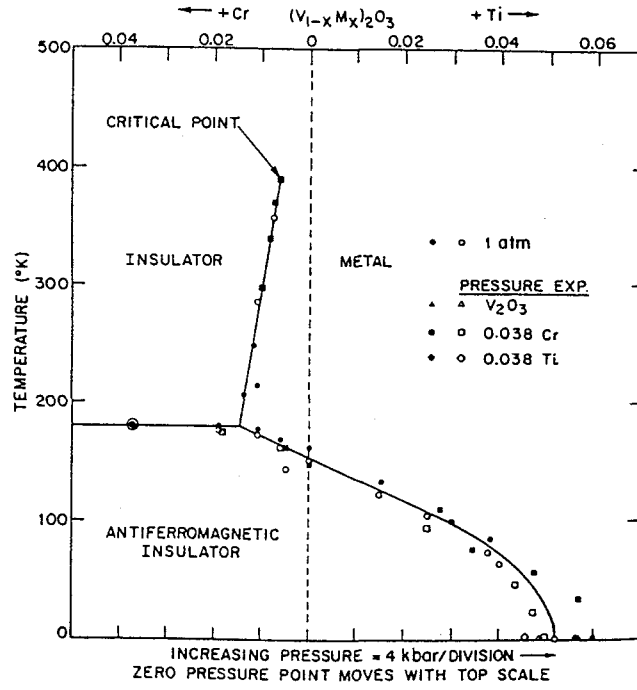


Figure 1.5: Phase diagram of  $V_2O_3$  as a function of dopant concentration with Cr or Ti and as a function of pressure [24, 25]. The metal-insulator boundary terminates at a critical point. The insulator in the high temperature and low pressure range is described by a Mott insulator. The increase of the pressure brings about a Mott metal-insulator transition and stabilize the paramagnetic metal state in the high pressure region. In the antiferromagnetic insulator state, the localized spins are aligned antiparallely.

### 1.3 Low-Dimensional Magnetism

Usually, the organic charge transfer complexes form the low-dimensional crystal structures. In these complexes, the anion arrangements are also composed of the low-dimensional structures. Thus, in the organic conductors with the counter anions having the localized magnetic moments, the magnetic sites consist of the low-dimensional magnetic structures. Moreover, in the Mott insulating regime ( $U > W$ ), the organic molecules having the magnetic moments also give the low-dimensional magnetic structures. In the present investigation, I have been studying the physical properties of organic conductors (BEDT-TTF)<sub>3</sub>CuBr<sub>4</sub> and (C<sub>1</sub>TET-TTF)<sub>2</sub>Br those are composed of the two-dimensional magnetic structures. Consequently, we need to have the knowledge of the low-dimensional magnetism to discuss the present consequences of magnetic properties.

The simple characteristics of the magnetic properties are described by the Heisenberg, XY and Ising interaction (ferro or antiferromagnet) on the magnetic lattice with one, two and three-dimensionality. Here, the generalized exchange Hamiltonian is written by the following equation,

$$\mathcal{H} = -2J \sum_{ij} (a(S_i^x S_j^x + S_i^y S_j^y) + b S_i^z S_j^z), \quad (1.2)$$

where  $i, j$  are the sites of the magnetic moments, which are summed up for all the adjacent sites and  $J$  is the constant of the exchange interaction. In  $a=b=1$ , the magnetic interaction shows the Heisenberg type nature, where the spin angular momentum  $S$  is isotropic. Moreover, the anisotropic Ising interaction is obtained by the setting  $a=0, b=1$ , and, for  $a=1, b=0$ , the system is called the XY model, where the orientation of spins are constrained within the  $xy$  plane.

The dimensionality of the magnetic lattice is defined as the dimensionality of the exchange interaction network. Depending on the relative strengths of exchange interactions, three, two and one-dimensional magnetic lattices are obtained for  $J_1 \sim J_2 \sim J_3$ ,  $J_1 \sim J_2 \gg J_3$  and  $J_1 \gg J_2 \sim J_3$ , respectively, as shown in Fig. 1.6.

The dimensionality of the interaction and the anisotropy of the spin influences

the magnetic phase transition governed by the fluctuation of the magnetic correlation between the magnetic moments. Figures 1.7 and 1.8 show the characteristic temperature dependence of the specific heat for the systems with different dimensionality of the interaction and the anisotropy of the spin [26]. For the three or two-dimensional Ising model, a phase transition of magnetic long-range-order, which is reflected as a divergence in the specific heat, occurs at a finite temperature  $T_c$ , whereas  $T_c$  is lowered in comparison with the prediction by the molecular field theory. Moreover, in pure one-dimensional Ising model, the ordered phase does not appear above zero temperature, and the entropy shows short range order feature with a Schottky-type anomaly. On the other hand, the three-dimensional Heisenberg lattice possess a phase transition at a finite temperature. However, in the two or one-dimensional Heisenberg lattice, the magnetic long-range-order does not appear at the finite temperature similar to the one-dimensional Ising system. As described above, the decreases of the dimensionality of the interaction and the magnetic anisotropy of the spin from Ising system to Heisenberg system enhances the magnetic short-range-order effect because the short-range-order is governed by the fluctuation of the magnetic moments which is enhanced by the decrease of the magnetic anisotropy.

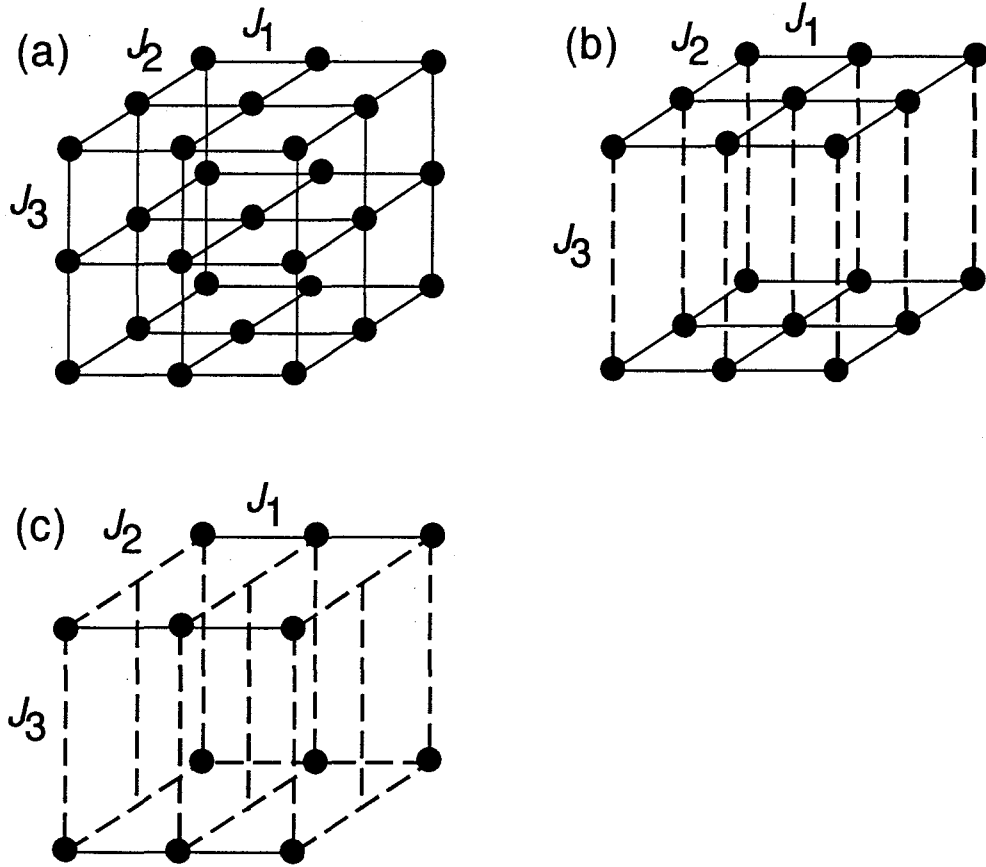


Figure 1.6: Dimensionality of the exchange interaction network. (a) three-dimensional ( $J_1 \sim J_2 \sim J_3$ ), (b) two-dimensional ( $J_1 \sim J_2 \gg J_3$ ), (c) one-dimensional ( $J_1 \gg J_2 \sim J_3$ ).

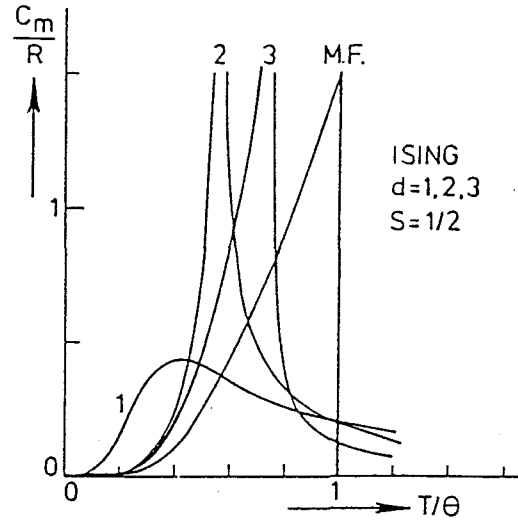


Figure 1.7: Specific heats  $C_m$  of the  $S=1/2$  Ising model in one, two and three-dimensions in comparison with molecular-field (MF) theory [26], where the temperature is nomarized by the Weiss temperature  $\theta$ .

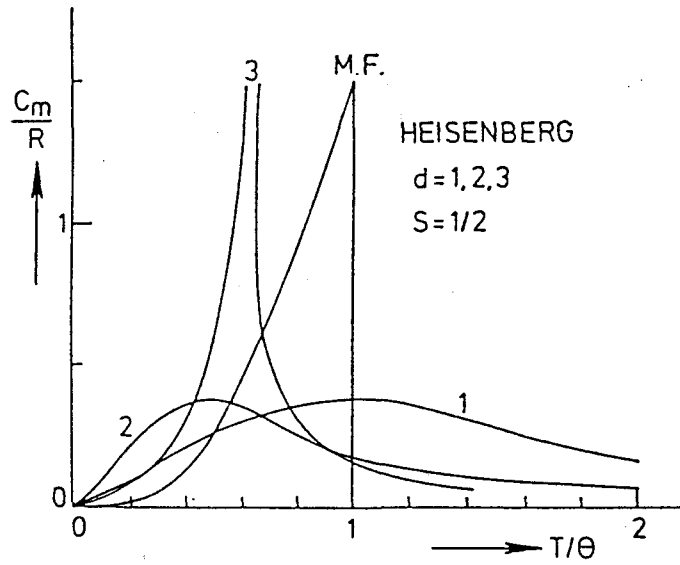


Figure 1.8: Specific heats of the  $S=1/2$  Heisenberg model in one, two and three-dimensions in comparison with molecular field theory [26], where the temperature is nomarized by the Weiss temperature  $\theta$ .



## 1.4 Magnetic Interactions

In the previous section, we describe the features of low-dimensional magnets, however, we did not characterize the origin of the magnetic interaction. Thus, we discuss the origin of magnetic interactions between the localized magnetic moments. In addition, we describe the ordinary *s-d* interaction which is the magnetic exchange interaction between the conduction *s*-electron and the localized *d*-electron.

At the beginning, we represent the magnetic interactions between the localized moments in the magnetic insulator. In the classical regime, the magnetic interaction is given by the magnetic dipole-dipole interaction as represented by the next equation,

$$\frac{\boldsymbol{\mu}_1 \cdot \boldsymbol{\mu}_2}{r_{12}^3} - 3 \frac{(\boldsymbol{\mu}_1 \cdot \mathbf{r}_{12})(\boldsymbol{\mu}_2 \cdot \mathbf{r}_{12})}{r_{12}^5}, \quad (1.3)$$

where  $\boldsymbol{\mu}_1$ ,  $\boldsymbol{\mu}_2$  refer to the magnetic moments and  $\mathbf{r}_{12}$  is the vector of the distance between the magnetic sites. In ordinary crystals with the inter-moment distance ranging 2Å, the magnitude of the dipolar energy is estimated at the order of 0.1 K. The value is too weak to explain the exchange energy and the magnetic transition temperature in the ordinary inorganic magnetic insulators. Thus, we need to reveal the other interactions as will be described below.

In the ordinary magnetic insulators, most of the magnetic properties are described by the quantum mechanism in the exchange interaction. The exchange interaction is given by

$$- 2JS_1 \cdot S_2, \quad (1.4)$$

where  $J$  denotes the exchange interaction energy between the magnetic sites, and  $S_1$  and  $S_2$  are the spin operators at magnetic sites. There are two kinds of exchange interaction mechanisms between the magnetic sites in a magnetic insulator. The one is the direct exchange interaction, which is generated by the exchange integral of Coulomb interaction in the direct orbital overlapping of the magnetic ions. The

exchange interaction is represented by the following equation,

$$J_{\text{direct}} = \int \varphi_i^*(\mathbf{r}_1) \varphi_j^*(\mathbf{r}_2) \frac{e^2}{r_{12}} \varphi_j(\mathbf{r}_1) \varphi_i(\mathbf{r}_2) d\tau_1 d\tau_2, \quad (1.5)$$

where  $\varphi(\mathbf{r}_1)$  and  $\varphi(\mathbf{r}_2)$  are the wave functions of the magnetic ions or molecules. The other is the superexchange interaction, which is generated by the exchange interaction through the non-magnetic site. The exchange energy of the superexchange interaction is given by

$$E_{\text{super}} = - \sum_{ij} \frac{|b_{ij}|^2}{U} \left( \frac{1}{2} - 2\mathbf{S}_i \cdot \mathbf{S}_j \right), \quad (1.6)$$

where  $b_{ij}$  is the transfer integral between the site  $i$  and  $j$ , and  $U$  is the energy of Coulomb repulsion. In this interaction, the parallel spin arrangement gives the zero value in the above equation, indicating that the superexchange interaction stabilizes the antiparallel spin arrangement.

The above is the interaction in the magnetic insulators, however, in the sea of the conduction electrons the magnetic moments give the other interesting phenomena through the magnetic interaction between the conduction electrons and the localized moment. We describe the magnetic interactions in the metal magnets below.

In a dilute alloy with  $3d$  impurities such as Fe, Mn in Cu, Au, Ag and in  $4f$  metals, the impurity atoms have localized magnetic moments which interact with conduction electrons through the exchange interaction called by  $s$ - $d$  or  $s$ - $f$  interaction. A model consisting of the conduction electrons and the localized  $d$  or  $f$  electrons is given by the following  $s$ - $d$  Hamiltonian,

$$\mathcal{H}_{s-d} = -\frac{1}{N_0} \sum_{kk'} \sum_j J_{kk'} [(a_{k\uparrow}^\dagger a_{k'\uparrow} - a_{k\downarrow}^\dagger a_{k'\downarrow}) S_{jz} + a_{k\uparrow}^\dagger a_{k'\downarrow} S_{j-} + a_{k\downarrow}^\dagger a_{k'\uparrow} S_{j+}], \quad (1.7)$$

where  $N_0$  is the number of atoms,  $J_{kk'}$  is the exchange interaction between the conduction electron and the magnetic moment,  $S_j$  is the localized spin at site  $j$ ,  $a_{k\uparrow}^\dagger$  and  $a_{k'\downarrow}$  are creation and annihilation operators of the electrons, respectively. In the well-diluted limit, there is the absence of the direct exchange interaction between the localized moments. In this case, the conduction electron is scattered by the

spin reversal process through the  $s$ - $d$  interaction, which causes the appearance of a minimum point in the resistivity vs temperature plots at low temperature as called the "Kondo effect".

The increasing the magnetic impurity concentration makes the indirect coupling between the localized moments through  $s$ - $d$  interaction, and then it gives rise to the ferromagnetism, antiferromagnetism and spin glasses states depending on the crystal structures. The indirect interaction is called as "RKKY (Ruderman, Kittel, Kasuya and Yoshida ) interaction". According to the theory of RKKY interaction, the spatial variation of the spin polarization leads to indirect coupling between two localized magnetic moments as given by the following equation,

$$V_{jl} = -J_{sd}^2(2mk_F^4/\pi^3)F_0(2k_FR_{jl})\mathbf{S}_j\mathbf{S}_l, \quad (1.8)$$

$$F_0(x) = -\frac{\cos x}{x^3} + \frac{\sin x}{x^4}, \quad (1.9)$$

where  $V_{jl}$  is the interaction energy between  $j$  and  $l$  sites,  $J_{sd} = v_0 J_{kk'}$ ,  $v_0$  being the atomic volume,  $m$  is magnetization on the  $j$  site,  $k_F$  is the Fermi radius,  $R_{jl}$  the distance between the  $j$ th and  $l$ th atoms, then  $\mathbf{S}_j$  and  $\mathbf{S}_l$  are the spin angular momentum operator at the localized site  $j$  and  $l$ . The interaction energy oscillates with changing the sign at a cycle of  $1/2k_F$  with increasing  $R_{jl}$ , where the amplitude decreases gradually as a function of  $1/R_{jl}^3$ . Thus, the magnetic interaction reaches to the other magnetic sites away from the scattering magnetic ion. Moreover, it is possible to cause the ferromagnetic interaction depending on the crystal structure because the magnetic interaction is transmitted with the changing the sign of the magnetisation of the conduction electron. In particular, RKKY interaction in the small  $k_F$  such as the organic  $\pi$ -conductor is expected to give the ferromagnetic interaction through the long distance derived from the oscillating cycle of  $1/2k_F$ .

## 1.5 Organic Conductors with Localized Magnetic Moments

There are mainly three kinds of cases to generate magnetic moments among organic charge transfer complexes and organic radical compounds. First, magnetic counter ions are introduced into the organic cation radical salts, where there is the coexistence of the magnetic moment on the counter anion and the conduction  $\pi$ -electrons on the organic donors. Secondly, Mott insulating state generates the magnetic moments of  $\pi$ -electron origin on the organic molecules due to the competition between the on-site Coulomb repulsion and the transfer integral. The magnetic properties are described in terms of the antiferromagnetic Heisenberg systems with the exchange interaction  $J=-2t^2/U$ . Thirdly, the stabilization of free radicals in the crystals provides the localized spins, some of which show the ferromagnetic transitions at low temperatures. In the present thesis, we discuss the first case in  $(\text{BEDT-TTF})_3\text{CuBr}_4$  and the second case in  $(\text{C}_1\text{TET-TTF})_2\text{Br}$ . To clarify the magnetic interactions in the present compounds, we review the solid state properties having the magnetic moment in the above two cases in what follows.

### 1.5.1 $\pi$ - $d$ systems

Organic conductors  $(\text{BEDT-TTF})_4(\text{H}_2\text{O})\text{Fe}(\text{C}_2\text{O}_4)_3\cdot\text{C}_6\text{H}_5\text{CN}$ ,  $\lambda$ -(BETS) $_2\text{FeCl}$  and  $(\text{DMe-DCNQI})_2\text{Cu}$  represent the materials belonging to the first class where the magnetic moments are presented by the localized 3- $d$  electrons.

$(\text{BEDT-TTF})_4(\text{H}_2\text{O})\text{Fe}(\text{C}_2\text{O}_4)_3\cdot\text{C}_6\text{H}_5\text{CN}$  is a novel system discovered as the first organic superconductor including magnetic anions [27, 28]. It consists of alternative stacking of BEDT-TTF and  $\text{Fe}(\text{C}_2\text{O}_4)_3^{3-}$  layers, where Fe ion has an  $S=5/2$  spin as shown in Fig. 1.9. It shows metallic behavior and a sharp transition to superconductivity at  $T_c=7.0$  K. The magnetic susceptibility above  $T_c$  is explained in terms of the contributions of the Pauli paramagnetism and the Curie-Weiss paramagnetism with the weak antiferromagnetic Weiss temperature  $\theta=-0.2$  K as shown

in Fig. 1.10. ESR spectra is characterized with two resonances signals due to the conduction electrons on the BEDT-TTF molecules and the localized  $3d$ -electrons on the Fe(III) ions, which indicates the significantly small magnetic interaction between the conduction  $\pi$ -electrons and the localized  $d$ -electrons. Usually, a superconducting state can not coexists with a ferromagnetic state because the superconducting state are broken by the internal field of the magnetic moments below the ferromagnetic transition temperature. For instance, the boride  $\text{ErRh}_4\text{B}_4$  shows a superconducting transition at 9 K, and then indicates ferromagnetic transition at 0.9 K with the breaking superconducting state [29]. On the other hand, an antiferromagnetic state coexists a superconducting state even below the antiferromagnetic transition. For example, in the Chevrel  $\text{GdMo}_8\text{S}_8$ , a superconducting transition appears at 1.3 K, and then, it shows an antiferromagnetic transition at 0.85 K with retaining the superconducting state below the antiferromagnetic transition [30]. These ferro- or antiferromagnetic superconductor have characteristic crystal structures, namely, the conduction carrier sites are composed far from the magnetic ion sites, resulting in the small exchange interaction between the conduction electrons and the magnetic moment. The features are similar to  $(\text{BEDT-TTF})_4\text{H}_2\text{OFe}(\text{C}_2\text{O}_4)_3\text{C}_6\text{H}_5\text{CN}$ , where the observation of EPR signal proves the absence of magnetic interaction between the conduction electrons on BEDT-TTF donors and the localized electron on  $\text{Fe}^{3+}$  ion. Consequently, in this organic magnetic superconductor, the significantly weak interaction between the conduction electron and the magnetic moment stabilizes the superconducting state. Moreover, the susceptibility measurement at the lower temperature is expected to observe an antiferromagnetic transition, which will clarify the characteristic of the superconducting state in this compound.

$\lambda\text{-(BETS)}_2\text{FeCl}_4$  has the alternate stacking structure of BETS donor layer and  $\text{FeCl}_4^{2-}$  magnetic layer as shown in Fig. 1.11 [31], where the shortest  $\text{Fe}^{3+}$  ion distance is 6.593 Å, and the shortest Cl...Se and Cl...S contacts are 3.528 and 3.417 Å, respectively. The resistivity shows a novel metal-insulator transition accompanied by an antiferromagnetic transition at 8 K as seen in Fig. 1.12 (a) [32]. The metal-

insulator transition temperature decreases rapidly with the application of pressure, then the resistivity indicates the metallic behavior in the whole temperature range above 4 kbar. Figure 1.12 (b) shows the band structure split in two sub-bands by the dimerization which cause the intrinsic half-filled band structure. The magnetic susceptibility shows the Curie-Weiss behavior with antiferromagnetic Weiss temperature  $\theta = -15$  K and an antiferromagnetic transition at  $T_N = 8$  K as shown in Fig. 1.13 [33]. The spin-flop field  $H_{sf}$  and the saturation field  $H_c$  are estimated at  $H_{sf} = 1$  T and  $H_c = 10$  T, respectively. Moreover, the resistivity measurement with applied field shows the characteristic behavior, namely, the insulating state below 8 K under ambient pressure disappears at 10 T and the metallic state is restored above 10 T as shown in Fig. 1.14 [32]. The observation of the metal-insulator transition and the antiferromagnetic transition at the same temperature suggests the presence of exchange interaction between the conduction  $\pi$ -electron and the localized moment. Here, the shortest distance between the magnetic  $\text{Fe}^{3+}$  ions is 6.593 Å [32] which is not so long distance for the exchange interaction within the anion layer. Thus, the antiferromagnetic transition is considered to be caused by the intralayer interaction between  $\text{Fe}^{3+}$  ions. Moreover, this antiferromagnetic transition is thought to cause the metal-insulator transition at 8 K. Namely, the metal-insulator transition is generated from a gap formation in the half-filled band induced by the periodic potential of the antiferromagnetic ordering. This consideration explains to restore the metallic state with the applied field below  $T_N$ . That is, the application of the field dissolves the periodic potential of the antiferromagnetic ordering with changing to the ferromagnetic state. Actually, the insulator-to-metal transition field  $H = 10$  T is in good agreement with the estimated magnetic saturation field  $H_c = 10$  T, which follows the above consideration. For the detailed discussion, we need to have the information of the exchange interaction energy between the conduction  $\pi$ -electrons and the localized  $d$ -spin using EPR measurement.

A family of organic compounds  $(2-R_1-5-R_2\text{-DCNQI})_2M$  ( $R_1, R_2 = \text{CH}_3, \text{CH}_3\text{O}, \text{Cl}, \text{Br}, \text{I}$ ;  $M = \text{Cu}, \text{Ag}, \text{Li}, \text{Na}, \text{K}, \text{NH}_4$ ) have 1D columnar network structure of DC-

NQI molecules, and show various physical properties by the substitution of  $R_1$ ,  $R_2$  sites and  $M$  metals. Among these DCNQI salts,  $(R_1R_2\text{-DCNQI})_2\text{Cu}$  ( $R_1, R_2 = \text{DMe, DMeO, MeBr, MeCl}$ ) show novel electrical and magnetic properties as functions of temperature and pressure. Thus, I describe the electrical and the magnetic properties in terms of the  $\pi$ - $d$  mixing effect.

$(R_1R_2\text{-DCNQI})_2\text{Cu}$  have a 1D column structure of DCNQI molecules and the column networks are bridged by Cu ions as shown in Fig. 1.15, where the column of DCNQI generates the conduction electrons [17]. Figure 1.16 shows the pressure-temperature phase diagram of  $(R_1R_2\text{-DCNQI})_2\text{Cu}$  obtained by the results of electrical resistivities [35]. In the pressure-temperature phase diagram, the metal-insulator boundaries of all  $(R_1R_2\text{-DCNQI})_2\text{Cu}$  salts, which are normalized by the critical pressure of  $(\text{DMe-DCNQI})_2\text{Cu}$ , are almost same one as shown in Fig. 1.16 [35]. Among the salts,  $(\text{DMe-DCNQI})_2\text{Cu}$  shows an interesting re-entrant metal-insulator-metal transition in the significantly low pressure region of 100-200 bar as mentioned later. Moreover, the deuterations of the methylene groups in  $(\text{DMe-DCNQI})_2\text{Cu}$  salt, as seen in Table 1.1, give drastic isotope effects, namely, the deuterated salts indicates the re-entrant metal-insulator-metal transition without the application of the pressure. This is considered that the deuterations of the methylene groups and/or the proton sites cause the slight decrease of the lattice constants, resulting in inducing the chemical pressure effects similar to the external pressure as shown in Table 1.1. The magnetic susceptibility indicates the re-entrant transition at the same temperature observed in the electrical properties as shown in Fig. 1.17. That is, the d8-salt shows the Pauli paramagnetic behavior above 80 K, and it shows a sharp increase at 80 K with the metal-insulator transition and Curie-Weiss behavior below 80 K. Furthermore, the susceptibilities of d2- or d3-salts also show the re-entrant transition with the metal-insulator-metal transition, where the susceptibility in the insulating state obeys Curie-Weiss law with  $1/3$  mol spin of  $\text{Cu}^{2+}$  [34].

Next, we discuss the origin of the interesting transition of  $(\text{DMe-DCNQI})_2\text{Cu}$  accompanied by the physical and the chemical pressure. Figure 1.18 (a) shows the

interaction diagram between the  $d$ -orbitals of Cu and the organic one-dimensional band, where the  $d_{xy}$  orbital forms the hybridized wave function with the HOMO of DCNQI molecule. The hybridized wave function of HOMO of DCNQI and  $d_{xy}$  forms multiple Fermi surfaces in (DMe-DCNQI)<sub>2</sub>Cu as shown in Fig. 1.18 [36]. Since the presence of the multiple Fermi surfaces works to avoid the 1D Peierls instability, (DMe-DCNQI)<sub>2</sub>Cu shows metallic behavior in the whole temperature range under ambient pressure. Meanwhile, under pressure, it shows a metal-insulator (M-I) transition accompanying with  $3k_F$  charge density wave and charge ordering of Cu ions. In the high temperature range above the M-I transition, the Cu ions have uniform charge distribution with  $+4/3$  per Cu ion, while, in the insulating phase Cu ions have the mixed valency of  $+1$  and  $+2$  [35]. Further, the drastic physical and chemical pressure effect mechanism is considered as below. Namely, the application of pressure causes a slight distortion of the ligands symmetry of Cu ion, and the distortion of the ligand symmetry raises the energy level of the  $d_{xy}$  orbital, which cause the increase of the strength of the charge transfer from Cu ion to DCNQI. The increase of the charge transfer to DCNQI under pressure causes the approach to  $+4/3$  valence on the Cu ion, resulting in inducing  $-2/3$  state of DCNQI molecules. As described above, in (DMe-DCNQI)<sub>2</sub>Cu salts, the slight structural deformation generates a drastic change in electrical and magnetic properties associated with  $\pi-d$  mixing interaction.

### 1.5.2 Mott-Hubbard systems

In many BEDT-TTF salts, some Mott insulators (BEDT-TTF)<sub>2</sub>X (X=AuBr<sub>2</sub>, CuCl<sub>2</sub>, ICl<sub>2</sub>, IBr<sub>2</sub>, Cu<sub>2</sub>(CN)[N(CN)<sub>2</sub>]<sub>2</sub>) are found out in Refs. [19]–[22]. They are expected to give new aspects in low-dimensional magnet because of interesting magnetic structures accompanying a variety of crystal structures. Here, I introduce the structures and the physical properties of the typical Mott insulator  $\beta'$ -(BEDT-TTF)<sub>2</sub>ICl<sub>2</sub>.



$\beta'$ -(BEDT-TTF) $_2$ ICl $_2$  has the two-dimensional donor arrangement, where the donor molecules dimerized in the  $bc$ -plane as shown in Fig. 1.19 [22]. The band structure has two sub-bands split by the strong donor dimerization, which leads to the intrinsic half-filled band structure as shown in Fig. 1.20. The electrical resistivity shows semiconductive behavior with the activation energy  $E_a=0.12$  eV. Figure 1.21 gives the magnetic susceptibility in the applied field parallel to  $a^*$ ,  $b$  and  $c$ -axes [20]. It shows a magnetic short range order hump around 110 K, and it indicates an antiferromagnetic transition at  $T_N=22$  K. Taking into account that the donor dimer units are described by the two-dimensional square lattice, the analysis of the magnetic hump using the two-dimensional square lattice Heisenberg antiferromagnet model results in the number of spins  $N=1$  spin/dimer and the exchange energy  $J=-59$  K. It is noticeable that the susceptibility is described by the point localized model although the distribution of the magnetic moment is extended to the whole area of the dimerized donor molecules. In addition, the ratio of the anisotropy field  $H_A$  to the exchange field  $H_E$  is estimated at  $H_A/H_E \sim 2.0 \times 10^{-5}$  [20]. The significantly small value proves the feature of an isotropic Heisenberg magnet in (BEDT-TTF) $_2$ ICl.

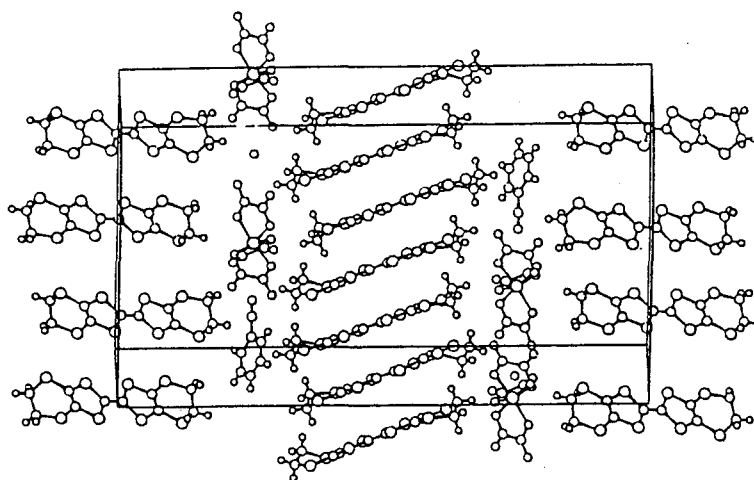


Figure 1.9: Alternating stacking of the BEDT-TTF conducting layers and magnetic  $\text{Fe}^{\text{III}}(\text{C}_2\text{O}_4)_3^{3-}$  anion layers in  $(\text{BEDT-TTF})_4(\text{H}_2\text{O})\text{Fe}(\text{C}_2\text{O}_4)_3 \cdot \text{C}_6\text{H}_5\text{CN}$  [28].

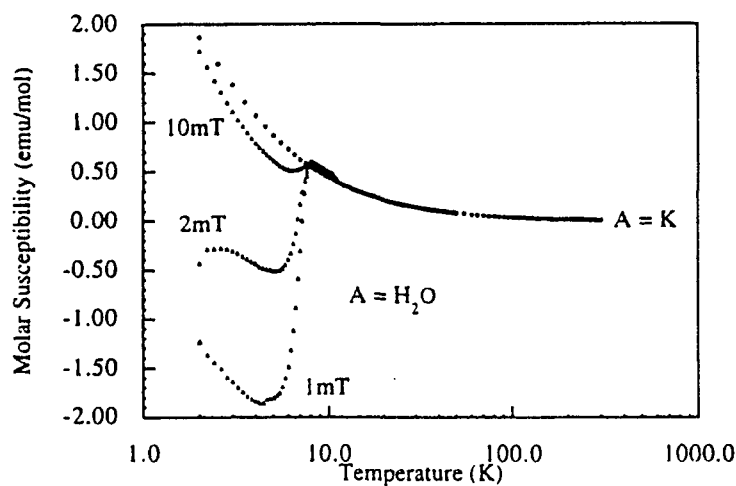


Figure 1.10: Temperature dependence of magnetic susceptibility of  $(\text{BEDT-TTF})_4\text{AFe}(\text{C}_2\text{O}_4)_3 \cdot \text{C}_6\text{H}_5\text{CN}$  under the magnetic field with different strength [28].  $\text{A}=\text{K}$  (dot) salt does not show superconducting state, while,  $\text{A}=\text{H}_2\text{O}$  salt shows the superconductivity. The superconducting state of  $\text{H}_2\text{O}$  salt is destroyed by significantly weak field.

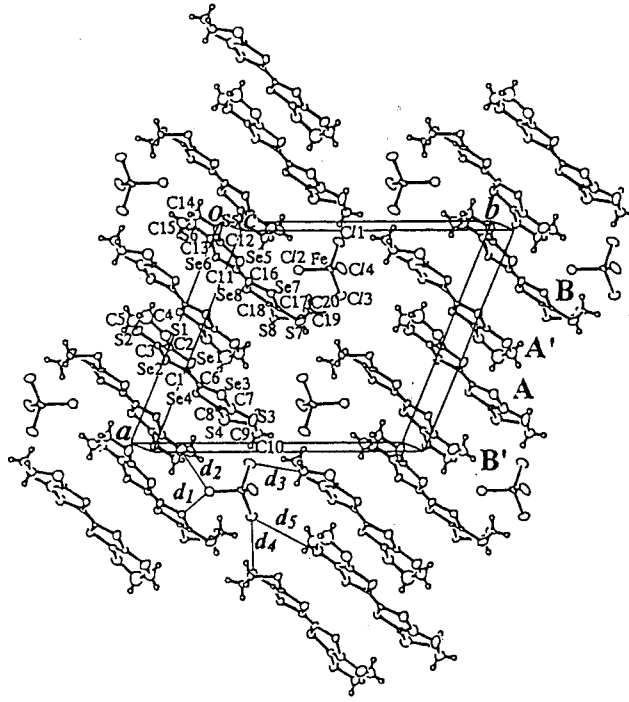


Figure 1.11: Crystal structure of  $\lambda$ -(BETS) $_2$ FeCl $_4$  [31]. A and B are two independent BETS molecules. The short Cl...S (Se) contacts are  $d_1$ (Cl...Se)=3.528,  $d_2$ (Cl...S)=3.417,  $d_3$ (Cl...S)=3.642,  $d_4$ (Cl...S)=3.648,  $d_5$ (Cl...S)=3.648 Å.

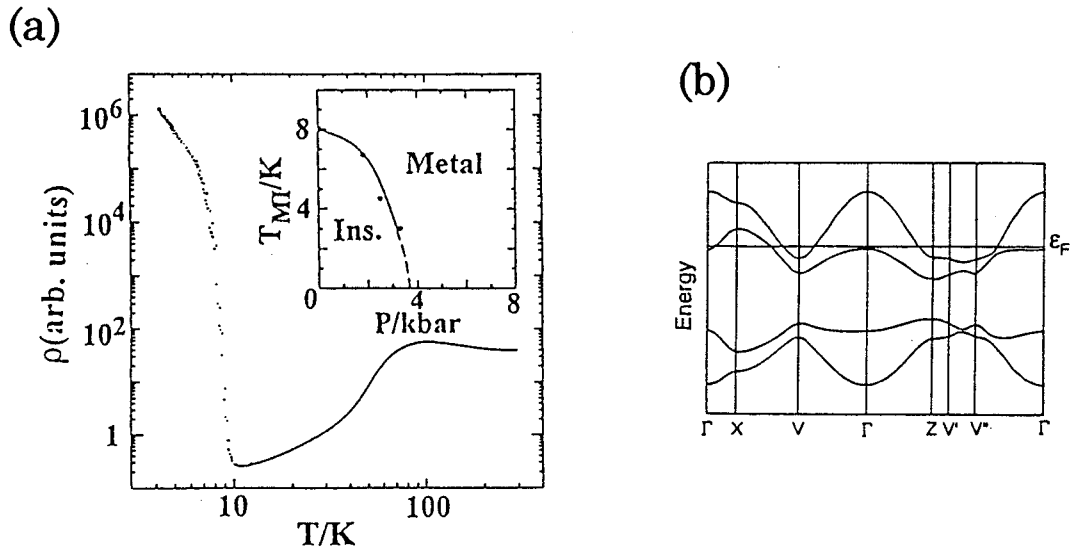


Figure 1.12: (a) Temperature dependence of resistivity and band structure of  $\lambda$ -(BETS) $_2$ FeCl $_4$  [32]. The resistivity shows a metal-insulator transition at 8 K. The inset indicates the pressure-temperature phase diagram, where the transition temperature decrease rapidly with the application of pressure. (b) The band structure has the intrinsic half-filled band structure.

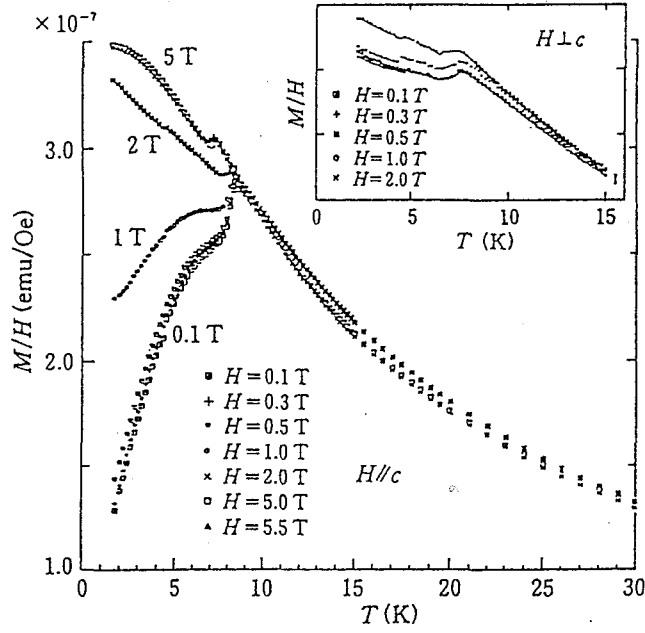


Figure 1.13: Magnetic susceptibility of  $\lambda$ -(BETS) $_2$ FeCl $_4$  [33]. It shows the temperature dependence of Curie-Weiss type just above an antiferromagnetic transition, and it shows the antiferromagnetic transition at 8 K.

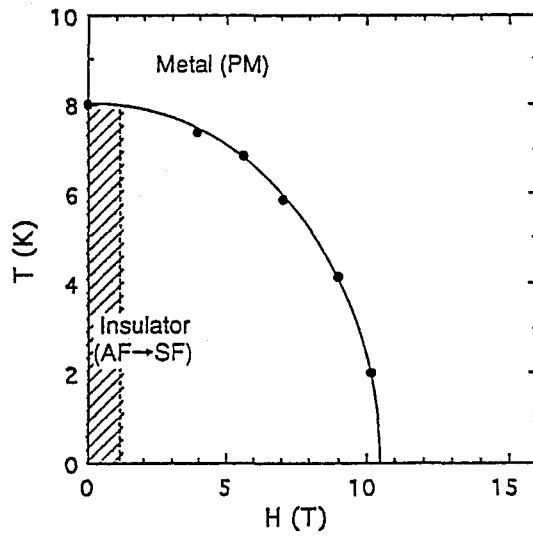


Figure 1.14: Schematic field-temperature phase diagram of  $\lambda$ -(BETS) $_2$ FeCl $_4$ , where the insulator-metal transition is given by the resistivity measurement in the magnetic field [33]. The estimated saturation field is  $H_c=10$  T at 2 K, suggesting that the saturation field corresponds to the insulator-metal transition field at 10 T.

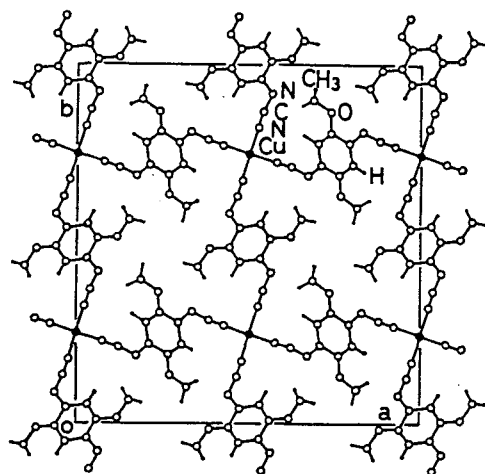


Figure 1.15: Crystal Structure of  $(2,5\text{-dimethoxy-DCNQI})_2\text{Cu}$  [17], where DCNQI molecules forms a 1D conduction column.

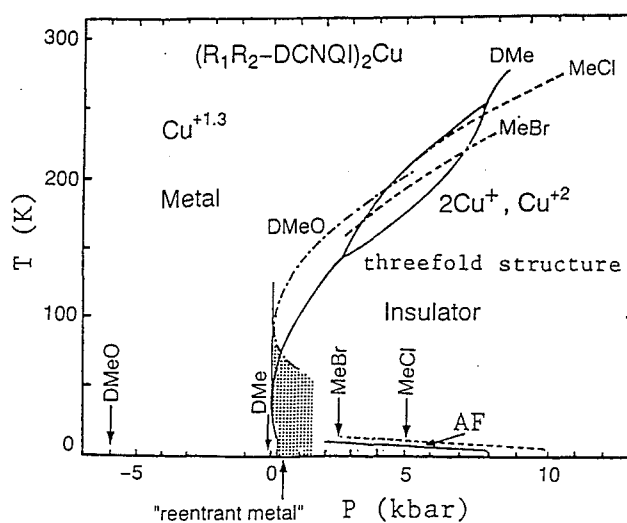
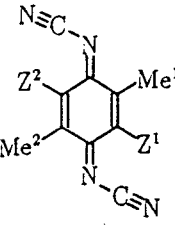


Figure 1.16: Pressure temperature phase diagram of  $(R_1, R_2\text{-DCNQI})_2\text{Cu}$  [35]. The pressure value of DMeO, MeCl, MeBr are normalized on the basis of the diagram of  $(\text{DMe-DCNQI})_2\text{Cu}$  salts. The re-entrant metal-insulator-metal transitions are observed in shaded areas.

	2-Methyl- $d_{a_1}$ -5-methyl- $d_{a_2}$ -DCNQI- $d_b$				
	$Me^1$	$Me^2$	$Z^1$	$Z^2$	$d_n [a_1, a_2; b]^a$
	$CH_3$	$CH_3$	H	H	$d_0 [0, 0, 0] \equiv h_8$
	$CH_2D$	$CH_2D$	H	H	$d_2 [1, 1; 0]$
	$CH_2D$	$CH_2D$	D	H	$d_3 [1, 1; 1]$
	$CD_3$	$CD_3$	D	D	$d_8 [3, 3; 2] \equiv d_8$

(a)

	$a/\text{\AA}$	$c/\text{\AA}$	$V/\text{\AA}^3$
$h_8$	21.611(2)	3.8783(6)	1811.2(4)
$d_2 [1, 1; 0]$	21.6078(8)	3.8771(6)	1810.2(3)
$d_3 [1, 1; 1]$	21.6071(17)	3.8757(5)	1809.5(3)
$d_8$	21.607(2)	3.8741(7)	1808.7(5)

(b)

Table 1.1: (a) Structural formula of  $d_n$ -DMe-DCNQI and lattice constants of (DMe- $d_n$ -DCNQI) $_2$ Cu. (b) The deuteration effects in the lattice constants [34].

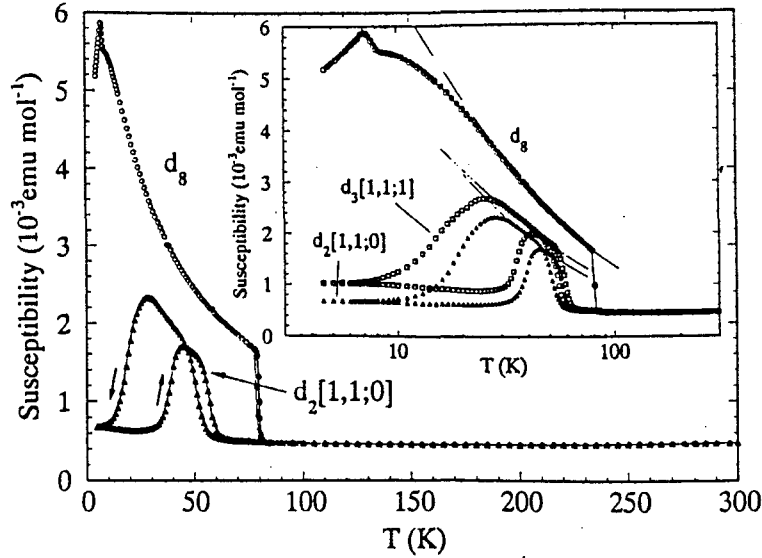


Figure 1.17: Temperature dependence of the magnetic susceptibility of DMe-DCNQI  $d_2[1,1;1]$ -salt and  $d_8$ -salt. In the inset,  $d_2[1,1;0]$ ,  $d_2[1,1;1]$  and  $d_8$  are defined in Table 1.1.  $d_2[1,1;0]$  and  $d_2[1,1;1]$ -salt show re-entrant metal-insulator-metal transitions with the first order transition, where their magnetic susceptibilities are described by Curie-Weiss behavior in the insulator phase.  $d_8$ -salt indicates Curie-Weiss behavior below the metal-insulator transition 80 K [34].

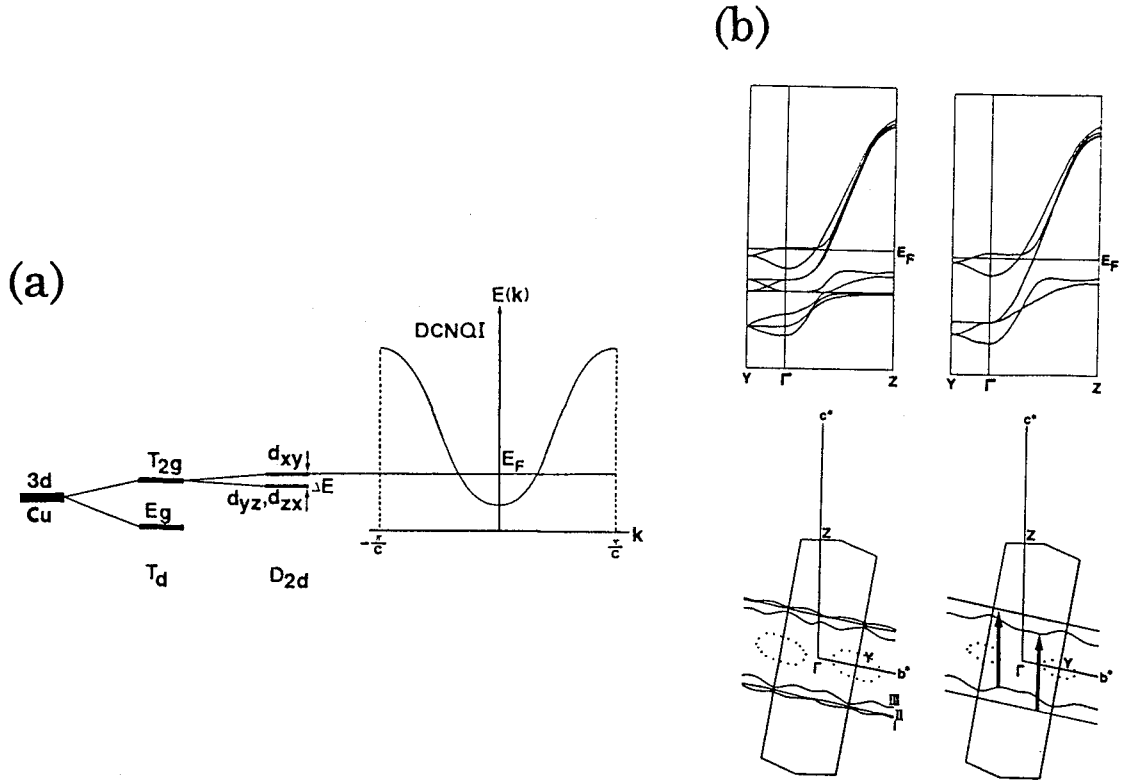


Figure 1.18: (a) Interaction diagram between the  $d$ -orbitals of Cu and the organic one-dimensional band. (b) Band structure with multiple Fermi surfaces in  $(DMe-DCNQI)_2Cu$  [36]. (left-hand)  $E(d_{xy}, d_{yz}) = 1.5E(d_{yz})$ . (right-hand) The difference of the energy levels of Cu  $\Delta E = E(d_{xy}) - E(d_{xz}, d_{yz})$  is enough large. The arrows are the approximate nesting vectors.

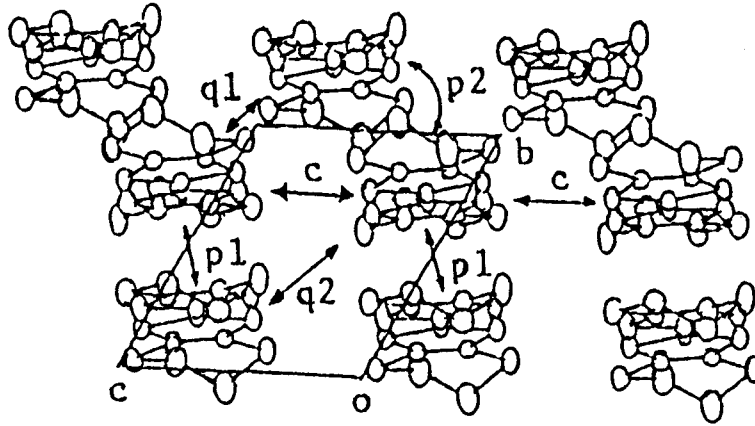


Figure 1.19: Crystal structure of  $\beta'-(BEDT-TTF)_2ICl_2$ . Overlap integrals are  $p1=27.2$  (15.4),  $p2=-1.6$  (-1.7),  $q1=10.0$  (7.2),  $q2=6.6$  (1.7) and  $c=1.6$  (0.1) ( $\times 10^{-3}$ ), where the values in brackets are estimated by another atomic orbital parameters. The donor dimerized unit is formed by the overlap integral  $p1$  [22].

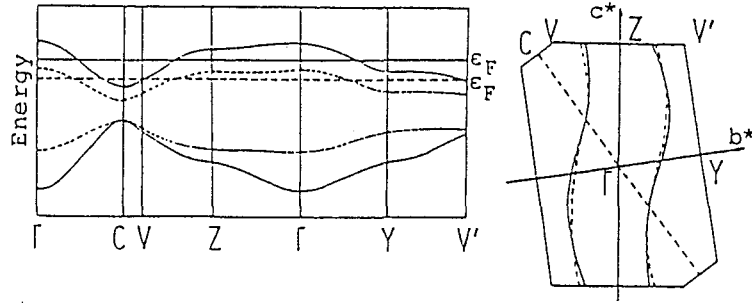


Figure 1.20: Band structure of  $\beta'$ -(BEDT-TTF) $_2$ ICl $_2$  [22]. The band structure split into two sub-bands, which is regarded as an intrinsic Mott insulator. The solid line and broken line correspond to the different strengths of the transfer integrals, where the solid lines are evaluated by the values in the bracket as shown in Fig. 1.19.

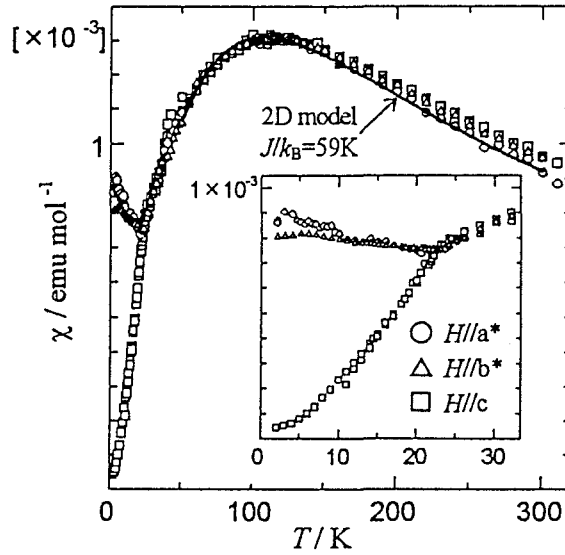


Figure 1.21: Magnetic susceptibility of  $\beta'$ -(BEDT-TTF) $_2$ ICl $_2$  [20]. It is analyzed by the two-dimensional square lattice antiferromagnet model around the magnetic short range order hump, which gives the number of spin  $N=1$  spin/donor dimer, the exchange energy  $J=-59$  K. It shows an antiferromagnetic transition at  $T_N=22$  K.



## 1.6 Aim of Thesis

As mentioned in the previous section, in ordinary inorganic compounds, the interaction between the localized  $d$ -electrons and the conduction electrons brings about the interesting phenomena such as Kondo effect and RKKY interaction generated by  $s$ - $d$  interaction. Meanwhile, in organic conductors, the competition among the transfer integral  $t$ , Coulomb interaction  $U$  and electron-phonon interaction causes unique electronic instabilities. In their electronic states, the localized  $d$ -electrons in the low-dimensional charge transfer complexes cooperate to give new types of electronic instabilities different from the ordinary metal magnets or charge transfer complexes. According to this motif, we discuss the magnetic interaction between the conduction electron and the localized moment in terms of the development of the  $\pi$ - $d$  system and the detailed investigation of  $(\text{BEDT-TTF})_3\text{CuBr}_4$ .

First, I report the crystal synthesis of new organic cation radical salts having the inorganic counter anions with the localized magnetic moments in Chapter 2. In the Chapter, we consider the selections of organic donors and the counter anions in terms of the stabilization of the metallic state in the low temperature and the realization of the strong  $\pi - d$  interaction. Moreover, I tried to synthesize new organic cation radical salts, and carry out the crystal structure analysis and the investigation of electrical and magnetic properties.

Secondly, I present the detailed investigation  $(\text{BEDT-TTF})_3\text{CuBr}_4$  in Chapter 3. In the Chapter, we discuss the crystal structure at room temperature and under high pressure region in order to obtain the basis of the consideration for the physical properties. Further, I measured the electrical resistivity under high pressure to investigate the electrical instability and to get information of the electronic structure. Furthermore, I carried out the detailed measurements of the magnetic susceptibility under ambient pressure and high pressure, EPR, antiferromagnetic resonance, heat capacity by relaxation method and ac calorimetry in order to clarify the magnetic and the thermal properties in the organic conductor having the localized magnetic

moments. In the susceptibility measurement under high pressure, I develop a specially designed clamp cell for the susceptibility measurement under high pressure using by a conventional SQUID magnetometer. Moreover, I improve the heat capacity system by the thermal relaxation method to measure the magnetic heat capacity of the small amount of the present sample.

From the other aspects of the magnetism in the organic conductors, I am interested in the Mott insulating state in view of the magnetism of the organic charge transfer complexes, because the unpaired electrons delocalized over the molecular  $\pi$ -orbitals on the molecules lead to novel magnetic properties in the Mott insulating state. Moreover, various types of low-dimensional structures will come to hand on the basis of the modification of the donor molecule arrangements as well as the designing of donor molecules, providing the diversity of magnetic behavior. Consequently, the detail investigations of organic magnetic insulators will provide new aspects of the magnetism in view of the low-dimensional magnetic systems that have been studied in inorganic compounds through many experimental and theoretical approaches. According to this motif, in Chapter 5, I present the crystal structure, band structure, electrical resistivity, ESR and magnetic susceptibility of  $(C_1TET-TTF)_2Br$  in order to clarify the correlation between the crystal structure, electronic structure and magnetic properties.

## **Chapter 2**

### **Development of Organic Conductors having $\pi - d$ interaction**

## 2.1 Introduction

I have been studying the solid state properties of organic conductor (BEDT-TTF)<sub>3</sub>CuBr<sub>4</sub> which indicates the remarkable characteristic of electrical and magnetic properties as described in Chapter 3. In addition to this compound, I am interested in the development of new organic cation radical salts having  $\pi$ - $d$  interaction. As mentioned in the previous chapter, the appearance of characteristic  $\pi$ - $d$  interaction requires the metallic state and the strong magnetic interaction between the conduction electrons and the magnetic moments. According to this guide, I investigated the appearance of this interaction with alternating stacking of organic  $\pi$ -donors whose structures are known as a common feature among the organic charge transfer complexes with high electrical conduction. In this introduction, we describe the policy of organic donor selection on the basis of the BEDT-TTF molecular structure, electronic structure of the molecule and crystal structure. The selected donors are shown in Fig. 2.1. Moreover, we describe the selection of inorganic anions having localized magnetic moments in view of the appearance of the strong magnetic interaction.

At the beginning, we discuss the selection of the organic cation radical donors in the materials designing on the basis of the stabilization of metallic states. For the fundamental guide to the stabilization of metallic states, it is considered that the electron correlation parameter  $t/U$  plays an important role in the designing, where  $t/U$  is in the range of  $t/U < 1$  for ordinary organic charge transfer complexes. Thus, the complexes tend to be in insulating state as mentioned in section 1.2. As a consequence, how to enhance the parameter is a key point to stabilize metallic state, which is realized by the lowering of the on-site Coulomb repulsion  $U$  and/or the increase of the transfer integral  $t$ .

First, I represent the policy of lowering the on-site Coulomb repulsion. Taking into account that the on-site Coulomb repulsion at a molecule is described as  $U = \langle e^2 / \alpha r_{12} \rangle$ , where the  $\alpha$  and  $r_{12}$  are the polarizability and distance between the

electrons on a molecule, respectively, one of the strategies of the lowering of  $U$  is the extension of HOMO of the  $\pi$ -electron which makes the distance of two electrons  $r_{12}$  extended on a molecule. Moreover, the other is the introduction of heavy element atoms which give the large polarizability  $\alpha$ . On the basis of the strategies, I employed the cation radical donors such as BDT-TTP (2,5-Bis(1',3'- dithiol-2'-ylidine)- 1,3,4,6-tetrathiapentalene), TMEO-TTP (2-(4',5'- bis(thiomethyl)- 1', 3'-dithiol- 2'-ylidene) -5-(4'', 5''- ethylenedioxy- 1'', 3''- dithiol- 2''-ylidine)-TTP), TMET-TTP (2-(4', 5'- bis(thiomethyl)- 1',3'- dithiol-2'-ylidene)- 5-(4'', 5''- ethylenedithio- 1'', 3''- dithiol- 2''-ylidine)-TTP) and CPTM-TTP (4,5- cyclopenteno-4', 5'- bis-(methylthio)-2,5-bis(1,3-dithio-2-ylidine)- TTP) as shown in Fig. 2.1. Actually, these donors indicate the remarkable lowering of the on-site Coulomb repulsion among  $\pi$ -donor molecules as shown in Table 2.1, and the cation radical salts using the above donors have yielded many metallic salts [37]–[44].

Table 2.1: Redox potentials of donors. See Fig. 2.1 for the structures of the donors.

donor	$^1E_{1/2}$ (V)	$^2E_{1/2}$ (V)	$\Delta E$ (V) <sup>d</sup>
BEDT-TTF <sup>a</sup> (ET)	+0.54	+0.92	0.38
BMDT-TTF <sup>a</sup> (MT)	+0.54	+0.84	0.30
BEDO-TTF <sup>a</sup> (BO)	+0.50	+0.80	0.30
EOPT <sup>a</sup>	+0.46	+0.91	0.45
EOOT <sup>a</sup>	+0.47	+0.88	0.41
EDT-TTF <sup>b</sup> (EDT)	+0.39	+0.69	0.30
C <sub>1</sub> TET-TTF <sup>b</sup>	+0.48	+0.72	0.24
BDT-TTP <sup>c</sup>	+0.44	+0.62	0.18
TMET-TTP <sup>c</sup>	+0.53	+0.74	0.21
TMEO-TTP <sup>c</sup>	+0.51	+0.72	0.21
CPTM-TTP <sup>c</sup>	+0.46	+0.69	0.23

<sup>a</sup>The redox potentials was measured in Bu<sub>4</sub>NPF<sub>6</sub>/benzonitrile at 25° vs. Ag/AgCl electrode [42]. <sup>b</sup>Et<sub>4</sub>NClO<sub>4</sub>/acetonitrile at R. T. vs. SCE, where  $^1E_{1/2}$  and  $^2E_{1/2}$  of ET are +0.49 and +0.74 (V) [43]. <sup>c</sup>Bu<sub>4</sub>NClO<sub>4</sub>/benzonitrile at 25° vs. SCE [38, 44]. <sup>d</sup> $\Delta E$  is defined by  $^1E_{1/2} - ^2E_{1/2}$  which regard as the magnitude of the on-site Coulomb repulsion.

Next, we describe how to select the donors in view of the increase of the transfer integral  $t$  on the basis of BEDT-TTF molecular structure and donor packing na-

ture. Usually, BEDT-TTF salts form two-dimensional conducting systems, where the structures have the features of the inter-molecular S-S contacts in the side-by-side direction. In the S-S contact, the significant contribution to the inter molecular overlapping originates from the contacts of the inner sulfur orbitals because the  $\pi$ -electron density of HOMO is larger at the inner sulfur atoms than at the outer sulfur atoms in BEDT-TTF as shown in Figs. 2.2 and 2.3. Here, the ratio of  $S_o/S_i$ , where the distances of inner sulfur atoms ( $S_i$ ) and outer sulfur atoms ( $S_o$ ) as defined in Fig. 2.2, is  $S_o/S_i \sim 1.2$  in a BEDT-TTF molecule [45, 46]. This implies that the S-S contacts between the inner sulfur atoms having large density of  $\pi$ -electrons are prevented from interacting with neighboring molecules geometrically by the outer sulfur atoms having small density of  $\pi$ -electrons along the side-by-side direction. Consequently, the ratio of the distances of sulfur atoms  $S_o/S_i$  close to 1 leads to the favorable S-S contacts for inner sulfur atoms, resulting in increasing the transfer integral  $t$  between the donor molecules. For instance, the substitution of the outer sulfur atoms with the small oxygen atoms (BEDO-TTF) and the substitution of the ethylenedithio bridge with methylthio bridge (BMDT-TTF) make the ratio  $S_o/S_i$  close to 1, where the latter refers to the change by the smaller membered rings. From this consideration, I selected the donors BMDT-TTF (bis(methylenedithio (tetrathiafulvalene))), BEDO-TTF (bis(ethylenedioxy) -TTF), EOPT (4,5-piropylenedioxy- 4',5'-ethylenedithio-TTF) and EOOT (4,5-ethylenedioxy- 4',5'- ethylenedithio-TTF).

Now let us move to the donor selection in view of the realization of the remarkable  $\pi$ - $d$  interaction. The realization of  $\pi$ - $d$  interaction requires the presence of the exchange interactions between the  $\pi$ -electron and the localized  $d$ -electron, where the exchange interaction is caused by the electron transfer mechanism as described in section 1.4. Thus, we discuss the selection of donors in view of the orbital overlap in typical crystal structures on the basis of BEDT-TTF molecule. As seen in Fig. 2.4, ordinary organic cation radical salts have alternating stacking of the organic donors and the inorganic anions which have the localized electrons here. In these structure, the orbital overlaps between the  $\pi$ -electrons and the lo-

calized  $d$ -electrons are thought to be disturbed geometrically by the external ethylene bridges, in the carbon atoms of which have no density of the  $\pi$ -electrons of HOMO as shown in Fig. 2.3. Consequently, it is suggested that the one of the strategies is to extend the  $\pi$ -electron distribution in comparison with BEDT-TTF molecule and the other is the removal of the structural disturbance against the intermolecular overlapping of the wave functions as mentioned below. As shown in Fig. 2.3, BDT-TTP and EDT-TTF (ethylenedithio-TTF) molecules have favorable extension of the  $\pi$ -electron distribution of HOMO to the external C atoms in comparison with BEDT-TTF molecule that is thought to be in favor for the appearance of the strong  $\pi$ - $d$  interaction for the designing of donor molecules. Meanwhile, C<sub>1</sub>TET-TTF (bis(methylthio)ethylenedithio-TTF), TMEO-TTP and TMET-TTP have methylthio groups on the short sides of the donor molecules. The methylthio group, where the  $\pi$ -electron distribution is extended to the outer S atoms, deviates from the molecular plane of the TTF skeleton as shown in Fig. 2.5. These donor structure are favorable to the orbital overlaps between the  $\pi$ -electron on the donor and the localized  $d$ -electron on the counter anion in comparison with BEDT-TTF molecule having the ethylene bridges without the distribution of  $\pi$ -electrons. In addition, since the methylene group of BMDT-TTF deviates from the molecular plane, it is also favorable to the  $\pi$ - $d$  interaction as same as the above reason.

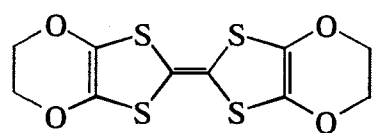
Leaving the policy of the donor selection, we now discuss the selection of the magnetic counter anions in the realization of  $\pi$ - $d$  interaction in the cation radical salts. As mentioned in the preceding, it is important that the strong exchange interaction requires large orbital overlapping between the  $\pi$ -electron orbitals and that of the localized electrons. Thus, we consider the selection of the inorganic counter anion having localized electrons in view of the orbital overlap on the basis of the ligand structure of the counter anion and the exchange path between the  $\pi$ -electrons and the localized electrons. Usually, the counter anions with localized moments have the structural component of  $\text{MX}_y^{a-}$ , where the central transition metal atom M possess the localized moments originating from  $3d$ ,  $4d$ ,  $5d$ ,  $4f$ ,  $5f$  unpaired electrons and

X refers to the ligands of the center atom. Here, the possible exchange interaction paths in the  $\pi$ - $d$  interactions are considered in the following two ways. The one is the direct path between the orbital of the central atom having the localized moments and that of the  $\pi$ -electrons, where the path is expressed by the  $M\cdots\pi$ . The other is the superexchange path between the orbital of the center atom having the localized moments and that of the  $\pi$ -electrons through the X atoms without the localized electrons, where the path way is expressed by  $M-X\cdots\pi$ . The direct path is expected to give the strong the  $\pi$ - $d$  interaction. In this path way, the tetrahedral ligand structure is thought to disturb the direct exchange path geometrically as shown in Fig. 2.6 (a). Thus, the direct orbital overlapping is suggested to require a nearly square planar structure of the ligands in terms of the removal of the disturbance by the tetrahedral ligands as shown in Fig. 2.6 (b). Moreover, it is important for the direct overlap that the orbital of the central atom with the localized moment is the vertical orbitals to the planar of ligands. Nonetheless, we regret to have no idea of the counter anion having the above ligand structure and the orbital with the localized moments. Therefore, we discuss the  $M-X\cdots\pi$  superexchange path below.

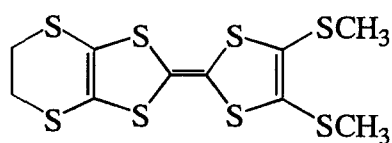
As described in section 1.4, the transfer integral between the magnetic moment on the central metal and the  $\pi$ -electron on the donor molecule governs the exchange energy in the superexchange interaction mechanism mainly. In the exchange path of  $M-X\cdots\pi$ , the transfer integral is enhanced by the hybridization of the  $d$ -orbital of M with the unpaired electron and the orbital of X. In other words, the strong covalency of the M-X bond causes the extension of the wave function of the unpaired electrons to the ligands. Thus, we should select the counter anion having the hybridization of the unpaired electron of the central metal and the orbital of the ligands. In this regard, the  $f$ -electrons are well localized in the inner-shell due to the screening effect of  $4s$  or  $5s$ -electrons, thus, it is difficult to realized the hybridization between the ligand orbitals and the  $f$ -electrons. Consequently, I employ  $d$ -transition metal ions for the central metal atoms. Generally, the magnitudes of the covalency of M-X bond have the trend on the order of the strength  $\text{Halogene} < \text{S} < \text{O}$  for the



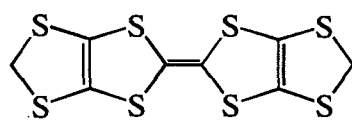
ligand atoms, although, the transition metal sulfides and oxides are difficult to introduce as anions in organic solvent because of their poor solubility. In addition, the counter ions of 4*d*, 5*d* transition metal halides are rather difficult to synthesize. Therefore, I used the 3*d* transition metal halides as the counter anions to form the organic cation radical salts having the  $\pi$ -*d* interactions. In particular, among these 3*d* transition metal halides,  $\text{CuX}_4^{2-}$  ( $\text{X}=\text{Cl}, \text{Br}$ ) anion are found to give the strong hybridization of the ligands and the localized *d*-electron as seen in the electronic state calculation of  $\text{CuX}_4^{2-}$  in Chapter 3. This feature of the hybridization affects the magnetic properties such as the Weiss temperature for 3-*d* transition dichlorides and dibromides as shown in Fig. 2.7 [49]. In the figure, the copper halides have the remarkable high Weiss temperature, suggesting that the hybridization of the ligand orbitals and the localized *d*-electrons governs the magnetic phenomena. From the motif on the above donor molecules and counter anions, I have been developed the cation radical salts with the 3*d* transition metal halide counter anions, particularly, divalent copper halides. I present the results of the synthesis and the solid state physics of new organic cation radical salts in the following section.



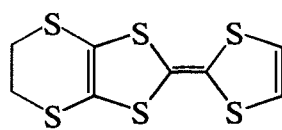
BEDO-TTF(BO)



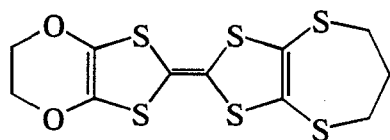
C<sub>1</sub>TET-TTF



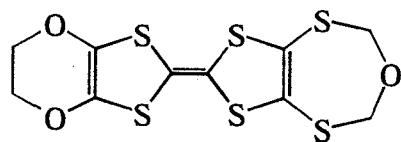
BMDT-TTF



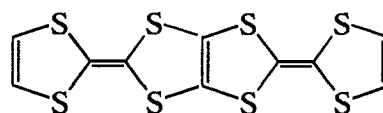
EDT-TTF



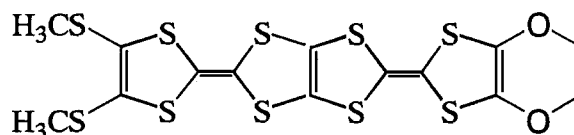
EOPT



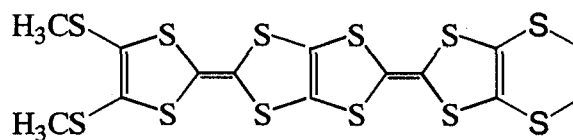
EOOT



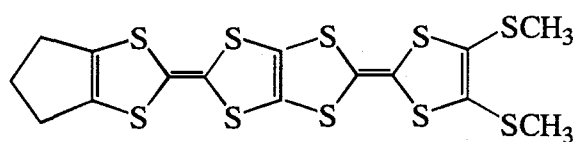
BDT-TTP



TMEO-TTP



TMET-TTP



CPTM-TTP

Figure 2.1: Molecular structures of BEDO-TTF, C<sub>1</sub>TET-TTF, BMDT-TTF, EDT-TTF, EOPT, EOOT, BDT-TTP, TMEO-TTP, TMET-TTP and CPTM-TTP.

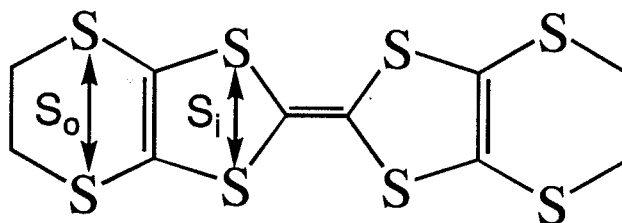


Figure 2.2: Distance between inner ( $S_i$ ) or outer ( $S_o$ ) sulfur atoms in a BEDT-TTF molecule. BEDT-TTF molecule has the ratio of  $S_o/S_i=1.2$ .

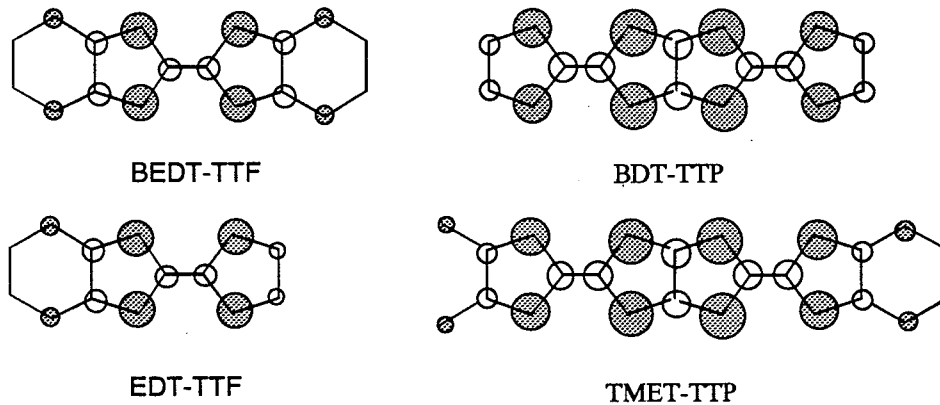


Figure 2.3: The electron density distributions of HOMO of BEDT-TTF, EDT-TTF, BDT-TTP and TMET-TTP [37, 39, 40].

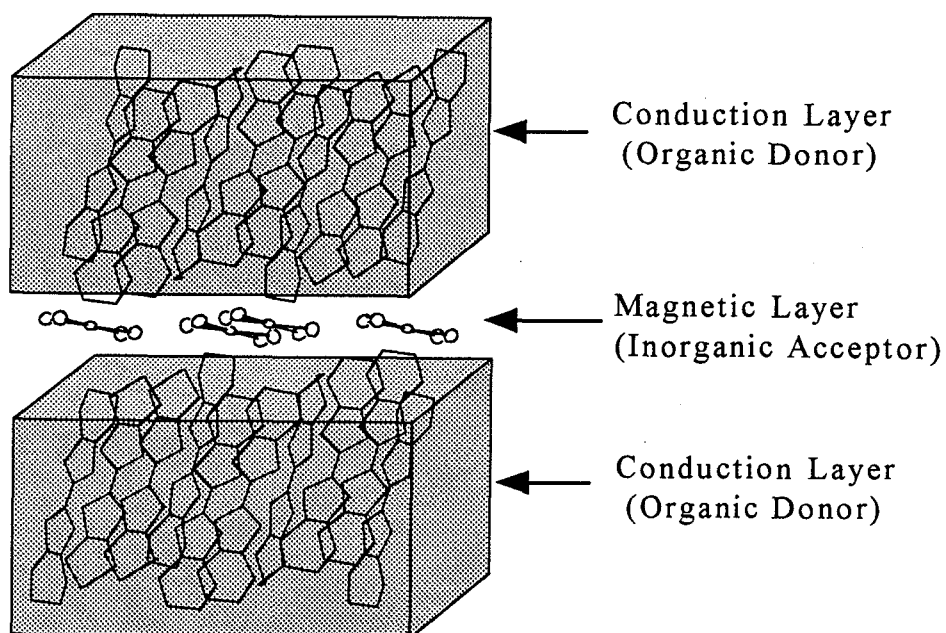


Figure 2.4: Schematic of alternating stacking between the conducting layer composed of organic donors and the magnetic acceptor layer composed of the inorganic anions having localized moments.

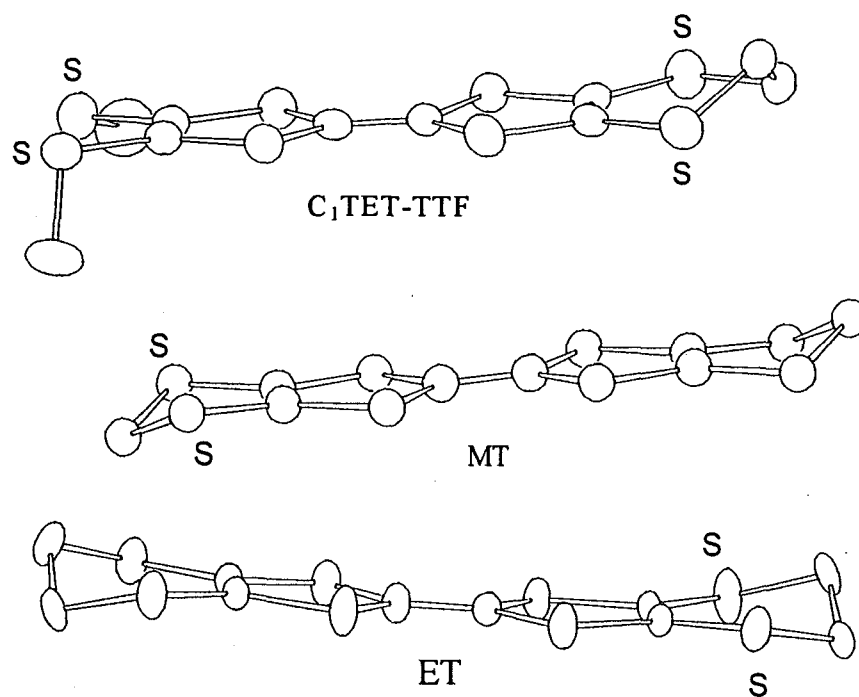


Figure 2.5: Side views of molecular structures of  $C_1TET-TTF$ , BMDT-TTF (MT) and BEDT-TTF (ET) in the charge transfer states which are +0.5, +1 and +1, respectively [13, 47, 48].

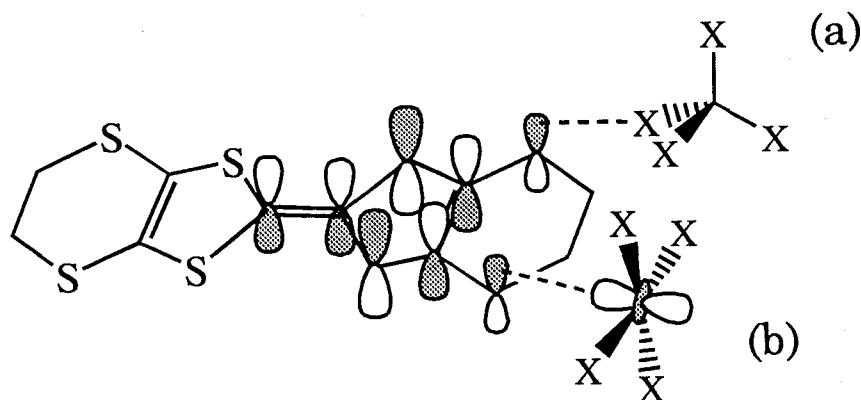


Figure 2.6: Schematic figures of the possible exchange path ways. (a) Orbital overlap between the orbital of the central metal atoms M and the  $\pi$ -orbital through the ligand X atoms without localized moments in the superexchange mechanism. (b) Orbital overlap between the vertical orbital of the counterlateral atom M and the  $\pi$ -orbital in the direct exchange path way.

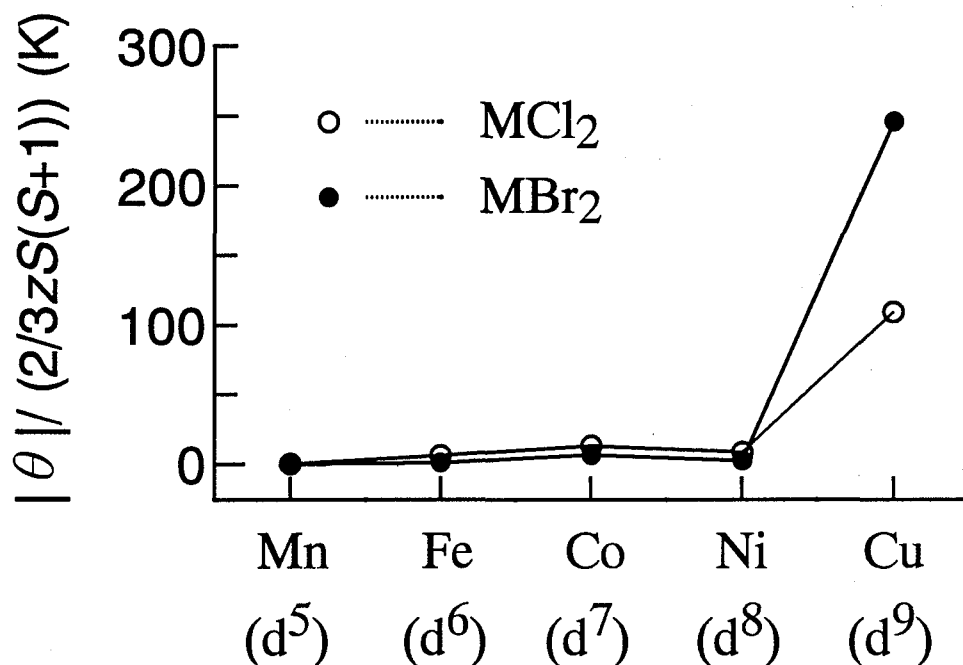


Figure 2.7: Weiss temperature  $\theta$  of 3-d transition metal dichlorides and dibromides. Weiss temperature is normalized with the number of nearest neighbors  $z$  and the spin values  $S$  to the equation of  $|\theta|/(2/3 \cdot zS(S+1))$ , which indicates the strength of exchange interaction  $J/k_B$ .

## 2.2 Experimental

Organic donors BEDT-TTF, BEDO-TTF(BO) and C<sub>1</sub>TET-TTF were provided by Prof. G. Saito, BDT-TTP, TMEO-TTP, TMET-TTP and CPTM-TTP were provided by Dr. Y. Misaki, BMDT-TTF(MT), EOPT and EOOT were provided by Associate Prof. T. Mori and EDT-TTF was provided by Associate Prof. R. Kato. The tetra-alkyl ammoniums, which were the sources of counter anions, were obtained from MX<sub>y</sub> (M=Fe<sup>III</sup>(y=3), Co<sup>II</sup>, Mn<sup>II</sup>, Cu<sup>II</sup>(y=2); X=Cl or Br) and (R<sub>4</sub>N)X (R=C<sub>2</sub>H<sub>5</sub>, C<sub>3</sub>H<sub>7</sub>) in absolute ethanol, where the alkyl ammonium to transition metal halide ratio are 1:1 for ((C<sub>3</sub>H<sub>6</sub>)<sub>4</sub>N)FeX<sub>4</sub> and 2:1 for ((C<sub>2</sub>H<sub>5</sub>)<sub>4</sub>N)<sub>2</sub>MX<sub>4</sub> (M=Co, Mn, Cu).

The cation radical salts were prepared by electrocrystallization of the donor and the electrolyte in several kinds of solutions under Argon gas atmosphere at 20-50 °C for 2-20 days in an H-shaped cell equipped with platinum electrodes under applied constant current of 0.1-1(μA) as shown in Fig. 2.8. The electrodes were immersed in 1 mol/l H<sub>2</sub>SO<sub>4</sub> solution for the activation of their surface prior to the application of the potential. The results of crystal synthesis are summarized in Table 2.2. In the table, the crystallized samples are classified from the aspects of the degree of the sample qualities, the solid state properties and the structure analysis. The crystal structures were determined only (BEDT-TTF)<sub>3</sub>CuBr<sub>4</sub> and (C<sub>1</sub>TET-TTF)<sub>2</sub>Br, however, the latter can not introduce Cu ions owing to the decomposition of the counter anions. Most of the samples were not characterized from the crystal structure, though, those are investigated the composition by EDX analysis (energy dispersion spectroscopy), electrical resistivity, ESR and magnetic susceptibilities. Also, several samples were not crystallized in preparation, or obtained as some microcrystals. The conditions for the sample preparation are shown in Table 2.3 (TTF derivatives) and Table 2.4 (TTP derivatives).

The electrical resistivities were measured by the standard four-probe method. EPR measurements were carried out by a conventional X-band ESR spectrom-

ter (JEOL JES-TE200) at room temperature. The temperature dependence of the magnetic susceptibility were measured by a SQUID magnetometer (Quantum Design MPMS-5) in the applied field up to  $H=10$  kOe in the temperature range 2-300 K. The samples were not oriented to the specific axis except  $\text{BO}_{3.8}\text{CoCl}_6$ . In the susceptibility measurement of  $\text{BO}_{3.8}\text{CoCl}_6$ , the samples were oriented in applied field parallel to the crystal long axis and to the short axis in the plate type samples. The calculated Pascal diamagnetic contribution was subtracted from the total magnetic susceptibility in order to obtain the spin paramagnetic contribution.

The intensity data in X-ray structure analyses were collected by Rigaku four-circle diffractometer AFC-7S with graphite-monochromated Mo  $K\alpha$  radiation. Since the qualities of the obtained crystals were too poor, the crystal structures were determined only  $(\text{C}_1\text{TET-TTF})_2\text{Br}$  and the cell constant was decided in  $(\text{BDT-TTP})_8\text{CuCl}_{8.6}$ . The crystal data were listed for  $(\text{C}_1\text{TET-TTF})_2\text{Br}$  in Table 2.5. The detailed data of the solutions and refinements of the crystal structures of  $(\text{C}_1\text{TET-TTF})_2\text{Br}$  will be discussed in Chapter 4.

Table 2.2: The results of electrocrystallization for samples of the cation radical donors and the counter anions of 3d transition metal halides.

	$\text{FeCl}_4^-$	$\text{FeBr}_4^{2-}$	$\text{CoCl}_4^{2-}$	$\text{MnCl}_4^{2-}$	$\text{CuCl}_4^{2-}$	$\text{CuCl}_2\text{Br}_2^{2-}$	$\text{CuBr}_4^{2-}$
BEDO-TTF	—	—	L2	L2	L2	L2	L2
$\text{C}_1\text{TET-TTF}$	Ref. [50]	Ref. [50]	Ref. [51]	—	L2	—	L3
BMDT-TTF	L2	—	N	—	N	—	L2
EDT-TTF	L2	—	L2	—	L2	—	L2
BDT-TTP	L1	L1	—	—	L2	L2	N
TMEO-TTP	—	—	—	—	—	—	L2
TMET-TTP	L2	—	—	—	—	—	N
CPTM-TTP	N	—	—	—	—	—	N
EOPT	N	—	—	—	—	—	N
EOOT	N	—	—	—	—	—	N
BEDT-TTF	Ref. [52]	Ref. [52]	Ref. [51]	Ref. [53]	Ref. [54]	Ref. [14]	L3

"N" refers to no sample was crystallized in the preparation. "L1" denotes that some microcrystals were obtained. "L2" denotes that several measurements of EDX, resistivity, ESR and magnetic susceptibility were carried out. "L3" denotes that several measurements and X-ray structure determination were carried out.

Table 2.3: Optimum Conditions for the sample preparation of TTF derivatives.

Counter Ion	BO (mg)	electro-lyte(mg)	Solvent <sup>a</sup> (15ml)	Temp (°C)	I (μA)	Time (days)	Shape <sup>b</sup>	D:A <sup>c</sup>	Anion <sup>d</sup>
CoCl <sub>4</sub> <sup>2-</sup>	8.9	45.1	TCE	25	0.2	13	P	3.8:1	CoCl <sub>6</sub>
MnCl <sub>4</sub> <sup>2-</sup>	22.9	39.7	AN	25	0.3	7	N	4:1	MnCl <sub>4</sub>
CuCl <sub>4</sub> <sup>2-</sup>	20.2	35.6	AN	25	0.5	7	P	5.3:1	CuCl <sub>1.3</sub>
CuBr <sub>4</sub> <sup>2-</sup>	16.5	64.7	AN	25	0.5	7	N	3.5:1	CuBr <sub>2</sub>
Counter Ion	EDT (mg)	electro-lyte(mg)	Solvent (15ml)	Temp (°C)	I (μA)	Time (days)	Shape	D:A	Anion
FeCl <sub>4</sub> <sup>2-</sup>	7.3	41.7	AN	25	0.5	9	P	3.2:1	FeCl <sub>4</sub>
CoCl <sub>4</sub> <sup>2-</sup>	7.1	41.7	AN	25	0.5	9	P	3.2:1	CoCl <sub>4</sub>
CuCl <sub>4</sub> <sup>2-</sup>	8.4	44.8	BN	25	0.5	16	P	3:1	CuCl <sub>4</sub>
CuBr <sub>4</sub> <sup>2-</sup>	9.7	40.3	AN	25	0.5	7	P	2.3:1	CuBr <sub>2</sub>
Counter Ion	MT (mg)	electro-lyte(mg)	Solvent (15ml)	Temp (°C)	I (μA)	Time (days)	Shape	D:A	Anion
FeCl <sub>4</sub> <sup>-</sup>	4.8	40.2	DCE	25	0.5	7	B,N	2.7:1	FeCl <sub>4</sub>
CuBr <sub>4</sub> <sup>2-</sup>	8.8	43.1	BN	50	1.0	2	B	2:1	CuBr <sub>2</sub>
Counter Ion	C <sub>1</sub> TET (mg)	electro-lyte(mg)	Solvent (15ml)	Temp (°C)	I (μA)	Time (days)	Shape	D:A	Anion
CuCl <sub>4</sub> <sup>2-</sup>	6.1	43.3	EtOH	25	0.8	13	B	1:1	CuCl <sub>2.2</sub>
CuBr <sub>4</sub> <sup>2-</sup>	5.7	40.9	EtOH	25	1.0	7	B,P	2:1	Br <sup>e</sup>

<sup>a</sup>TCE:1,1,2-Trichloroethane(including 5% EtOH), AN:Acetonitrile, BN:Benzonitrile, DCE:1,2-Dichloroethane. <sup>b</sup>P:Plate, N:Needle, B:Block. <sup>c</sup>the composition ratio of donor and anion (D:A) were determined by EDX(Energy dispersive spectroscopy) except (C<sub>1</sub>TET-TTF)<sub>2</sub>Br salt, the ratio of donor and anion were determined by X-ray structure analyses. <sup>d</sup>Anion refer to the component in the crystal after the preparation, determined by EDX. <sup>e</sup>the components of the anion in the crystals were determined by the X-ray structure analysis.



Table 2.4: Optimum conditions for the preparation of TTP derivatives.

Counter Ion	BDT (mg)	electro-lyte(mg)	Solvent <sup>a</sup> (15ml)	Temp (°C)	I (μA)	Time (days)	Shape <sup>b</sup>	D:A <sup>c</sup>	Anion <sup>d</sup>
FeCl <sub>4</sub> <sup>-</sup>	2.6	47.7	THF	40	0.15	18	N	5:2	FeCl <sub>4</sub>
FeBr <sub>4</sub> <sup>-</sup>	2.6	36.6	DCE	45	0.25	11	N	—	—
CuCl <sub>4</sub> <sup>2-</sup>	1.0	38.6	BN	25	0.2	11	P	8:1	CuCl <sub>8.6</sub>
CuCl <sub>2</sub> Br <sub>2</sub> <sup>2-</sup>	2.1	45.5	DCE	50	0.15	7	N	3:2	Cl
Counter Ion	TMET (mg)	electro-lyte(mg)	Solvent (15ml)	Temp (°C)	I (μA)	Time (days)	Shape	D:A	Anion
FeCl <sub>4</sub> <sup>-</sup>	1.3	32.1	DCE	25	0.1	9	P	4:1	FeCl <sub>4</sub>
Counter Ion	TMEO (mg)	electro-lyte(mg)	Solvent (15ml)	Temp (°C)	I (μA)	Time (days)	Shape	D:A	Anion
CuBr <sub>4</sub> <sup>2-</sup>	3.6	39.5	BN	25	0.2	8	N	3:2	Br

<sup>a</sup>THF:Tetrahydrofuran, DCE:1,2-Dichloroethane, BN:Benzonitrile. An H-shaped cell was filled with the solvent 15ml. <sup>b</sup>P:Plate, N:Needle. <sup>c</sup>the ratio of donor and anion (D:A) were determined by EDX. <sup>d</sup>Anion refer to the component in the crystal after the preparation, determined by EDX.

Table 2.5: Crystal Data of Cation radical Salts		
	$(C_1TET-TTF)_2Br$	$(BDT-TTP)_8CuCl_{8.6}$
Cell setting	Monoclinic	
Space group	$P2_1/a$	
$a$ (Å)	27.71(5)	20.30(4)
$b$ (Å)	11.11(2)	11.62(2)
$c$ (Å)	5.037(8)	11.62(2)
$\alpha$ (°)		90.0(1)
$\beta$ (°)	90.6(1)	106.6(2)
$\gamma$ (°)		73.1(1)
$V$ (Å <sup>3</sup> )	1551(4)	2504(8)
$Z$	2	
independent ref.	3537	
observed ref.	2394( $I > 2\sigma(I)$ )	
$R$	0.0685	
$wR$	0.1988	

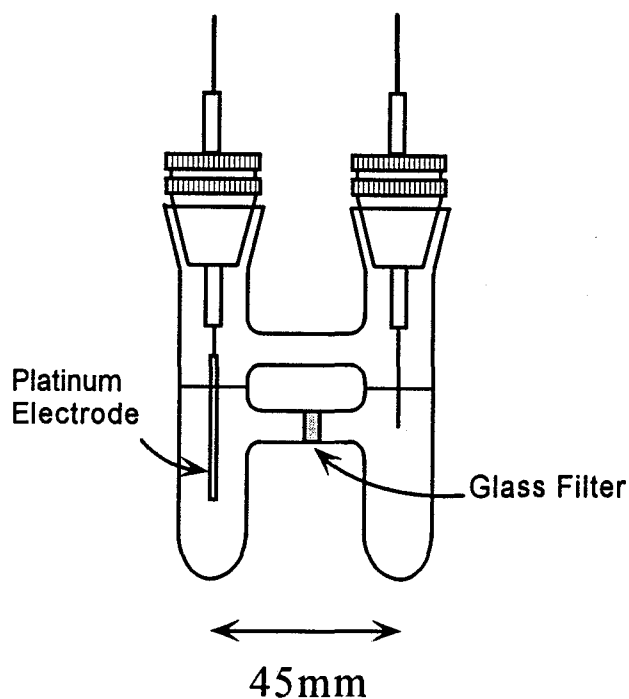


Figure 2.8: H-shaped cell and platinum electrodes. 15 ml solvent is put in usual, the size of the platinum electrodes is 40 mm $\times$ 1 $\phi$ , and the glass filter mesh is G2.

## 2.3 Results and Discussion

I synthesized the cation radical salts with the magnetic counter parts in view of the stabilization of the metallic state and the appearance of the strong exchange interaction between the  $\pi$ -electrons of organic donors and the localized moments. Actually, several salts indicate the metallic behavior or the semiconductive behavior with low activation energies. In the obtained salts, the magnetic susceptibilities show simple Curie-Weiss behaviors with small antiferromagnetic Weiss temperatures. Moreover, EPR measurements do not indicate the presence of the strong exchange interaction between the  $\pi$ -electrons of donors and the localized moments of anions. We discuss the properties of the obtained salts in following parts on the basis of the experimental results, and we summarize the results of EDX analysis, electrical and magnetic properties in Tables 2.6 and 2.7.

### *BEDO-TTF(BO) salts*

Figure 2.9 shows the resistivity of  $\text{BO}_{3.8}\text{CoCl}_6$  salt. It decreases gradually with lowering the temperature, and indicates a slight hump around 70 K and the nearly constant nature below 10 K, where the ratio of the residual resistivity  $R(295\text{K})/R(4.2\text{K})=2.7$ . Generally, the temperature dependence of the resistivity in simple metallic compounds without the scattering of the magnetic moments is given by

$$R(T) = R(T)_{\text{phonon}} + R_{\text{impurity}}, \quad (2.1)$$

where the  $R(T)_{\text{phonon}}$  is the temperature dependence resistivity generated by the electron-phonon scattering, and  $R_{\text{impurity}}$  is the temperature independent term of impurity scattering. The low residual resistivity and less temperature dependence of the resistivity suggest the presence of large impurity scattering. Figure 2.10 shows the magnetic susceptibility and the reciprocal susceptibility as a function of temperature in the applied field parallel to the crystal long axis, indicating the simple Curie-Weiss nature. The Curie-Weiss analysis gives the antiferromagnetic Weiss

temperature  $\theta = -1.3$  K and the Curie constant  $C = 3.64$  emu/mol·K. The small antiferromagnetic Weiss temperature indicates the weak magnetic interaction between the localized moments on  $\text{Co}^{2+}$  ions. Figure 2.11 shows the magnetization curve up to 50 kOe in the applied field parallel to the crystal long axis at 2 K, and the inset shows the behavior in the low field range. The magnitude of the saturation in the magnetization at 50 kOe is about 70% of the saturate value of  $\text{Co}^{2+}$  ( $S=2/3$ ), where the deviation is thought to be caused by the ambiguity to estimate the composition. In the inset of Fig. 2.11, the hysteresis of the magnetization indicates the feature of weak ferromagnetism. Figure 2.12 shows the temperature dependence of the residual magnetization, indicating the presence of a weak ferromagnetic transition at  $T_{\text{WF}} = 7.5$  K. Usually, the weak ferromagnetic transition is caused by the canted spin of the antiparallel arrangement in the antiferromagnetic state. However, the antiferromagnetic transition is not observed apparently in the susceptibility for the applied field parallel to the crystal long and short axes below  $T_{\text{WF}}$ , and then the resistivity shows no anomaly at  $T_{\text{WF}}$ . We have no favorable explanation for this discrepancy now. The observed  $g$ -value and the line width  $\Delta H_{\text{pp}}$  at room temperature are  $g = 2.001 - 2.011$  and  $\Delta H_{\text{pp}} = 56$  Oe, respectively. Here, EPR  $g$ -value and line width not oriented samples in the  $\text{BO}_5(\text{HCTMM})\text{C}_6\text{H}_5\text{CN}$  [55] are  $g = 2.006$  and  $\Delta H_{\text{pp}} = 35$  Oe, respectively, at room temperature, while usually  $\text{Co}^{2+}$  ( $S=2/3$ ) ion indicates the large anisotropic  $g$ -value, for instance,  $g$ -values of inorganic salt  $\text{CoCl}_2 \cdot 6\text{H}_2\text{O}$  was observed at  $g = 2.9 - 4.9$  [56]. Thus, the observed  $g$ -value at room temperature is thought to be assigned to the conduction electrons on the BO molecules. The  $g$ -value of  $\text{Co}^{2+}$  ion is thought to be observed in low temperature EPR measurement. The details in the magnetic and electronic properties can not be discussed owing to the lack of the information of the crystal structure, which will be clarified in the future.

$\text{BO}_4\text{MnCl}_4$  salt shows metallic behavior down to 77 K as shown in Fig. 2.9. It decreases gradually with lowering the temperature, where the ratio of the resistivity is  $R(295\text{K})/R(77\text{K}) = 6.2$ . The value is five times larger than that in  $\text{BO}_{3.8}\text{CoCl}_6$

at 77 K, which suggests that the metallic state in  $\text{BO}_4\text{MnCl}_4$  is well stabilized in comparison with Co salt. The magnetic property obeys the Curie-Weiss type without anomaly in the magnetic susceptibility and the magnetization above 2 K. The Curie-Weiss analysis gives the antiferromagnetic Weiss temperature  $\theta = -1.8$  K and the Curie constant  $C = 3.49$  emu/mol·K. EPR at room temperature indicates the presence of two resonance signals, where  $g$ -values and the line widths are  $g = 2.05$ - $2.11$  and  $\Delta H_{\text{pp}} = 500$ - $450$ ,  $28$ - $50$  Oe. Here, the usual  $g$ -value of  $\text{Mn}^{2+}$  ion is the isotropic value of  $g \sim 2$  [57], while, EPR  $g$ -value and line width in  $\text{BO}_5(\text{HCTMM})\text{C}_6\text{H}_5\text{CN}$  [55] are  $g = 2.006$  and  $H_{\text{pp}} = 35$  Oe at room temperature.

These suggest that the observed EPR signals of broad and narrow line widths in  $\text{BO}_4\text{MnCl}_4$  are assigned to the  $\text{Mn}^{2+}$  ion and the conduction  $\pi$ -electrons on the BO molecules, respectively. The split of the EPR signal suggests the absence of the exchange interaction between the localized moments on  $\text{Mn}^{2+}$  ion and the conduction  $\pi$ -electrons. Using the observed EPR  $g$ -value  $g = 2.05$  at room temperature, the number of spins is estimated at  $N \sim 0.8$  ( $S = 5/2$ )/Mn ion.

$\text{BO}_{5.3}\text{CuCl}_{1.3}$  salt shows the semiconductive behavior with the single activation energy of  $E_a = 545$  K and the room temperature resistivity of  $\rho_{\text{rt}} = 6.2$   $\Omega\text{cm}$  as shown in Fig. 2.9. The semiconductive behavior is unusual observation in BO salts because almost of all BO salts indicate the metallic behavior down to 4.2 K [58]. The magnetic susceptibility shows less temperature dependent without anomaly above 2 K, suggesting the absence of the  $\text{Cu}^{2+}$  localized spins. The EPR line width and the  $g$ -value are  $\Delta H_{\text{pp}} = 48$ - $150$  Oe and  $g = 2.010$ - $2.242$  in the applied field parallel to the crystal short axis and perpendicular to the surface of plate of the sample. Here, EPR  $g$ -value and line width in  $\text{BO}_5(\text{HCTMM})\text{C}_6\text{H}_5\text{CN}$  [55] are  $g = 2.006$  and  $H_{\text{pp}} = 35$  Oe at room temperature, while the  $g$ -value of  $\text{Cu}^{2+}$  with the tetragonal ligand is  $g = 2.047$ - $2.274$  [59]. Thus, the observed EPR resonance is considered as that of  $\text{Cu}^{2+}$  ion. This is discrepant to the result of the susceptibility which suggests the absence of  $\text{Cu}^{2+}$  spins. However, we have no idea for these contradiction now, it will be resolved after the crystal structure determination.

$\text{BO}_{3.5}\text{CuBr}_2$  salt shows the metallic behavior down to 120 K as shown in Fig. 2.13, where the resistivity value at room temperature and the ratio for the resistivity at room temperature and at 120 K are  $\rho_{\text{rt}}=3.4\times 10^{-2}$  and  $R(295\text{K})/R(120\text{K})=1.6$ , respectively. The value of  $\rho_{\text{rt}}$  is one order of magnitude larger than that of  $\text{BO}_{3.8}\text{CoCl}_6$  and  $\text{BO}_4\text{MnCl}_4$  salts, although, the ratio of the resistivity  $R(295\text{K})/R(120\text{K})$  is close to the value of 1.2 in  $\text{BO}_{3.8}\text{CoCl}_6$ . The magnetic susceptibility shows the Pauli paramagnetic nature without anomaly above 2 K, suggesting the absence of the localized magnetic moments. Taking account of the absence of the localized moments, the divalent Cu may be changed to the monovalent Cu by the reduction in the sample preparation.

### *EDT-TTF salts*

$(\text{EDT-TTF})_{3.2}\text{CoCl}_4$  salt shows the metallic behavior around room temperature and the resistivity value  $\rho_{\text{rt}}=3.5\times 10^{-4}$  at room temperature. The magnetic susceptibility indicates the Curie-Weiss behavior without anomaly above 2 K. The Curie-Weiss analysis gives the antiferromagnetic Weiss temperature  $\theta=-0.4$  K and the Curie constant  $C=2.89$  emu/mol·K. The EPR line width and the  $g$ -value of the polycrystalline samples are estimated at  $\Delta H_{\text{pp}}\sim 200$  Oe and  $g\sim 2.07$ . From the measurement of the polycrystalline sample, the magnitude of the exchange interaction between the conduction electron and the localized moments was not obtained. For the detailed discussion of the magnetic interaction, it is necessary to measure single crystal EPR at low temperatures and the magnetic susceptibility.

$(\text{EDT-TTF})_3\text{CuCl}_4$  salt shows the semiconductive behavior with the single activation energy  $E_{\text{a}}=203$  K and the room temperature resistivity of  $\rho_{\text{rt}}=90$   $\Omega\text{cm}$  as shown in Fig. 2.13. The magnetic susceptibility exhibits the Curie type and shows the absence of anomaly above 2 K. The Curie constant is estimated at  $C=0.418$  emu/mol·K, resulting in the number of spins  $N=1.0$  ( $S=1/2$ )/Cu ion using the observed  $g$ -value  $g=2.115$ . Judging from the observed number of spins and the semiconductive behavior with a small activation energy, this compound is character-

ized as a band insulator with a narrow band gap. In addition, it is suggested to form the crystal structure having weak trimerized nature taking into account the donor to anion ratio of 3:1 and the semiconductive behavior with a small activation energy. In the applied field parallel to the plate of the sample, EPR signal shows the single Lorentzian with the line width  $\Delta H_{pp}=11.1$  Oe and  $g=2.032$ , where the sample shape is rectangle plate type. Meanwhile, EPR shows two resonance signals in the applied field perpendicular to the plane, where the line widths and  $g$ -values are obtained at  $\Delta H_{pp}=84.2, 22.5$  Oe and  $g=2.115, 2.007$ , respectively. Here, the typical  $g$ -value of  $\text{Cu}^{2+}$  ion with square planar structure of Cl ligands gives  $g=2.05\text{--}2.15$  [60], while it is suggested that the  $g$ -value of EDT-TTF cation radical is almost  $g\sim 2$  judging from the  $g$ -value of BEDT-TTF [62] having the similar electronic structure of the molecule. Thus, in the applied field perpendicular to the sample plate, the broad EPR signal shape with  $g=2.115$  is assigned to the  $\text{Cu}^{2+}$  ion and the narrow one is assigned to the  $\pi$ -electrons on EDT-TTF molecule. Now, from the split of the EPR signal, the exchange interaction  $J_{\pi-d}$  is estimated by the following equation,

$$J_{\pi-d}/k_B \simeq \mu_B H_0 (g_{\text{Cu}} - g_{\pi}) / k_B \sim 0.02 \text{ K}. \quad (2.2)$$

This value indicates the presence of the weak exchange interaction between the localized  $\text{Cu}^{2+}$  spin and the  $\pi$ -electrons on EDT-TTF molecule.

(EDT-TTF)<sub>2.3</sub>CuBr<sub>2</sub> salt shows the weakly temperature independent resistivity down to 77 K and the resistivity value is estimated at  $\rho_{rt}=3.0\times 10^{-2}$  as seen in Fig. 2.13. The temperature independent nature in spite of the low resistivity value suggests that this compound lies on the boundary of the metal-insulator transition. The magnetic susceptibility behaves Pauli paramagnetic type without anomaly above 2 K, where the Pauli paramagnetic susceptibility is estimated at  $\chi=2.5\times 10^{-4}$  emu/mol. The EPR indicates the line width  $\Delta H_{pp}=15.3\text{--}14.5$  Oe and the  $g$ -value  $g=2.01\text{--}2.001$ . Here, taking into account the typical  $g$ -value of  $g=2.04\text{--}2.14$  of  $\text{Cu}^{2+}$  with tetragonal structure [61], the component of the anion and the Pauli like nature in the susceptibility, the counter anion is suggested to be decom-

posed into  $\text{Cu(I)Br}_2^-$ , which has no magnetic moment, in preparation. Thus, the observed EPR signal is thought to be associated with the conduction electron on the EDT-TTF molecules.

### *BMDT-TTF(MT) salts*

$(\text{MT})_{2.7}\text{FeCl}_4$  salt shows the Curie type behavior without anomaly in the magnetic susceptibility above 2 K. The Curie-Weiss analysis gives the antiferromagnetic Weiss temperature  $\theta = -2.6$  K and the Curie constant  $C = 3.45$  emu/mol·K. Using  $g$ -value of  $\text{Fe}^{3+}$  spin, which gives the isotropic value of  $g \sim 2$  usually, the number of spins is estimated at  $N \sim 0.8$  spin ( $S = 5/2$ )/Fe ion.

$(\text{MT})_2\text{CuBr}_2$  shows the temperature independent nature in the magnetic susceptibility. The signal of EPR shows the line width  $\Delta H_{\text{pp}} \sim 150$  Oe and the  $g$ -value  $g = 2.007$ - $2.010$ . Here, the typical  $g$ -value of  $\text{Cu}^{2+}$  ion with tetragonal ligands structure indicates  $g = 2.04$ - $2.14$  [61], while, it is suggested that the  $g$ -value of EDT-TTF cation radical is almost  $g \sim 2$  judging from the  $g$ -value of BEDT-TTF [62] having similar electronic structure. Consequently, the EPR line shape is assigned to the conduction electron on MT molecules and there is the absence of the localized spin of  $\text{Cu}^{2+}$ . This result suggests that the counter anion is decomposed into  $\text{Cu(I)Br}_2^-$ , which has no the magnetic moment, in preparation.

### *C<sub>1</sub>TET-TTF salts*

$(\text{C}_1\text{TET-TTF})\text{CuCl}_{2.2}$  salt behaves Pauli paramagnetic type of  $\chi_{\text{Pauli}} = 1.1 \times 10^{-4}$  emu/mol without anomaly in the magnetic susceptibility above 2 K. It suggests the absence of the localized moment on  $\text{Cu}^{2+}$  ion. Judging from the component of the anion and the Pauli like susceptibility,  $\text{Cu}^{2+}$  in the counter anion is suggested to be reduced to monovalent in preparation.

$(\text{C}_1\text{TET-TTF})_2\text{Br}$  salt shows the semiconductive behavior with the single activation energy  $E_a = 0.6$  eV and the room temperature resistivity of  $\rho_{\text{rt}} = 40$   $\Omega\text{cm}$ . The



magnetic susceptibility indicates the low-dimensional feature with an antiferromagnetic transition at  $T_N=3$  K. However, the X-ray structure and EDX analysis show the absence of Cu ions. Nonetheless, this salt indicates the interesting feature of the magnetism on the organic donors away from the  $\pi$ - $d$  interaction. The detailed physical properties will be discussed in Chapter 4.

### *TTP derivatives salts*

The EPR line width and  $g$ -value in  $(\text{BDT-TTP})_8\text{CuCl}_{8.6}$  shows  $\Delta H_{\text{pp}} \sim 185$  Oe and  $g=2.10$  in the polycrystalline sample. Here, the typical  $g$ -value of  $\text{Cu}^{2+}$  ion with square planar structure of Cl ligands gives  $g=2.05$ - $2.15$  [60], however, we do not have any information on EPR line width and  $g$ -value of BDT-TTP salts. It will be important in the future to measure the magnetic susceptibility and EPR after the synthesized sample enough to measure the magnetic properties.

In Fig. 2.14,  $(\text{TMET-TTP})_4\text{FeCl}_4$  shows the semiconductive behavior with the activation energy  $E_a=145$  K around room temperature and the room temperature resistivity of  $\rho_{\text{rt}}=0.11$   $\Omega\text{cm}$ . The resistivity indicates the semiconductor-semiconductor transition around 120 K, and it gives the activation energy of  $E_a=264$  K below the transition. The activation energy above the transition is significantly small one, which is expected to be reduced strongly under pressure. The magnetic susceptibility indicates the Curie-Weiss nature without anomaly above 2 K. The Curie-Weiss analysis gives the antiferromagnetic Weiss temperature  $\theta=-0.2$  K and the Curie constant  $C=4.20$  emu/mol·K. Using isotropic  $g$ -value of  $g \sim 2$  expected for  $\text{Fe}^{3+}$  spin, the number of spins is estimated at  $N \sim 1.0$  spin ( $S=5/2$ )/Fe. In addition, the susceptibility does not have an apparent change at the semiconductor-semiconductor transition. This observation suggests the weak magnetic interaction between the conduction electrons on TMET-TTP molecule and the localized moments on  $\text{Fe}^{2+}$ .

$(\text{TMEOTTP})_3\text{Br}_2$  shows the EPR signal with the line width  $\Delta H_{\text{pp}} \sim 18$  Oe and the  $g$ -value  $g=2.005$  in polycrystalline sample, which is thought to be assigned to the free  $\pi$ -carrier spin judging from the absence of magnetic sites.

Table 2.6: Electrical and magnetic properties for TTF derivatives salts.

Cation Radical	$\rho_{rt}$	Temperature <sup>a</sup>	$\chi^c$	EPR	
Salts of BO	( $\Omega\text{cm}$ )	dependence of $\rho$		$H_{pp}(\text{Oe})$	$g\text{-value}$
$\text{BO}_{3.8}\text{CoCl}_6$	$2.6 \times 10^{-3}$	M down to 4.2K	C-W ( $\theta = -1.3\text{K}$ )	$\sim 56$	2.001-2.011
$\text{BO}_4\text{MnCl}_4$	$1.6 \times 10^{-2}$	M down to 77K	C-W ( $\theta = -1.8\text{K}$ )	500-450	2.05-2.11
				28-50	2.05-2.11
$\text{BO}_{5.3}\text{CuCl}_{1.3}$	6.2	$E_a = 545\text{K}^b$	P like	48-150	2.010-2.242
$\text{BO}_{3.5}\text{CuBr}_2$	$3.3 \times 10^{-2}$	M down to 77K	P	$\sim 37$	2.005-2.013
Cation Radical	$\rho_{rt}$	Temperature	$\chi$	EPR	
Salts of EDT	( $\Omega\text{cm}$ )	dependence of $\rho$		$H_{pp}(\text{Oe})$	$g\text{-value}$
$\text{EDT}_2\text{FeCl}_4$	61	—	—	—	
$\text{EDT}_{3.2}\text{CoCl}_4$	$3.5 \times 10^{-4}$	M around R.T.	C-W ( $\theta = -0.4\text{K}$ )	$\sim 200\text{G}$	2.07
$\text{EDT}_3\text{CuCl}_4$	90	$E_a = 203\text{K}^b$	C	11.1-84.2	2.032-2.115
				22.5	2.007
$\text{EDT}_{2.3}\text{CuBr}_2$	$3.0 \times 10^{-2}$	M down to 77K	P	15.3-14.5	2.010-2.004
Cation Radical	$\rho_{rt}$	Temperature	$\chi$	EPR	
Salts of MT	( $\Omega\text{cm}$ )	dependence of $\rho$		$H_{pp}(\text{Oe})$	$g\text{-value}$
$\text{MT}_{2.7}\text{FeCl}_4$	0.01	—	C-W ( $\theta = -2.6\text{K}$ )	—	
$\text{MT}_2\text{CuBr}_2$	—	—	P	$\sim 150$	2.007-2.010
Cation Radical	$\rho_{rt}$	Temperature	$\chi$	EPR	
Salts of $\text{C}_1\text{TET}$	( $\Omega\text{cm}$ )	dependence of $\rho$		$H_{pp}(\text{Oe})$	$g\text{-value}$
$\text{C}_1\text{TET} \cdot \text{CuCl}_{2.2}$	—	—	P	—	
$\text{C}_1\text{TET}_2\text{Br}_2$	40	$E_a = 0.6\text{eV}$	2D-AF ( $T_N = 3\text{K}$ )	14.6-17.6	2.006-2.011

<sup>a</sup>M: Metallic behavior. <sup>b</sup>Single activation type. <sup>c</sup>WF: Weak ferromagnetism, C-W: Curie-Weiss behavior, P: Pauli paramagnetism, C: Curie behavior, 2D-AF: two-dimensional antiferromagnetism.

Table 2.7: Electrical and magnetic properties for TTP derivatives salts.

Cation Radical	$\rho_{rt}$	Temperature	$\chi$	EPR	
Salts of BDT	( $\Omega\text{cm}$ )	dependence of $\rho$		$H_{pp}(\text{Oe})$	$g\text{-value}$
(BDT-TTP) <sub>8</sub> CuCl <sub>8.6</sub>	20	—	—	~185	2.102
Cation Radical	$\rho_{rt}$	Temperature	$\chi$	EPR	
Salts of TMET	( $\Omega\text{cm}$ )	dependence of $\rho$		$H_{pp}(\text{Oe})$	$g\text{-value}$
(TMET-TTP) <sub>4</sub> FeCl <sub>4</sub>	0.11	$T_{s-s} \sim 120\text{K}^a$	C-W <sup>b</sup> ( $\theta = -0.2\text{K}$ )	Unobserved	
Cation Radical	$\rho_{rt}$	Temperature	$\chi$	EPR	
Salts of TMEO	( $\Omega\text{cm}$ )	dependence of $\rho$		$H_{pp}(\text{Oe})$	$g\text{-value}$
(TMEO-TTP) <sub>3</sub> Br <sub>2</sub>	20	—	—	18	2.005

<sup>a</sup> $T_{s-s}$ : Semiconductor-semiconductor transition. <sup>b</sup>C-W: Curie-Weiss behavior.

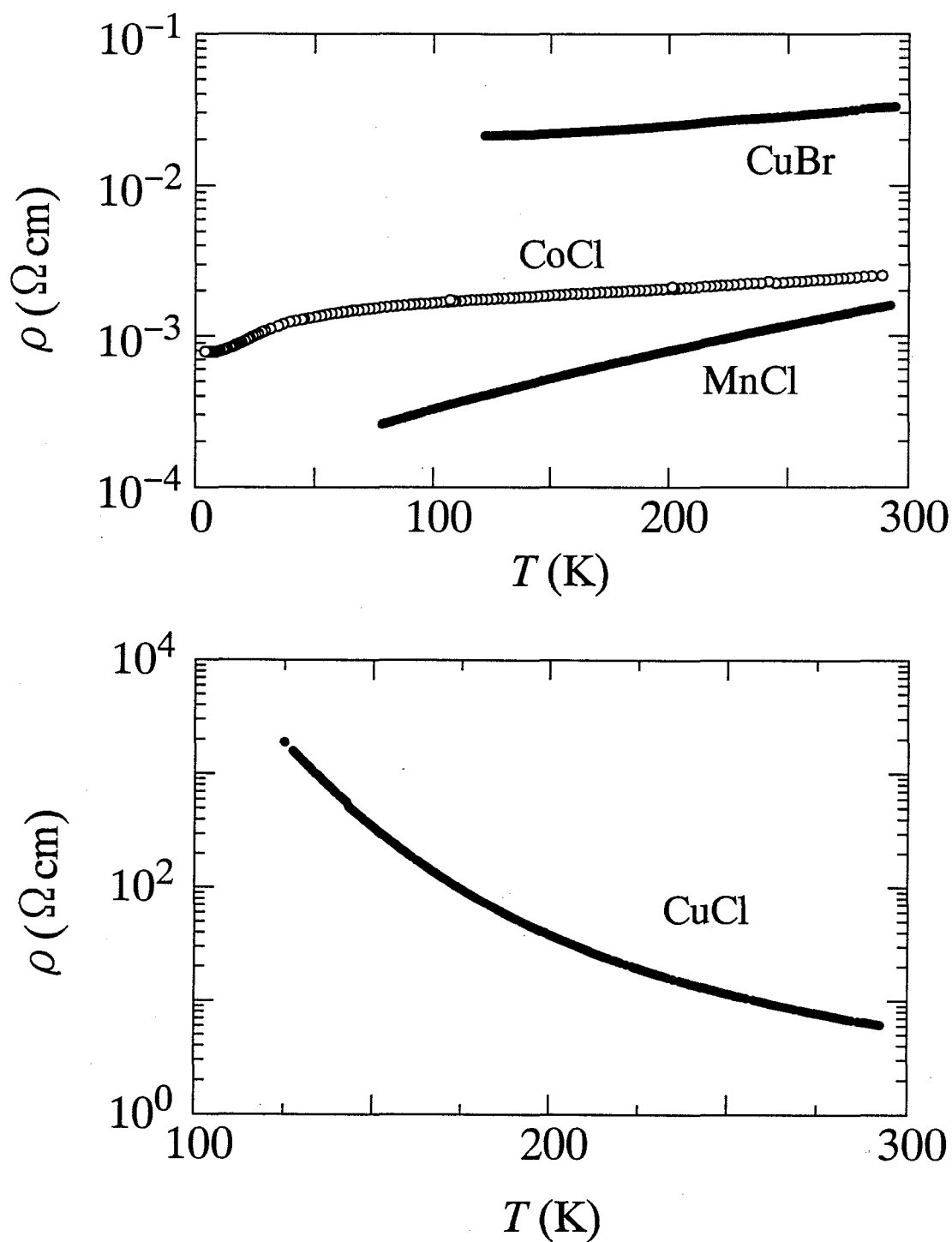


Figure 2.9: Temperature dependence of resistivity of BO salts. The compositions of the salts represented as MnCl, CoCl, CuCl, CuBr are  $\text{BO}_4\text{MnCl}_4$ ,  $\text{BO}_{3.8}\text{CoCl}_6$ ,  $\text{BO}_{5.3}\text{CuCl}_{1.3}$  and  $\text{BO}_{3.5}\text{CuBr}_2$ , respectively. The MnCl, CoCl and CuBr salts shows metallic behavior in the investigated temperature range. The CuCl salt gives semi-conductive behavior with the activation energy  $E_a=545$  K.

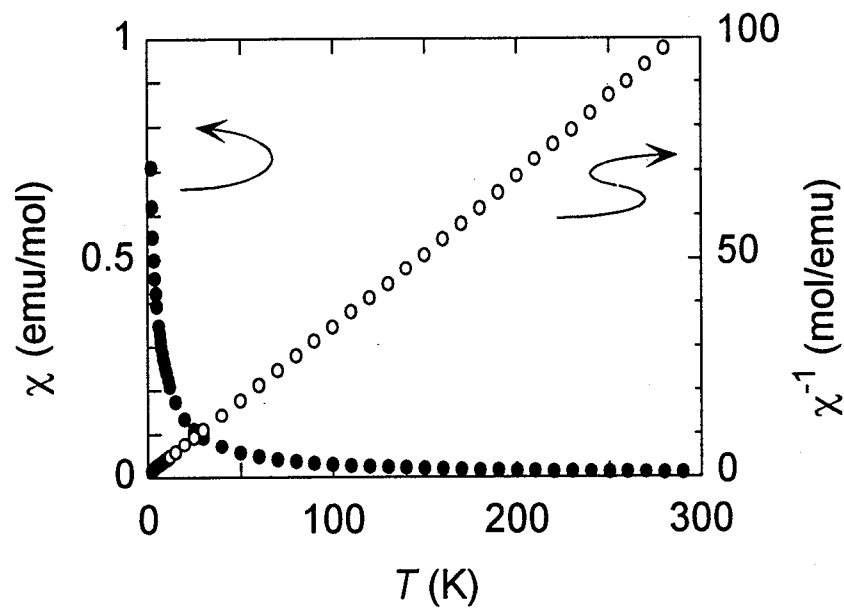


Figure 2.10: Magnetic susceptibility and reciprocal susceptibility as a function of temperature for  $\text{BO}_{3.8}\text{CoCl}_6$ . The Curie-Weiss analysis indicates the antiferromagnetic temperature  $\theta = -1.3\text{K}$ .

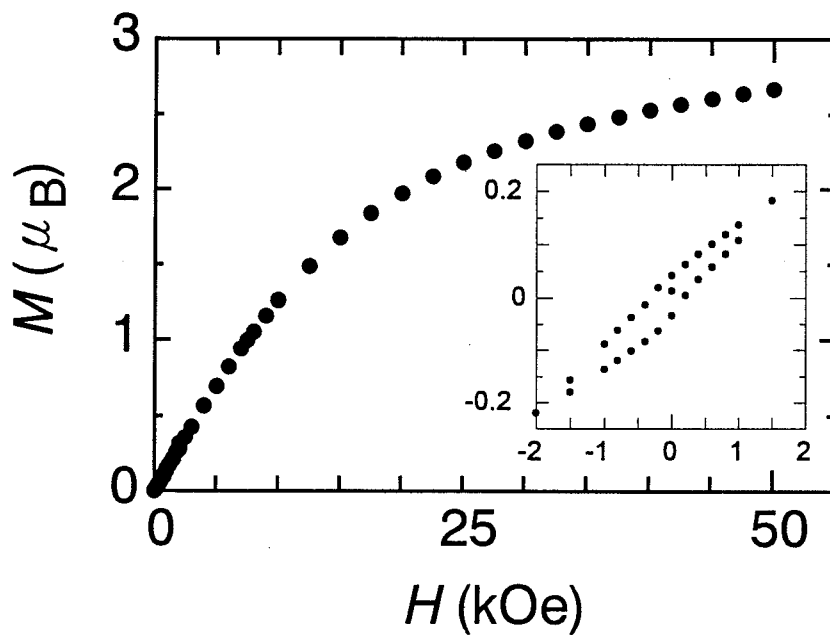


Figure 2.11: Magnetization of  $\text{BO}_{3.8}\text{CoCl}_6$  at 2 K. The inset shows the hysteresis in the low field range, suggesting the presence of weak ferromagnetism.

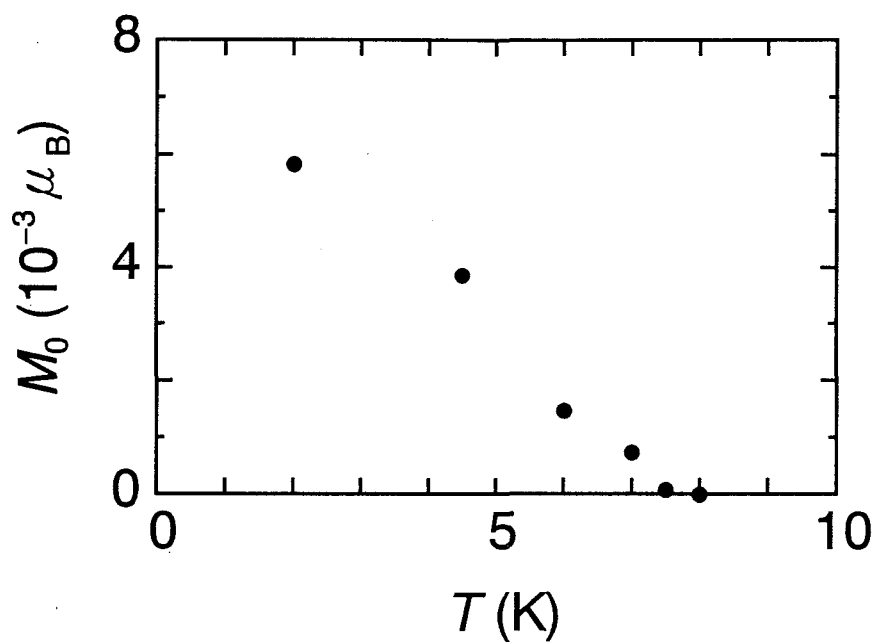


Figure 2.12: Temperature dependence of residual magnetization of  $\text{BO}_{3.8}\text{CoCl}_6$ , indicating a weak ferromagnetic transition at  $T_{\text{WF}}=7.5$  K.

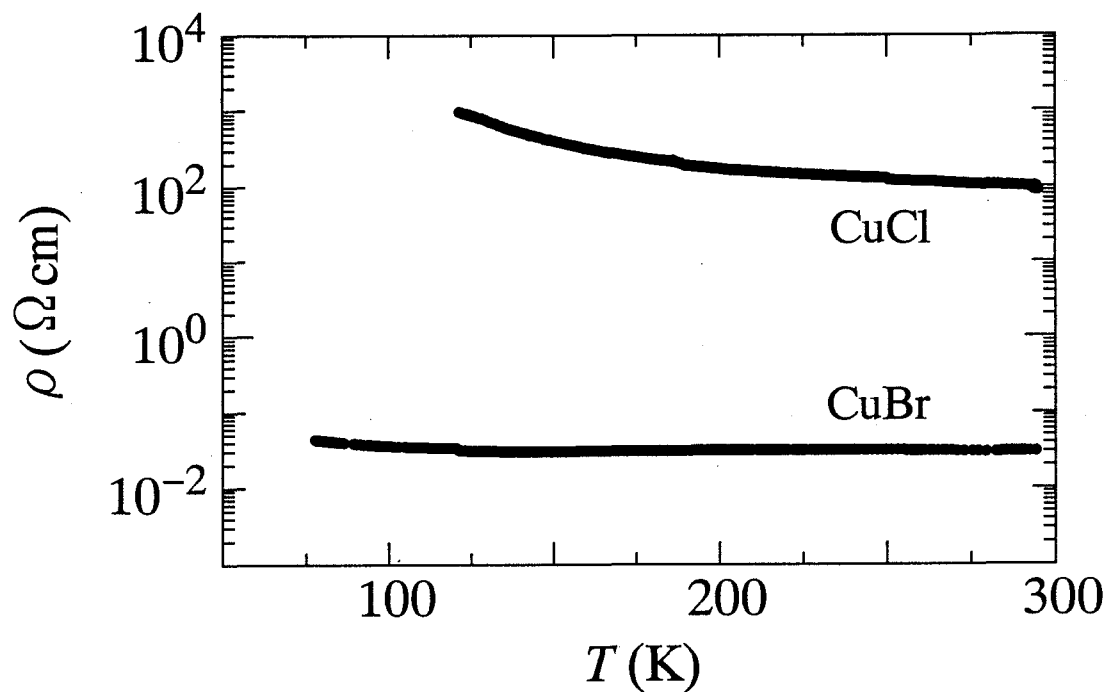


Figure 2.13: Temperature dependence of resistivity of EDT salts. The composition of the salts represented as CuCl and CuBr are  $(\text{EDT-TTF})_3\text{CuCl}_4$  and  $(\text{EDT-TTF})_{2.3}\text{CuBr}_2$ , respectively. The CuCl salt shows the semiconductive behavior with the activation energy  $E_a=203$  K.

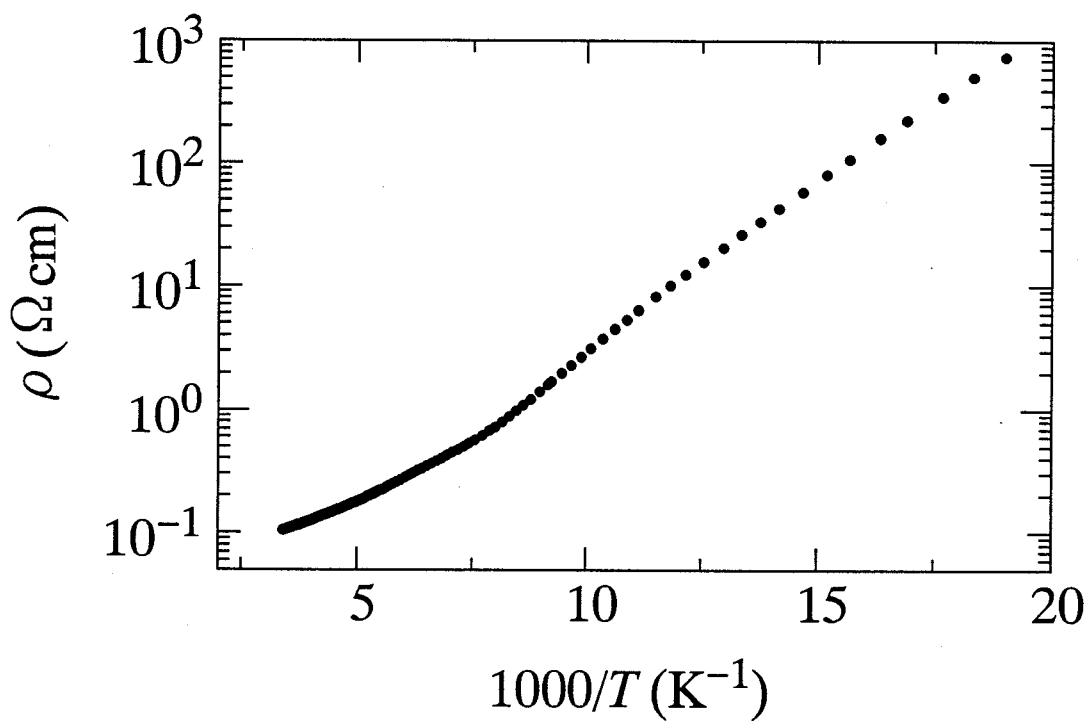


Figure 2.14: Temperature dependence of resistivity  $(\text{TMET-TTP})_4\text{FeCl}_4$ . It shows the semiconductive behavior with the activation energy  $E_a=145 \text{ K}$  and  $264 \text{ K}$  above and below a semiconductor-semiconductor transition around  $120 \text{ K}$ , respectively.

## 2.4 Summary

In this Chapter, I have developed new class of the organic magnetic cation radical salts to obtain the metallic organic systems with the strong  $\pi$ - $d$  interaction. The cation radical donors BEDO-TTF, C<sub>1</sub>TET-TTF, BMDT-TTF, EDT-TTF, EOPT, EOOT, BDT-TTP, TMEO-TTP, TEMT-TTP and CPTM-TTP were employed in the sample preparation to stabilize the metallic state in the low temperature range and to realize the strong exchange interactions between the  $\pi$ -electrons and the localized  $d$ -electrons. Meanwhile, the transition metal halides were employed for the counter anions having the localized magnetic moments, where the copper dihalides anions were expected to give strong of  $\pi$ - $d$  interaction particularly.

We summarize the results of sample crystallization, structural determination, electrical and magnetic properties below. The single crystals were obtained in about a half of the materials, and then the crystal structure were not characterized for the crystallized samples except for (C<sub>1</sub>TET-TTF)<sub>2</sub>Br. In particular, we regret the decomposition of the counter anions of copper dihalides in the sample preparation although these are likely to realize the strong  $\pi$ - $d$  interactions. The composition analysis could be carry out by EDX, and the electrical resistivities, EPR and magnetic susceptibilities were measured in many samples. Actually, from the resistivity measurements we obtained the crystals having the metallic behavior BO<sub>3.8</sub>CoCl<sub>6</sub>, BO<sub>4</sub>MnCl<sub>4</sub>, (EDT-TTF)<sub>3.2</sub>CoCl<sub>4</sub> or the semiconductor (EDT-TTF)<sub>3</sub>CuCl<sub>4</sub>, (TMET-TTP)<sub>4</sub>FeCl<sub>4</sub> with low activation energies. Thus, the approaches to the magnetic metallic cation radical salts are partly successful for the donor selection in view of the stabilization of metallic states. However, EPR and magnetic susceptibility measurements suggest the absence of strong exchange interactions for BO<sub>3.8</sub>CoCl<sub>6</sub>, BO<sub>4</sub>MnCl<sub>4</sub>, (EDT-TTF)<sub>3.2</sub>CoCl<sub>4</sub>, (EDT-TTF)<sub>3</sub>CuCl<sub>4</sub> and MT<sub>2.7</sub>FeCl<sub>4</sub>.

We can not discuss the appearance of  $\pi$ - $d$  interactions in detail because of the lack of information on the crystal structures. The crystal structure analysis of the



obtained samples remain unsolved for the future work after the synthesis for high quality samples.

## **Chapter 3**

### **Solid State Properties of (BEDT-TTF)<sub>3</sub>CuBr<sub>4</sub>**

### 3.1 Introduction

As described in Chapter 1, the interactions between the organic  $\pi$ -electrons and the localized magnetic moments are likely to cooperate to give new types of electronic instabilities different from the ordinary metal magnets or the charge transfer complexes. According to this motif, I have been developing a new class of conducting TTF and TTP-based cation radical salts on the basis of BEDT-TTF with 3d-transition metal halide anions as seen in the Chapter 2 [63, 64]. However, most of the obtained salts are not well characterized due to the poor qualities of the crystals and they are likely not to show interesting phenomena originating from the strong  $\pi$ - $d$  interaction. Thus, in the present chapter, we discuss the detailed results of (BEDT-TTF)<sub>3</sub>CuBr<sub>4</sub>, which shows prototypical behavior for the  $\pi$ - $d$  interaction system. In the present compound, I investigate the structural, electrical, magnetic and thermal properties in order to understand systematically the magnetic interactions between the  $\pi$ -electrons on the BEDT-TTF molecule and the localized magnetic moment. In section 3.2, we discuss the lattice dynamical behavior of (BEDT-TTF)<sub>3</sub>CuBr<sub>4</sub> from the measurement of X-ray diffraction at several temperatures or under pressures. Further, in section 3.3, we describe the detailed electrical properties in the temperature-pressure phase diagram obtained by the measurement of the high pressure resistivity. Furthermore, in section 3.4, we discuss the novel magnetic properties of this compound from the measurement of static susceptibility under ambient and high pressure, EPR, antiferromagnetic resonance (AFMR), ac calorimetry, magnetic specific heat, <sup>1</sup>H-NMR and DV-X $\alpha$  calculation. According to these results and discussions, we reveal the characteristic of the  $\pi - d$  interaction in the organic molecular conductors.

### 3.2 Structural Properties

The crystal structure determination is the fundamental process for the detailed discussion of the physical properties. In the past, the crystal structure analysis of

the present compound was reported by Mori et al [65]. The result indicates that the anion has the mixed valence states of  $\text{Cu(I)Br}_2^{-1}$  and  $\text{Cu(II)Br}_4^{-2}$ , however the estimated number of  $\text{Cu}^{2+}$  spins in the magnetic susceptibility was in disagreement with the structural result by the X-ray analysis. Thus, we determine the crystal structure using the crystal synthesized carefully with no defects of Br atoms, where the result indicates that the anion has divalent  $\text{Cu}^{2+}$  in  $\text{CuBr}_4^{2-}$ . Next, we present the results of X-ray structure analysis at low temperature under ambient pressure obtained in collaboration with Okayama Univ. group, indicating the important feature for the origin of the structural phase transition at  $T_c=59$  K in the present compound. Third, we show the results of the X-ray diffraction under high pressure at room temperature in order to clarify the metal insulator transition under about 7 kbar. Finally, we discuss the correlations between the structure and the electronic structure, and the lattice dynamics of  $(\text{BEDT-TTF})_3\text{CuBr}_4$ .

### 3.2.1 Experimental

#### *Crystal Synthesis*

Single crystals of  $(\text{BEDT-TTF})_3\text{CuBr}_4$  were prepared by the diffusion method. We put 0.1mmol BEDT-TTF in the one compartment and 0.2mmol  $\text{Cu(II)Br}_2$  mixed with 0.4mmol 18-crown 6-ether and 0.4mmol KBr in another compartment of an H-formed cell, then filled it with 50 ml distilled benzonitrile under argon gas atmosphere at room temperature. BEDT-TTF and 18-crown 6-ether were recrystallized from chlorobenzene and from acetonitrile, respectively, while I used commercial high grade  $\text{Cu(II)Br}_2$  and KBr without further purification. After the crystal growth period of one month, I obtained black plate-like single crystals with typical dimension of  $3 \times 1 \times 0.05$  mm<sup>3</sup>. Magnetic susceptibility measurement indicated the absence of any detectable amount of magnetic impurities.

#### *X-ray Structure Analysis at room temperature*

In the X-ray crystal structure analysis at room temperature, the intensity

Table 3.1: Crystallographic data of (BEDT-TTF)<sub>3</sub>CuBr<sub>4</sub> at room temperature.

Chemical Formula	C <sub>30</sub> H <sub>24</sub> S <sub>24</sub> CuBr <sub>4</sub>
Chemical Formula Weight	1537.12
Cell setting	Monoclinic
Space group	$P2_1/c$
$a$ (Å)	16.999(3)
$b$ (Å)	10.137(2)
$c$ (Å)	14.200(3)
$\beta$ (°)	102.77(1)
$V$ (Å <sup>3</sup> )	2386.4(8)
$Z$	2
$D_c$ (Mg·m <sup>-3</sup> )	2.139
Radiation type	Mo $K\alpha$
Wavelength(Å)	0.71069
Temperature(K)	293
Crystal size (mm <sup>3</sup> )	0.48×0.60×0.02
No. of independent reflections	5807
No. of observed reflections	2853( $I > 3\sigma(I)$ )
$R$	0.051
$wR$	0.045

data were collected from Rigaku four-circle diffractometer AFC-7S with graphite-monochromated Mo  $K\alpha$  radiation using  $\omega$ - $2\theta$  scan technique ( $2\theta < 55^\circ$ ). The absorption correction was performed by the numerical absorption program. The observed 2853 reflections were refined by full-matrix block diagonal least-square method using the starting atomic coordinates of Mori et al [65]. Anisotropic temperature factors were used for all non-hydrogen atoms, and for hydrogen atoms we adopted calculated positions and isotropic temperature factors. The final refinement  $R$ -factor was significantly smaller for full occupancy of 1.00 at the Br atoms ( $R=0.051$ ) than that for the partial occupancy of 0.75 ( $R=0.089$ ). Thus, we conclude that the Br atom occupancy of CuBr<sub>4</sub> anion is evaluated at the value of 1.00, which is in good agreement with both result of Watanabe et al. [66] and Guionneau et al [67]. The crystallographic data are listed in Table 3.1.

### *X-ray Study under High Pressure*

A diamond anvil cell (DAC) was used for the high pressure generation. In the

experiments under pressure up to 40 kbar, the single crystal or the powder sample was put into a 200  $\mu\text{m}$  diameter hole of a metal gasket (INCONEL alloy) with both a ruby chip and Flurinert FC-70 and 77 mixed with 1:1 which were used for a pressure indicator and pressure medium, respectively, as shown in Fig. 3.1. The screwing up the retaining screw generates the pressure in the hole by the diamond anvils with a 400  $\mu\text{m}$  top surface. We used a synchrotron radiation source (SR) on beam line 4C (BL-4C) at the Photon Factory National Laboratory for High Energy Physics (KEK). The white X-ray beam was monochromatized with a Si(111) double crystal to a wavelength of 0.6888 Å calibrated by the Zr absorption edge. The pressure values were determined by the ruby luminescence method in the accuracy of  $\pm 0.5$  kbar.

The intensity data of the single crystal were collected from Huber six-circle diffractometer in the pressurized range of 0-14 kbar. In the experiment of powder samples, a photostimulatable fluorescent plate (imaging plate (IP); Fuji Film Co. Ltd.) was used, and typical exposure times were 1-5 hours. Take-off angle  $2\theta_{\text{max}}$  was about  $\pm 35^\circ$ . The two dimensional powder patterns recorded on the IP were integrated for the intensity along each Debye-Scherrer ring to give conventional one dimensional profiles [68] as shown in Fig. 3.2. The distance from the sample to the IP is estimated by the measurement of the standard sample ( $\text{Cr}_2\text{O}_3$ ) to derive a powder profile as a function of  $2\theta$ . In the measurement time of the powder samples, the DAC on the diffractometer was swinging around the  $\chi$ -circle to avoid the spotted peaks by selective orientation on the IP. The applied pressure range was 0-40 kbar for the powder samples. All the measurements of the single crystal and powder samples were carried out at room temperature.

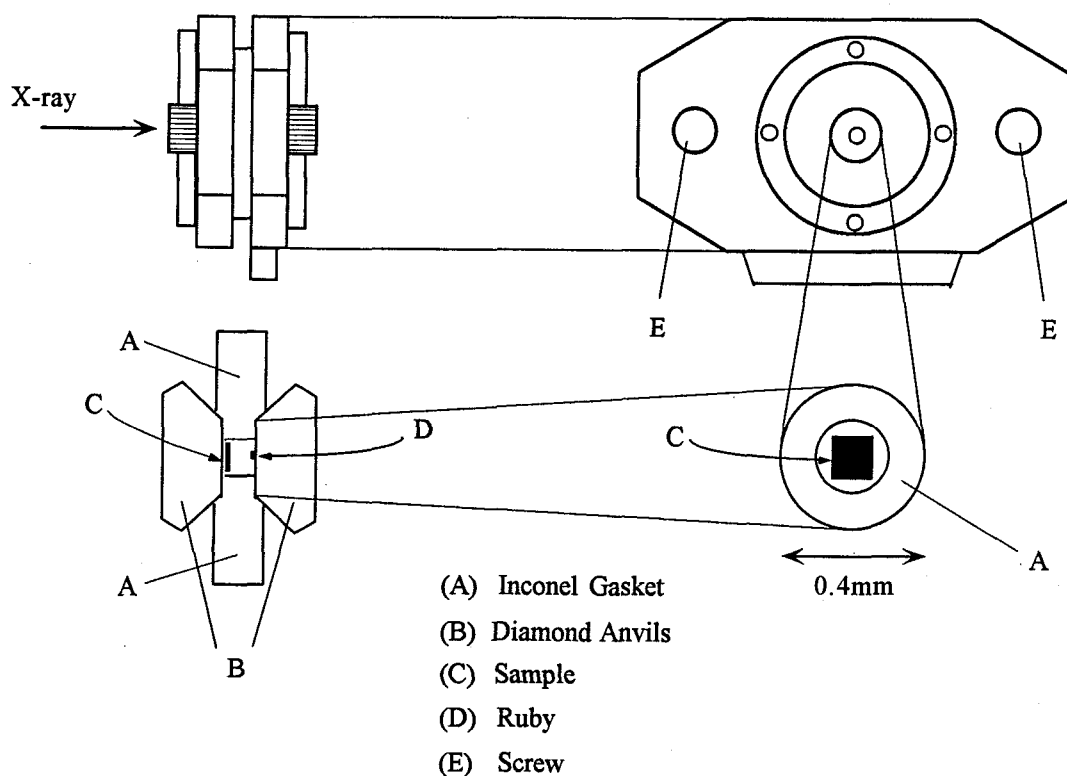


Figure 3.1: Schematic figure of a diamond anvil cell and the experimental setting of the single crystal and the ruby pressure indicator. The pressure is generated by tightening the screw.

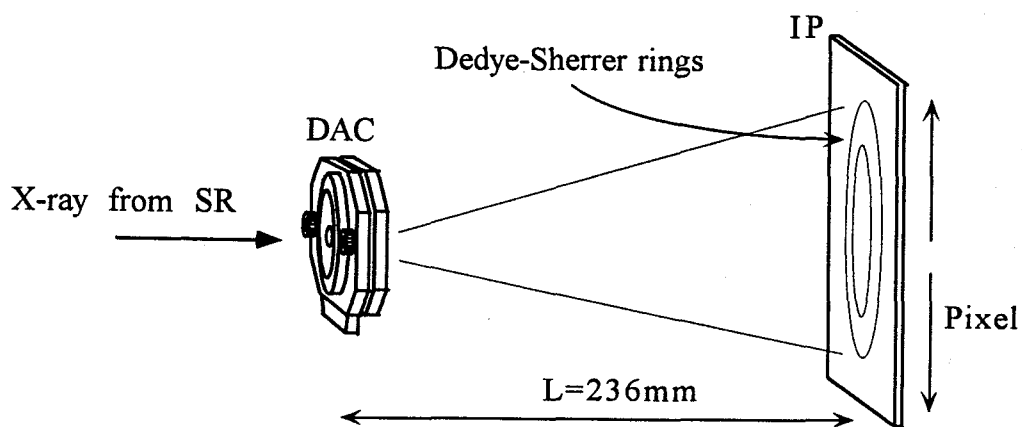


Figure 3.2: Schematic drawing of the setup of DAC and IP. A scanning step (Pixel size) of IP is 0.1mm. The distance L between DAC and IP was determined by the lattice parameters of the standard sample ( $\text{Cr}_2\text{O}_3$ ).

### 3.2.2 Experimental Results

#### *X-ray Structure Analysis at room temperature*

The atomic coordinates, thermal parameters and isotropic, anisotropic temperature factors are listed in Table 3.2 and Table 3.3, and the intermolecular distances and bond angles are in Table 3.4, where the molecular structure and the atom indices are shown in Fig. 3.3. These atomic parameters are in good agreement with the results of Mori et al [65], whereas, the occupancy of Br atoms indicates 1.00 in the present work, namely, the composition of the present compound is (BEDT-TTF)<sub>3</sub>CuBr<sub>4</sub>; this result will be utilized in the discussion of the physical properties. The crystal structure is shown in Fig. 3.4, where the structure consists of alternating stacking of BEDT-TTF  $\pi$  conducting sheets and magnetic Cu<sup>2+</sup> sheets. The donor A and B molecules are crystallographically independent, and the A molecule and the Cu atom lie on the inversion center. There is the absence of disordered sites of ethylene groups in all the donors.

Figure 3.5 shows the donor structure projected along the central C=C bonds of BEDT-TTF molecule. Every BEDT-TTF molecule is surrounded by six neighboring donor molecules, resulting in consisting two-dimensional hexagonal packing structure. Several intermolecular short S...S contacts exist in the intercolumn direction (*b*-axis), where the distances of 3.360(4) Å (S4-S5) and 3.492(4) Å (S5-S8) are shorter than the sum of the corresponding van der Waals radii 3.60 Å as shown in Fig. 3.6. Meanwhile, in the intracolumn direction (*c*-axis), there are no short S...S contacts within the sum of van der Waals radii. These features are predicted by the anisotropic lattice structural dynamical behavior in this compound, which will be discussed in this section.

The presence of two independent molecules A and B demonstrates the significant difference in the valence states between the two molecules because the different valence states of the molecules give the different bond lengths and angles. Here, the bond lengths of the donor molecules in (BEDT-TTF)<sub>3</sub>CuBr<sub>4</sub> are com-



pared with those of BEDT-TTF molecules having different charges as presented in Table 3.5 [69]. Guionneau et al. [70] determined the charge distribution in BEDT-TTF donors from the bond lengths of a, b, c, d defined in Table 3.5, where they suggest that the oxidation of BEDT-TTF molecule lengthens the central C=C bond (a), the external C=C bonds (d) and shortens the internal C-S bonds (b), the external C-S bonds (c). In their report, the charge value  $\delta$  is estimated by the following equation obtained phenomenologically,

$$\delta = 6.347 - 7.463(b + c - (a + d)). \quad (3.1)$$

Using this equation, the charges of BEDT-TTF A and B molecules are estimated at the values of 0 and +0.57 charge, respectively, which are in disagreement with the stoichiometry of  $(\text{BEDT-TTF})_3\text{CuBr}_4$ . Thus, taking account of the donor-to-anion( $\text{CuBr}_4^{2-}$ ) ratio of 3:1, BEDT-TTF is suggested to have 0 and +1 charges for A and B molecules, respectively, which are in good agreement with the number of spins in the magnetic susceptibility measurement as described in section 3.4. Moreover, Marsden et al. suggest the charge separation between A and B molecules from the splitting of the C-S stretching mode in the measurement of reflectance spectra [14].

Finally, we consider the magnetic interaction in this compound using the atomic distances. As will be mentioned in the result of the DV- $X\alpha$  electronic structure calculation of  $\text{CuBr}_4^{2-}$ , the vertical orbital to the ligand plane of  $\text{Cu}^{2+}$  ion has no localized  $d$ -electron. This suggests that the magnetic interactions between  $\text{Cu}^{2+}$  ions or between the  $\text{Cu}^{2+}$  ion and the  $\pi$ -electron are caused by the superexchange mechanism through the Br ligand atoms of  $\text{Cu}^{2+}$  ion. As described in section 1.4, the magnitude of the exchange energy  $J_{ij}$  through the superexchange mechanism is evaluated by  $J_{ij} = -2t_{ij}^2/U$ , where  $t_{ij}$  is the transfer integral between the site  $i$  and  $j$ , and  $U$  is the Coulomb repulsion. Thus, the exchange energy is governed by the magnitude of the transfer integral mainly. Nonetheless, we do not have the values of the transfer integrals between the  $\text{CuBr}_4^{2-}$  anions or between the  $\text{CuBr}_4^{2-}$  anion and BEDT-TTF molecule. Consequently, we consider the magnetic interaction between

the BEDT-TTF molecule and the  $\text{CuBr}_4^{2-}$  anion using the anion-anion and donor-anion distances. Figures 3.7 and 3.8 show the anion-anion and the donor-anion distances. In the magnetic layer of the anions, the  $\text{Cu}^{2+}$  ions form the quasi-two-dimensional square lattice, where the Cu-Cu distance 8.724(1) Å is thought to be too long to realize the strong magnetic interactions. Moreover, the anion-anion distances 4.190(1) Å (Br1-Br2) and 4.817(1) Å (Br1-Br1) are larger than the sum of van der Waals radii 3.70 Å. Meanwhile, in the donor-anion contacts, there are several particularly close contacts 3.699(3) Å (Br2-S8), 3.752(3) Å (Br2-S11), 3.774(3) Å (Br1-S8) and 3.821(3) Å (Br1-S6) in comparison with the sum of corresponding van der Waals radii 3.65 Å, where the above S atoms (S6, S8, S11) are the external S atoms of BEDT-TTF molecule having the small density of  $\pi$ -electrons in the HOMO level. Consequently, in the present compound, the donor-anion interaction is considered to dominate the magnetic interaction over the anion-anion interaction in terms of the distances of the atoms.

Table 3.2: Fractional atomic coordinates and equivalent isotropic thermal parameters of (BEDT-TTF)<sub>3</sub>CuBr<sub>4</sub> at room temperature (see Fig. 3.3 for the atom indices). Equivalent isotropic parameter  $B_{\text{eq}}$  is defined by the following equation  $B_{\text{eq}} = (8/3)\pi^2 \sum_i \sum_j U_{ij} a_i^* a_j^* \mathbf{a}_i \mathbf{a}_j$ .

Atom	x	y	z	$B_{\text{eq}}(\text{\AA}^2)$
Br1	0.47917(7)	0.3305(1)	0.11085(8)	3.35(5)
Br2	0.47403(7)	0.6674(1)	0.11120(8)	3.27(5)
Cu1	0.5000	0.5000	0	1.82(6)
S1	-0.0474(1)	0.1348(3)	0.7170(2)	2.9(1)
S2	0.1453(1)	0.1341(3)	0.8243(2)	2.6(1)
S3	-0.0191(1)	-0.0963(3)	0.6071(2)	2.6(1)
S4	0.1663(1)	-0.0973(3)	0.7118(2)	2.4(1)
S5	-0.2196(1)	0.1590(3)	0.6262(2)	2.7(1)
S6	0.3177(1)	0.1634(3)	0.9177(2)	2.5(1)
S7	-0.1843(1)	-0.1203(3)	0.4939(2)	2.7(1)
S8	0.3406(1)	-0.1190(3)	0.7818(2)	3.1(1)
S9	0.8943(1)	0.1246(3)	0.9961(2)	2.8(1)
S10	0.9168(2)	-0.1251(3)	0.8989(2)	2.9(1)
S11	0.7189(1)	0.1417(3)	0.9176(2)	2.7(1)
S12	0.7468(2)	-0.1587(3)	0.8030(2)	3.0(1)
C1	0.0208(5)	0.018(1)	0.6937(6)	2.4(4)
C2	0.1005(5)	0.019(1)	0.7388(6)	1.9(4)
C3	-0.1300(5)	0.072(1)	0.6332(6)	2.0(4)
C4	0.2428(5)	0.073(1)	0.8392(6)	1.8(4)
C5	-0.1164(5)	-0.032(1)	0.5833(6)	1.8(4)
C6	0.2539(5)	-0.034(1)	0.7871(6)	1.7(4)
C7	-0.2917(5)	0.040(1)	0.5654(6)	2.4(4)
C8	0.4030(5)	0.053(1)	0.9302(6)	2.1(4)
C9	-0.2715(5)	-0.013(1)	0.4737(6)	2.7(4)
C10	0.4152(5)	0.001(1)	0.8362(6)	2.4(4)
C11	0.9614(4)	0.000(1)	0.9782(6)	2.2(4)
C12	0.8180(5)	-0.063(1)	0.8798(6)	2.0(4)
C13	0.8077(5)	0.051(1)	0.9242(6)	1.9(4)
C14	0.6539(6)	-0.081(1)	0.8175(7)	2.9(5)
C15	0.6546(6)	0.066(1)	0.8128(7)	2.8(5)
H1	-0.2932	-0.0359	0.6104	2.9
H2	-0.3462	0.0823	0.5487	2.9
H3	0.4529	0.1008	0.9632	2.6
H4	0.3942	-0.0242	0.9713	2.6
H5	-0.2606	0.0637	0.4339	3.2
H6	-0.3189	-0.0636	0.4369	3.2
H7	0.4697	-0.0415	0.8470	2.8
H8	0.4130	0.0767	0.7906	2.8
H9	0.6087	-0.1142	0.7653	3.4
H10	0.6440	-0.1074	0.8819	3.4
H11	0.5981	0.0987	0.8072	3.3
H12	0.6740	0.0930	0.7540	3.3

Table 3.3: Isotropic (for H atoms) and anisotropic temperature factors ( $\text{\AA}^2$ ) at room temperature.

atom	U11	U22	U33	U12	U13	U23
Br1	0.0568(8)	0.0341(7)	0.0378(6)	0.0016(6)	0.0131(5)	0.0069(6)
Br2	0.0477(7)	0.0373(7)	0.0424(6)	-0.0040(6)	0.0172(5)	-0.0110(6)
Cu1	0.0189(8)	0.0234(9)	0.0260(8)	-0.0006(9)	0.0028(6)	-0.001(1)
S1	0.020(1)	0.046(2)	0.041(1)	0.002(1)	-0.003(1)	-0.016(1)
S2	0.019(1)	0.037(2)	0.041(1)	0.004(1)	-0.001(1)	-0.008(1)
S3	0.020(1)	0.035(2)	0.040(1)	0.005(1)	-0.001(1)	-0.007(1)
S4	0.018(1)	0.032(2)	0.037(1)	-0.001(1)	-0.001(1)	-0.005(1)
S5	0.020(1)	0.036(2)	0.045(1)	0.004(1)	-0.000(1)	-0.009(1)
S6	0.023(1)	0.030(2)	0.037(1)	0.004(1)	-0.004(1)	-0.008(1)
S7	0.026(1)	0.033(2)	0.039(1)	0.002(1)	-0.004(1)	-0.010(1)
S8	0.017(1)	0.041(2)	0.058(2)	0.003(1)	0.001(1)	-0.021(2)
S9	0.021(1)	0.031(2)	0.049(2)	-0.001(1)	-0.002(1)	-0.011(1)
S10	0.025(1)	0.034(2)	0.050(2)	0.002(1)	0.003(1)	-0.008(1)
S11	0.025(1)	0.031(2)	0.041(1)	0.003(1)	-0.002(1)	-0.006(1)
S12	0.031(1)	0.031(2)	0.045(2)	0.003(1)	-0.008(1)	-0.010(1)
C1	0.018(5)	0.036(7)	0.033(5)	0.003(5)	0.001(4)	-0.003(5)
C2	0.021(5)	0.025(6)	0.027(4)	-0.003(5)	0.001(4)	-0.001(5)
C3	0.016(5)	0.030(6)	0.027(5)	0.000(4)	0.003(4)	0.002(5)
C4	0.014(5)	0.022(6)	0.029(5)	0.004(4)	0.000(4)	0.007(4)
C5	0.017(5)	0.023(6)	0.028(5)	0.003(4)	0.001(4)	0.003(4)
C6	0.016(5)	0.023(6)	0.022(4)	-0.007(4)	-0.001(4)	-0.003(4)
C7	0.013(5)	0.036(7)	0.043(6)	-0.004(4)	0.006(4)	-0.005(5)
C8	0.012(5)	0.027(6)	0.039(5)	0.000(4)	0.001(4)	0.005(5)
C9	0.026(5)	0.042(7)	0.029(5)	0.005(6)	-0.007(4)	-0.006(6)
C10	0.014(4)	0.032(6)	0.044(5)	-0.009(5)	0.007(4)	-0.007(6)
C11	0.017(5)	0.029(5)	0.037(5)	0.001(6)	0.000(4)	-0.007(6)
C12	0.019(5)	0.016(5)	0.035(5)	-0.000(4)	-0.005(4)	-0.001(5)
C13	0.018(5)	0.021(5)	0.031(5)	0.002(4)	-0.004(4)	0.006(5)
C14	0.025(6)	0.040(7)	0.037(6)	-0.011(6)	-0.007(5)	0.001(6)
C15	0.025(6)	0.041(7)	0.037(6)	-0.004(6)	-0.001(5)	0.003(6)
H1	0.0372					
H2	0.0372					
H3	0.0324					
H4	0.0324					
H5	0.0409					
H6	0.0409					
H7	0.0360					
H8	0.0360					
H9	0.0428					
H10	0.0428					
H11	0.0423					
H12	0.0423					

Table 3.4: Bond lengths and angles of (BEDT-TTF)<sub>3</sub>CuBr<sub>4</sub> at room temperature without hydrogen atoms (see Fig. 3.3 for the atom indices).

Bond length (Å)			
Br1-Cu1	2.409(1)	S8-C10	1.800(9)
Br2-Cu1	2.424(1)	S9-C11	1.76(1)
S1-C1	1.74(1)	S9-C13	1.760(9)
S1-C3	1.748(9)	S10-C11	1.75(1)
S2-C2	1.736(9)	S10-C12	1.758(9)
S2-C4	1.737(8)	S11-C13	1.751(9)
S3-C1	1.72(1)	S11-C15	1.81(1)
S3-C5	1.740(9)	S12-C12	1.737(9)
S4-C2	1.724(9)	S12-C14	1.82(1)
S4-C6	1.751(8)	C1-C2	1.36(1)
S5-C3	1.744(9)	C3-C5	1.32(1)
S5-C7	1.802(9)	C4-C6	1.35(1)
S6-C4	1.753(9)	C7-C9	1.52(1)
S6-C8	1.810(9)	C8-C10	1.49(1)
S7-C5	1.759(9)	C11-C11	1.32(1)
S7-C9	1.81(1)	C12-C13	1.35(1)
S8-C6	1.722(9)	C14-C15	1.50(1)
Bond angle (°)			
C1-S1-C3	95.2(4)	S6-C4-C6	126.7(7)
C2-S2-C4	96.0(4)	S3-C5-S7	113.2(5)
C1-S3-C5	95.5(4)	S3-C5-C3	117.8(7)
C2-S4-C6	97.0(4)	S7-C5-C3	129.0(7)
C3-S5-C7	100.4(5)	S4-C6-S8	114.3(5)
C4-S6-C8	101.1(4)	S4-C6-C4	115.2(7)
C5-S7-C9	101.1(4)	S8-C6-C4	130.6(7)
C6-S8-C10	100.0(4)	S5-C7-C9	112.8(6)
C11-S9-C13	95.7(4)	S6-C8-C10	113.5(6)
C11-S10-C12	95.8(4)	S7-C9-C7	114.1(6)
C13-S11-C15	100.4(5)	S8-C10-C8	113.5(6)
C12-S12-C14	100.9(5)	S9-C11-S10	114.2(4)
S1-C1-S3	114.9(5)	S9-C11-C11	123(1)
S1-C1-C2	122.7(8)	S10-C11-C11	123(1)
S3-C1-C2	122.3(8)	S10-C12-S12	113.9(6)
S2-C2-S4	114.1(5)	S10-C12-C13	117.1(7)
S2-C2-C1	124.7(8)	S12-C12-C13	129.0(7)
S4-C2-C1	121.2(7)	S9-C13-S11	114.2(6)
S1-C3-S5	114.5(6)	S9-C13-C12	117.1(7)
S1-C3-C5	116.6(7)	S11-C13-C12	128.6(7)
S5-C3-C5	128.9(7)	S12-C14-C15	114.3(8)
S2-C4-S6	115.5(5)	S11-C15-C14	113.2(8)
S2-C4-C6	117.7(7)		

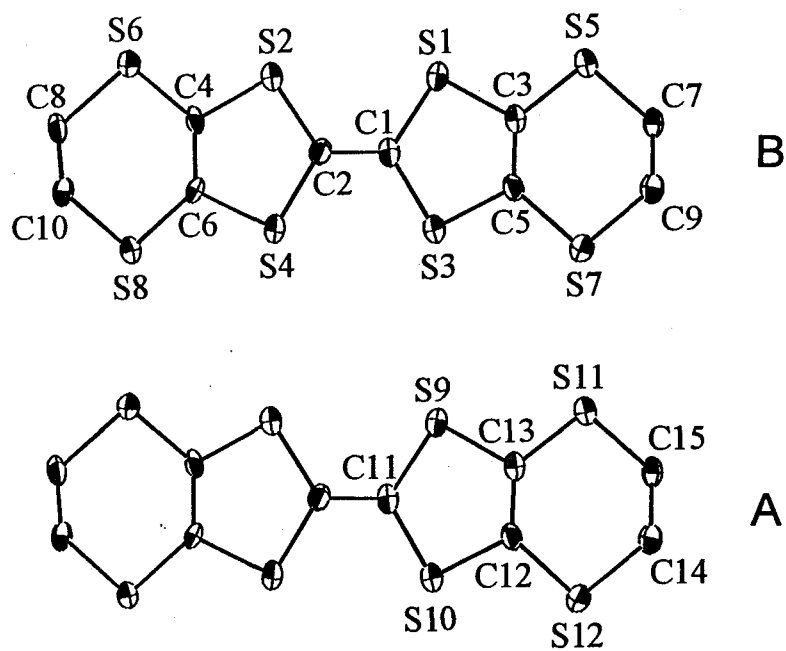


Figure 3.3: Molecular structure of BEDT-TTF drawn by ORTEP (see Ref. [71]). At room temperature, the A and B molecules have 0 and +1 charges, respectively.

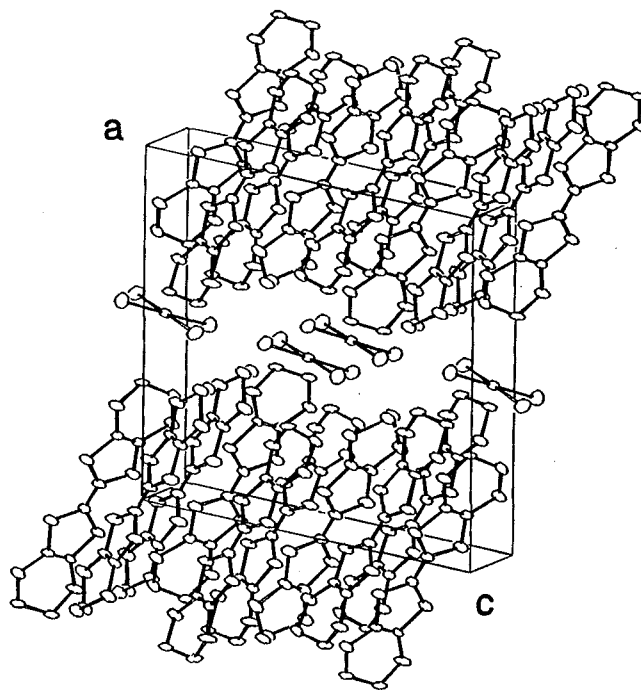


Figure 3.4: Crystal structure of  $(\text{BEDT-TTF})_3\text{CuBr}_4$ , which has the alternating stacking between the BEDT-TTF layers and the magnetic layers of  $\text{CuBr}_4^{2-}$  at room temperature.

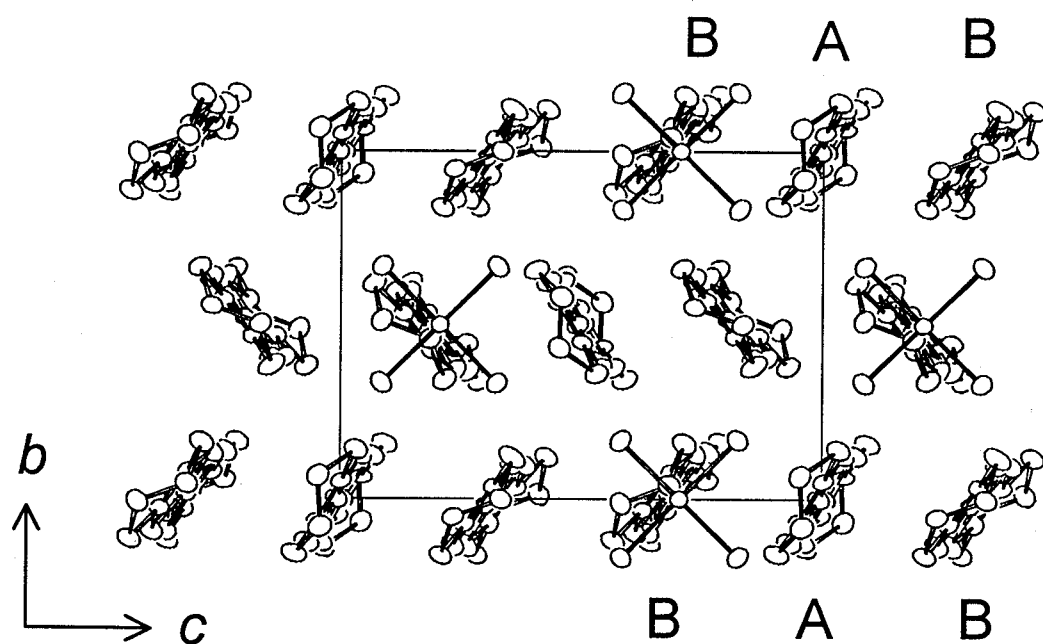


Figure 3.5: Structure of  $(\text{BEDT-TTF})_3\text{CuBr}_4$  projected along the central  $\text{C}=\text{C}$  bonds in the BEDT-TTF molecules. The  $\text{Cu}^{2+}$  ions form a two-dimensional quasi-square lattice. BEDT-TTF molecules have the trimerized BAB feature along the  $c$ -axis.

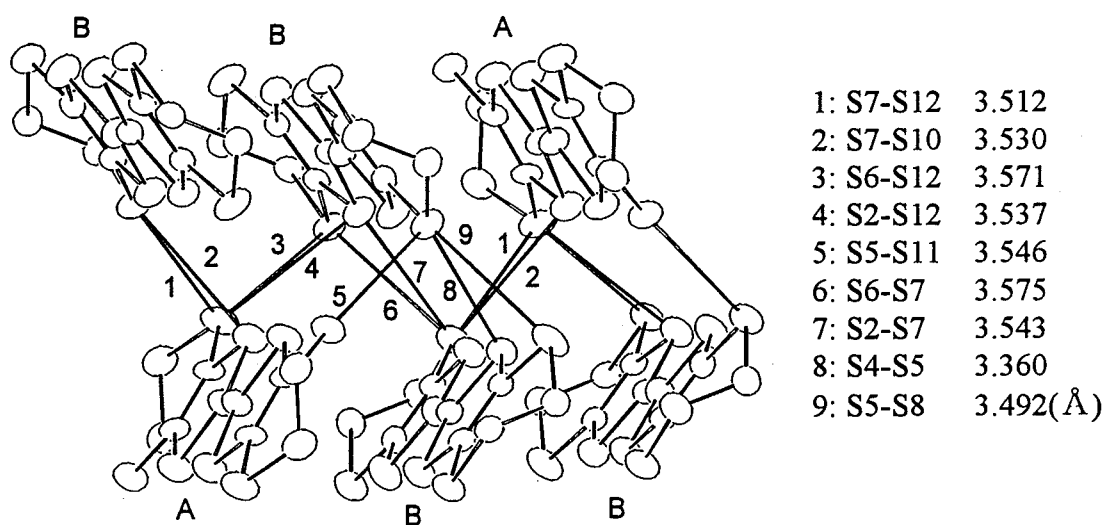
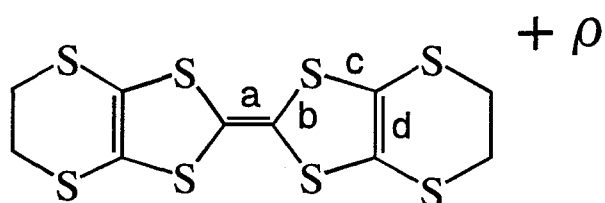


Figure 3.6: Intermolecular distances in the BEDT-TTF layer within the corresponding van der Waals radii  $3.60\text{\AA}$ .

Table 3.5: Comparison of the bond lengths between (BEDT-TTF)<sub>3</sub>CuBr<sub>4</sub> and the other BEDT-TTF salts [69].

Compound	$\rho^1$	Bond length (Å)			
		<i>a</i>	<i>b</i>	<i>c</i>	<i>d</i>
neutral BEDT-TTF	0	1.312(12)	1.757(7)	1.754(8)	1.332(7)
$\alpha$ -(BEDT-TTF) <sub>2</sub> PF <sub>6</sub>	1/2	1.365(4)	1.740(2)	1.750(2)	1.345(3)
(BEDT-TTF) <sub>3</sub> (ClO <sub>4</sub> ) <sub>2</sub>	2/3	1.366(7)	1.731(7)	1.743(5)	1.345(9)
(BEDT-TTF)ReO <sub>4</sub> (THF) <sub>0.5</sub>	1	1.375(28)	1.719(10)	1.729(10)	1.365(18)
A molecule of (BEDT-TTF) <sub>3</sub> CuBr <sub>4</sub>	0	1.32(1)	1.76(1)	1.759(9)	1.35(1)
B molecule of (BEDT-TTF) <sub>3</sub> CuBr <sub>4</sub>	~1	1.36(1)	1.730(9)	1.744(9)	1.34(1)



<sup>1</sup>Formal charge of BEDT-TTF<sup>+</sup> $\rho$ . <sup>2</sup>The bond lengths *b*, *c* and *d* of (BEDT-TTF)<sub>3</sub>CuBr<sub>4</sub> were estimated by the average of the corresponding bond lengths. The bond lengths *a*, *b*, *c*, *d* are defined in the inset molecule.

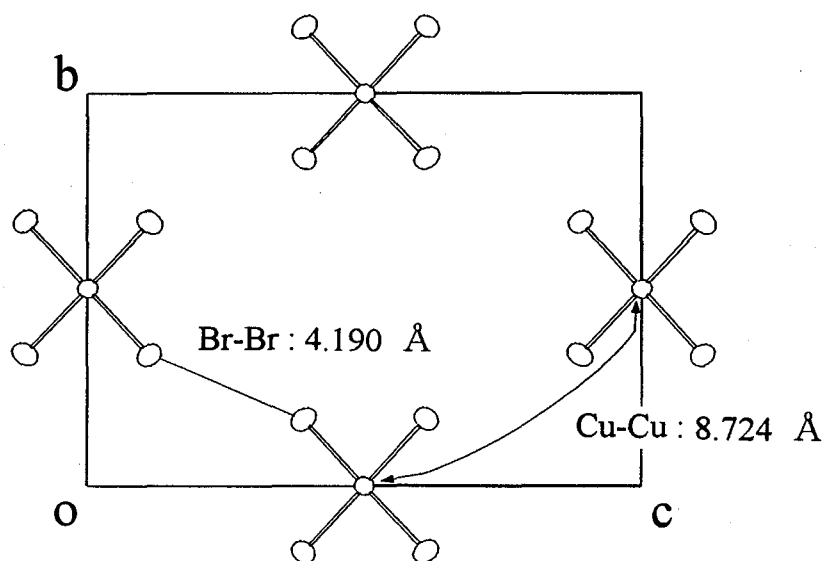


Figure 3.7: Anion-anion distances between the neighboring CuBr<sub>4</sub><sup>2-</sup>.



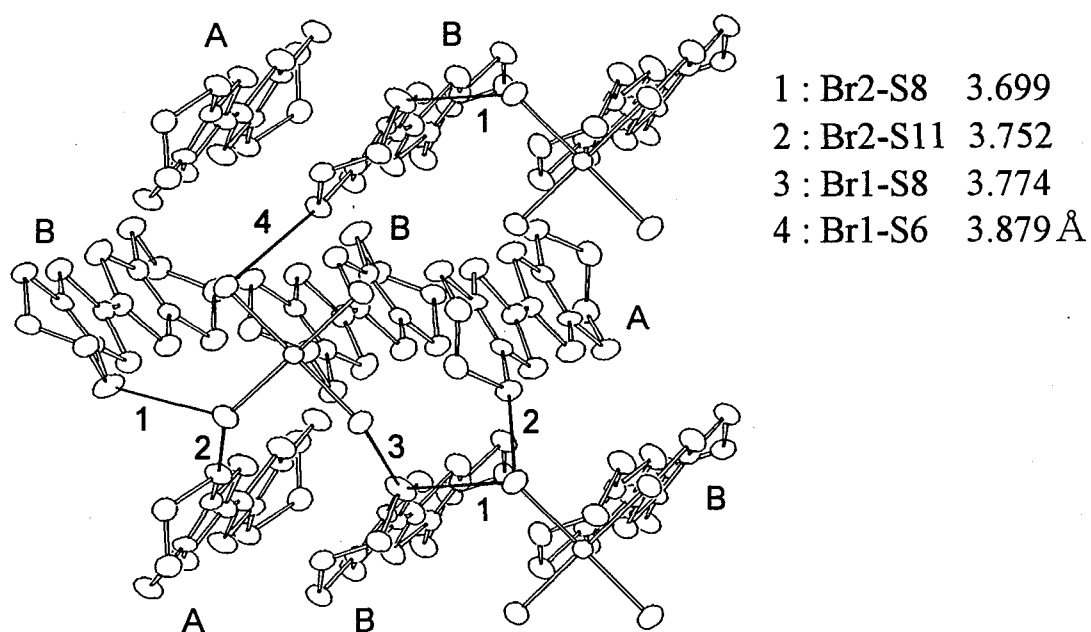


Figure 3.8: Donor-anion distances close to the van der Waals radii 3.65Å.

### *X-ray Study at low temperature*

The X-ray structure analysis of (BEDT-TTF)<sub>3</sub>CuBr<sub>4</sub> in the low temperature range under ambient pressure is the collaborating work with Okayama Univ. group, which is reported in the results of Watanabe et al [66, 72, 73]. In this part, we summarize the results of the X-ray structure analysis in the low temperature range.

Figure 3.9 shows the temperature dependence of lattice parameters of (BEDT-TTF)<sub>3</sub>CuBr<sub>4</sub> in the temperature range 25-300 K. The lattice parameters indicate large changes at  $T_c=59$  K, where the resistivity has an anomaly and the magnetic susceptibility shows a remarkable decrease. Here, the linear and thermal expansion coefficients are defined as

$$\alpha_x = \frac{d \ln x}{dT} = \frac{\Delta x}{x \times \Delta T}, \quad (3.2)$$

where  $x$  are lattice parameters  $a, b, c$  and  $V$ ,  $\Delta=298-T$  and  $\Delta x=x(298\text{K})-x(T)$ . Assuming that the changes of the lattice parameters are proportional to temperature from room temperature to just above  $T_c$ , the thermal expansion coefficients are estimated at  $\alpha_x=0.85, 3.2, 6.7$  and  $10.4 \times 10^{-5} \text{ K}^{-1}$  for  $x=a, b, c$  and  $V$  in the temperature range of 300-65 K, which are in the ordinary magnitudes in comparison to the other organic conductors [74]. The thermal expansion coefficients below  $T_c$  are estimated at  $\alpha_x=-1.1, 1.3, 3.0$  and  $3.4 \times 10^{-5} \text{ K}^{-1}$  for  $x=a, b, c$  and  $V$  in the temperature range 65-298 K. The magnitudes of the thermal expansion coefficients below  $T_c$  are smaller than those above  $T_c$ . The volume contraction  $\Delta V$  at  $T_c$  is estimated at  $\Delta V=6.7 \text{ \AA}^3$  which corresponds to 0.3% of the cell volume just above  $T_c$ .

Next, we represent the change in the valence state of BEDT-TTF molecules depending on the temperature. As mentioned in the structure determination at room temperature, the charges of the BEDT-TTF A and B molecules are 0 and +1, respectively. Watanabe et al. [73] suggests the disappearance of the charge disproportionation between BEDT-TTF A and B molecules with decreasing the temperature. Figure 3.10 shows the temperature dependence of the charges on BEDT-TTF (A) and BEDT-TTF (B) with the result of Chasseau et al. [75], where

the charges are estimated by the Guionneau's equation as mentioned before. The results are thought to indicate the uniformity of the valence of BEDT-TTF molecules below  $T_c$ .

Watanabe et al. [66] investigates the extinction rule of  $P2_1/c$  ( $h0l$ :  $l=2n+1$ ,  $0k0$ :  $k=2n+1$  disappearance) and finds out the disappearance of the  $(0k0)$  reflection below  $T_c$ , indicating that the change of symmetry from  $P2_1/c$  above  $T_c$  to  $P_c$  below  $T_c$ . Figure 3.11 shows the temperature dependence of the  $(050)$  reflection profile and the  $(050)$  integrated intensity, where the reflection appears below  $T_c$  with changing the symmetry. Since the X-ray integrated intensity corresponds to the order parameter, the step wise behavior of the intensity indicates the first order transition of  $T_c$  at ambient pressure, which is in good agreement with the results of the resistivity and the specific heat as will be described in sections 3.3 and 3.4.

Watanabe et al. observed the trimerization of BEDT-TTF molecules in the low temperature phase from the X-ray structure analysis, and they calculated the overlap integral below and above  $T_c$  as represented in Fig. 3.12. The values of overlap integrals at room temperature are in good agreement with the result of Mori et al [65]. The overlap integrals  $b_2$  and  $b_3$  below  $T_c$  are enhanced from the values above  $T_c$ , which suggests that the donor molecules are trimerized through the increase of the overlaps of  $b_2$  and  $b_3$ .

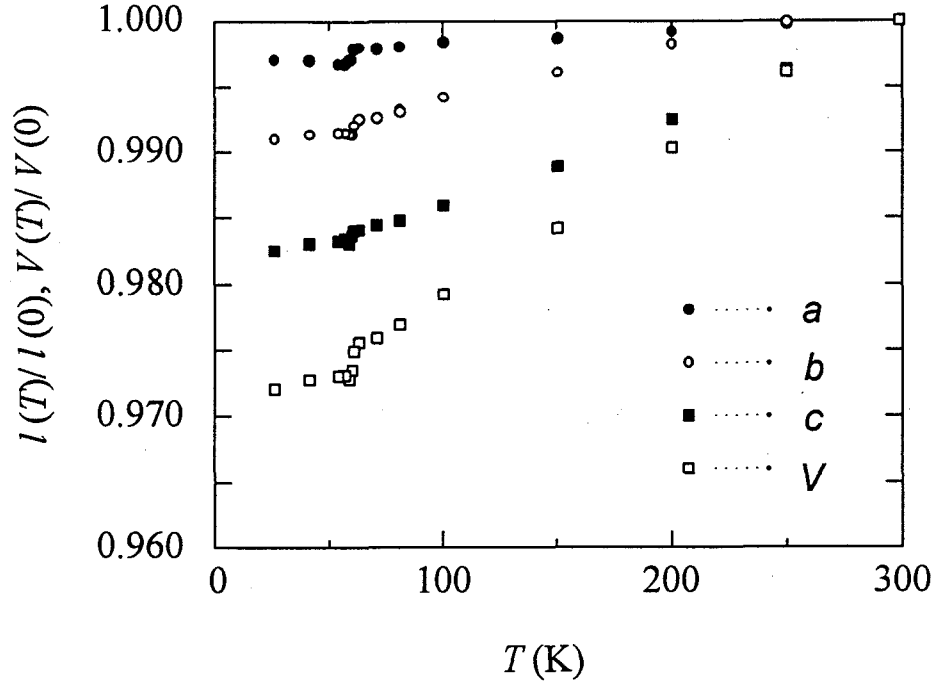


Figure 3.9: Temperature dependence of the lattice parameters  $l(p)/l(0)$  ( $l=a, b, c$ ) and  $V(p)/V(0)$  of  $(\text{BEDT-TTF})_3\text{CuBr}_4$  under ambient pressure [73].

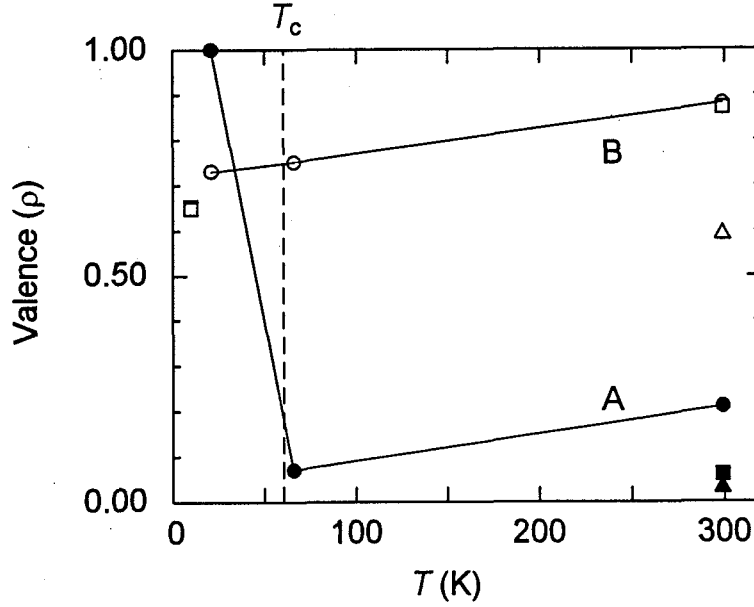


Figure 3.10: Temperature dependence of the charges of BEDT-TTF A (solid symbol) and B (open symbol) molecules in  $(\text{BEDT-TTF})_3\text{CuBr}_4$ . The circles denote the results of Watanabe et al. [73], the triangles are the present results at room temperature, and the squares are the results of Chasseau et al [75]. The solid lines are guides for the eyes. The broken line denotes the location of the phase transition at  $T_c$ .

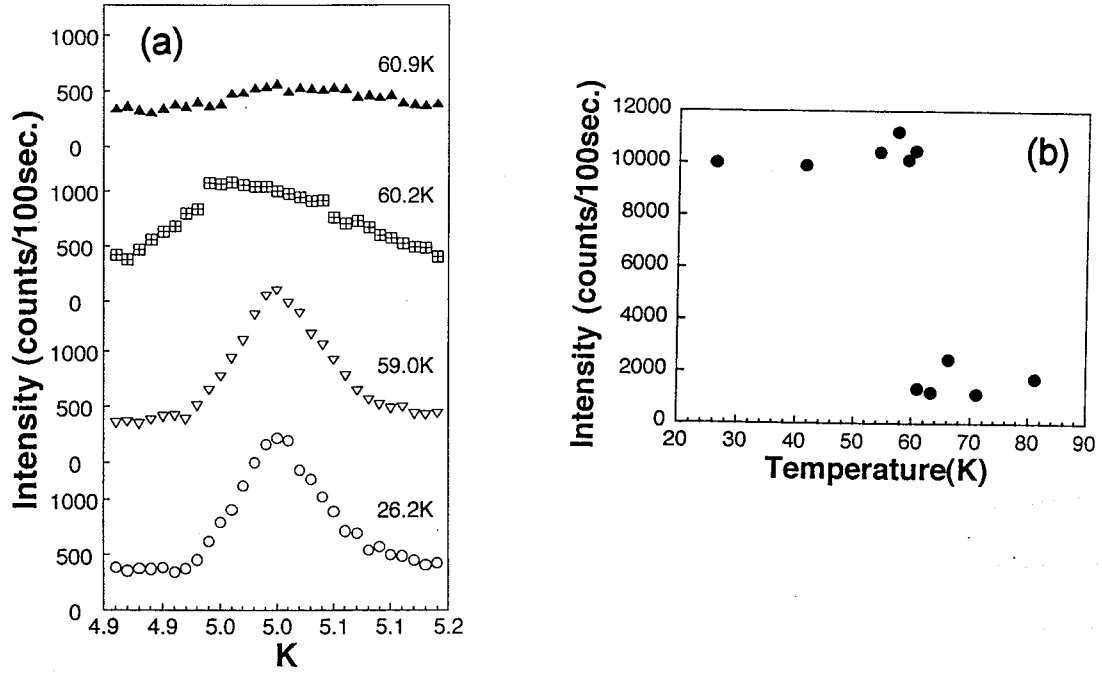
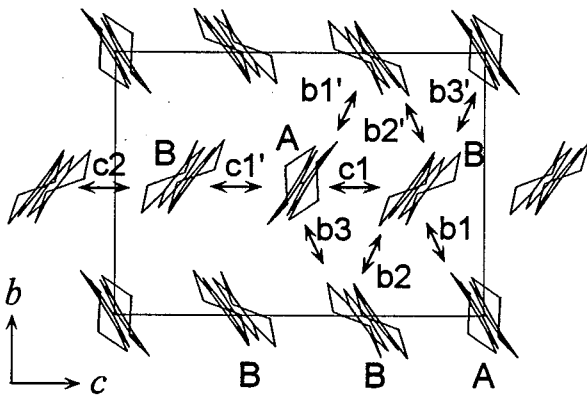


Figure 3.11: Temperature dependence of (050) reflection profile (a) and its integrated intensity (b) [66]. The step wise behavior at  $T_c=59$  K indicates the first order transition with changing the symmetry from  $P2_1/c$  above  $T_c$  to  $Pc$  below  $T_c$ .



	21.0 K	65.9 K	299 K
$b1$	-7.4	-6.6	-6.4
$b2$	10.2	8.9	8.2
$b3$	16.2	14.7	13.2
$b1'$	6.1	6.6	6.4
$b2'$	9.0	8.9	8.2
$b3'$	-14.6	-14.7	-13.2
$c1$	5.5	5.2	4.9
$c1'$	-5.2	-5.2	-4.8
$c2$	0.7	1.0	0.6

( $\times 10^{-3}$ )

Figure 3.12: Overlap integrals of  $(BEDT-TTF)_3CuBr_4$  at three temperatures. The magnitudes of overlap integrals suggest the trimerization of the BEDT-TTF molecules through the overlap integrals  $b2$  and  $b3$  below  $T_c$  [72].

### *X-ray Study under High Pressure*

Figure 3.13 shows the integrated profiles of X-ray diffractions under 0, 7 and 15 kbar, and Figure 3.14 shows the pressure dependence of the  $d$  values for the obtained diffraction lines in the range of 0-40 kbar. The apparent appearance or disappearance of the diffraction lines are not observed with increasing the pressure. The integrated intensity profiles and the diffraction lines change gently and successively with applying the pressure, suggesting the absence of the change in the crystal system and large reconstruction in the structure.

Figure 3.15 shows the integrated powder diffraction pattern and the intensity of the single crystal data as a function of  $2\theta$  at 0 kbar obtained from the  $F_o$  values of the structure analysis in the present work at room temperature. The scattering intensity  $I$  of the single crystal data in the present experiment was calculated from the following equation,

$$I = K|F_{hkl}|^2 f(\theta), \quad (3.3)$$

$$f(\theta) = \cos^2(2\theta), \quad (3.4)$$

where  $K$  is the scale factor,  $F$  is the structure factor and  $f(\theta)$  is the function of the scattering angle factor of the polarization in the experimental using the synchrotron radiation source. In the present setup, the Lorentz factors was not considered because of the use of an imaging plate, and the absorption coefficient was neglected. Then, the difference of wavelength between  $\lambda=0.6888$  Å (present experiment) and  $\lambda=0.71073$  Å (Mo-K $\alpha$ ), which causes the difference of the atom scattering factors, was not also considered. The diffraction lines in the low angle range at 0 kbar can be indexed on the basis of the intensity of the X-ray analysis, then, the lines up to 20 kbar can be analyzed by the indices at ambient pressure keeping the monoclinic unit cell. Table 3.6 shows the observed and the calculated  $d$  values, and indicates the refined lattice parameters under pressure in the range of 0–20 kbar. Above 20 kbar, the error of the cell parameters are large, which is supposed to be caused by the deviation of the X-ray beam from the ideal setup. The weak diffractions, the repeated lines and the diffractions in the high angle range were omitted because of

the difficulty in the analysis. Figure 3.16 shows the pressure dependence of the cell parameters. The slope of the changes of the  $a$  and  $b$ -axis lattice parameters decrease gradually below 14 kbar, while the pressure dependence of the  $c$ -axis lattice parameter is larger than that of the  $a$  or  $b$ -axis one. The linear and volume compressibilities  $\kappa_x$  are defined as

$$\kappa_x = \frac{-d \ln x}{dp} = \frac{-\Delta x}{x \times \Delta p}, \quad (3.5)$$

where  $x$  are  $a, b, c, \beta, V$ , and  $\Delta x(p)$  is  $x(p) - x(0)$ . Using the cell parameters at 0 kbar and 7.1 kbar in the low pressure range, the linear and volume compressibilities  $\kappa_x$  are estimated at  $\kappa_x = 2.0, 1.4, 4.7, 1.7, 7.6 \times 10^{-3} \text{ kbar}^{-1}$  for  $x = a, b, c, \beta$  and  $V$ , respectively, at room temperature. We will discuss the lattice dynamical properties of this compound in the low pressure range in terms of the compressibility.

In the measurement of the single crystal, the reflections along the  $a$ -axis were not refined well because only several reflections were observed because of the restricted scattering angle in the instrument of DAC. Table 3.7 shows the pressure dependence of the cell parameters in the  $b$  and  $c$ -axes, which are roughly in good agreement with the result of the powder samples. A little differences of the cell parameters between the single crystal and the powder samples are thought to be caused by the determination of the cell parameters using a few reflections in the measurement of the single crystal.

The reflection peaks along the  $c$ -axis split into two peaks at 14 kbar as shown in Fig. 3.17, which indicates the presence of two kinds of cell parameters. Moreover, the observation suggests that the first order transition appear at 14 kbar, which is in good agreement with the resistivity anomaly at 13.5 kbar as seen in section 3.3.

In order to study the change of symmetry, I investigated the extinction rule under pressure. At the room temperature under ambient pressure, the space group of this compound has monoclinic  $P2_1/c$  with the extinction rule of ( $h0l$ :  $l=2n+1$ ,  $0k0$ :  $k=2n+1$  disappearance). Thus, I measured the several reflections of ( $0k0$ ) and ( $00l$ ) and then find out the disappearance of reflections ( $0k0$ ) and ( $00l$ ) up to 14 kbar, suggesting to retain the space group  $P2_1/c$  up to 14 kbar. However, ( $002$ )

and (006) reflections were not observed up to 14 kbar, which is thought to be caused by their unobservably weak intensities.



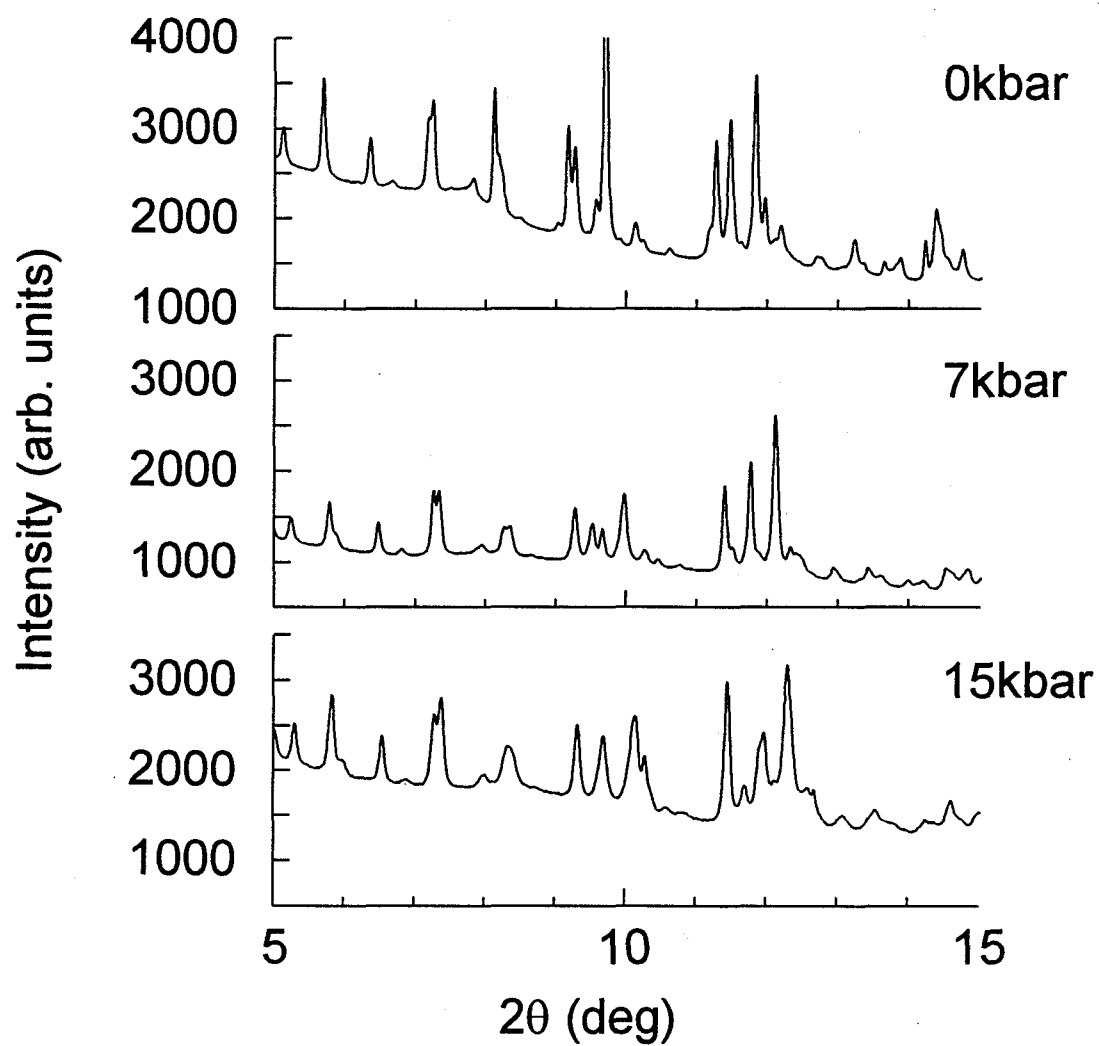


Figure 3.13: The integrated diffraction profiles in the low angle range under 0, 7 and 15 kbar with the X-ray exposure times of 1, 1 and 2 hours, respectively.

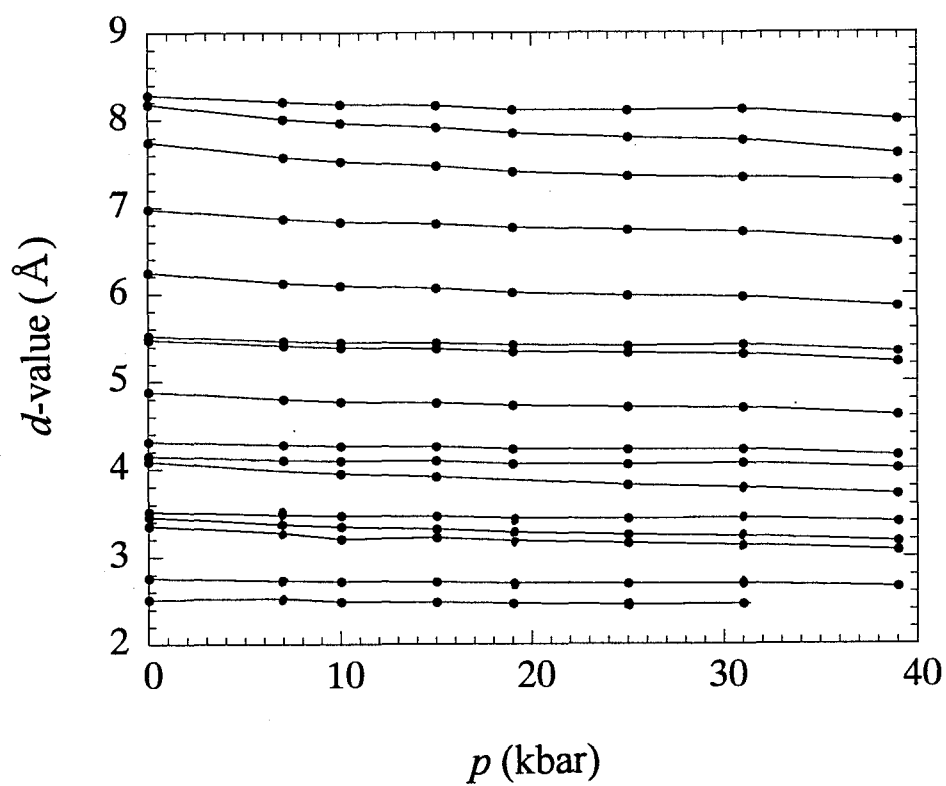


Figure 3.14: Pressure dependence of the  $d$  values of the diffraction lines in the range of 0-40 kbar. The closed circles indicate the collected data and the lines denote guides to the eye.

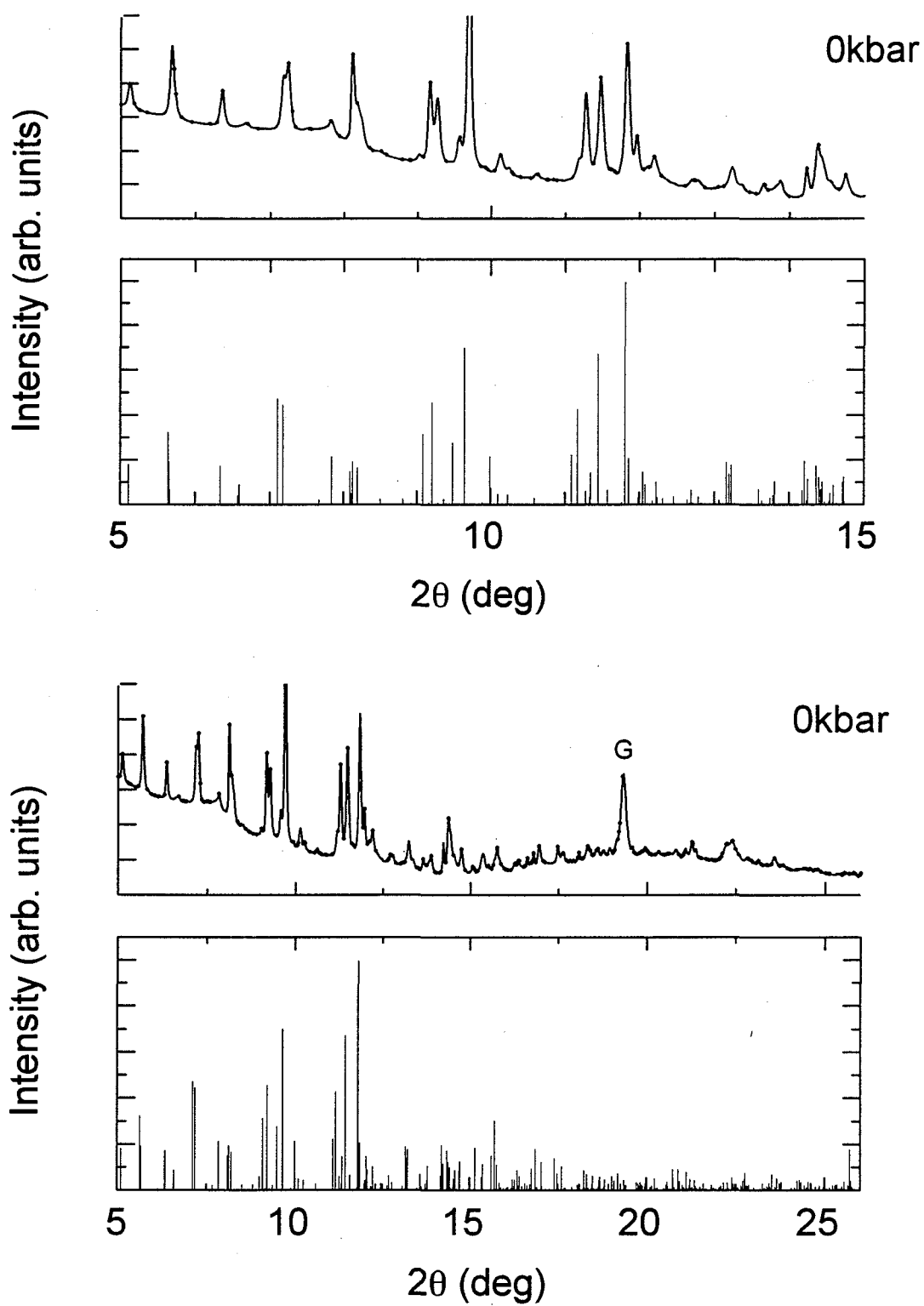


Figure 3.15: Integrated powder diffraction pattern at 0 kbar and the calculated intensity from the  $F_o$  value of the single crystal structure analysis at room temperature under ambient pressure. G refers to the gasket peak.

Table 3.6: The observed and the calculated  $d$  values, the refined lattice parameters and the cell volume under pressures. The weak lines, the repeated lines and the undetermined  $d$ -values in the high angle range are omitted.

$hkl$	0 kbar		7.1 kbar		10 kbar	
	$d_{\text{obs}}$ Å	$d_{\text{calc}}$ Å	$d_{\text{obs}}$ Å	$d_{\text{calc}}$ Å	$d_{\text{obs}}$ Å	$d_{\text{calc}}$ Å
-200	8.280	8.298	8.205	8.203	8.177	8.178
011	8.178	8.155	8.010	8.017	7.964	7.978
-111	7.746	7.727	7.576	7.585	7.525	7.545
-211	6.242	6.236	6.125	6.127	6.094	6.097
-300	5.525	5.532	5.463	5.469	5.449	5.452
211	5.476	5.472	5.408	5.407	5.388	5.390
020	5.072	5.036	4.990	4.986	4.988	4.976
311	4.316	4.325	4.277	4.277	4.264	4.264
400	4.147	4.149	4.104	4.102	4.094	4.089
-213	4.091	4.101	3.980	3.981	3.948	3.944
411	3.518	3.518	3.480	3.480	3.470	3.470
-123	3.456	3.452	3.373	3.375	3.350	3.352
-223	3.353	3.351	3.276	3.274	3.251	3.252
-422	3.117	3.118	3.064	3.064	3.048	3.049
040	2.515	2.518	— <sup>a</sup>	— <sup>a</sup>	2.488	2.488
$a$ (Å)	17.019(6)	[16.999(3)] <sup>a</sup>	16.778(1)		16.713(2)	
$b$	10.072(4)	[10.137(2)]	9.9714(9)		9.953(1)	
$c$	14.252(5)	[14.200(3)]	13.785(1)		13.636(2)	
$\beta$ (°)	102.79(4)	[102.77(1)]	102.076(9)		101.838(1)	
$V$ (Å <sup>3</sup> )	2382(3)	[2386.4(8)]	2255.2(5)		2219.8(3)	
$hkl$	15 kbar		19 kbar			
	$d_{\text{obs}}$ Å	$d_{\text{calc}}$ Å	$d_{\text{obs}}$ Å	$d_{\text{calc}}$ Å		
-200	8.162	8.169	8.111	8.123		
011	7.917	7.933	7.850	7.862		
-111	7.475	7.501	7.411	7.442		
-211	6.060	6.070	6.019	6.029		
-300	5.442	5.446	5.416	5.416		
211	5.375	5.375	5.336	5.333		
020	4.968	4.966	— <sup>b</sup>	—		
311	4.254	4.256	4.225	4.225		
400	4.091	4.084	4.059	4.062		
-213	3.911	3.901	3.872	3.855		
411	3.464	3.465	3.443	3.441		
-123	3.321	3.325	3.286	3.290		
-223	3.224	3.225	3.189	3.193		
-422	3.033	3.035	— <sup>b</sup>	—		
040	2.484	2.483	2.470	2.469		
$a$ (Å)	16.677(4)		16.588(6)			
$b$	9.933(2)		9.877(3)			
$c$	13.458(3)		13.263(4)			
$\beta$ (°)	101.59(2)		101.64(3)			
$V$ (Å <sup>3</sup> )	2184(2)		2128(2)			

<sup>a</sup>Cell parameters of the single crystal structure analysis. <sup>b</sup>The peak was too weak for the fitting.

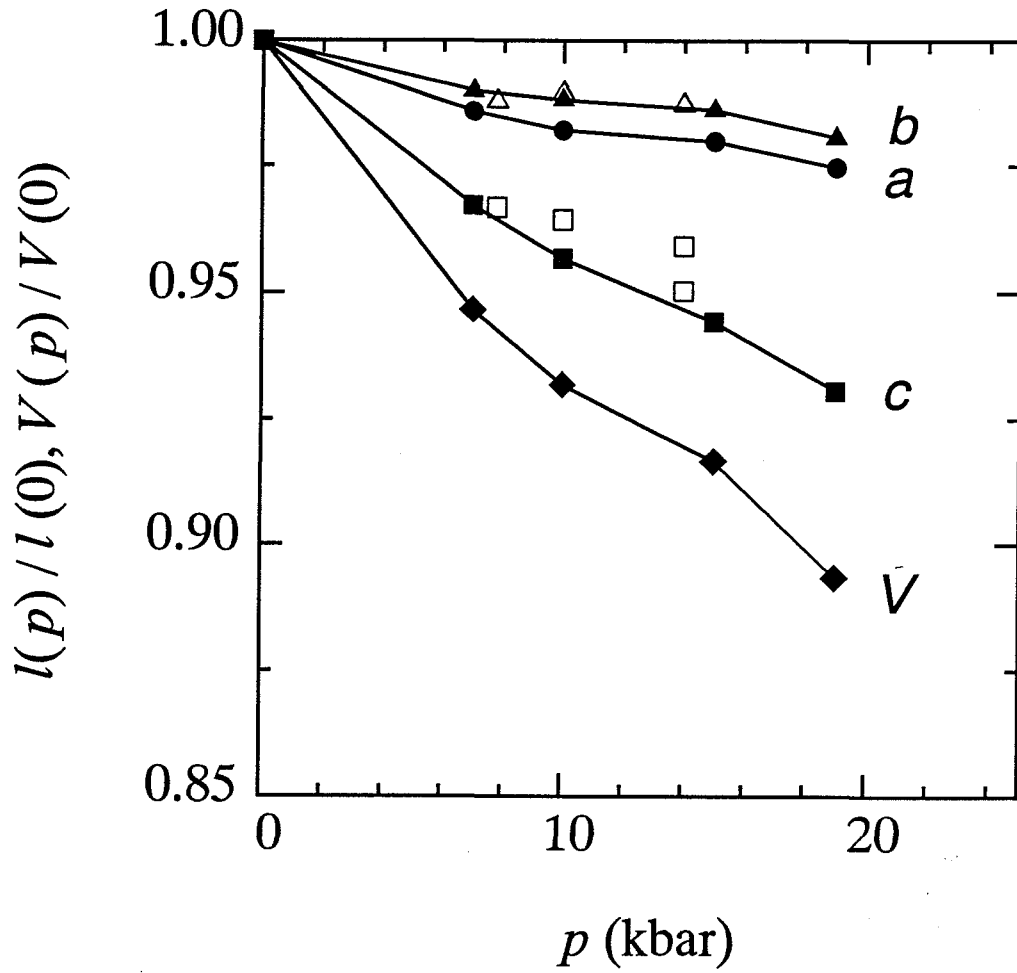


Figure 3.16: Pressure dependence of the cell parameters  $l(p)/l(0)$  ( $l=a, b, c$ ) and  $V(p)/V(0)$  of  $(\text{BEDT-TTF})_3\text{CuBr}_4$  obtained from the powder sample at room temperature. The cell parameters of the single crystal are also shown with the open triangles ( $b$ -axis) and the open squares ( $c$ -axis), and the results along the  $a$ -axis lattice parameter are omitted above 14 kbar owing to their quality.

Table 3.7: Pressure dependence of the lattice parameters of the single crystal.

$p$ (kbar)	$b$ (Å) <sup>a</sup>	$c$ (Å) <sup>b</sup>
7.8	10.014	13.729
10	10.031	13.695
14	10.008	13.496, 13.622 <sup>c</sup>

<sup>a</sup> From (040) reflection. <sup>b</sup> From (008) reflection.

<sup>c</sup> The peak is split into two peaks.

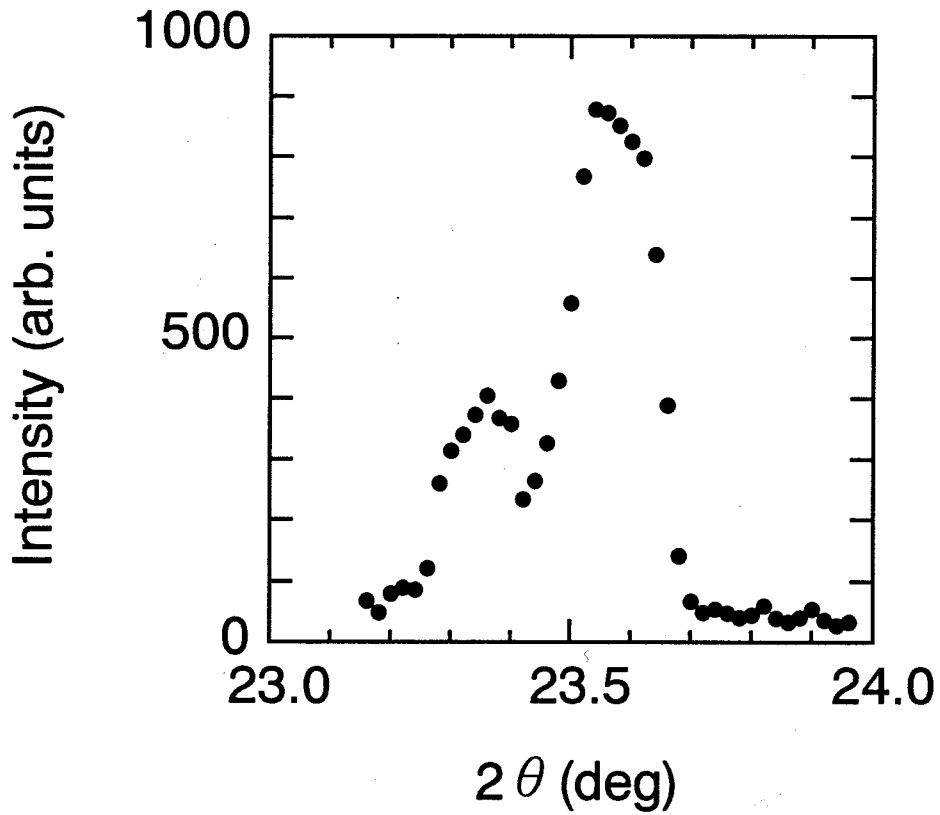


Figure 3.17: Split peak profile of (008) at 14 kbar, indicating the presence of the two kinds of unit cells due to the first order transition.

### 3.2.3 Discussion

The present compound has a structural transition at  $T_c=59$  K with the large change of the electrical and magnetic properties, which is strongly related to the electronic structure as will be discussed later. Here, we summarize the results of the structural analysis in addition to the results of the electronic and magnetic properties in the preceding discussion. The crystal structure has the alternating stacking of BEDT-TTF layer and  $\text{CuBr}_4^{2-}$  anion layer with the  $\text{Cu}^{2+}$  magnetic moments. In the BEDT-TTF layer, the overlap integrals of molecules are large for the  $b$ -axis, while, in the  $c$ -axis the overlap between BEDT-TTF B molecules is significantly small as shown in Fig. 3.12. Below  $T_c$ , the overlaps of b2 and b3 as defined in Fig. 3.12 are enhanced with the BEDT-TTF molecular trimerization. In particular, for the consideration of the electronic structure, it is important to investigate the change of the charges of BEDT-TTF molecules as a function of temperature. That is, above  $T_c$ , the charges of BEDT-TTF A and B molecules are separated into the values of 0 and +1, respectively, however, the charge separation changes to uniformity below  $T_c$ . In the electrical properties, the resistivity has a semiconductive behavior with the temperature dependence of the activation energy  $E_a=1500-250$  K, then, it indicates an anomaly with the thermal hysteresis at  $T_c$ . Applying the pressure causes an abruptly decrease of the resistivity at room temperature, and the resistivity shows the metallic behavior in the high temperature range of  $T_c$  above 9 kbar. In the magnetic properties, the susceptibility shows the Curie-Weiss behavior with the spin number of the corresponding two BEDT-TTF B molecules and one  $\text{Cu}^{2+}$  ion above  $T_c$ . Then, the susceptibility indicates the large reduction at  $T_c$ , and it is governed only by the  $\text{Cu}^{2+}$  ions below  $T_c$ . The observation implies the disappearance of the magnetic moments on BEDT-TTF B molecules below  $T_c$ . According to these results, we discuss the electronic structure, the origin of the structural transition at  $T_c$  and the structural dynamical properties of  $(\text{BEDT-TTF})_3\text{CuBr}_4$  below.

At the beginning, we discuss the electronic structure at room temperature under

ambient pressure. The band structure calculated by Marsden et al. [14] on the basis of the extended Hückel method as shown in Fig. 3.18, where the HOMO level is split into upper four-fold and lower two-fold sub-levels owing to the charge separation between A and B molecules. Taking into account the ratio for the donor and the  $\text{CuBr}_4^{2-}$  anion is 3:1, the half of the upper four-fold sub-bands and the lower two-fold sub-bands are occupied by electrons. Thus, the Fermi level lies on the narrow band gap which indicates that the electronic structure is described as the band insulating state with the semiconductive behavior. However, the band insulating state can not explain the presence of the magnetic moments on BEDT-TTF molecules observed in the susceptibility. This implies that the electronic band structure of the present compound is characterized as a Mott insulator as described in section 1.2. Namely, Mott insulator requires the half-filled band structure in the one electron band approximation without the consideration for the Coulomb repulsion. Thus, the density of states shows the features of degeneracy at the Fermi level in the band structure as represented the schematic density of state in Fig. 3.19. In conclusion, the feature of the band structure in the present compound is the intrinsic half-filled band in the upper four-fold bands generated by the charge separation between BEDT-TTF A and B molecules.

Next, we discuss the phase transition at  $T_c=59$  K under ambient pressure in view of the electronic structure. As discussed above, the charge separation of BEDT-TTF molecules generates the Mott insulating state at room temperature, which is closely related to the presence of magnetic moments on BEDT-TTF molecules. However, the charge distribution between A and B molecules are almost uniformity below  $T_c$  estimated by the bond lengths of BEDT-TTF molecules. The disappearance of the charge separation implies not to realize the Mott insulating state below  $T_c$ , which is just in agreement with the experimental findings that the magnetic moments on BEDT-TTF molecules disappear at  $T_c$ . Moreover, the electrical resistivity shows the semiconductive behavior with small activation energy below  $T_c$ . These suggest that the band structure below  $T_c$  is described by the band insulator with a narrow band



gap. As a consequence, the structural transition at  $T_c$  with the disappearance of the magnetic moments on BEDT-TTF molecules is thought to be the transition from Mott insulator above  $T_c$  to the band insulator below  $T_c$  as represented in Fig. 3.19. We will discuss the origin of the disappearance of the charge separation and the aspect for the magnetic properties of the transition in the section 3.4.

Leaving aside the consideration for the electronic structure, let us now discuss the lattice dynamics at  $T_c$  in the present compound in terms of the anharmonicity of the phonons.

First, we evaluate the anharmonicity which is characterized by the Grüneisen relation. The Grüneisen relation is given by [76],

$$\gamma_{G,i} = \frac{V}{C_\epsilon} \sum_{j=1}^6 \alpha_j (c_{ij})_T, \quad (3.6)$$

where suffices  $i, j=1-6$  are defined as the lattice parameters  $a, b, c, \alpha, \beta$  and  $\gamma$ , the  $\gamma_{G,i}$  are the six components of the thermodynamical Grüneisen parameters for the longitudinal acoustic phonon modes ( $i=1-3$ ) and the shear modes ( $i=4-6$ ),  $V$  is the cell volume,  $C_\epsilon$  is the specific heat at the constant strain component  $\epsilon$ ,  $\alpha_j$  is the thermal expansion coefficient and  $c_{ij}$  is the elastic stiffness constant. The elastic constants  $c_{ij}$  are estimated from the linear compressibilities  $\kappa_j$  using the next Hooke's law,

$$\sum_{j=1}^6 c_{ij} \kappa_j = 1. \quad (3.7)$$

where the suffices  $i, j=1-6$  are defined as  $a, b, c, \alpha, \beta$  and  $\gamma$ , respectively. Here, we neglect the off-diagonal terms of the elastic constants in the Hook's law (eq. 3.7) as a first approximation. Consequently, the ratio of the Grüneisen parameter  $\gamma_{G,i}$  are estimated at  $\gamma_{G,a}:\gamma_{G,b}:\gamma_{G,c}=1:5:3$ , indicating that the anharmonicities in the  $b$  and  $c$ -axes are larger than the anharmonicity in the  $a$ -axis.

Using the obtained Grüneisen constants, we now consider the lattice dynamics at the structural transition  $T_c$ . Generally, in the phase transition with lowering the symmetry, the phonon mode having the eigenvector of the structural displacement at the transition shows a frequency shift of the phonon mode above  $T_c$ . Thus, we relate

the frequency shift to the mode Grüneisen parameter using the thermodynamical Grüneisen parameter in order to discuss the lattice dynamics. Here, the mode Grüneisen parameter  $\gamma(\mathbf{q})$  is given by [76],

$$\gamma(\mathbf{q}, \lambda, \varepsilon_i) = -\frac{1}{\omega(\mathbf{q}, \lambda)} \left( \frac{\partial \omega(\mathbf{q}, \lambda, \varepsilon_i)}{\partial \varepsilon_i} \right)_{\varepsilon'_i}, \quad (3.8)$$

where  $\mathbf{q}$  is the phonon wave vector,  $\lambda$  is the phonon branch index,  $\omega(\mathbf{q})$  is the phonon frequency of the mode  $\omega(\mathbf{q}, \lambda)$ ,  $\varepsilon_i$  ( $\varepsilon_i \neq \varepsilon'_i$ ) is the elastic strain, and  $i=1-6$  refers to the lattice parameters of  $a, b, c, \alpha, \beta$  and  $\gamma$ , respectively. Moreover, the thermodynamical Grüneisen parameter  $\gamma_{G,i}$  is expressed by [76]

$$\gamma_{G,i} = \frac{\sum_{\mathbf{q}, \lambda} \gamma(\mathbf{q}, \lambda, \varepsilon_i) C_\varepsilon(\mathbf{q}, \lambda)}{\sum_{\mathbf{q}, \lambda} C_\varepsilon(\mathbf{q}, \lambda)}. \quad (3.9)$$

Now we assume that the only one longitudinal acoustic phonon mode causes the change of the lattice constants as a function of temperature and that the specific heats  $C_\varepsilon$  are independent of the directions. In the assumption, the above equations (eq. 3.6 and 3.8) suggest that the change of the frequency shift corresponds to the thermodynamical Grüneisen parameter  $\gamma_{G,i}$ . In the present compound, the X-ray analysis reveals the trimerization of BEDT-TTF molecules at  $T_c$  as shown in Fig. 3.12. Judging from the enhancement of the overlap integral, the displacements of the molecules are larger for the  $b$ -axis than that for the  $c$ -axis in the trimerization. Thus, it is suggested that the frequency shifts of the phonon modes corresponding the molecular displacements are large for the  $b$ -axis, resulting in the increase of the magnitude of  $\gamma_{G,i}$  for the  $b$ -axis. This is good agreement with the ratio of the Grüneisen parameters  $\gamma_{G,a} : \gamma_{G,b} : \gamma_{G,c} = 1:5:3$ . Consequently, the structural deformations of BEDT-TTF molecules are thought to cause the anharmonicities of the longitudinal acoustic phonon modes corresponding to the molecular displacements.

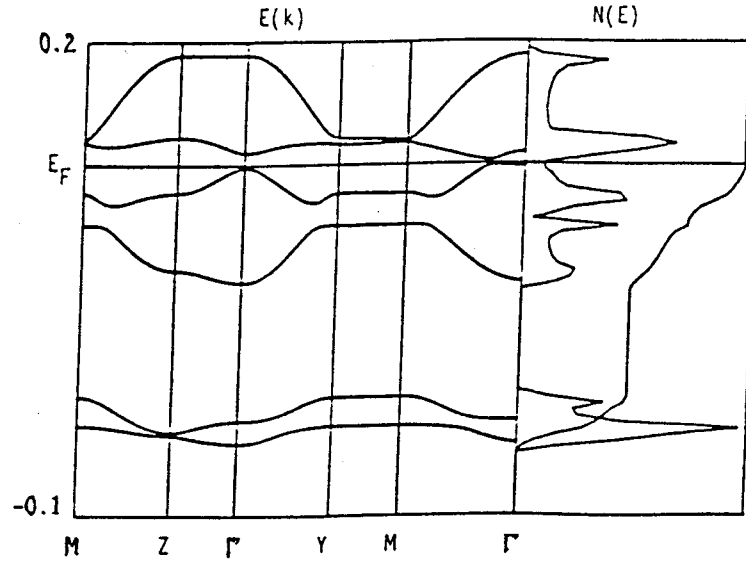


Figure 3.18: Band structure based on the extended Hückel method in Ref. [14]. The band is split into upper four-fold and lower two-fold sub-bands due to the charge disproportionation between BEDT-TTF A (0) and B (+1) molecules.

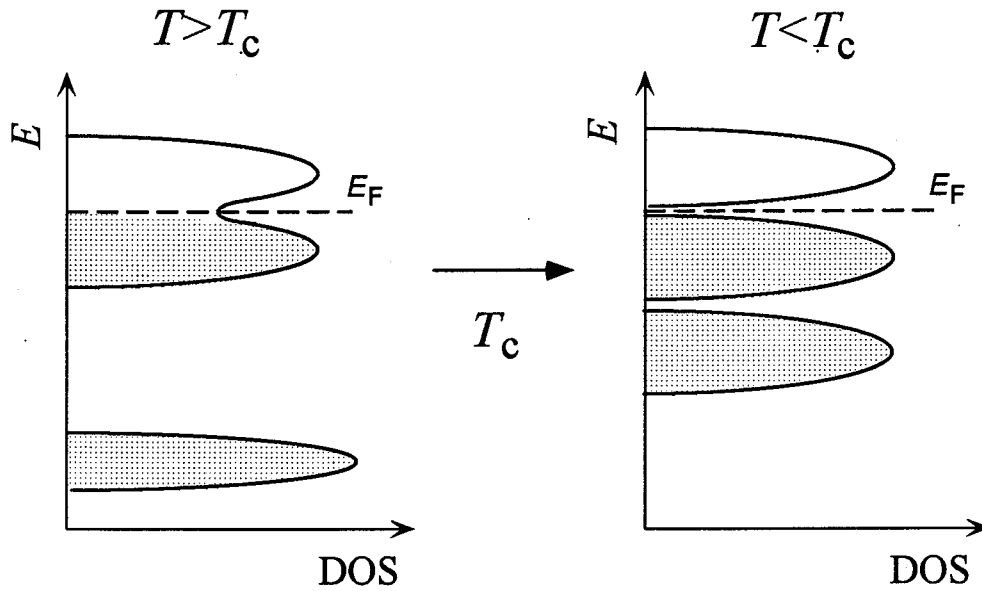


Figure 3.19: Schematic representation of the density of states in the high temperature region (left-hand side) and the low temperature region (right-hand side). The left-hand figure indicates the Mott insulating state above  $T_c$ , and the right-hand figure indicates the band insulating state below  $T_c$ .

### 3.3 Electronic Properties

In general, the electrical conduction properties give useful information on electronic structure because the conduction mechanism reflects the number of carrier, relaxation time, effective mass and band gap. In addition, the experiments under high pressures give important information to consider the electronic structure because the organic salts are usually soft against the external pressure. The feature of the soft solids is expected to give remarkable changes in the physical properties with applying the pressure. Consequently, in this section, I present the investigation of the temperature dependence of the electrical resistivities under ambient and high pressures in order to clarify the electronic structure of (BEDT-TTF)<sub>3</sub>CuBr<sub>4</sub>.

#### 3.3.1 Experimental

The *b*-axis electrical resistivities under ambient pressure and high pressure up to 23 kbar were measured by the four-probe method in the temperature range 4.2-300 K. In the pressure range of 0-15.5 kbar, a Be-Cu clamp cell with the pressure medium of Daphne 7243 Oil (Idemitsu Kosan Co. Ltd.) was used for the high pressure generation. The Be-Cu clamp cell and the sample setup are shown in Fig. 3.20. The values of the pressure were determined by the resistance of Manganin wire (0.05 $\phi$ ) annealed for a day in vacuum at 200 °C and under 10 kbar. The pressure values in the whole temperature range were estimated by the following equation [77],

$$C_p = \frac{1}{R(T)} \times \frac{dR(T)}{dp}, \quad (3.10)$$

where  $C_p$  is the temperature independent coefficient of the pressure determined by the phase transition point of NH<sub>4</sub>F at 3.63 kbar at room temperature,  $R(T)$  is the resistance of Manganin wire and  $p$  is the pressure value. In the pressure range 20-23 kbar, the resistivity measurements were carried out by the cubic-anvil device at The Institute for Solid State Physics in University of Tokyo, where the load was kept at a constant pressure during the measurement of the temperature dependence. The

sample setting in a cubic-anvil is shown in Fig. 3.21. The pressure value was used the calibrated value by means of the phase transitions of  $\text{NH}_4$ , Hg, Bi and Sn.

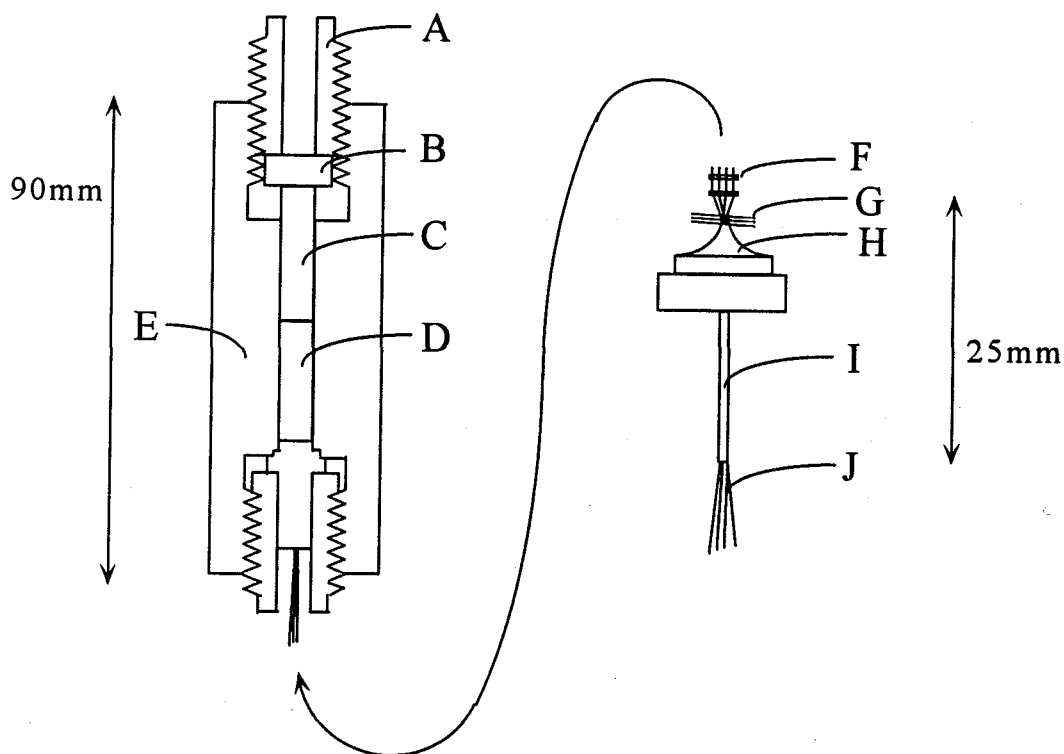


Figure 3.20: Be-Cu clamp cell and sample setting in the measurement under pressure. A: retaining screw, B: backing plate (WC), C: piston (WC), D: Teflon bucket, E: clamp body (BeCu), F: sample, G: manganin wire, H: Stycast 2850 (Grace Japan K. K. ), I: Cupronickel tube, J: Cu wire (0.14 $\phi$ ).

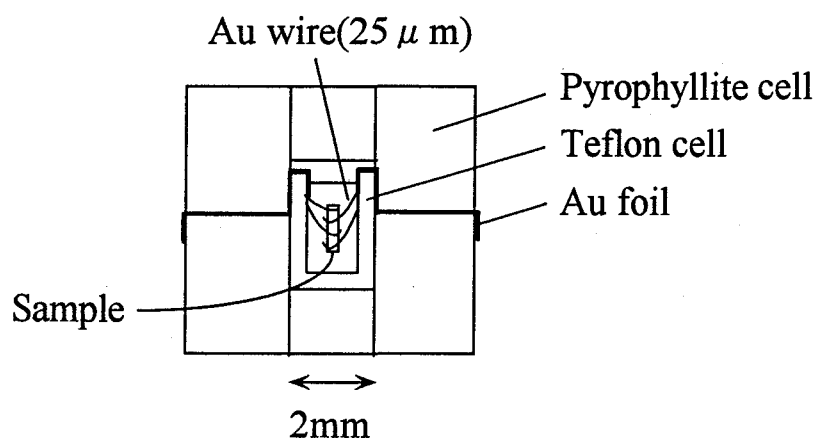


Figure 3.21: Configuration of a cubic type gasket in a cubic-anvil cell and sample setting in the measurement under 20 and 23 kbar [78].

### 3.3.2 Experimental Results

Figure 3.22 shows the temperature dependence of the resistivity and the activation energy at ambient pressure. The resistivity behaves the semiconductive in the investigated temperature range 40-300 K with the resistivity value  $\rho_{rt}=3.2 \Omega\text{cm}$  at room temperature. It shows an anomaly at  $T_c=58.8 \text{ K}$  with a thermal hysteresis, which indicates the presence of a semiconductor-semiconductor transition at  $T_c$  with the first order nature agreeable to the result of the X-ray analysis in the previous section. Moreover, the resistivity shows a novel temperature dependence of the activation energy  $E_a=1500\text{-}250 \text{ K}$  above  $T_c$ , and then, it indicates nearly temperature independence of the activation energy  $E_a\sim 300 \text{ K}$  below  $T_c$ . As shown in Fig. 3.23, at room temperature, the resistivity decreases rapidly with applying the pressure, and it reaches 1/120 ( $0.01 \Omega\text{cm}$ ) of the value at ambient pressure ( $1.5 \Omega\text{cm}$ ) at 12 kbar. Above 12 kbar the resistivity upturns gradually up to 13 kbar, and then it decreases again above 13 kbar.

Figure 3.24 shows the temperature dependence of the resistivity under high pressures, where the pressure values  $p$  are the clamped values at room temperature. In the measurement with a clamp type cell, the pressure values at room temperature decrease with lowering the temperature. On the high temperature side of  $T_c$ , the resistivity decreases rapidly with the application of pressure, and then, it changes from the semiconductive behavior to metallic one above 7 kbar. In particular, at 7 kbar the resistivity changes from the semiconductive behavior to the metallic one although the decrease of the pressure value due to the thermal contraction of the pressure medium. The semiconductor-semiconductor transition temperature  $T_c=59 \text{ K}$  under ambient pressure raises up to  $T_c=102 \text{ K}$  under 9 kbar, and the feature of the transition is modified to metal-insulator one above 9 kbar. Below  $T_c$ , the activation energies of the resistivities at 55 K are evaluated at  $E_a=320\text{-}350 \text{ K}$  under 0-9 kbar.

Figure 3.25 shows the temperature dependence of the resistivity under 0 and

11-15.5 kbar. In the pressure range 11-13 kbar, the resistivities show the similar temperature dependence in the whole temperature range with the metal-insulator transition at  $T_c \sim 96$  K. However, the resistivity above 13.5 kbar are different behavior from that under 11-13 kbar on the high temperature side of  $T_c$ . Namely, the resistivity raises up gradually with decreasing the temperature above 13.5 kbar. Moreover, a step like increase of the transition temperature is observed with applying the pressure from 13 to 13.5 kbar. The anomalous behavior above 13.5 kbar is considered to be associated with a first order transition observed in the measurement of high pressure X-ray diffraction. The activation energies of the resistivity at 55 K are evaluated at  $E_a \sim 350$  K under 11-15.5 kbar.

Figure 3.26 shows the temperature dependence of the resistivity under 20 and 23 kbar. It indicates a weak temperature dependence on the high temperature side of the metal-insulator transition. The transition temperatures are observed at 50 and 48 K under 20 and 23 kbar, respectively, suggesting that the application of pressure makes the transition temperature lowered from the value at 15 kbar. However, the temperature dependence below  $T_c$  under 20 and 23 kbar could not be measured owing to the poor contact of the Au wires used for electrodes.

It should be noted that the temperature dependence just below  $T_c$  seems to be changed gently with applying the pressure. In order to clarify the nature of the transitions, the temperature dependence of the resistivity are analyzed around  $T_c$  under high pressures in terms of the gap formations. In the semiconductor, the temperature dependence of the resistivity  $\rho(T, P)$  is represented by the following equation,

$$\rho(T, P) = \rho_0(T, P) \exp(E_g(T, P)/2k_B T), \quad (3.11)$$

where  $\rho_0(T, P)$  is the pre-exponential factor,  $E_g(T, P)$  is the band gap and  $k_B$  is the Boltzmann constant. The above equation is transformed as seen below.

$$\frac{d \ln \rho(T, P)}{d(1/T)} = \frac{d \ln \rho_0(T, P)}{d(1/T)} + \frac{E_g(T, P)}{2k_B}. \quad (3.12)$$

Now we assume the semiconductor-semiconductor or the metal-insulator transition



is governed by the band gap formation around  $T_c$ . Around the transition, the band gap  $E_g(T, P)$  is thought to be proportional to the order parameter  $\sigma(T, P)$  of the transition, and then, the order parameter  $\sigma(T, P)$  is considerably larger than that of the pre-exponential factor  $\rho_0(T, P)$ . Thus, the eq. (3.12) is represented by the following equation around  $T_c$ ,

$$\frac{d \ln \rho(T, P)}{d(1/T)} \simeq K \cdot \frac{\sigma(T, P)}{2k_B}, \quad (3.13)$$

where  $K$  is the renormalized factor. Figure 3.27 shows  $d \ln \rho(T, P)/d(1/T)$  vs  $T$  plots. In the experiment, the finite values of  $d \ln \rho(T, P)/d(1/T)$  just above  $T_c$  are caused by the critical fluctuation effect of the phase transition. In order to describe the nature of the phase transition quantitatively, we employ the half width  $\Delta T_{1/2}$  of the peak as defined in Fig. 3.28. The half width  $\Delta T_{1/2}$  reflects the nature of the phase transition, namely, in the pure first order transition  $\Delta T_{1/2}$  become zero, while, in the pure second order transition,  $\Delta T_{1/2}$  gives the value of  $\Delta T_{1/2} = 0.094 T_c$  according to the BCS theory of the gap formation [79]. In Fig. 3.28, the normalized width  $\Delta T_{1/2}/T_c$  increases gradually with increasing the pressure, which is thought to be caused by the change in the transition feature from the first order nature to the second order one. However,  $\Delta T_{1/2}/T_c$  is abruptly changed to nearly zero at 13.5 kbar, suggesting the resumption of the first order nature above this pressure, which is in good agreement with the result of the X-ray measurement at 14 kbar. These observations of the change in the transition nature are followed by the change of thermal hysteresis in the resistivity. Namely, the thermal hysteresis shows the width of about 3 K under ambient pressure at  $T_c$  between the heating and cooling runs, and the width narrows gradually with increasing the pressure up and reaches to zero just below  $P_{c2}$ . Nonetheless, the width is suddenly broaden at the metal-metal transition pressure  $P_{c2} = 13.5$  kbar. These observations are in good agreement with the pressure dependence of  $\Delta T_{1/2}$ .

As a summary of the resistivity behavior, the pressure-temperature phase diagram is shown in Fig. 3.29, where the pressure values due to the thermal contraction

of the pressure medium are corrected using the resistance of the manganin wire. The insulator phase I(I) exists in the low pressure and high temperature region, and I(I) changes to the metallic phase M(I) with the application of the pressure. And then, the increase of the pressure leads to the another metallic phase M(II) through the first order transition as mentioned above. Here, the transition from I(I) to M(I) is defined  $P_{c1}$ , and the transition from M(I) to M(II) is defined  $P_{c2}$ . In the measurement of the temperature dependence, the insulator phase I(I) changes to the another insulator phase I(II) through the structural transition at  $T_c$  with decreasing the temperature. The structural transition temperature under  $T_c=59$  K at ambient pressure increases to about 100 K gradually up to 5 kbar and shows less pressure dependent feature to 13.5 kbar. Moreover,  $T_c$  shows a step wise increase at  $P_{c2}$ , and then it decreases remarkably in the high pressure region above 20 kbar.

Further, the temperature dependence of the resistivity under 7 kbar changes from the semiconductive behavior to the metallic one with decreasing the temperature. It is explained that the measurement process at 7 kbar crosses over the phase transition boundary of  $P_{c1}$ , so that, the slope of the phase boundary line at  $P_{c1}$  is negative tilted to the M(I) phase.

Furthermore, the difference of the temperature dependence between 13 and 13.5 kbar is significantly large, however, the measurement processes at 13 kbar and 13.5 kbar have no apparent change of the resistivity accompanied by the crossing the phase boundary of  $P_{c2}$ . Thus, the phase boundary line of  $P_{c2}$  is also negatively tilted to the M(II) phase.

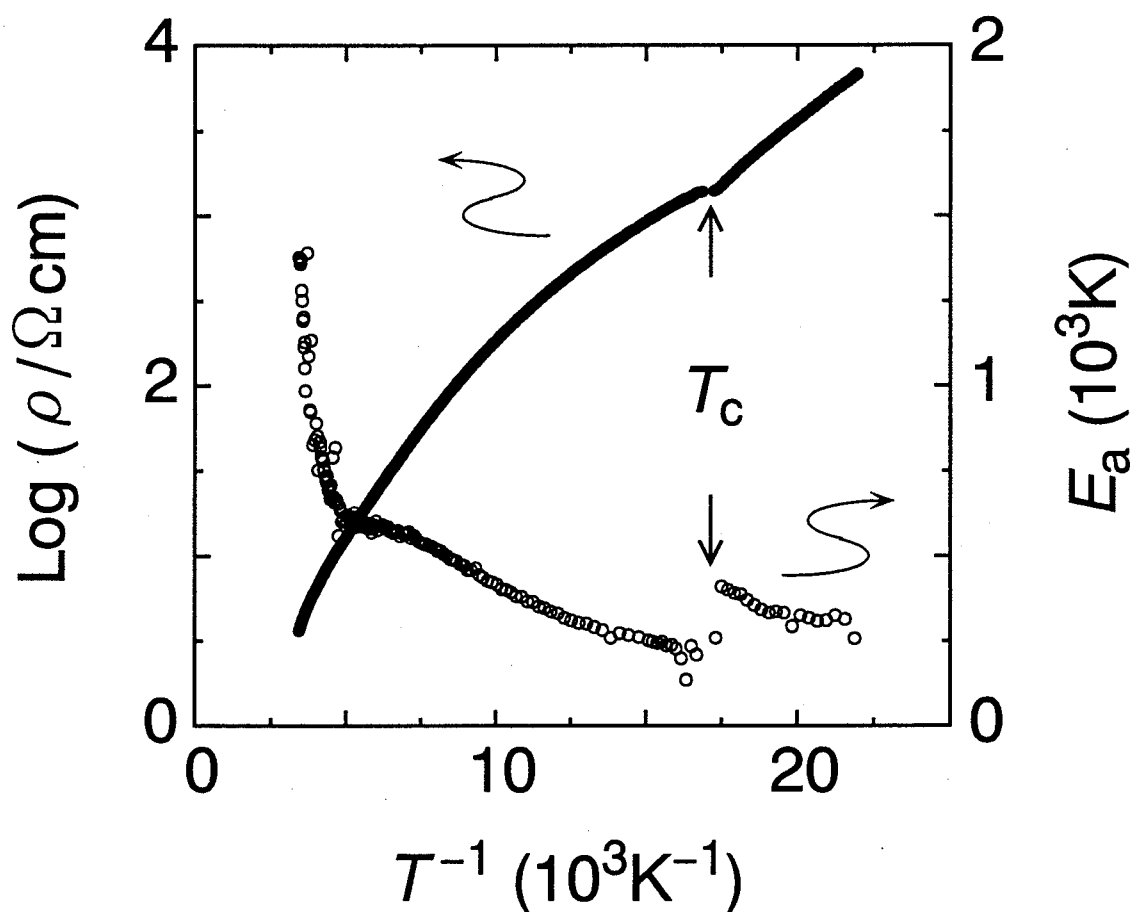


Figure 3.22: Temperature dependence of the  $b$ -axis resistivity and the activation energy  $E_a$  of  $(\text{BEDT-TTF})_3\text{CuBr}_4$  at ambient pressure. It shows an anomaly at  $T_c=59 \text{ K}$  with a thermal hysteresis.

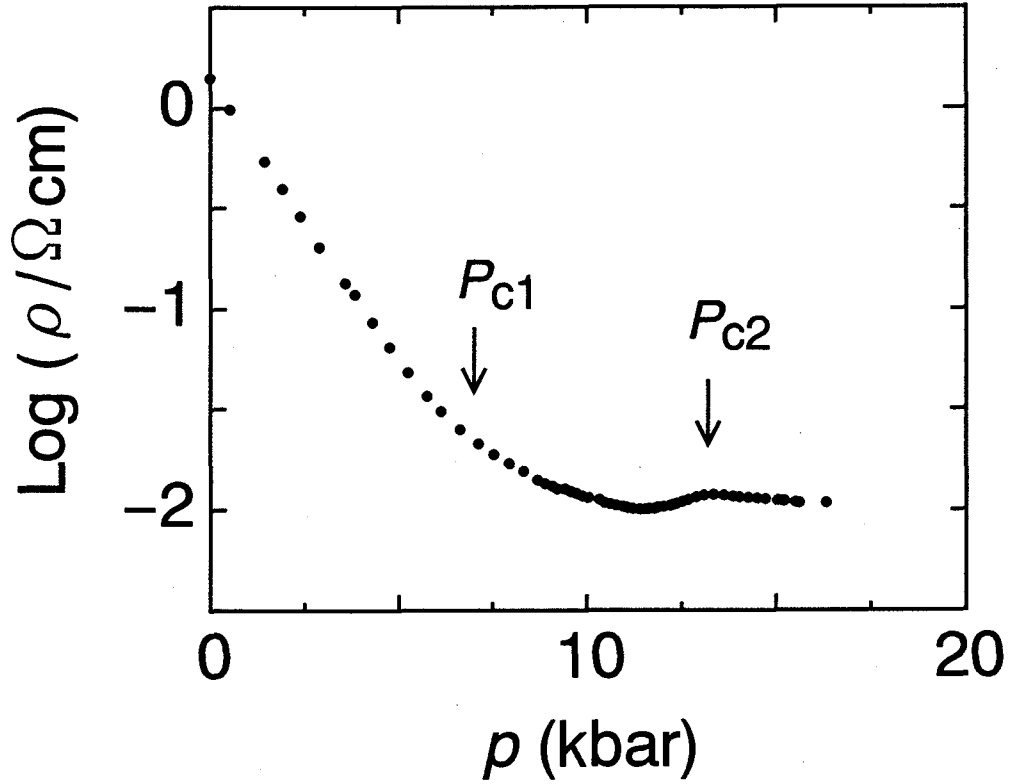


Figure 3.23: Pressure dependence of the resistivity at room temperature. It decreases rapidly with the application of pressure, and reaches the magnitude of  $1/120$  ( $0.01 \Omega \text{ cm}$ ) at 12 kbar to the value of  $1.5 \Omega \text{ cm}$  under ambient pressure.  $P_{c1}$  and  $P_{c2}$  refer to the critical pressures for the insulator-metal and the metal-metal transition, respectively.

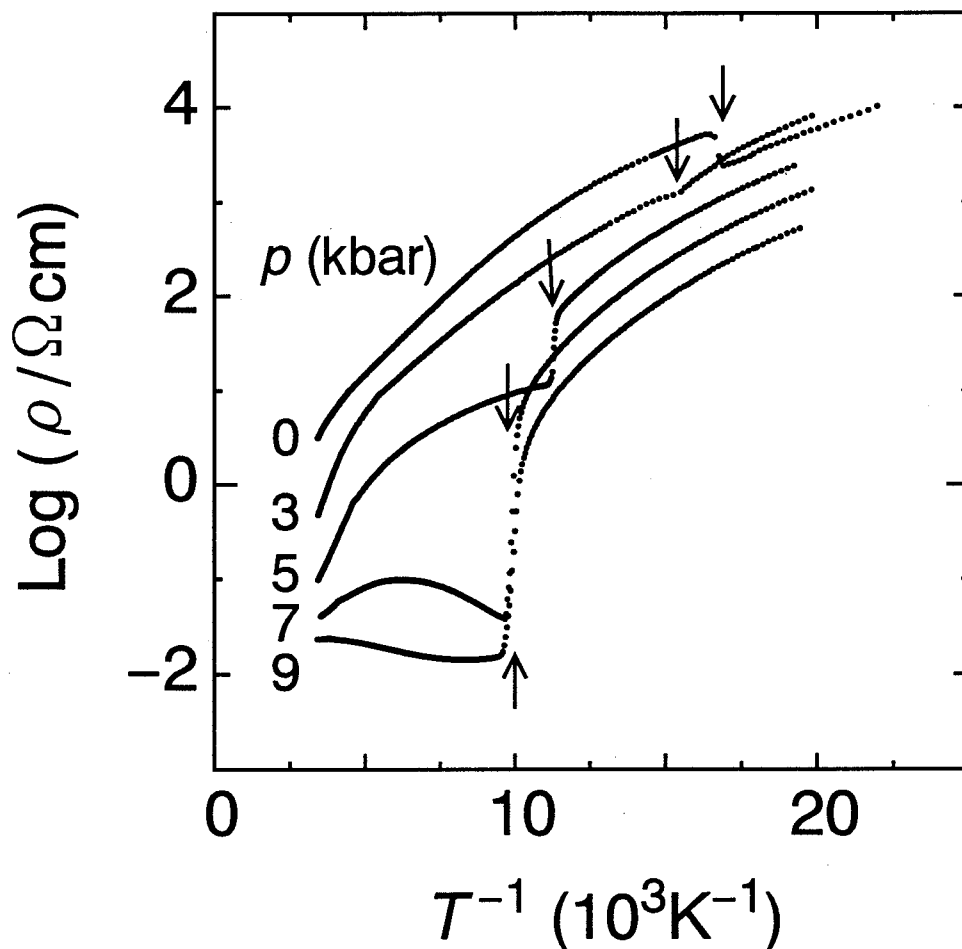


Figure 3.24: Temperature dependence of the resistivity under several pressures 0-9 kbar. The pressure values in the parentheses of  $p$  are the clamped values at room temperature, which decrease gradually with lowering the temperature. The same sample is used to measure in the pressure of 0-9 kbar. The resistivity changes to the metallic behavior rapidly with the application of pressure on the high temperature side of  $T_c$ . The transition at  $T_c$  is represented by the inset arrows. The transition temperature  $T_c$  increases gradually by applying pressure, and reaches to about 102 K at 9 kbar.

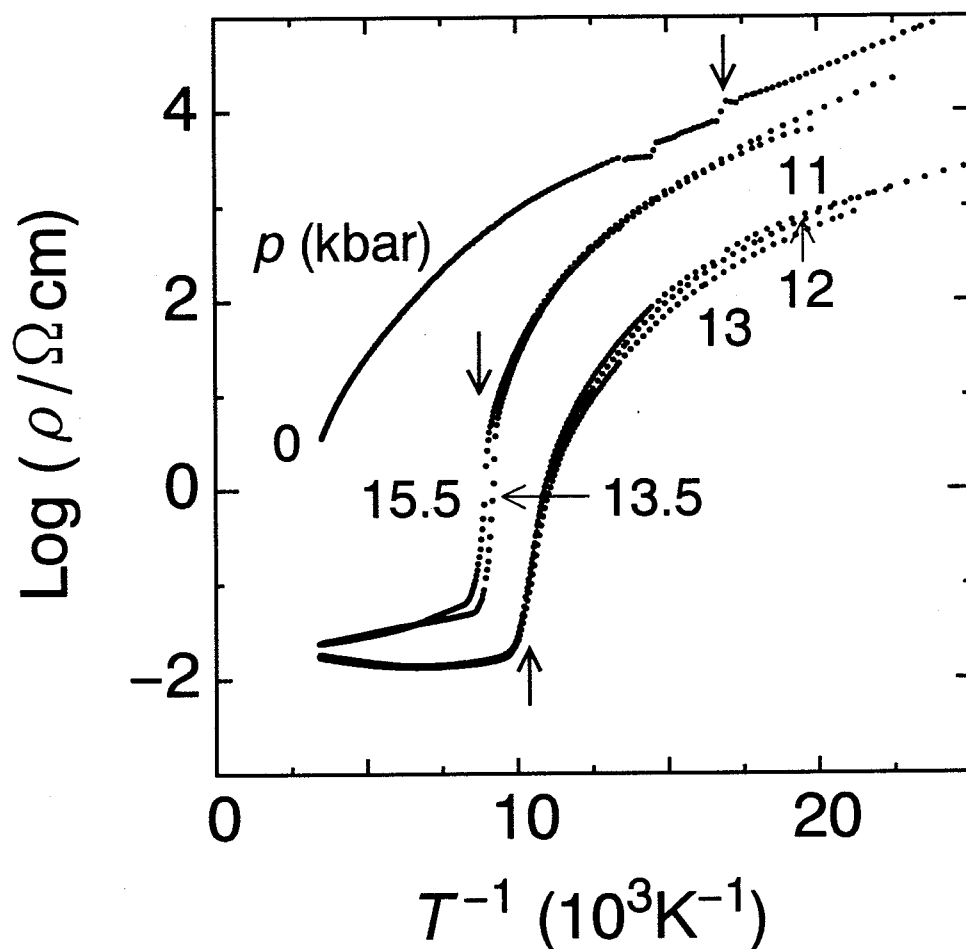


Figure 3.25: Temperature dependence of the resistivity under 0 and 11-15.5 kbar. The measured sample is different from the sample used for the pressure range of 0-9 kbar. The transition temperature  $T_c$  is represented by the inset arrows. Apparent difference of the temperature dependence between 13 and 13.5 kbar is observed, which suggests the presence of a phase transition at 13.5 kbar.

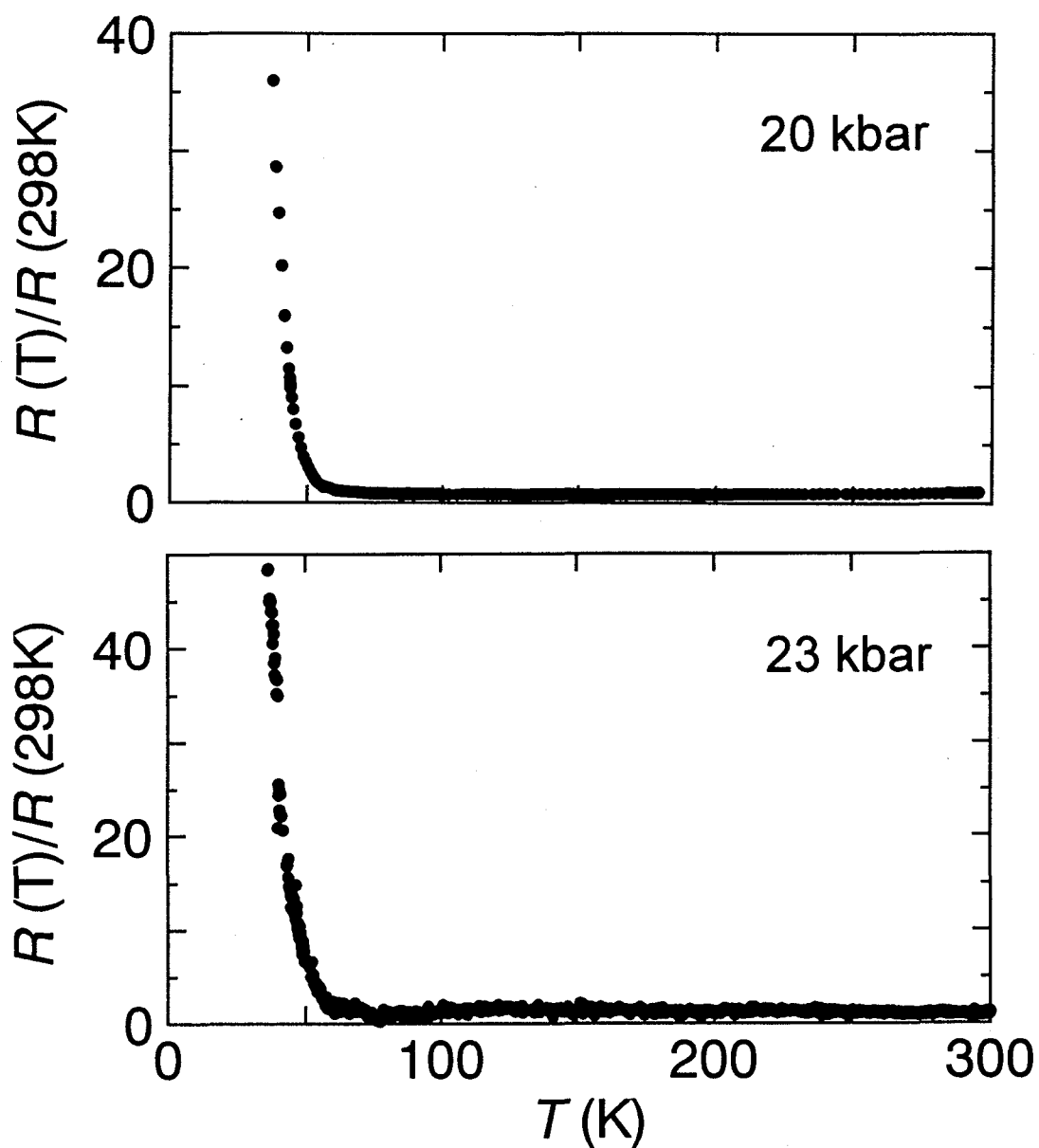


Figure 3.26: Temperature dependence of the resistivity at 20 and 23 kbar measured by the cubic-anvil instrument, where the pressure was kept at a constant value in the measurement of the temperature dependence. The transition temperatures are determined by the onset.

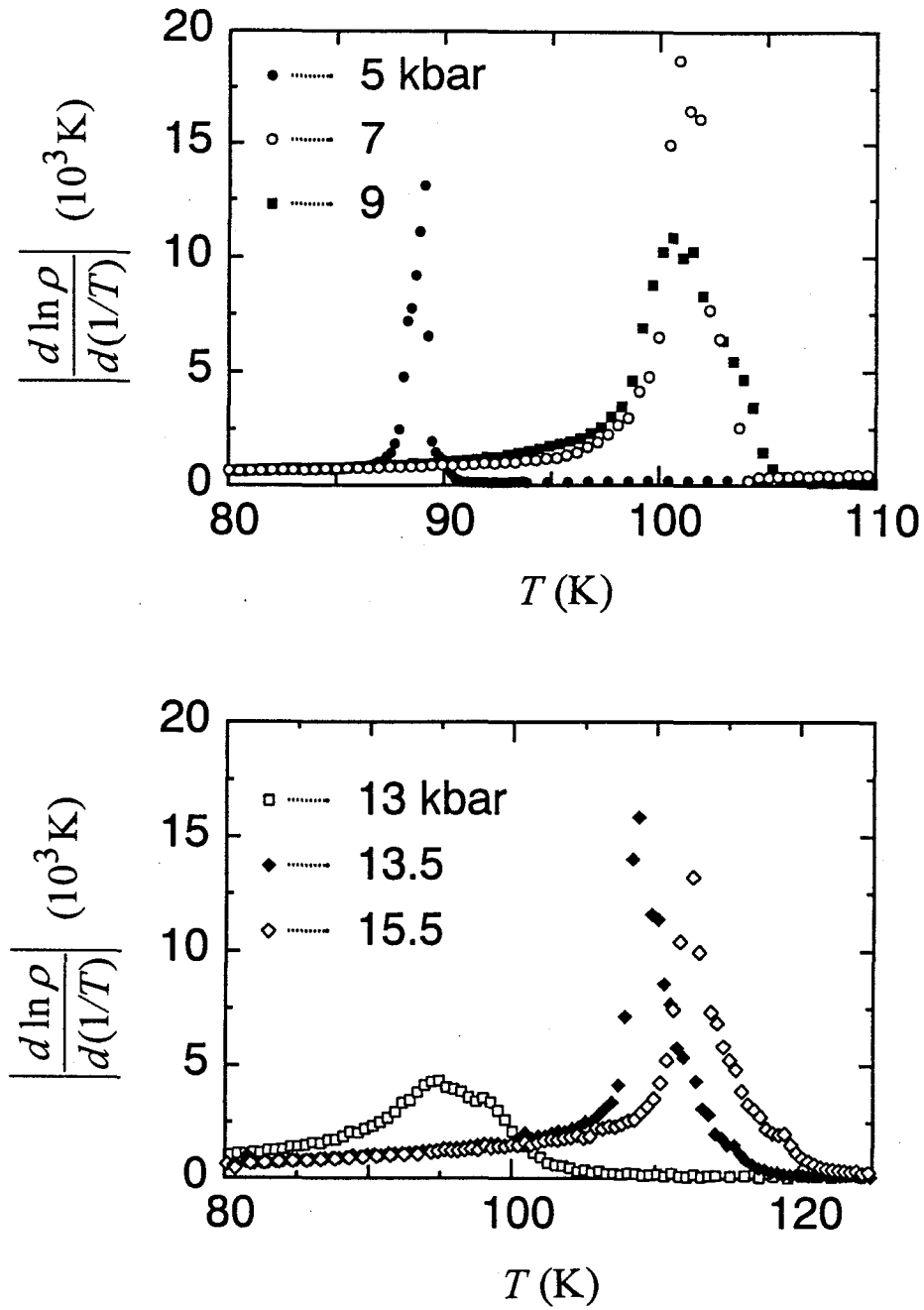


Figure 3.27: The temperature derivatives of the resistivity vs  $T$  plots at several pressures. At 5 kbar, it shows a sharp peak due to the first order transition. The transition broadens with applying the pressure, suggesting the change of transition nature from the first order transition to the second order ones. However, the sharpness in the transition peaks is restored above 13.5 kbar.



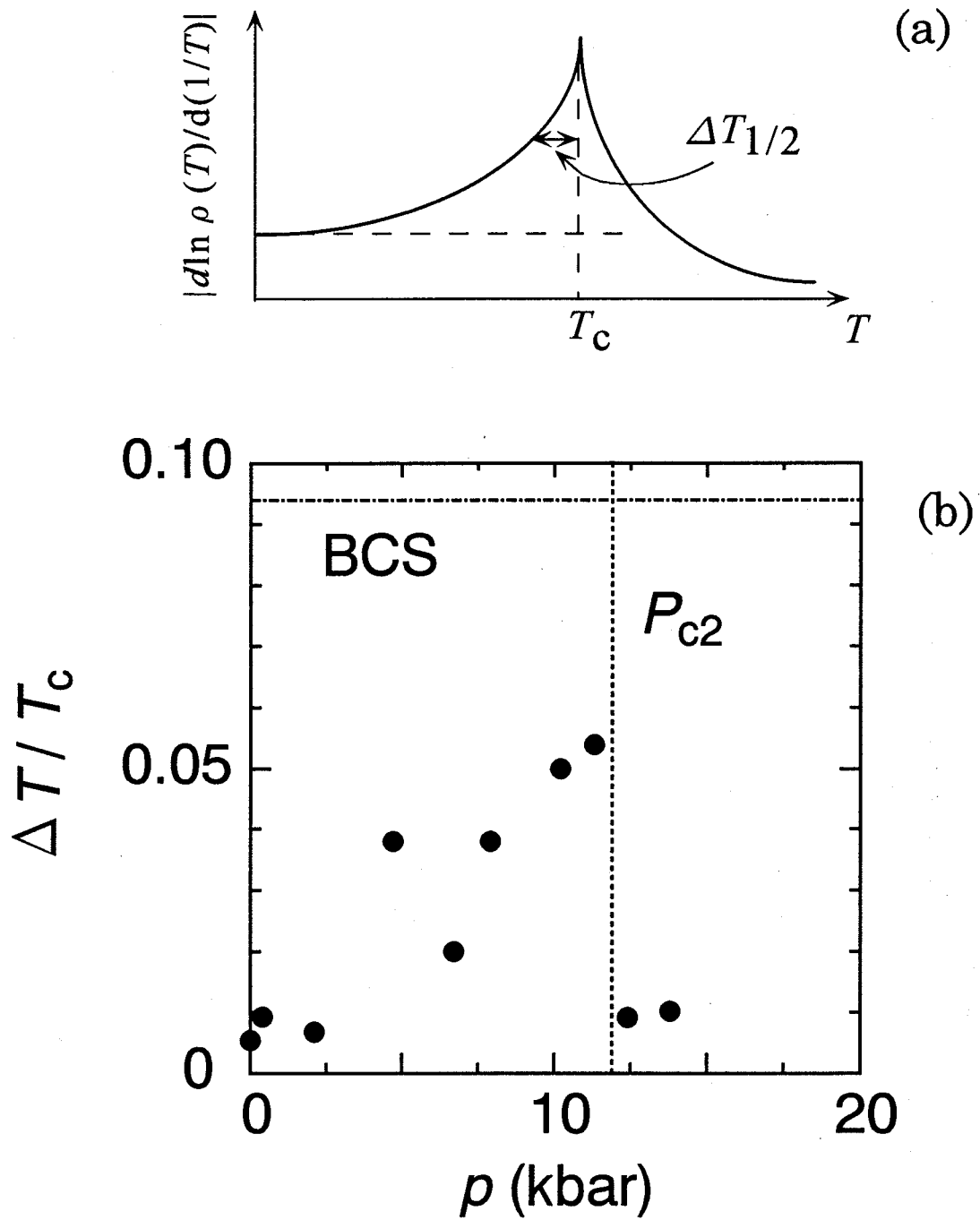


Figure 3.28: The definition of the half width  $\Delta T_{1/2}$  of the peak around  $T_c$  in the differential logarithmic resistivity (a) and pressure dependence of  $\Delta T_{1/2}/T_c$  (b). The pressure values are corrected by the resistance of Manganin wire. There is a discontinuous change in  $\Delta T/T_c$  at the critical pressure  $P_{c2}$ , represented by the dotted line. The critical pressure  $P_{c2}$  is the phase boundary between the M(I) and M(II) phase. The dash-dotted line denotes  $\Delta T_{1/2}=0.094T_c$  estimated by the gap formation of BCS type for the pure second order transition.

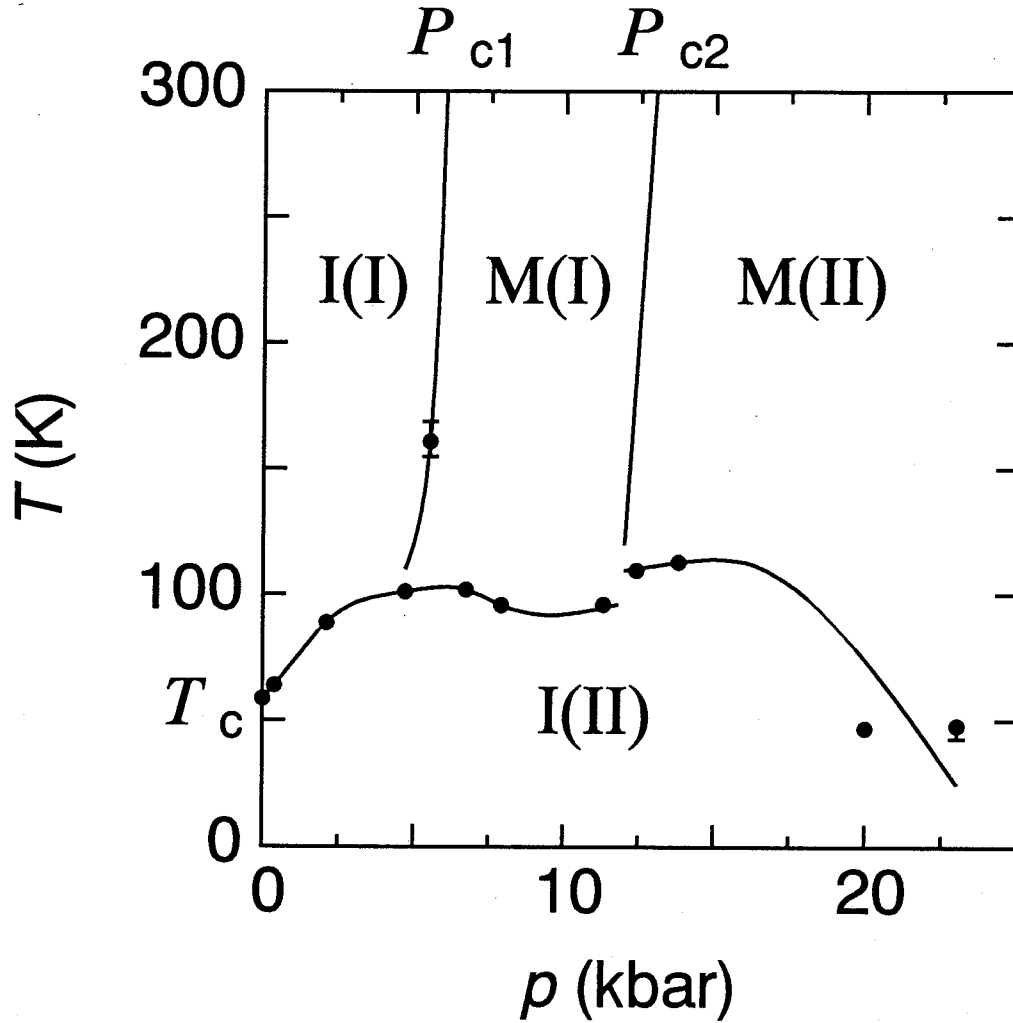


Figure 3.29: Pressure-temperature phase diagram of  $(\text{BEDT-TTF})_3\text{CuBr}_4$  obtained by the measurements of resistivity under pressures, where the pressure values are calibrated to avoid the effect of thermal contraction. The transition temperatures are defined by the mid-point of the transition between the cooling and heating processes. I(I), I(II), M(I) and M(II) denote the insulator (I), insulator (II), metal (I) and metal (II) phases, respectively.  $T_c$  is the insulator-insulator or metal-insulator transition with changing the temperature.  $P_{c1}$  is the critical pressure for the transition between I(I) and M(I), and  $P_{c2}$  is the critical one between M(I) and M(II).

### 3.3.3 Discussion

From the results and discussion of the structural properties and the magnetic properties in section 3.2 and 3.4, the high temperature insulator phase I(I) of the present compound is described by a Mott insulating state which has the magnetic moments on BEDT-TTF molecules. The lowering of temperature leads to the transition at  $T_c=59$  K from the Mott insulator to the band insulator at ambient pressure, accompanied by the disappearance of the charge disproportionation of the BEDT-TTF molecules. In this part, we discuss the behavior of the resistivity as a function of the temperature or the pressure on the basis of the above considerations.

First, we discuss the change in the electrical resistivity under pressure at room temperature. With increasing the pressure, the resistivity at room temperature shows a remarkable decrease and reaches 1/120 of the ambient pressure value at 12 kbar. The remarkable decrease with the slightly application of pressure is thought to be caused by the change from the insulator phase I(I) to the metallic phase M(I) at 7 kbar. Thus, we discuss the origin of the insulator-metal transition now. Here, taking into account that the I(I) phase is described as a Mott insulator, we remind the pressure-temperature phase diagram of the ordinary Mott insulator  $V_2O_3$ . As the phase diagram of  $V_2O_3$  shown in Fig. 1.5, the Mott insulator phase exists facing to the paramagnetic metal state on the high pressure side through the boundary of the Mott transition on the critical pressure at  $W/U \sim 1$  ( $W$ : band width,  $U$ : on-site Coulomb), which is explained by the increase of the band width with applying the pressure. In the present compound, the application of pressure also increases the band width with reducing in the intermolecular distance, while, the on-site Coulomb interaction does not change under pressure. Thus, we can compare the phase diagram between  $V_2O_3$  and  $(BEDT-TTF)_3CuBr_4$  in terms of the pressure effect. From the above consideration, this phase diagram is significantly similar to that of  $(BEDT-TTF)_3CuBr_4$ , suggesting that the origin of the insulator-metal transition at  $P_{c1}=7$  kbar is the same as that in  $V_2O_3$ . Moreover, the magnetic

susceptibility decreases with increasing the pressure as described in section 3.4, which is explained by the change from Curie-Weiss nature in the Mott insulator phase to Pauli paramagnetism in the paramagnetic metal phase. Consequently, the feature of the abrupt decrease in the resistivity with the application of pressure is explained by the change from Mott insulator phase to the paramagnetic metal one through Mott transition at  $P_{c1}$ . This proves that the present compound lies near the Mott boundary. The increasing the pressure from M(I) causes to change to the M(II) phase through the phase boundary of  $P_{c2}$  characterized as the first order transition. In the M(II) phase, the resistivity raises up gently with lowering the temperature, which is unusual behavior judging from the behavior of ordinary semiconductors. In Mott-Hubbard system, this behavior is often observed in the metallic phase near the Mott transition, which originates from the strong electron-electron correlation [24, 25]. However, in the present compound, the metallic phase with the highly correlated metal behavior is not placed near the Mott transition. This contradict is considered to be caused by the structural change accompanying the first order transition at  $P_{c2}$ . Nonetheless, we do not have the information of the crystal structure above  $P_{c2}$ , thus, it is difficult to discuss the resistivity behavior above  $P_{c2}$ . It will be resolved in the future investigation.

Leaving the pressure effect at room temperature, we discuss the temperature dependence of resistivity under ambient pressure. As seen in Fig. 3.22, the feature of the resistivity is the large temperature dependence of the activation energy in the high temperature region. In Mott insulator, the activation energy corresponds to the band gap which is generated by the on-site Coulomb repulsion. As the result, the temperature dependence of the activation energy indicates the temperature dependence of the band gap. Here, the application of pressure causes the increase of the band width accompanied by the reduction in the intermolecular distance of BEDT-TTF, resulting in the occurrence of the Mott transition at  $W/U \sim 1$ . From the consideration the above, the decrease of the temperature is also suggested to cause the increase of the band width with the reduction in the intermolecular dis-

tance associated by the thermal contraction of the crystal. Therefore, the change of the band width generated by the thermal contraction causes to narrow the band gap with lowering the temperature, resulting in the temperature dependent of the activation energy.

Finally, we discuss the pressure dependence of the transition temperature of  $T_c$ . The result of the change of the transition temperature under pressure is summarized below. The structural transition temperature of  $T_c$  increases gradually in the pressure range 0-4 kbar, and it shows nearly constant nature in 4-12 kbar, where the resistivity in the high temperature side of  $T_c$  changes from the insulator to the metal. Then, it decreases abruptly above  $P_{c2}$  and tends to stabilize the metallic state at the low temperature. In sections 3.2 and 3.4, the origin of the structural transition is described by the disappearance of the charge separation between BEDT-TTF A and B molecules, which is caused by the competition of the Madelung energy between the charge separation state and the charge uniform state of the BEDT-TTF molecules. The change of Madelung energy is generated by the reduction in the intermolecular distance of BEDT-TTF with the thermal contraction. Here, under pressure at low temperature the reduction in the intermolecular distance is larger than that at ambient pressure because the increase of pressure also causes the lattice contraction. Thus, the reduction in the intermolecular distance under pressure is suggested to stabilize the charge uniform state in comparison with that at ambient pressure. Consequently, the increase of the transition temperature at low pressure range of 0-4 kbar is explained by the stabilization of the charge uniform state related to the Madelung energy under pressure.

In the higher pressure region of 4-12 kbar, the transition temperature is nearly constant. From the above consideration, the origin of the change of the transition temperature is caused by the reduction of the intermolecular distance between BEDT-TTF molecules. Here, in the trimerization at  $T_c$ , the overlap integrals of BEDT-TTF molecules are enhanced for the  $b$ -axis, which suggests that the overlap for  $b$ -axis is predominant to that for the  $c$ -axis at the transition. However, in the

pressure range of 7-14 kbar, the slope of the change of the  $b$ -axis lattice constant decreases gradually, suggesting that the intermolecular distances are hardly shortened for the  $b$ -axis with applying the pressure. This is in good agreement with the weak pressure dependence of the transition temperature in the range of 7-13 kbar. Consequently, the feature of the transition temperature is explained by the decreasing the slope of the change of the lattice constant in the  $b$ -axis. Nonetheless, the transition temperature decreases abruptly above  $P_{c2}$  although the slope of the change of the lattice parameters shows the similar behavior below  $P_{c2}$ . This is in disagreement with the above consideration for the origin of the transition. The discrepancy is suggested to originate from the slightly reconstruction of the structure accompanied by the first order transition at  $P_{c2}$ . It will be investigated by X-ray structure analysis above  $P_{c2}$  in the future.

### 3.4 Magnetic and Thermal Properties of (BEDT-TTF)<sub>3</sub>CuBr<sub>4</sub>

The investigations of the magnetic and thermal properties of (BEDT-TTF)<sub>3</sub>CuBr<sub>4</sub> are motivated by the relation between the localized Cu<sup>2+</sup> *d*-spins and the  $\pi$ -electrons on the BEDT-TTF molecules. The structural transition at  $T_c$  and the electrical properties under pressure are discussed in sections 3.2 and 3.3. However, there still remain the problems of the origin of the phase transition at  $T_c=59\text{K}$  in view of the magnetic properties, and we do not understand the role of  $\pi$ -conduction electrons in the exchange interaction mechanism at the magnetic phase transition. In this section, we present the results and the detailed discussion of magnetic susceptibility under ambient and high pressures, EPR, antiferromagnetic resonance (AFMR), ac calorimetry, heat capacity by relaxation method and DV-X $\alpha$  calculation of the electronic structure of CuBr<sub>4</sub><sup>2-</sup> in order to understand systematically the magnetic properties of (BEDT-TTF)<sub>3</sub>CuBr<sub>4</sub>.

#### 3.4.1 Experimental Details

##### *Magnetic Susceptibility*

Magnetic susceptibility and magnetization were measured by a SQUID magnetometer (Quantum Design MPMS-5) in the temperature range 1.8K-290K, where the magnetic field (0-5T) was applied parallel to the crystallographic *a*\*, *b* and *c*-axes to get the information on the magnetic anisotropy. The several single crystals collimated to each other in the same batch were mounted on a plastic straw using Apiezon N grease. The weight of the samples were 0.586, 0.866 and 0.556mg for the measurements with the field parallel to the *a*\*, *b* and *c*-axes, respectively. The spin susceptibility was obtained by subtracting the diamagnetic core contribution  $\chi_{\text{dia}}=-8.12\times 10^{-4}$  (emu/mol) (1mol=one formula unit (BEDT-TTF)<sub>3</sub>CuBr<sub>4</sub>) [80] from the observed susceptibility.

It is difficult to measure the magnetic susceptibility under high pressure for

significantly small magnitude of the volume magnetization and small sample mass using a conventional SQUID magnetometer. Consequently, as shown in Fig. 3.30, I employed a small size Co free Be-Cu clamp cell specially designed for the SQUID system in the magnetic susceptibility measurement under high pressure. The clamp cell having the diameter of 7mm, the length of 25mm and the weight of 7.1g could reach the maximum pressure of 4 kbar with the loaded sample, where the applied pressure was calibrated by the pressure dependence of superconducting transition temperature of lead [81]. In this measurement, the pressure medium was not used owing to the restricted space for the sample loading, resulting in the generation of inhomogeneity of the pressure distribution in the sample which was estimated at  $\Delta P = \pm 0.15 \text{ kbar}$  under  $P = 1.9 \text{ kbar}$ . We neglected the movement of the piston and the change of magnetization of the blank cell by the application of pressure, because of the slight influence to the measurement in the low pressures. Since the magnetometer gave a field variation of at most 0.03% even for the maximum stroke of  $\pm 2.5 \text{ cm}$ , this variation gave no appreciable influence for the value of magnetization. In this measurement, I subtracted the SQUID response of the blank cell from that of the cell having the sample 6.8mg, then analyzed the net response using the fitting function of the SQUID magnetometer as shown in Fig. 3.31. The fitting function is represented by the following equation [82],

$$f(Z) = X(1) + X(2) * Z + \frac{X(3)}{R} \cdot [2\{R^2 + (Z + X(4))^2\}^{-2/3} - \{R^2 + (\Lambda + Z + X(4))^2\}^{-2/3} - \{R^2 + (-\Lambda + Z + X(4))^2\}^{-2/3}], \quad (3.14)$$

where  $Z$  is the sample position,  $f(Z)$  is the amplitude of the response curve. The pick-up coil radius and the coil separation of SQUID are  $R = 0.97 \text{ cm}$  and  $\Lambda = 1.519 \text{ cm}$ , respectively,  $X(1)$  and  $X(2)$  are a linear electronic drift and  $X(4)$  is a shift of the sample from the center of magnet. The magnetic susceptibility is estimated from the amplitude  $X(3)$  dividing by the sensitivity calibration factor and multiplied by the device dependent calibration factor. The experimental error of this method is 5-20 % in the temperature region 50 K-290 K.



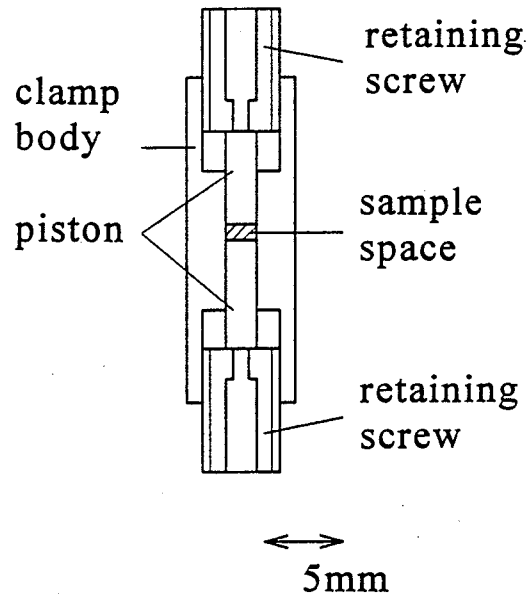


Figure 3.30: Co-free Be-Cu pressure clamp cell for high pressure magnetic susceptibility measurement with a SQUID magnetometer [13].

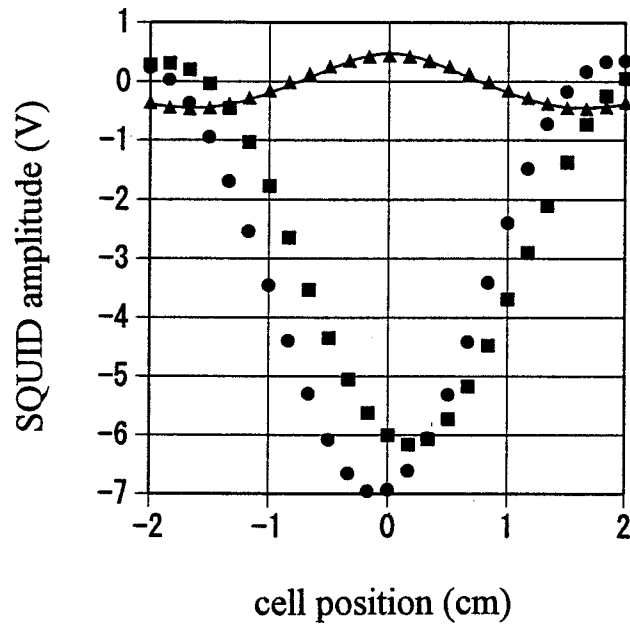


Figure 3.31: Response curve of SQUID magnetometer. Solid circles (●) and squares (■) are the response of the BeCu cell without and with the sample, respectively. Solid triangles (▲) are the net amplitude obtained by subtracting the response of the BeCu blank cell from that of the BeCu cell with the sample, and the solid line represents the result of the fitting by eq. (3.14).

## *Electron Paramagnetic Resonance*

Electron paramagnetic resonance (EPR) measurement was carried out in the temperature range 4.2 K-300 K using an X-band ESR spectrometer (JEOL JES-RE2X). The magnetic field and the microwave frequency were detected by a gaussmeter (JEOL NMR field meter ES-FC5) and a frequency counter (ADVENTEST microwave counter TR5212). A single crystal was mounted on a Teflon rod using silicone grease in a sealed ESR tube with thermal exchange gas (He 10 Torr). Angular dependence of the EPR signal was investigated at room temperature and 45 K to rotate around the crystallographic  $a^*$ ,  $b$  and  $c$ -axes in every 10 degree.

## *Antiferromagnetic Resonance*

Antiferromagnetic resonance (AFMR) is related to the resonance measurement between the magnon mode and the microwave in an antiferromagnetic ordered state. The detailed analysis of AFMR gives significant information to consider the magnetic anisotropy.

We discuss the magnetic anisotropy of  $\text{Cu}^{2+}$  spin before the description of the principle of AFMR. In the consideration for the origin of the magnetic anisotropy, the dipole-dipole interaction is predominant because the spin value of  $S=1/2$  and the nearly isotropic  $g$ -value, as show in the EPR results, suggest the absence of the one-ion magnetic anisotropy and the negligibly small contribution of the anisotropic exchange interaction. Here, the magnetic anisotropy energy in the two sublattice model is represented by

$$E_a = \frac{1}{2}K_1(\beta_1^2 + \beta_2^2) + \frac{1}{2}K_2(\gamma_1^2 + \gamma_2^2), \quad (K_2 > K_1 > 0) \quad (3.15)$$

where  $K_1$  and  $K_2$  are the anisotropy constants, the direction cosine of the sublattice magnetic moments  $M_1$  and  $M_2$  are  $(\alpha_1, \beta_1, \gamma_1)$  and  $(\alpha_2, \beta_2, \gamma_2)$ , respectively, and the direction of  $x$ ,  $y$ ,  $z$  are the magnetic easy, intermediate, hard axes, respectively. The magnetic anisotropy represented by the above equation is called as the biaxial type. In the case of  $K_1=K_2$ , the magnetic anisotropy is called as the uniaxial type. Since the dipole-dipole interaction depends on the positions of the magnetic

ions, the present  $\text{Cu}^{2+}$  structure leads to the difference of anisotropic constants between  $K_1$ ,  $K_2$ , resulting in the biaxial type anisotropy in ordered state. Thus, we describe the principle of AFMR for the two-sublattice model with the biaxial magnetic anisotropy, where all the magnetic moments are antiparallelly aligned to the nearest neighbors.

We introduce the analysis procedure for the AFMR experimental results in what follows. Now, we do not describe four-sublattice model but two-sublattice model because the experimental result is explained by the two-sublattice model. Generally, the equation of motion in the sublattice  $\mathbf{M}_i$  is given by [83]–[85]

$$\frac{d\mathbf{M}_i}{dt} = \gamma_e [\mathbf{M}_i \times \mathbf{H}_i^{\text{eff}}] \quad (i = 1, 2), \quad (3.16)$$

where the suffix  $i$  is the number of sublattice and  $\gamma_e$  is the gyromagnetic ratio. In the molecular field theory, the effective field  $\mathbf{H}_i^{\text{eff}}$  is represented by

$$\mathbf{H}_1^{\text{eff}} = \mathbf{H} - A\mathbf{M}_2 + \mathbf{H}_{1a} \quad (3.17)$$

$$\mathbf{H}_2^{\text{eff}} = \mathbf{H} - A\mathbf{M}_1 + \mathbf{H}_{2a}, \quad (3.18)$$

where  $\mathbf{H}$  is the external field,  $\mathbf{H}_{ia}$  is the anisotropy field affecting sublattice  $i$ ,  $A$  is the coefficient of molecular field that comes from the other sublattice. The sublattice magnetic moments are replaced as follows;

$$\mathbf{M} = \mathbf{M}_1 + \mathbf{M}_2, \quad \mathbf{M}' = \mathbf{M}_1 - \mathbf{M}_2. \quad (3.19)$$

Using eqs. (3.16)–(3.18), we obtain the following equations.

$$\frac{1}{\gamma_e} \frac{d\mathbf{M}}{dt} = \mathbf{M} \times \mathbf{H} + \frac{1}{2} \mathbf{M} \times (\mathbf{H}_{1a} + \mathbf{H}_{2a}) + \mathbf{M}' \times \frac{1}{2} (\mathbf{H}_{1a} - \mathbf{H}_{2a}) \quad (3.20)$$

$$\frac{1}{\gamma_e} \frac{d\mathbf{M}'}{dt} = \mathbf{M}' \times (\mathbf{H} - A\mathbf{M}) + \frac{1}{2} \mathbf{M} \times (\mathbf{H}_{1a} - \mathbf{H}_{2a}) + \mathbf{M}' \times \frac{1}{2} (\mathbf{H}_{1a} + \mathbf{H}_{2a}). \quad (3.21)$$

Here, in the antiparallelly spin axis, the direction cosines of the sublattices of eq. (3.15) are  $\beta_1^2 \sim \beta_2^2$ ,  $\gamma_1^2 \sim \gamma_2^2$ . Thus, the biaxial anisotropy energy  $E_a$  is represented by

$$E_a = \frac{1}{2} K_1 \beta^2 + \frac{1}{2} K_2 \gamma^2 \quad (K_2 > K_1 > 0). \quad (3.22)$$

In the above case, the anisotropy fields to the crystal axes are given by

$$H_{1ax} = 0, \quad H_{1ay} = -(K_1/M_0^2)M_{1y}, \quad H_{1az} = -(K_2/M_0^2)M_{1z}, \quad (3.23)$$

where  $M_0$  is the strength of the saturation moment in the sublattice. From the above equation, the sum and the difference of the anisotropy fields are represented by

$$\mathbf{H}_{1a} + \mathbf{H}_{2a} = [0, -(K_1/M_0^2)M_y, -(K_2/M_0^2)M_z] \quad (3.24)$$

$$\mathbf{H}_{1a} - \mathbf{H}_{2a} = [0, -(K_1/M_0^2)M'_y, -(K_2/M_0^2)M'_z]. \quad (3.25)$$

In eq. (3.20), the second term is neglected by  $|\mathbf{M}'| \gg |\mathbf{M}|$ , while in eq. (3.21), the second and third terms are negligible to the first term. Using the above approximation, the equations of motion for the oscillatory part  $\delta\mathbf{M}$  of  $\mathbf{M}$  are given by

$$\frac{1}{\gamma_e} \frac{d\delta\mathbf{M}'}{dt} = -\mathbf{H} \times \delta\mathbf{M} + \begin{pmatrix} -\frac{1}{2} \frac{K_1-K_2}{M_0^2} (M'_y \delta M'_z + M'_z \delta M'_y) \\ \frac{1}{2} \frac{K_2}{M_0^2} (M'_z \delta M'_x + M'_x \delta M'_z) \\ -\frac{1}{2} \frac{K_1}{M_0^2} (M'_y \delta M'_x + M'_x \delta M'_y) \end{pmatrix}, \quad (3.26)$$

$$\frac{1}{\gamma_e} \cdot \frac{d\delta\mathbf{M}'}{dt} = \frac{a(\mathbf{M}' \cdot \mathbf{H})}{4M_0^2} \cdot \mathbf{M}' \times \delta\mathbf{M}' - A\mathbf{M}' \times \delta\mathbf{M}, \quad (3.27)$$

where  $a$  is equal to  $1-\chi_{\parallel}/\chi_{\perp}$ . Eq. (3.26) and (3.27) are general equations of AFMR in the two-sublattice system with biaxial anisotropy.

As the result of the magnetic susceptibility suggests that the magnetic easy axis lies nearly on the  $b$ -axis, we analyze the AFMR spectra using the resonance condition with the applied field parallel to the crystallographic  $a^*b$  and  $bc$ -plane. First, in the magnetic field applied parallel to the  $xy$ -plane ( $x$ :easy,  $y$ :intermediate-axes), the components of the applied field for the crystallographic unique axes are  $H_x = H \cos \beta$ ,  $H_y = H \sin \beta$ ,  $H_z = 0$ . Here, the components of the magnetic moments are given by

$$M_x = \chi_{\parallel} H \cos \psi \cos(\psi - \beta) + \chi_{\perp} H \sin(\psi - \beta), \quad (3.28)$$

$$M_y = -\chi_{\parallel} H \cos \psi \sin(\psi - \beta) + \chi_{\perp} H \cos(\psi - \beta), \quad (3.29)$$

$$M'_x = 2M_0 \cos(\psi - \beta), \quad (3.30)$$

$$M'_y = -2M_0 \sin(\psi - \beta). \quad (3.31)$$

In the above equations, the relation between  $\psi$  and  $\beta$  is represented by

$$\tan 2\psi = \frac{\sin 2\beta}{\cos 2\beta - (\chi_{\perp} - \chi_{\parallel})H^2/2K_1}. \quad (3.32)$$

And,  $\psi$ ,  $\beta$  are defined in Fig. 3.32. Here, from the substitution of eqs. (3.28)-(3.31)

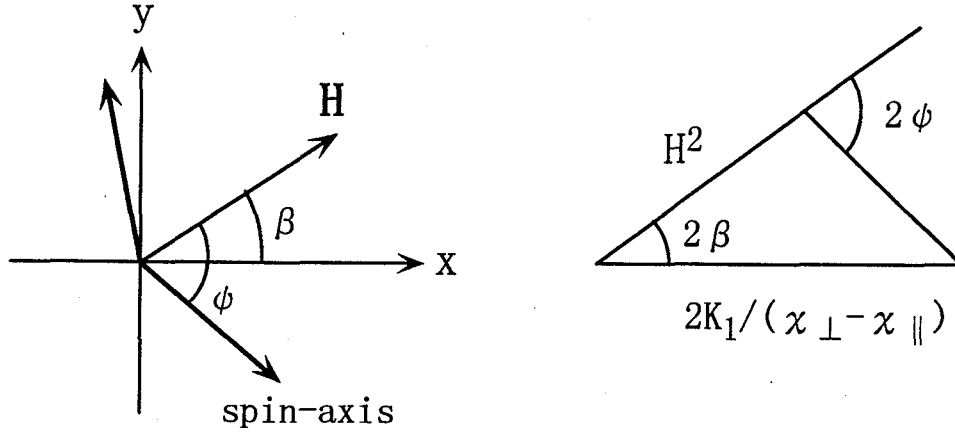


Figure 3.32: Definitions of angles  $\psi$  and  $\beta$  (left-hand) and relation between  $\phi$  and  $\beta$  (right-hand).

into the general equations eqs. (3.26), (3.27) and the replacement of  $d/dt$  by the microwave frequency  $i\omega$ , the resonance frequency is determined by the resolution of the determinant constructed by the magnetic moments and differential moments as shown in below,

$$\begin{aligned} \left(\frac{\omega}{\gamma_e}\right)^4 - \left(\frac{\omega}{\gamma_e}\right)^2 &\cdot [H^2(a^2 \cos^2 \psi + 1) + 2AK_2 - 2AK_1 \sin^2(\psi - \beta) - \cos^2(\psi - \beta)] \\ &+ a^2 H^4 \cos^2 \psi - H^2 [2AK_1 \{ \cos \beta \sin \psi \sin(\psi - \beta) \\ &+ a \cos^2 \psi \cos 2(\psi - \beta) + a \sin \beta \cos \psi \sin(\psi - \beta) \} + 2AK_2 (a \cos^2 \psi - \sin^2 \psi)] \\ &+ 2AK_1 \cos 2(\psi - \beta) 2AK_2 - 2AK_1 \sin^2(\psi - \beta) = 0 \quad (H < H_{sf}), \end{aligned} \quad (3.33)$$

where  $H_{sf}$  is the spin-flop field. The spin-flop field is defined by the critical field at which the spin axis flops from the direction of the external field to the direction perpendicular to the field, resulting in the rotation of the spin axis to the intermediate axis. The spin-flop field is given by

$$H_{sf} = \sqrt{\frac{2K_1}{\chi_{\perp} - \chi_{\parallel}}}. \quad (3.34)$$

For  $H > H_{sf}$ , eq. (3.32) is substituted by

$$\tan 2\psi = \frac{\pi}{2} - \frac{\sin 2\beta}{\cos 2\beta - (\chi_{\perp} - \chi_{\parallel})H^2/2K_1}. \quad (3.35)$$

Next, in the applied field parallel to the  $xz$ -plane ( $x$ :easy,  $z$ :hard-axis), the resonance frequency is determined by the same equation as eq. (3.33) after we exchange suffices between 1 and 2 within the shaded area surrounded by the hyperbola in Fig. 3.33 as defined the following equation,

$$\frac{H_x^2}{2K_1} - \frac{H_z^2}{2(K_2 - K_1)} = \frac{1}{\chi_{\perp} - \chi_{\parallel}}. \quad (3.36)$$

The hyperbola is shown in Fig. 3.33. Within the shaded area, the resonance

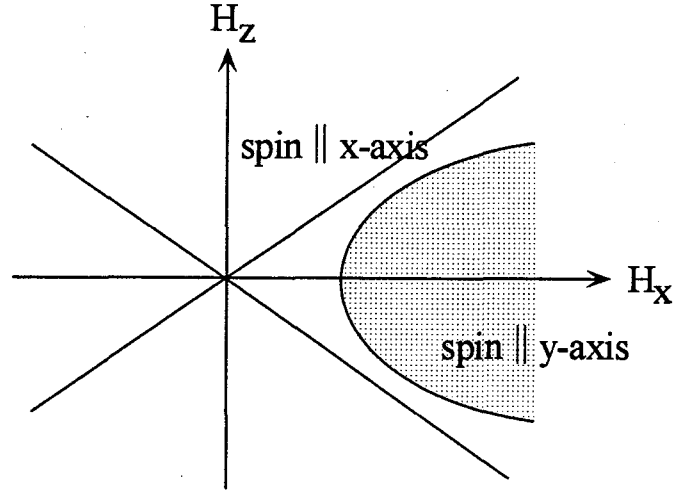


Figure 3.33: Definition of critical hyperbola. The applying the field parallel to the  $x$ -axis (easy axis) in the region of  $H > H_{sf}$ , the spin axis flops to the  $y$ -axis (intermediate axis). The flopped spin returns to the  $x$ -axis by the rotation of the field from the  $x$ -axis to the  $z$ -axis. The straight line is as asymptote to the hyperbola.

frequency is determined by

$$\frac{H_x^2}{2AK_1 + (\omega/\gamma_e)^2} - \frac{H_z^2}{(2AK_2 - 2AK_1) - (\omega/\gamma_e)^2} = 1. \quad (3.37)$$

The schematic field-frequency diagrams of antiferromagnetic resonance, drawn by eqs. (3.33), (3.37) and (3.33) with exchanging between the suffices 1 and 2, are shown in Fig. 3.34. Moreover, the schematic angular dependence of antiferromagnetic resonance is represented in Fig. 3.35. The resonance frequencies show the

characteristic angular dependence for the magnetic axis. The present experiments of  $(\text{BEDT-TTF})_3\text{CuBr}_4$  were carried out with the angular dependence for the crystallographic  $a^*b$  and  $bc$  planes in the X-band region at 3.67 K and 3.53 K. A single crystal was mounted on a Teflon rod using silicone grease in a sealed ESR tube with the heat exchange gas (He 10 Torr). The magnetic field and the microwave frequency were detected by a Gaussmeter (JEOL NMR field meter ES-FC5) and a frequency counter (ADVENTEST microwave counter TR5212). The temperature is determined by the  $^4\text{He}$  vapor pressure.

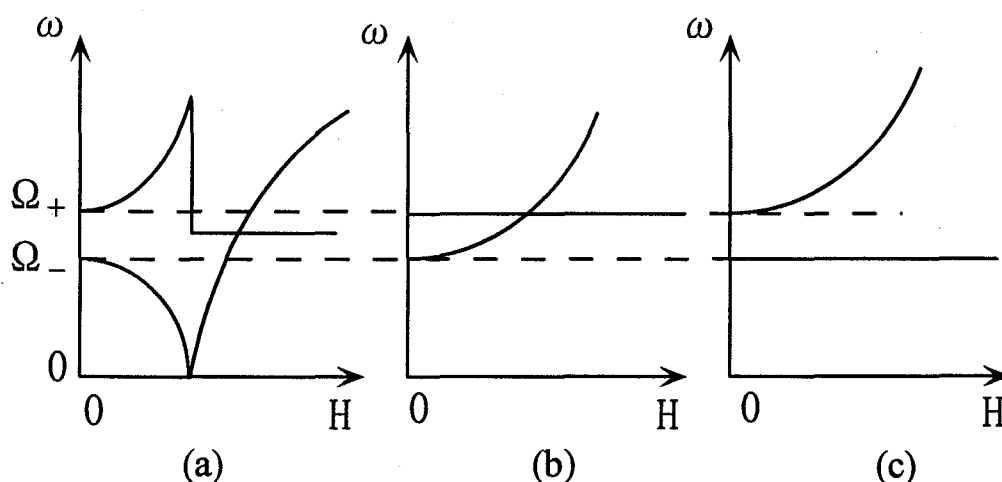


Figure 3.34: Schematic field-frequency diagram of antiferromagnetic resonance in the applied field parallel to the three principal axes; (a) easy axis, (b) intermediate axis and (c) hard axis. The solid lines denote the antiferromagnetic resonance modes with biaxial anisotropy. The broken line is the resonance line with uniaxial anisotropy.

### *Electronic Structure Calculation by DV- $X\alpha$ Method*

The electronic structures of  $\text{CuBr}_4^{2-}$  anion and isostructural anion  $\text{CuCl}_4^{2-}$  were calculated by molecular orbital calculation using the discrete variational (DV)- $X\alpha$  method in collaboration with Professor Y. Kaizu in Tokyo Institute of Technology [13]. In the DV- $X\alpha$  method, the radial distribution functions of atomic orbitals

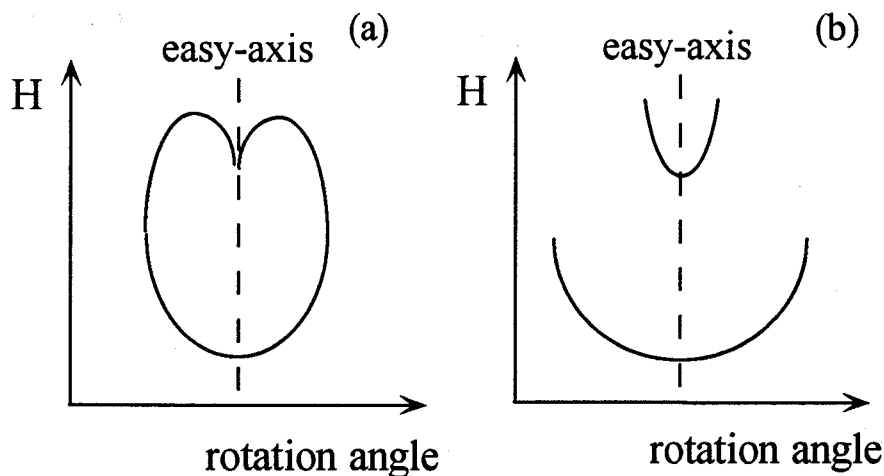


Figure 3.35: Schematic angular dependence of the resonance field the fixed frequency below  $\Omega_-$  defined in Fig. 3.34, where the sample is rotated from the easy axis to intermediate axis (a) and from easy axis to hard axis (b).

were estimated by the resolution of Schrödinger equation using the numerical calculations, where the electron-electron interaction is represented by the local density functional method as given by

$$\int \frac{\rho(\mathbf{r}_2)}{r_{12}} d\mathbf{r}_2 - 3\alpha \left( \frac{3}{4\pi} \rho(\mathbf{r}) \right)^{1/3}, \quad (3.38)$$

where  $\rho(\mathbf{r})$  is electron density,  $r_{12}$  is the distance between the electrons. This calculation was carried out with 4000 DV sampling points, where the exchange potential was given by Slater's  $X\alpha$  potential with  $\alpha=0.7$ . The geometry of the  $\text{CuCl}_4^{2-}$  and  $\text{CuBr}_4^{2-}$  were taken to be the  $D_{4h}$  configuration with the Cu-Cl distance of 2.25Å and the Cu-Br distance of 2.42Å.

### Ac Calorimetry

Heat capacity measurement was carried out by ac calorimetry in the temperature range 30-280 K. The periodical heat pulses were given to the sample by the chopped light from a halogen lamp. The temperature oscillation of the sample was detected



by an Alumel-Chromel (25  $\mu\text{m}$ ) thermocouple using a lock-in amplifier (EG&G Inst. Co. Model 124A) with a preamplifier (EG&G Inst. Co. Model 116). The sample was mounted on the thermocouple by GE7031 varnish. The chopping frequency  $\omega=3$  Hz was employed in order to satisfy the condition of  $1/\tau_e < \omega < 1/\tau_i$ , where  $\tau_e$  and  $\tau_i$  is the external thermal relaxation time of the sample to the thermal bath and the inner relaxation time within the sample, respectively. Under the condition, the heat capacity  $C_p$  is given by,

$$C_p = \Delta Q / (\omega \Delta T_{ac}), \quad (3.39)$$

where  $\Delta Q$  is the incident heat and  $\Delta T$  is the amplitude of the temperature oscillation of the sample. Though  $\Delta Q$  was not determined in the present apparatus, the absolute value of the heat capacity was estimated independently by a DSC thermal analyzer (Rigaku Co. TAS-300) and a cooling unit (Rigaku Co. DSC 8230) in the temperature range of 130-330 K with the sample mass of 9.37 mg.

### *Heat Capacity Measurement by Relaxation Method*

In the investigation of the magnetism, the heat capacity measurement gives important information on the magnetic phase transition and the magnetic interactions. Here, I carried out the heat capacity measurement by the relaxation method in the temperature range of 4.4-13 K to measure the heat capacity of the present sample whose amount was not enough for an ordinary adiabatic calorimeter. First, we describe the principle of the thermal relaxation method [86]. Figure 3.36 shows the schematic of the method, where the sample mounted on a bolometer is linked to the heat reservoir through the lead wires with the thermal conductance  $k$ . The net power  $P$  applied to the sample is given by the following equation,

$$P = \int_{T_0}^T k(T') dT' + C \frac{dT}{dt}, \quad (3.40)$$

where  $T_0$  is the temperature of the heat reservoir,  $t$ ,  $C$  and  $T$  are the time, the heat capacity and the temperature of the sample with the bolometer, respectively. Under the constant temperature with the supplied power, we obtain the following equation

from eq. (3.40),

$$P = k(T_{av})\Delta T \quad (T_0 \gg \Delta T), \quad (3.41)$$

where  $T_{av}$  is  $(T_1 + T_0)/2$ ,  $T_1$  is the temperature under the supplied power, and  $\Delta T = T_1 - T_0$ . At the time of the power-off, the temperature of the sample is relaxed to the temperature of the thermal reservoir  $T_0$  with the relaxation time  $\tau$ . The temperature relaxation is represented by

$$T(t) = T_0 + \Delta T \exp(-t/\tau) \quad (k \gg k_{\text{int}}), \quad (3.42)$$

where  $k_{\text{int}}$  is the thermal conductance between the sample and the bolometer. In the above equation, the heat capacity  $C$  of the sample is given by,

$$\tau = C/k. \quad (3.43)$$

Thus, the heat capacity  $C$  is evaluated by the measurement of the relaxation time  $\tau$  and the thermal conductance  $k$ .

Next, we describe the apparatus of the relaxation method. Figure 3.37 shows the bolometer consisting of a sample mount plate, thermometer, heater and lead wire. The sample mount plate was the silicon single crystal wafer with the surface of (111) (manufactured by Sharp;  $5 \times 5 \times 0.15$  mm, 6mg), the thermometer was a chip of carbon resistance (Allen-Bradley), the heater was formed by vacuum evaporation of Moleculoy (Ni, Cr, Al, Co alloy), and the thermal leak wire ( $0.08 \phi$ ) as used for the lead wire is 0.05% Ga doped Au. Figure 3.38 shows the schematic of the cryostat [87]. The thermometer on the bolometer was calibrated by the carbon glass standard thermometer (Lake Shore Cryotronics Inc. ) in the heat reservoir in the temperature range of 4.4-13 K at each measurement cycle. And, the thermal exchange He gas (10 Torr) was put into the outer jacket.

Finally, the heat capacity measurement is mentioned below. In the measurement, at the beginning, the thermal conductance was evaluated by the supplied power  $P$  and the temperature difference  $\Delta T$ . Turning off the power, the temperature of the

bolometer was relaxed to the temperature of the heat reservoir, and the relaxation time was estimated by the fitting of the relaxation curve as shown in Fig. 3.39. Figure 3.40 shows the heat capacity of the bolometer without the sample in the temperature range of 4.4-12.8 K. The heat capacity of the sample was estimated by subtracting the heat capacity of the bolometer from that of the bolometer with the sample attached by Apiezon N grease. In the measurement, the weight of the samples and the grease were 1.427 mg and 0.233 mg, respectively.

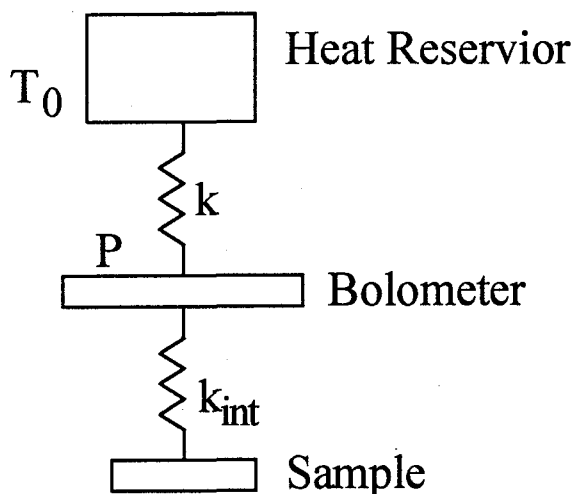


Figure 3.36: Schematic of heat capacity measurement by the thermal relaxation method. The sample is mounted on the bolometer, which is connected to the heat reservoir by lead wires with the thermal conductance  $k$ .  $T_0$  is the temperature of the heat reservoir,  $P$  is the power supplied to the bolometer, and  $k_{int}$  is the thermal conductance between the sample and the bolometer.

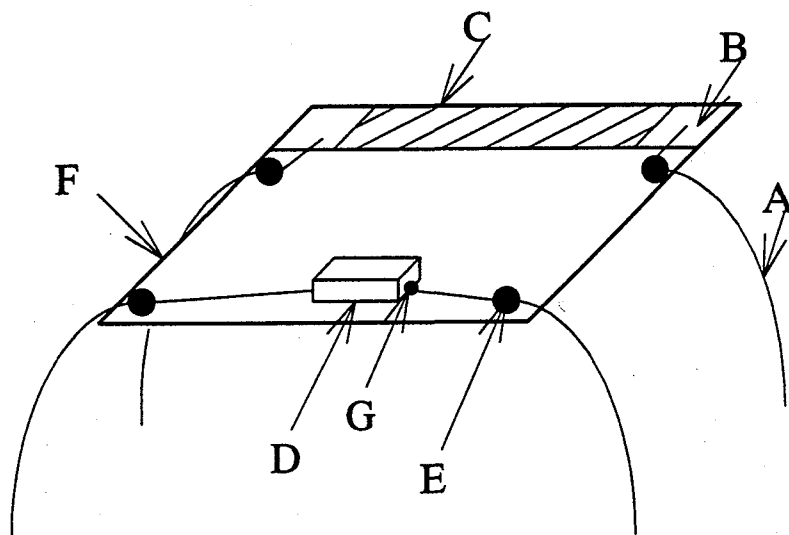


Figure 3.37: Bolometer in the relaxation method calorimeter. A: Lead wire combining with a thermal leak wire ( $0.08\phi$  Au doped 0.05% Ga), B: Au evaporated film, C: Molecule evaporated film, D: Carbon thermometer (Allen-Bradley) coated by Stycast, E: Stycast (2850FT, Grace Japan K. K.), F: Silicon plate ( $5 \times 5 \times 0.15\text{mm}$ ) and G: Ag paste.

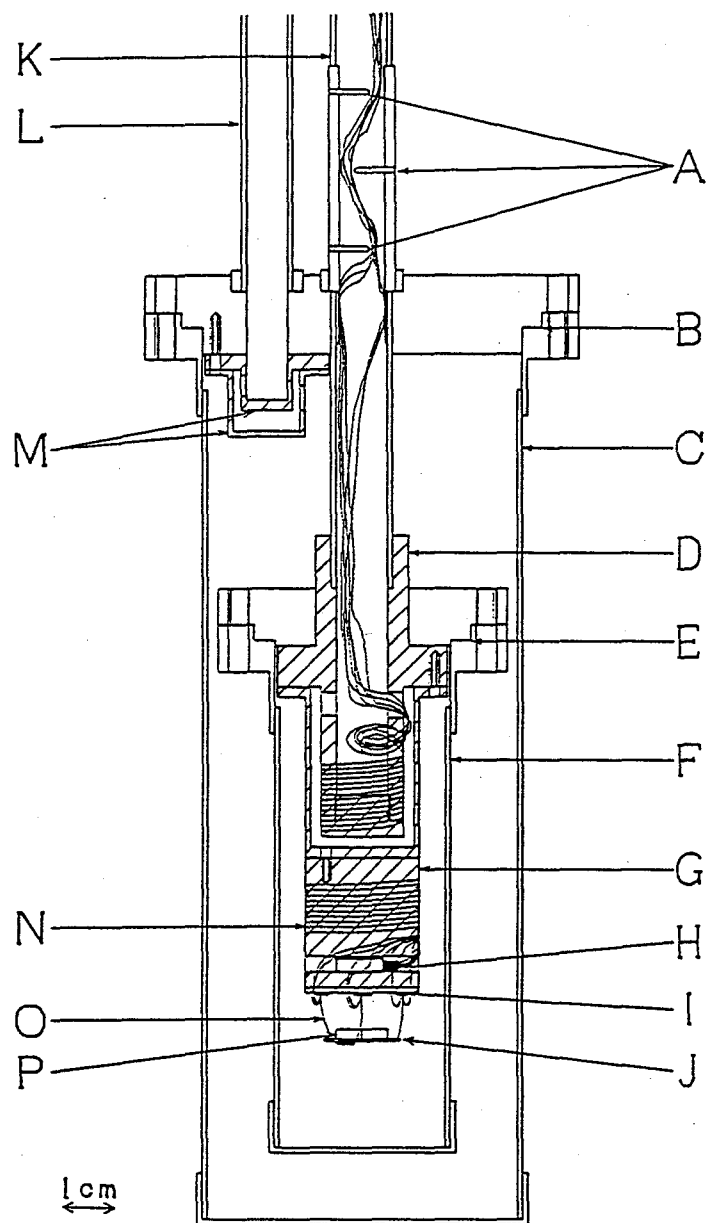


Figure 3.38: Cryostat of the calorimeter by the thermal relaxation method. A: Radiation shields, B: Indium seal flange, C: Outer jacket, D: Upper part of the heat reservoir, E: Indium seal flange, F: Inner jacket, G: Lower part of the heat reservoir, H: Carbon glass thermometer, I: Sapphire plate, J: Bolometer, K: Evacuation tube of the inner chamber, L: Evacuation tube of the outer chamber, M: Radiation shields, N: Heater of the heat reservoir, O: Lead wires and P: Sample [87].

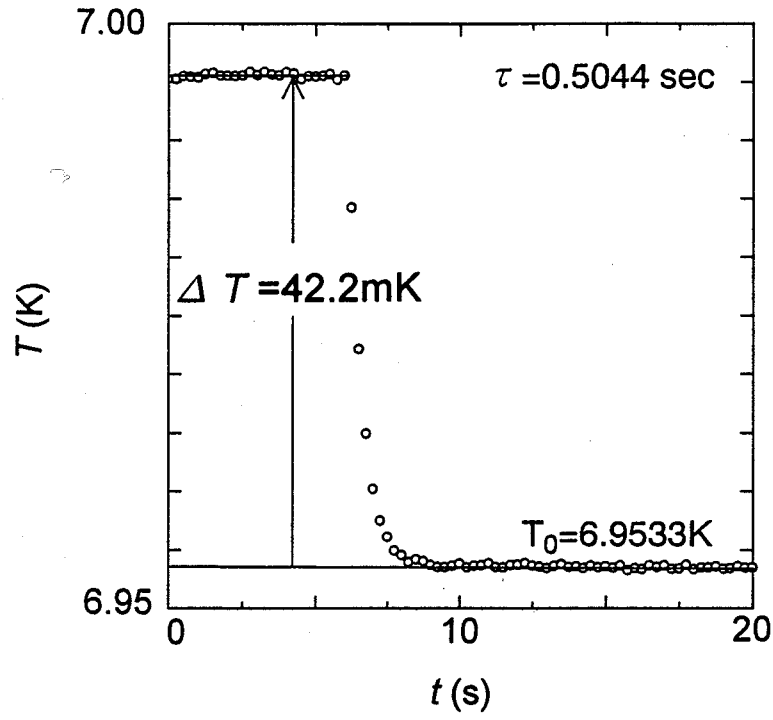


Figure 3.39: Time dependence of the bolometer temperature in the measurement of relaxation time.  $\Delta T$  is determined with the accuracy of 1% of the reservoir temperature.

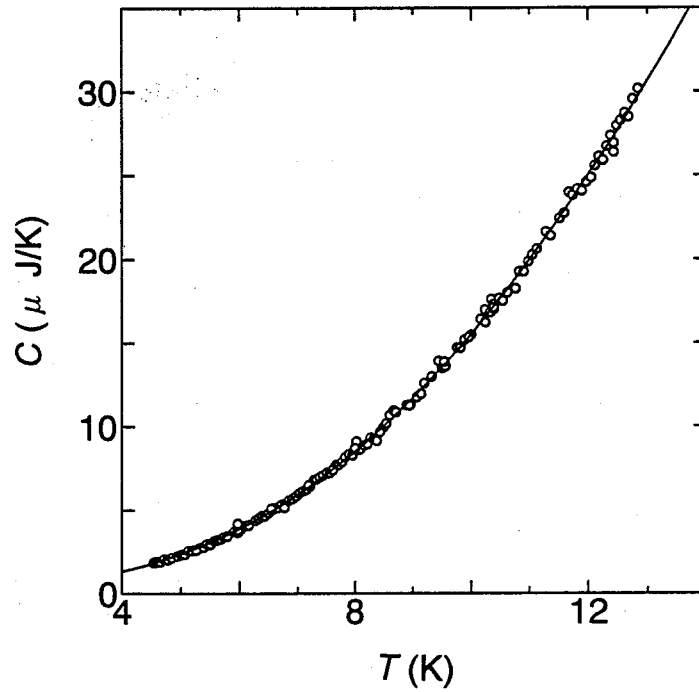


Figure 3.40: Heat capacity of only the bolometer in the temperature range of 4.4-12.8 K. The solid line implies the fitting curve of  $C = AT + BT^3 + CT^5$  ( $A = 7.51 \times 10^{-2}$ ,  $B = 1.66 \times 10^{-2}$ ,  $C = -1.84 \times 10^{-5}$ )  $\mu$  J/K.

### 3.4.2 Experimental Results

#### *Magnetic Susceptibility*

Figure 3.41(a) shows the temperature dependence of the spin susceptibility in the applied field ( $H=4$  kOe) parallel to the  $b$ -axis after the subtraction of the Pascal diamagnetic contribution. Above  $T_c=59$  K, the magnetic susceptibility shows the Curie-Weiss behavior, and it has a discontinuous change at  $T_c$ . For the behavior above  $T_c$ , it is impossible to separate the respective contributions of the BEDT-TTF layer and the  $\text{Cu}^{2+}$  layer from the observed susceptibility, since there is the strong exchange interaction between the localized  $\pi$ -electrons on the BEDT-TTF molecules and the localized Cu  $d$ -electrons, as we will discuss later. Consequently, we employ a single Curie-Weiss equation for the analysis of the observed susceptibility above  $T_c$ . The analysis gives the antiferromagnetic Weiss temperature  $\theta=-100$  K and the Curie constant  $C=1.07$  emu/mol-K. Using the  $g$ -value  $g=2.02$  observed from the EPR measurement ( $H\parallel b$ ), the spin density is estimated at  $N\sim 3$  spins ( $S=1/2$ )/formula unit. Taking into account that BEDT-TTF B molecules are in the cation radical state with  $+1$  charge, the observed spins are assigned to two BEDT-TTF B molecules and one  $\text{Cu}^{2+}$  ion having magnetic moments with  $S=1/2$ . Namely, the experimental findings prove that the behavior of the susceptibility above  $T_c$  is described in terms of the localized magnetic moments of the  $\pi$ -electrons of the BEDT-TTF B molecules and the localized  $d$ -electrons of  $\text{Cu}^{2+}$  ions coupled by the strong antiferromagnetic interaction ( $\theta=-100$  K), which is consistent with the result of EPR measurement. At  $T_c=59$  K, the susceptibility discontinuously drops by 40% from the value just above  $T_c$ , indicating the occurrence of the first order phase transition accompanied by the disappearance of a part of the localized spins. The change of the susceptibility at  $T_c$  has no dependence on the directions of the applied field among the  $a^*$ ,  $b$  and  $c$ -axes as shown in Fig. 3.41(b).

Below  $T_c$ , the susceptibility has a hump around 28K, then it shows a small peak of an antiferromagnetic transition at  $T_N=7.65$  K (see Fig. 3.42 for details). The data

of the field dependence of susceptibility give the estimate of the transition temperature  $T_N=7.65\pm0.05$  K from the extrapolation to  $H=0$  kOe. The broad hump is considered to be brought about by the magnetic short-range-order effect which is characteristic of a low-dimensional antiferromagnets. Taking into account the angular dependence of EPR signal which will be mentioned later, the decrease of the spin density at  $T_c$  is interpreted as the disappearance of the localized  $\pi$ -electron spins on BEDT-TTF cation radicals at the B sites. As a consequence, only  $\text{Cu}^{2+}$  spins contribute to the magnetic behavior below  $T_c$ . The  $\text{Cu}^{2+}$  sites in the structure of  $(\text{BEDT-TTF})_3\text{CuBr}_4$  form a distorted square lattice, thereby, the susceptibility with the hump can be fitted to the theory of a two-dimensional Heisenberg antiferromagnet model [88] in the temperature range from 20 K to 55 K. The result of the fitting gives the spin density of  $N_{\text{Cu}}\sim 1$  spin/formula unit and the intralayer exchange interaction of  $J_{d-d}=-15.7$  K. These results are in a good agreement with the  $^1\text{H}$ -NMR measurement [89], which gives  $T_N=8$  K and  $J_{d-d}=-20$  K.

Figure 3.42 shows the detailed temperature dependence of the magnetic susceptibility in the temperature region below 30 K in the field applied parallel to the  $a^*$ ,  $b$  and  $c$ -axes. Below  $T_N$ , the susceptibility shows the anisotropy, namely, the susceptibility for the  $b$ -axis drops while it is elevated for the  $a^*$  and  $c$ -axes with decreasing the temperature. This behavior proves that the magnetic easy axis lies almost in the  $b$ -axis in the antiferromagnetic ordered state. However, the susceptibility parallel to the  $b$ -axis does not approach to zero at  $T=0$  K. Moreover, the susceptibility parallel to the  $a^*$ -axis is slightly lower than the susceptibility for the  $c$ -axis. This discrepancy from the typical behavior of the angular dependence in ordinary antiferromagnets is interpreted by that the easy axis deviates slightly from the  $b$ -axis. The presence of the antiferromagnetic transition evidences the important role of the interlayer interaction between the  $\text{Cu}^{2+}$  layers because no long range order exists at a finite temperature in pure two-dimensional Heisenberg antiferromagnets. [26]

Magnetization curves in the magnetic field parallel to the  $a^*$ ,  $b$  and  $c$ -axes are shown for several temperatures in Fig. 3.43. The magnetization curve paral-



parallel to the  $b$ -axis exhibits a spin-flop transition as characterized by a discontinuous change around 6 kOe in the temperature region below  $T_N$ , although it shows a monotonous increase for the  $a^*$  and  $c$ -axes. The spin-flop transition field is estimated at  $H_{sf}(0)=6.0$  kOe by extrapolating the spin-flop field values to  $T=0$  K. Using the exchange field  $H_E=-2z_{Cu}J_{d-d}S/g_{Cu}\mu_B=467$  kOe with the number of the nearest neighbor  $Cu^{2+}$  ions  $z_{Cu}=4$ ,  $J_{d-d}=-15.7$  K,  $g_{Cu}=2.02$  and  $S=1/2$ , the anisotropy field is estimated at  $H_A=38.5$  Oe from the relation;

$$H_{sf}=\sqrt{H_A(2H_E-H_A)}\sim\sqrt{2H_EH_A}\quad (H_A\ll H_E). \quad (3.44)$$

The obtained result of the small anisotropy field suggests that the origin of the anisotropy energy is caused mainly by the magnetic dipole-dipole interaction. Moreover, the small magnetic anisotropy  $H_A/H_E\sim 10^{-4}$  is consistent with the Heisenberg nature of the spin system.

The susceptibility under high pressure is shown in Fig. 3.44. The susceptibility under 1.7 kbar decreases by about 13% from the value under 1 bar at  $T=100$  K, where the experimental error is 5%. The large change of the susceptibility suggests the decrease of the spin density and/or the increase of the Weiss temperature. The transition at  $T_c=59$  K is found to be shifted to higher temperature by the application of pressure, consistent with the pressure dependence of the resistivity measurements. The broad features in the changes of the susceptibility at the transition temperature region are considered to be caused mainly by the inhomogeneous distribution of the pressure due to the absence of pressure medium. In Fig. 3.45, we plot the pressure dependence of the observed susceptibility at  $T=100$  K. This is compared to the susceptibility expected on the assumption that only the  $Cu^{2+}$  spins exist at the same temperature estimated by the two-dimensional Heisenberg antiferromagnet model using the exchange interaction energy  $J_{d-d}$  obtained from the  $^1H$ -NMR measurement under high pressures [89]. The ratio of the susceptibility change is calculated at  $\partial \ln \chi / \partial P = -8.2 \pm 0.4\% / \text{kbar}$  as a function of pressure. It is supposed that the observed susceptibility reaches the limit value expected for only  $Cu^{2+}$  magnetic

moments (dashed line in Fig. 3.45) around 6kbar at which the insulator-to-metal transition takes place.

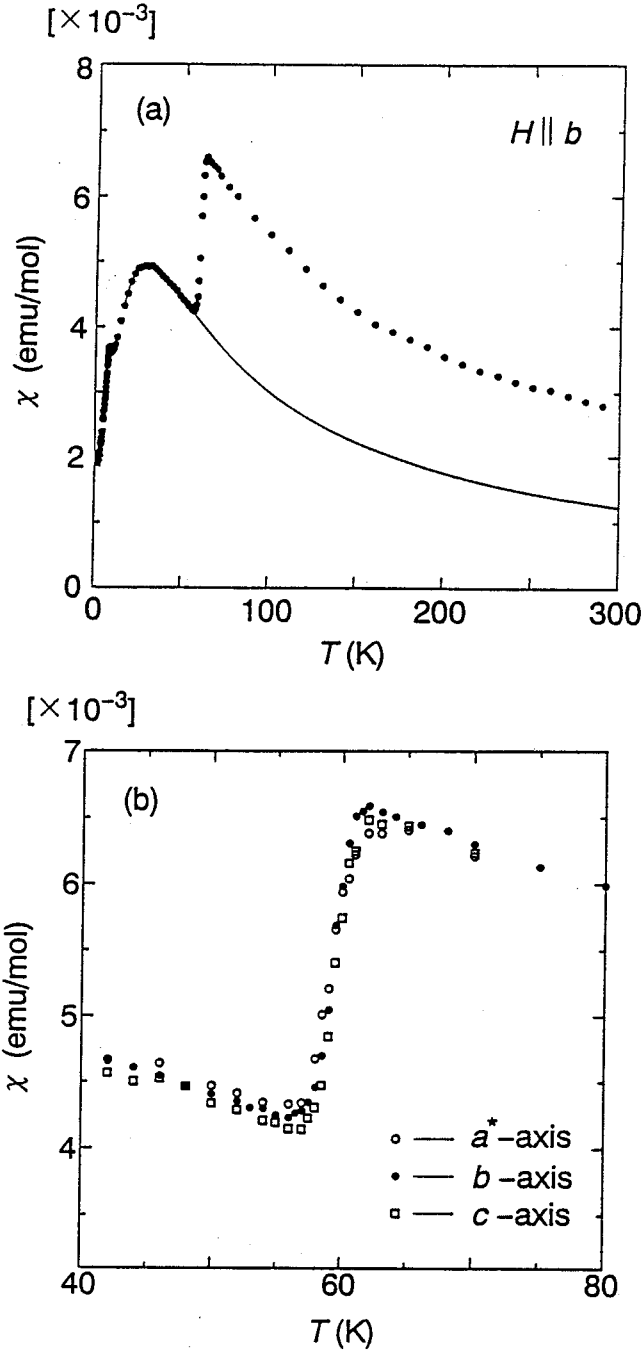


Figure 3.41: (a) Temperature dependence of magnetic susceptibility in the field of  $H=4$  kOe applied parallel to the  $b$ -axis. The mole unit corresponds to the formula unit of  $(\text{BEDT-TTF})_3\text{CuBr}_4$ . The solid line denotes the theoretical fitting for the two-dimensional square lattice Heisenberg antiferromagnet model (ref. [88]) with two fitting parameters ( $N_{\text{Cu}}, J_{\text{d-d}}$ ) in the temperature range 20-55 K. The number of spins and the intralayer exchange interaction between  $\text{Cu}^{2+}$  spins are estimated at  $N_{\text{Cu}} \sim 1$  spin/unit and  $J_{\text{d-d}} = -15.7$  K. (b) The detailed temperature dependence of the susceptibility in the applied field parallel to the  $a^*$ ,  $b$  and  $c$ -axes around  $T_c$  [13].

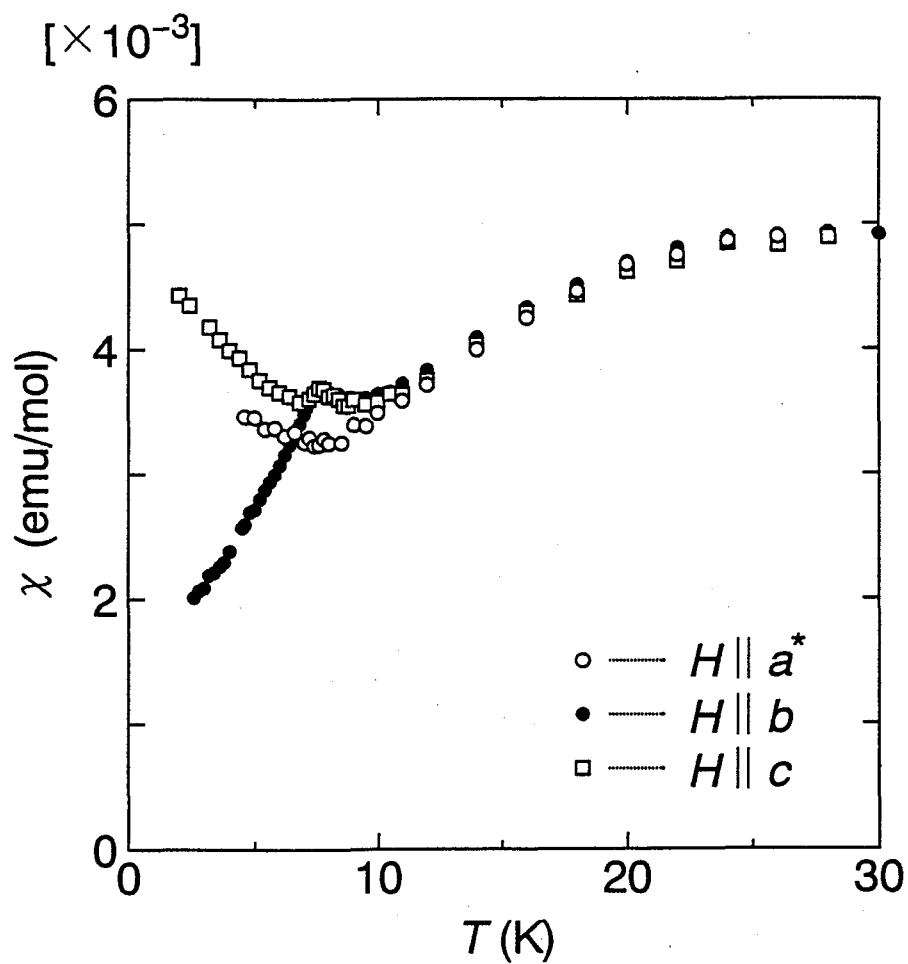


Figure 3.42: Temperature dependence of magnetic susceptibility in the applied field of  $H=4$  kOe parallel to the  $a^*$ ,  $b$  and  $c$ -axes. The antiferromagnetic transition temperature is obtained to be  $T_N=7.65\pm0.05$  K from the appearance of the anisotropic behavior [13].

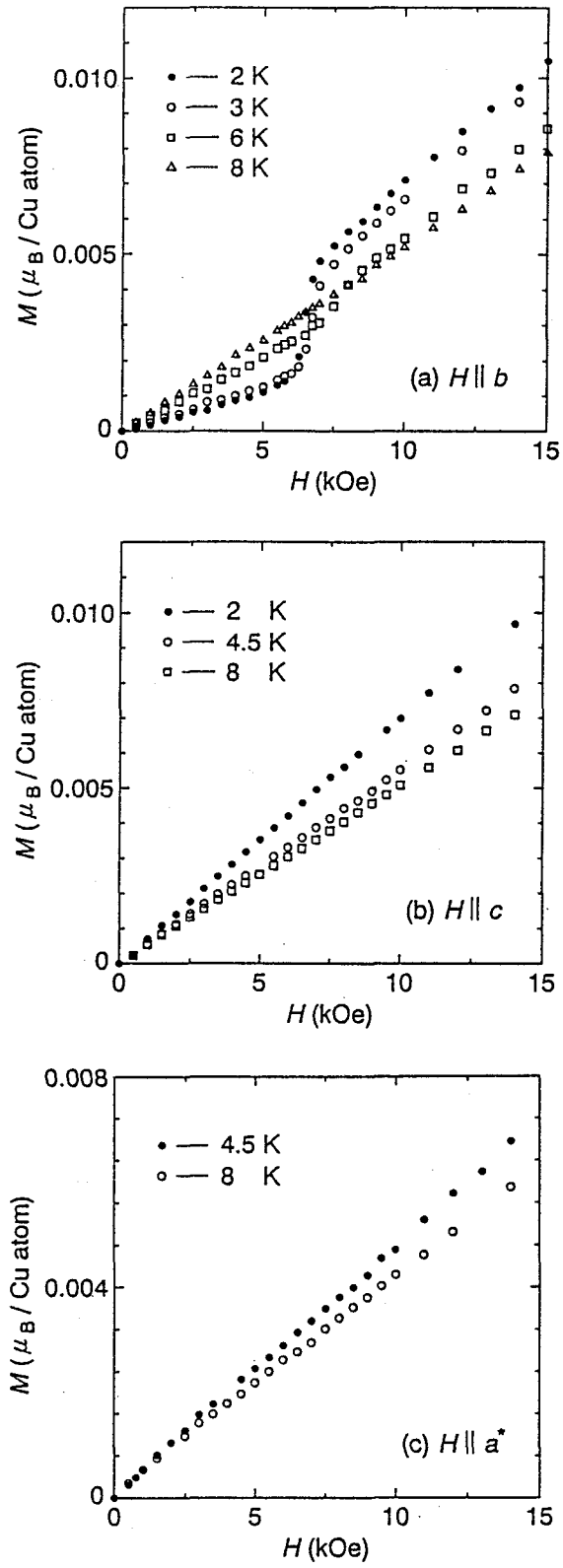


Figure 3.43: Magnetization curves at several temperatures in the field parallel to the  $a^*$ ,  $b$  and  $c$ -axes. The spin flop transition is observed at  $H_{\text{sf}}(0) = 6$  kOe when the field is applied parallel to the  $b$ -axis [13].

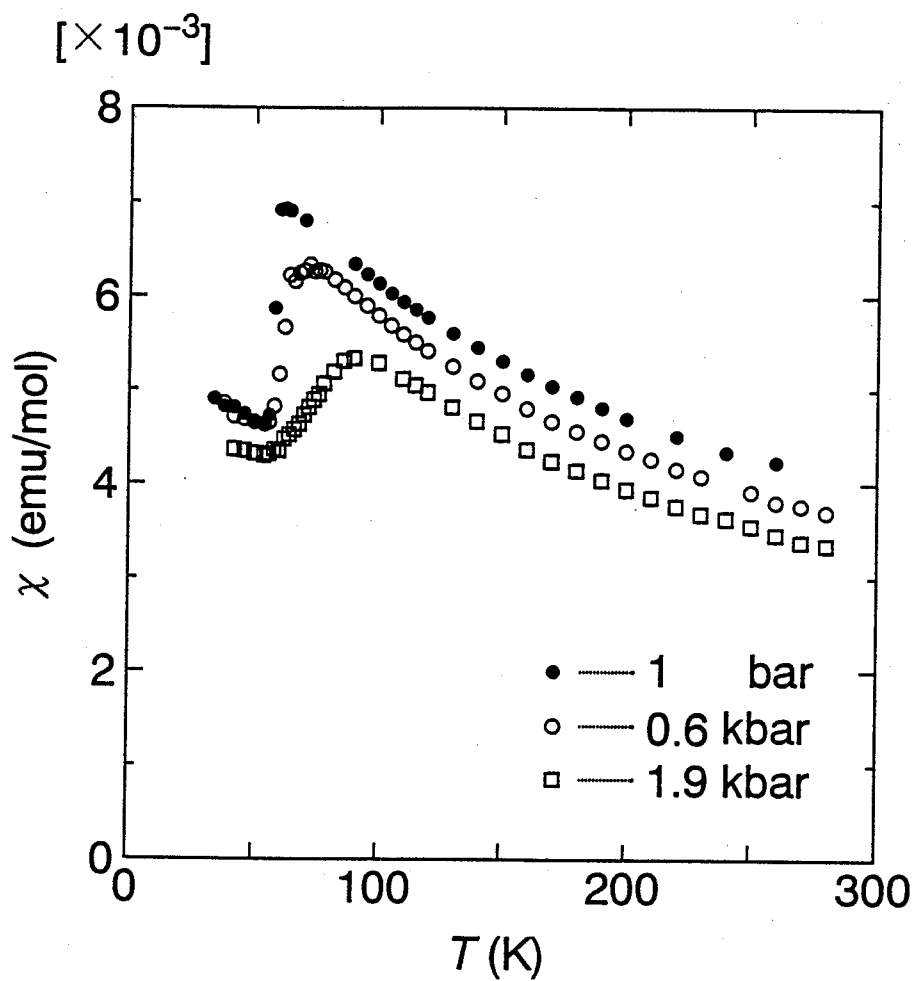


Figure 3.44: Temperature dependence of magnetic susceptibility under high pressures in the magnetic field  $H=10\text{kOe}$ , where the samples are randomly oriented. The broad feature in the changes of the susceptibility at the transitions are caused by the inhomogeneous distribution of the applied pressure due to the absence of pressure medium [13].

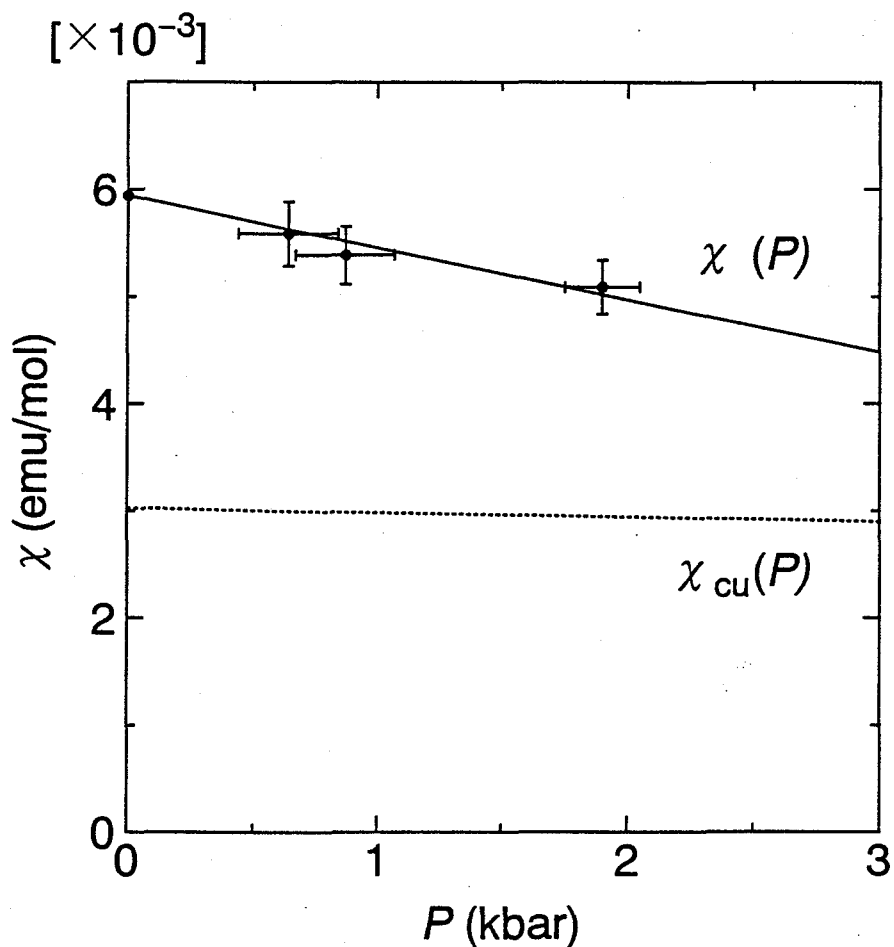


Figure 3.45: Pressure dependence of the susceptibility  $\chi(P)$  at 100 K. The solid line represents the linear line for the best fitting to the result. The dashed line with  $\chi_{\text{Cu}}(P)$  is the susceptibility expected on the assumption that only  $\text{Cu}^{2+}$  spins contribute to the susceptibility at 100 K.  $\chi_{\text{Cu}}(P)$  is estimated based on the two-dimensional square lattice Heisenberg antiferromagnet model [88] using the value of the exchange interaction  $J_{\text{d-d}}$  obtained from the result of the  $^1\text{H}$ -NMR measurement under high pressure [13, 89].

## Electron Paramagnetic Resonance

The temperature dependence of EPR line width and  $g$ -value in applied field parallel to the  $b$ -axis is shown in Fig. 3.46, where the absorption signal is described by a single Lorentzian in the whole temperature range. Above  $T_c$ , the line width shows a constant value of 110 Oe and decreases to 50 Oe discontinuously at  $T_c$ . The  $g$ -value is almost independent of the temperature in the whole temperature range except a discontinuous step at  $T_c$ . And, they exhibit a broaden-out abruptly below 10 K. Figure 3.47 shows the detailed temperature dependence of the line width and  $g$ -value in the low temperature range below  $T_c$ . The line widths decreases gently with decreasing the temperature, suggesting the presence of the magnetic short-range-order effect. It is broadened abruptly below around 10 K, which is characteristic of the critical broadening to the magnetic long-range-order in the low-dimensional antiferromagnet. The  $g$ -values show the temperature independent behavior above ca. 15 K, and then, a slight decrease appears for the  $b$ -axis with lowering the temperature below 12 K which is generated by the short-range-order effect. From the temperature, they increase suddenly with the concomitance of the broaden-out in the line width below 10 K.

Castner et al. analyzed the critical broadening of the line width  $\Delta H_c$  in  $S=1/2$  two-dimensional quasi-square lattice antiferromagnet  $\text{Cu}(\text{HCOO})_2 \cdot 4\text{H}_2\text{O}$  [90] above  $T_N$  using the following equation,

$$\Delta H_c = B \frac{\omega_p^2}{\omega_{\text{ex}}} \left[ \frac{\xi}{a} \right]^3 \frac{(T/2\pi\rho_s)^{5/2}}{(1 + T/2\pi\rho_s)^4}, \quad (3.45)$$

where  $\omega_p^2$  is the second moment,  $\omega_{\text{ex}}$  is the exchange frequency,  $\rho_s$  is the spin-stiffness constant and  $B$  is renormalization factor. The critical broadening in the line width  $\Delta H_c$  is estimated by subtracting the short-range-order contribution of the line width from the total line width, where the short-range-order contribution is evaluated by the polynomial fitting in the temperature range of 15-45 K as shown in Fig. 3.47. Then,  $\xi/a$  is the ratio of the temperature-dependent spin correlation length to the



nearest neighbor distance as given by

$$\frac{\xi}{a} = C_{\xi} \frac{\exp(2\pi\rho_s/T)}{(1 + T/2\pi\rho_s)}, \quad (3.46)$$

where  $C_{\xi}$  is the constant prefactor and they employ  $\rho_s=0.18J$  with the exchange energy  $J$ . In the temperature range with critical broadening, eqs.(3.45) and (3.46) are simplified by neglecting  $(1+T/2\pi\rho_s)$  term in the following equation,

$$\ln(\Delta H_c) = 3 \cdot \frac{2\pi\rho_s}{T} + \frac{5}{2} \ln \left( \frac{T}{2\pi\rho_s} \right). \quad (3.47)$$

In eq. (3.47), the first term on the right hand side is predominant term in the two-dimensional magnet. Consequently, the exchange interaction energy  $J$  is estimated by the slope of the  $\ln(\Delta H_c)$  vs  $1/T$  plot. Figure 3.48 shows the critical broadening of the EPR line width represented by the  $\ln(\Delta H_c)$  vs  $1/T$  plot, where the slopes are given by  $6\pi kJ$ . From the analysis with the above equation, the exchange energies  $J$  are estimated at  $J=-18$  K, 19 K and 18 K for the  $a$ ,  $b$  and  $c$ -axes, respectively, which are almost in good agreement with the result of the magnetic susceptibility.

Figure 3.49 shows the angular dependence of  $g$ -values around the  $a^*$ ,  $b$  and  $c$ -axes at room temperature and below  $T_c$  ( $T=45$  K). From the angular dependence, the principal values of the  $g$ -tensor are calculated to be  $g_1=2.061$ ,  $g_2=2.021$ ,  $g_3=2.020$  at room temperature and  $g_1=2.114$ ,  $g_2=2.041$  and  $g_3=2.040$  at  $T=45$ K (see Fig. 3.50) for the geometry of  $\text{CuBr}_4^{2-}$ . The obtained values at room temperature are almost the same to the mean values between the  $g$ -values of the  $\pi$ -electrons of typical BEDT-TTF salt (ex.  $\alpha$ -(BEDT-TTF) $_2\text{I}_3$ ;  $g_1=2.0113$ ,  $g_2=g_3=2.0033$  [62]) and the  $g$ -values of the square planar  $\text{CuBr}_4^{2-}$  [61]. The Lorentzian line shape with the intermediate  $g$ -value between the BEDT-TTF cation and the  $\text{Cu}^{2+}$  ion proves the presence of exchange interaction  $J_{\text{B-d}}$  between BEDT-TTF (B) and  $\text{Cu}^{2+}$  spins, where the estimation gives  $J_{\text{B-d}} \gg (g_{\text{Cu}} - g_{\text{ET}})\mu_B H \sim 0.01$  K. The principal values of the  $g$ -tensor at 45 K are in good agreement with the  $g$ -values of the square-planar  $\text{CuBr}_4^{2-}$ . Moreover, the directions of the  $g$ -tensor principal axes at  $T=45$ K are in good agreement with the orientation for the  $\text{CuBr}_4^{2-}$  expected from the X-ray

analysis within the experimental error as shown in Fig. 3.50. These results suggest the disappearance of  $\pi$ -electron spins on BEDT-TTF B molecules below  $T_c$ , while the square planar structure of  $\text{CuBr}_4^{2-}$  remains unchanged.

### *Antiferromagnetic Resonance*

Figure 3.51 shows the angular dependence of the resonance field in the  $bc$ -plane. Two resonance peaks were observed within  $-28^\circ < \theta < 12^\circ$  and show the characteristic bubble like pattern, where the  $b$ -axis is  $\theta = 0^\circ$ . This angle dependence is the feature of the resonance pattern when we rotate the field direction from the easy axis to the intermediate axis. It indicates that the easy and intermediate axes are the  $b$  and  $c$ -axes, respectively, which is in good agreement with the result of the susceptibility. The analysis on the basis of eq. (3.33) results in  $\Omega_+ = \sqrt{2AK_2} = 6.6$  kOe,  $\Omega_- = \sqrt{2AK_1} = 5.9$  kOe and  $a = 1 - \chi_{\parallel} / \chi_{\perp} = 0.47$ ,  $\theta_0 = 8.0^\circ$ , where the relation  $\theta_0$  between the field direction and the easy axis is represented by  $\beta = \theta + \theta_0$ . Meanwhile, Fig. 3.52 shows the angular dependence of the resonance field in the  $a^*b$ -plane. The upper mode (spin-flop mode) and the lower mode are observed within  $-16^\circ < \theta < 28^\circ$  and  $-38^\circ < \theta < 28^\circ$ , respectively. The angle dependence of double parabola is the feature of the rotation pattern from the easy axis ( $b$ -axis) to the hard axis ( $a^*$ -axis), where the easy axis is in good agreement with the result of the susceptibility and AFMR in the  $bc$ -plane. The analysis by eq. (3.33) with the exchange between suffices 1 and 2 and eq. (3.35) results in  $\Omega_+ = 6.6$  kOe,  $\Omega_- = 5.9$  kOe and  $a = 0.50$ ,  $\theta_0 = 2.0^\circ$ , which are in good agreement with the result in the  $bc$ -plane.

The difference between  $\Omega_+$  and  $\Omega_-$  proves the presence of the biaxial anisotropy, though the small difference in the anisotropic implies that the magnetic anisotropy is approximately uniaxial type. The estimated values of  $\Omega_- = 5.9$  kOe at  $T = 3.53$  K and 3.67 K are almost consistent to the spin-flop field  $H_{sf} = 7.0$  kOe at the temperatures in the susceptibility. Moreover,  $a = 0.47$  and  $a = 0.50$  in the  $bc$  and  $a^*b$  planes, respectively, are in good agreement with  $a = 0.46$  and 0.43 in the result of the susceptibility at the corresponding temperatures. These results demonstrate that

the crystallographic  $a^*$ ,  $b$  and  $c$ -axes nearly correspond to the magnetic hard, intermediate and easy axes, respectively. Moreover, the result of  $\theta_0$  suggests that the magnetic easy axis lies at  $(\theta, \phi)=(-2, -8)$  defined by Fig. 3.51, which explains the deviation of the easy axis from the  $b$ -axis in the susceptibility measurement. In this measurement, the temperature dependence of resonance peak could not be observed near the antiferromagnetic transition temperature because of the weakly resonance peak.

### *Electronic Structure Calculation*

From the DV- $X\alpha$  calculations of the electronic states of  $\text{CuCl}_4^{2-}$  and  $\text{CuBr}_4^{2-}$ , the wave functions of the HOMO levels, which consists of one  $\text{Cu-}3d_{x^2-y^2}$  orbital and four ligand orbitals, has the strong mixing with the character ratio  $\text{Cu-}3d_{x^2-y^2}/\text{Cl-}3p=0.40/0.59$  and  $\text{Cu-}3d_{x^2-y^2}/\text{Br-}4p=0.34/0.65$ , respectively. These results suggest that the distribution of the  $3d$ -electrons of  $\text{Cu}^{2+}$  are widely extended to the ligands in the  $\text{CuCl}_4^{2-}$  and  $\text{CuBr}_4^{2-}$  anions. In particular, the unpaired electron of the  $\text{CuBr}_4^{2-}$  anion is extended widely superior to the  $\text{CuCl}_4^{2-}$  anion.

### *$^1\text{H-NMR}$ measurement*

$^1\text{H-NMR}$  measurements under ambient and high pressure are collaborating work with Prof. Takahashi's group in the Gakushuin University. As the results of the measurements were reported in Refs. [89, 91], we summarized the results of  $^1\text{H-NMR}$ . Figure 3.53 shows the temperature dependence of the spin-lattice relaxation rate  $T_1^{-1}$  under ambient pressure.  $T_1^{-1}$  decreases gently with lowering the temperature, and shows a slight anomaly at  $T_c=59$  K in spite of the abrupt disappearance of the magnetic moments on BEDT-TTF B molecules. Below  $T_c$ ,  $T_1^{-1}$  indicates a minimum around 18 K, and then, it increases suddenly below the minimum temperature owing to the critical spin-fluctuation in the vicinity of the temperature of magnetic long-range-order. From the peak of  $T_1^{-1}$ , the antiferromagnetic ordering temperature is estimated at  $T_N=8$  K, which is in good agreement with the result of the susceptibility  $T_N=7.65$  K. Moreover, the line width shows remarkable broadening

Table 3.8: Pressure dependence of antiferromagnetic transition temperature  $T_N$ , exchange energy  $J$  and expectation value  $\langle S \rangle$  of the Cu spin from the result of  $^1\text{H}$ -NMR, where  $S_0=1/2$  [89, 91].

$p$ kbar	$T_N$ (K)	$J$ (K)	$\langle S \rangle / S_0$
0	8	20	0.65
6.5	11	27	0.52
20	15	32	0.49

from ca. 20 G above  $T_N$  to 200 G below  $T_N$ , accompanying the magnetic ordering. Under 9 kbar,  $T_1^{-1}$  is smaller than that at ambient pressure as shown in Fig. 3.54. The exchange interactions between the  $\text{Cu}^{2+}$  ions under 0, 6.5 and 20 kbar are estimated at 20, 27 and 32 K, respectively, using the results of  $T_1^{-1}$  at 20 K. The antiferromagnetic ordering temperatures under 6.5 and 20 kbar raise up to 11 and 15 K, respectively, from the value at ambient pressure. The expected value of the localized  $\text{Cu}^{2+}$  magnetic moment under 0, 6.5 and 20 kbar are evaluated at 0.65, 0.52 and  $0.49 \mu_B$ , respectively, using the second moments of the line widths at 1.4 K. The large decreases from one  $\mu_B$  of  $\text{Cu}^{2+}$  are due to the quantum spin fluctuations related to the feature of the Heisenberg antiferromagnet. The estimated value of the Néel temperature, exchange energy and spin reduction under pressures are summarized in Table 3.8.

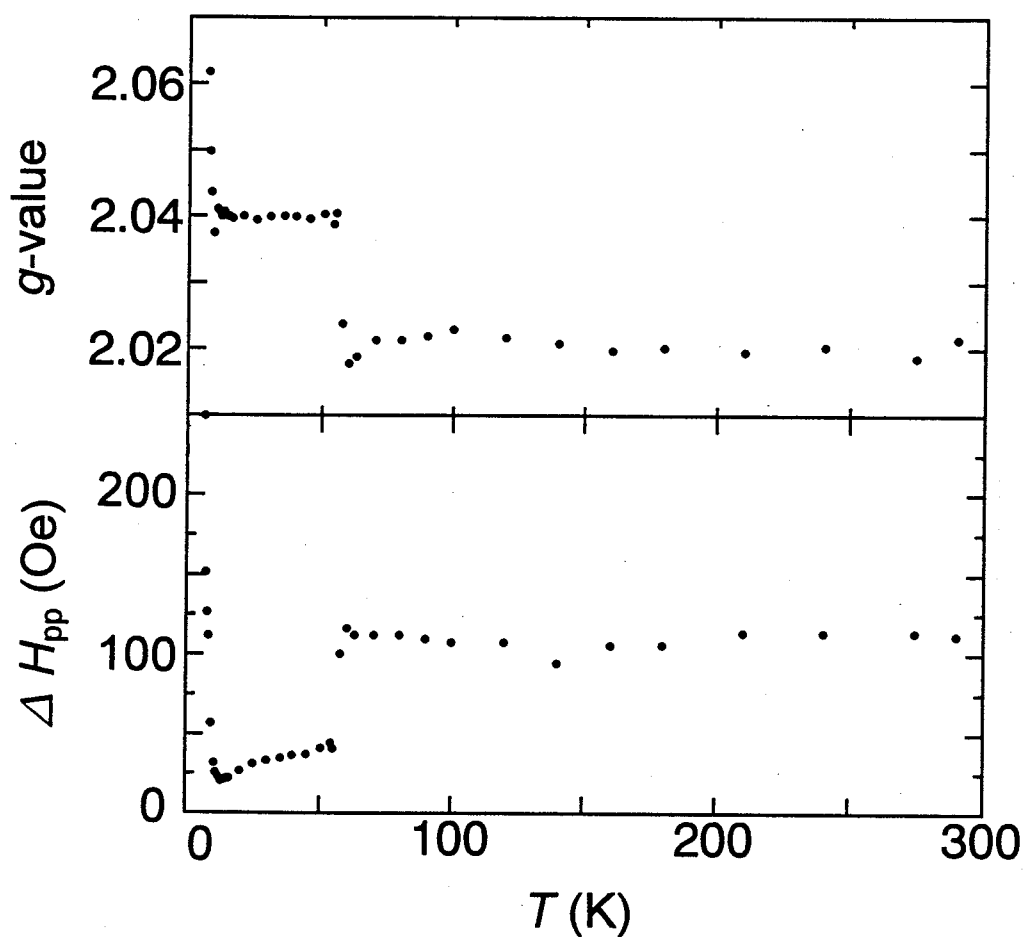


Figure 3.46: Temperature dependence of EPR line width and  $g$ -value in applied field parallel to the  $b$ -axis. Line width shows the constant value and decreases to 50 Oe discontinuously at  $T_c=59$  K. Below  $T_c$ , the line width decreases gently with decreasing the temperature owing to the short-range-order effect. The  $g$ -value is almost temperature independent in the whole temperature range except a discontinuous step at  $T_c$ .

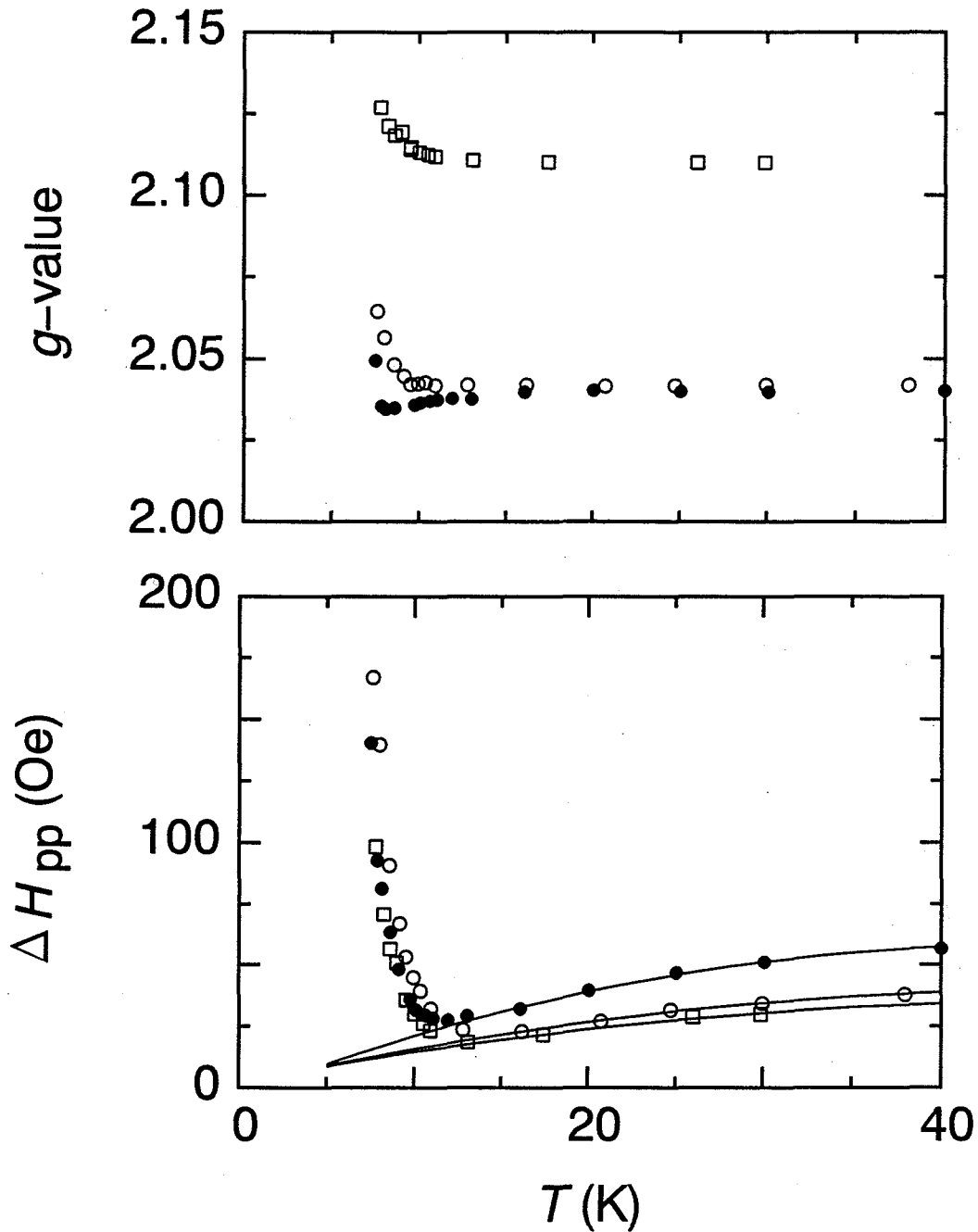


Figure 3.47: Detailed temperature dependence of EPR line widths and  $g$ -values in the applied field parallel to the  $a^*$  ( $\square$ ),  $b$  ( $\bullet$ ) and  $c$  ( $\circ$ ) -axes in the low temperature range. Line widths show the characteristic of the critical broadening in the vicinity of the magnetic long-range-order with the large shift of the  $g$ -value. Solid lines indicate to evaluate the short-range-order effect fitted by the second order polynomial equation in the temperature range 15-45 K. The critical broadening of the line widths are estimated by the subtracting the short-range-order components from the total line widths.

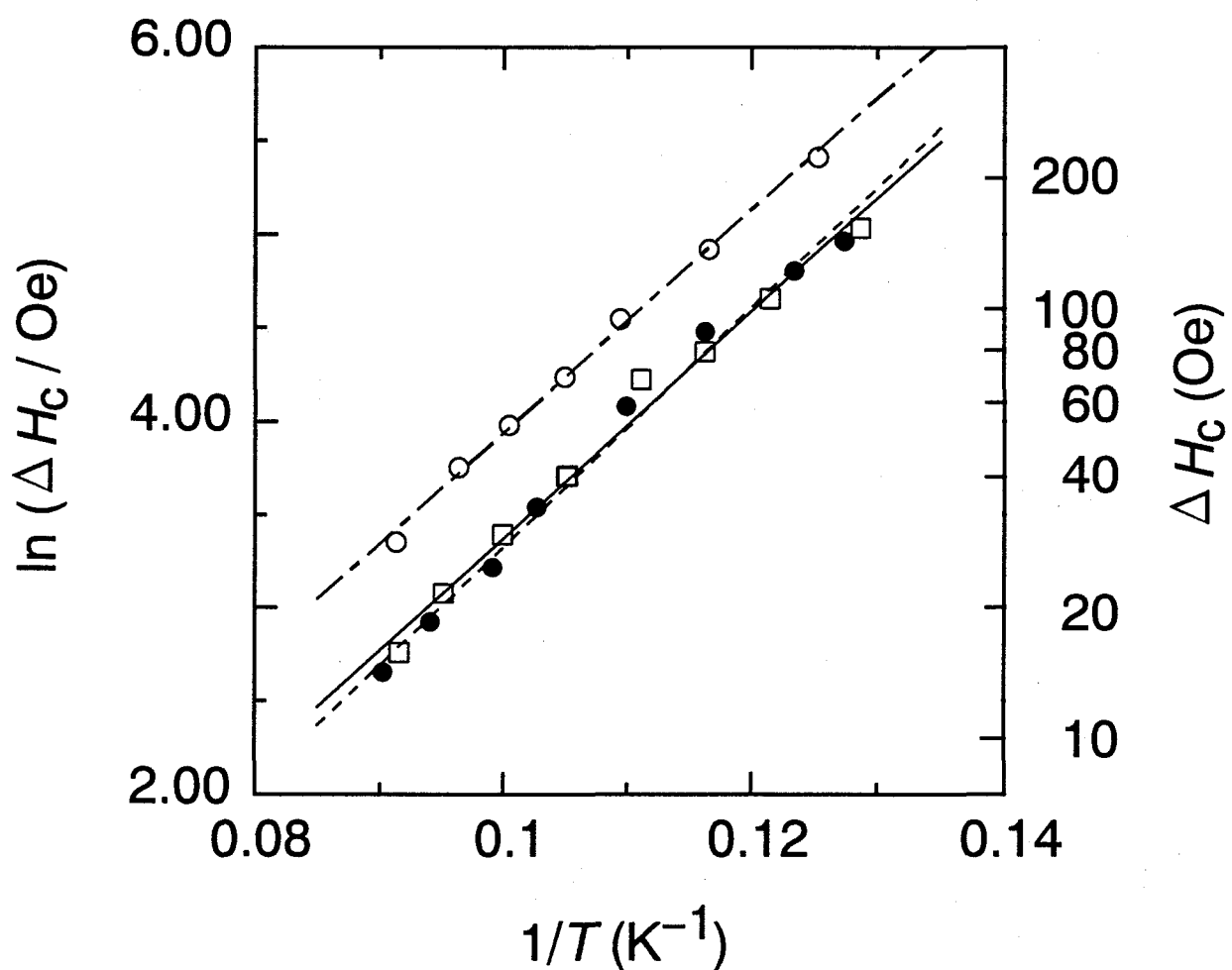


Figure 3.48: The critical broadening of the line widths vs  $1/T$  in the critical region above  $T_N$  for the  $a^*$  ( $\square$ ),  $b$  ( $\bullet$ ) and  $c$  ( $\circ$ ) -axes. The slopes of  $\ln(\Delta H_c)$  vs  $1/T$  plots are equivalent to  $6\pi kJ$ , where  $J$  is the exchange energy. The straight, dotted and dash-dotted lines are the fitting ones for the  $a^*$ ,  $b$  and  $c$ -axes, respectively, using the first term of eq. (3.47) in the temperature range  $1.1T_N < T < 1.5T_N$ .

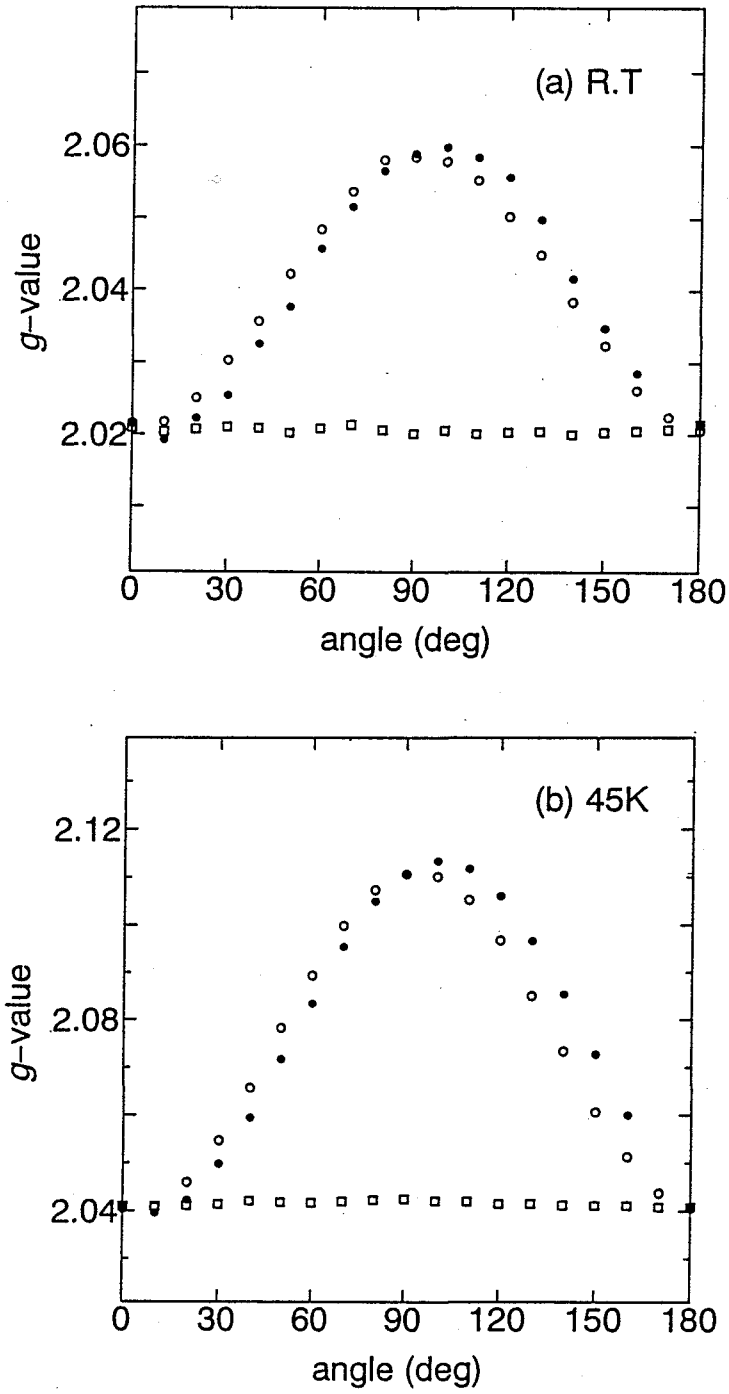
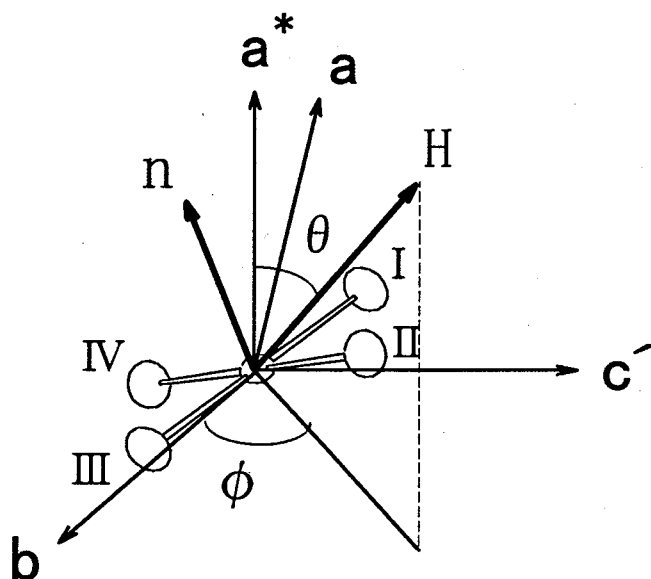


Figure 3.49: Angular dependence of  $g$ -values around the  $a^*$ ,  $b$  and  $c$ -axes at room temperature (a) and  $T=45\text{K}$  (b). The data plots shown with open squares( $\square$ ), full circles( $\bullet$ ) and open circles( $\circ$ ) are the rotations in the  $b$ - $c$ - $b'$ ,  $c'$ - $a$ - $a^*$ - $c$  and  $b$ - $a^*$ - $b'$  planes. The initial values (zero degree) of the setting angles are  $(\theta, \phi)=(90,0)$ ,  $(90,90)$ ,  $(90,0)$ , respectively, whose definitions are shown in Fig. 3.50 [13].





<i>g</i> -tensor (45K)	X-ray data (R. T. )
$g_1=2.114$ (−10.8, 74.1)	<i>n</i> (−13.2, 84.3)
$g_2=2.041$ (85.7, 141)	Cu-Br(I) (81.8, 136)
$g_3=2.040$ (80.1, 50.1)	Cu-Br(II) (79.8, 44.3)

Figure 3.50: The orientation of the square planar  $\text{CuBr}_4^{2-}$  with *g*-values and their principal axes ( $\theta, \phi$ ) at  $T=45\text{K}$ . The Cu ion at the origin is coordinated with four Br ligand atoms (I, II, III, IV). The orientations of the ligand atoms (I, II, III, IV) determined by X-ray data at room temperature are shown in the second column. The principal axes for  $g_1, g_2$  and  $g_3$  at  $T=45\text{K}$  correspond to the normal direction *n* to the ligand plane, the Cu-Br(I) and the Cu-Br(II) directions at room temperature, respectively.

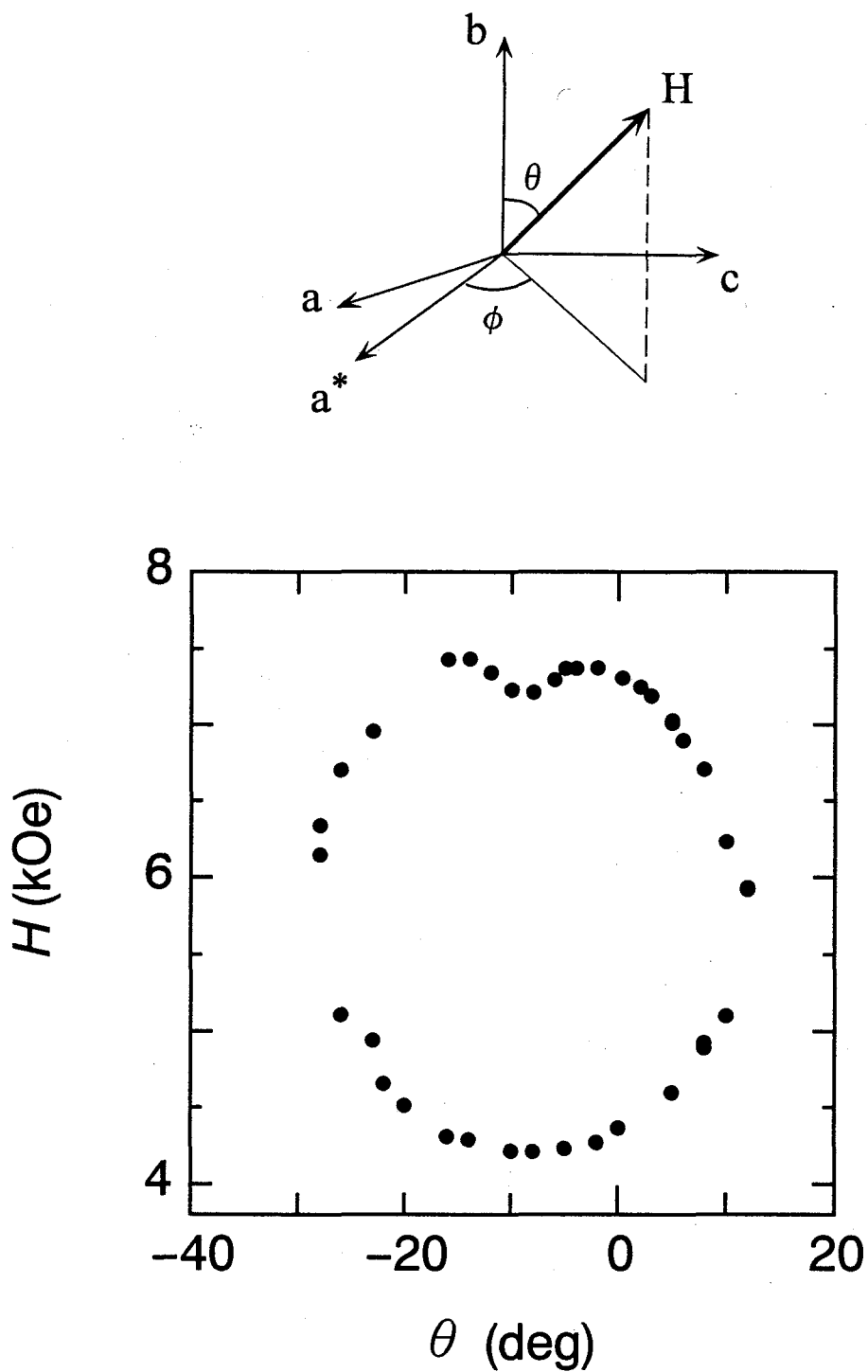


Figure 3.51: Angular dependence of AFMR field in the  $bc$ -plane ( $\phi=90^\circ$ ) at  $T=3.53$  K. The external field at the origin  $\theta=0^\circ$  lies on the  $b$ -axis. The analysis by eq. (3.33) results in  $\Omega_+=6.6$  kOe,  $\Omega_-=5.9$  kOe and  $a=0.47$ ,  $\theta_0=8.0^\circ$ . The definitions of  $\theta, \phi$  are shown in the upper figure.

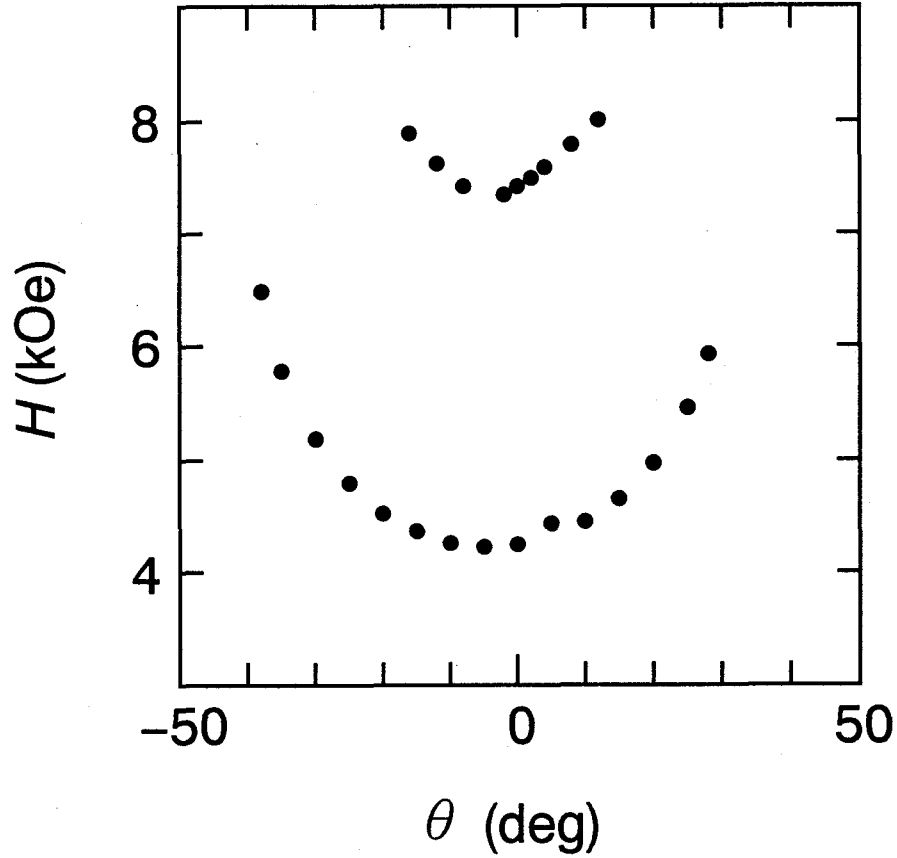


Figure 3.52: Angular dependence of AFMR field in the  $a^*b$ -plane ( $\phi=0^\circ$ ) at  $T=3.67$  K. The external field at the origin  $\theta=0^\circ$  lies in the  $b$ -axis. Analysis by eq. (3.33) with exchange between suffices 1 and 2, (3.35) results in  $\Omega_+=6.6$  kOe,  $\Omega_-=5.9$  kOe and  $a=0.47$ ,  $\theta_0=8.0^\circ$ . The definition  $\theta, \phi$  are shown in the upper figure of Fig. 3.51.

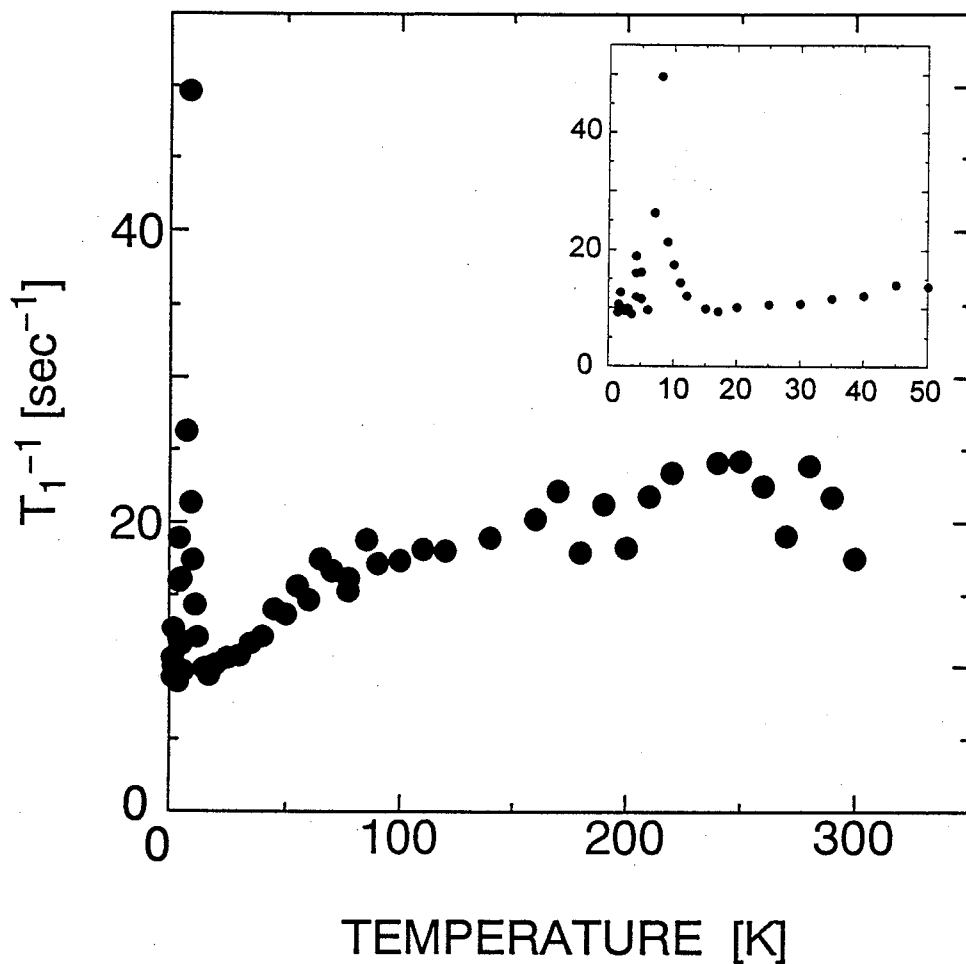


Figure 3.53: Temperature dependence of the spin lattice relaxation rate  $T_1^{-1}$  of  $^1\text{H}$ -NMR [89].  $T_1^{-1}$  decreases gradually with lowering the temperature above 18 K, and  $T_1^{-1}$  shows a slight anomaly at  $T_c$ . It shows a minimum around 18 K, and then, it increases abruptly owing to the critical fluctuation in the vicinity of the antiferromagnetic transition temperature.

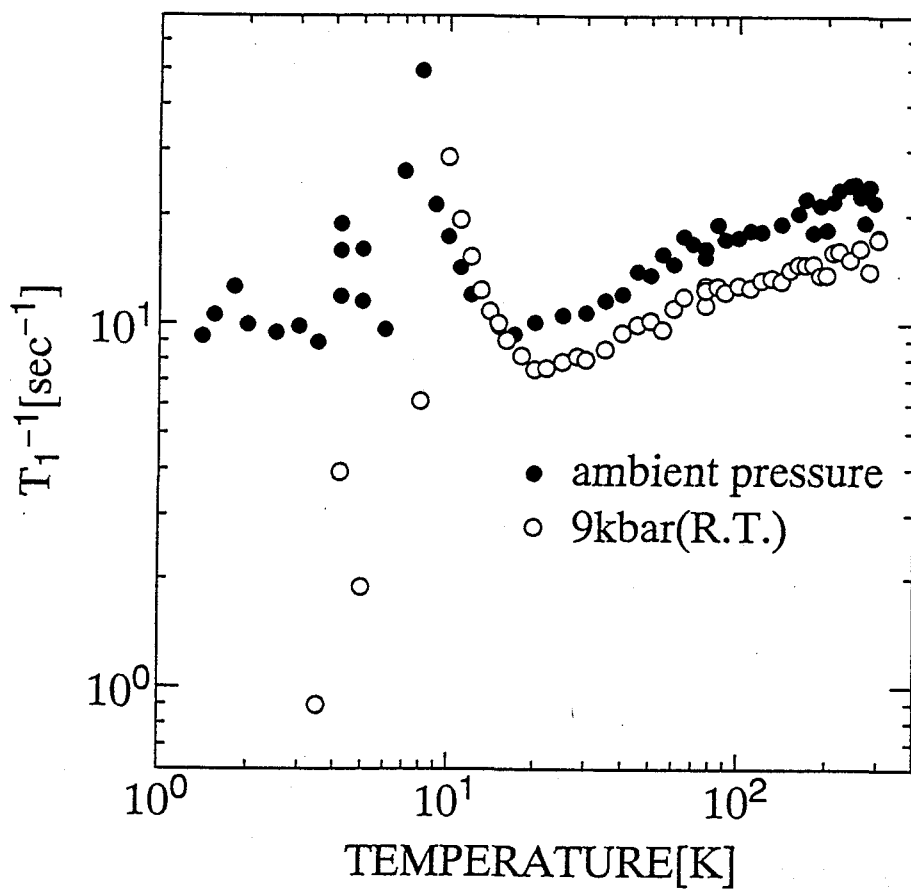


Figure 3.54: Temperature dependence of the spin lattice relaxation rate  $T_1^{-1}$  under ambient pressure and 9 kbar [91].  $T_1^{-1}$  at 9 kbar is smaller than that at ambient pressure, suggesting the enhancement of the exchange interaction. The antiferromagnetic ordering temperature  $T_N$  shifts from  $T_N=8$  K at ambient pressure to  $T_N=11$  K under 9 kbar.

### *Ac Calorimetry Measurement*

Figure 3.55 shows the temperature dependence of the heat capacity after calibrated by the DSC data at 273 K, where the accuracy is within 5%. It shows a slight hump around 100 K, and indicates a sharp peak with a  $\lambda$ -type anomaly at  $T_c=58.8\pm0.2$  K in the heating process with a step of the base line in the heat capacity above and below  $T_c$ . Figure 3.56 shows the temperature dependence around  $T_c$ . The sharp peak proves the first order transition at  $T_c$  which is in good agreement with the results of the X-ray study [66], resistivity [92] and magnetic susceptibility.

### *Heat Capacity by Relaxation Method*

Figure 3.57 shows the temperature dependence of the heat capacity by the relaxation method after subtracting the heat capacity of the bolometer and Apiezon grease. The heat capacity indicates a small anomaly around 9 K. The peak of the heat capacity associated with the antiferromagnetic order is not observed at  $T_N=7.65$  K. In ordinary low-dimensional Heisenberg magnet, the magnetic entropy expense is significantly small at the long range ordering temperature. This is the case for the present compound with the absence of appreciable peak at  $T_N$ . Figure 3.58 shows  $C/T$  vs  $T^2$  plot, where a small hump exists around 9 K. In general, as the heat capacity of a substance is described in terms of the lattice, conduction electron and magnetic heat capacity, the estimation of the magnetic heat capacity requires to subtract precisely the other two contributions. Here, the heat capacity of the conduction electron is negligible because the present compound is the insulator at low temperature. However, the heat capacity of the lattice can not be estimated precisely in the present compounds. Here, assuming that the lattice contribution has a cubic temperature dependence, it is suggested that the magnetic heat capacity obeys the cubic temperature dependence after subtracting the lattice contribution from the total heat capacity. This feature of the cubic temperature dependence is thought to be the presence of the three-dimensional antiferromagnetic ordering below 9 K on the basis of the spin wave theory of the antiferromagnet.

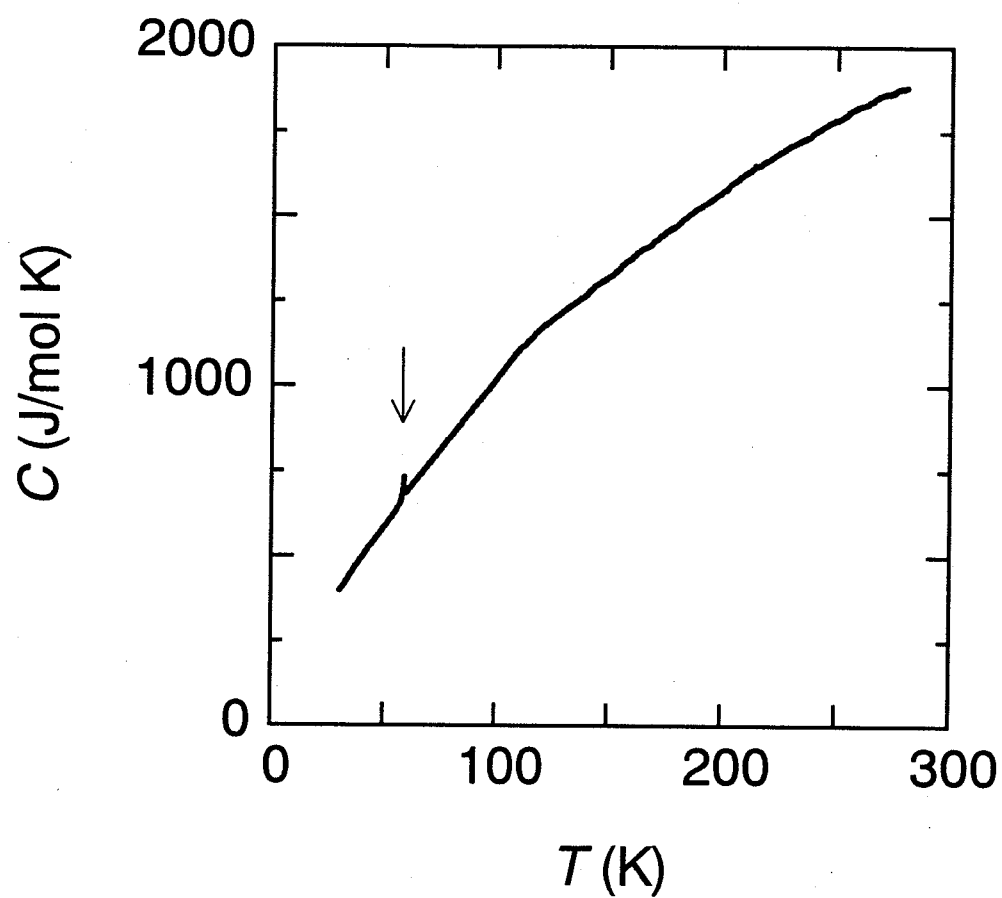


Figure 3.55: Temperature dependence of the heat capacity measured by ac calorimetry. The absolute value of heat capacity is calibrated by the DSC measurement at 273 K. The one mol is defined as one unit cell here. The arrow indicates the structural transition at  $T_c=58.8$  K.

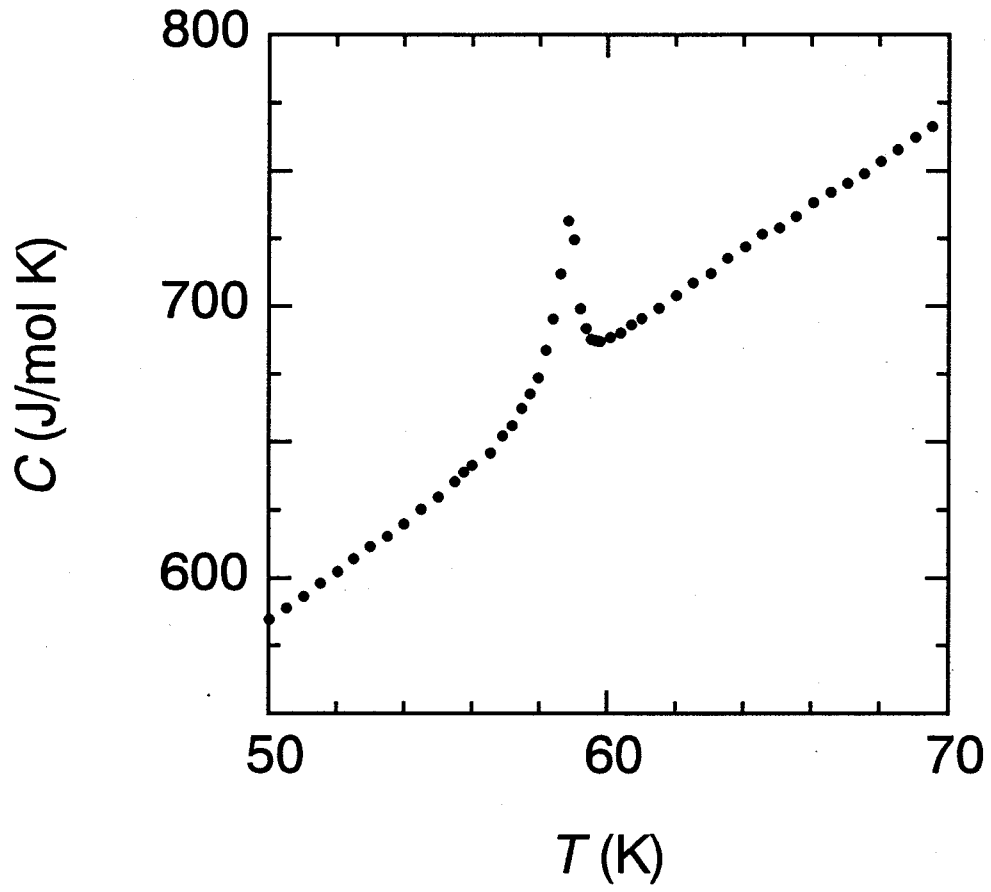


Figure 3.56: Temperature dependence of the heat capacity around  $T_c = 58.8 \pm 0.2$  K. The sharp peak and the step of heat capacity below and above  $T_c$  proves the first order type.



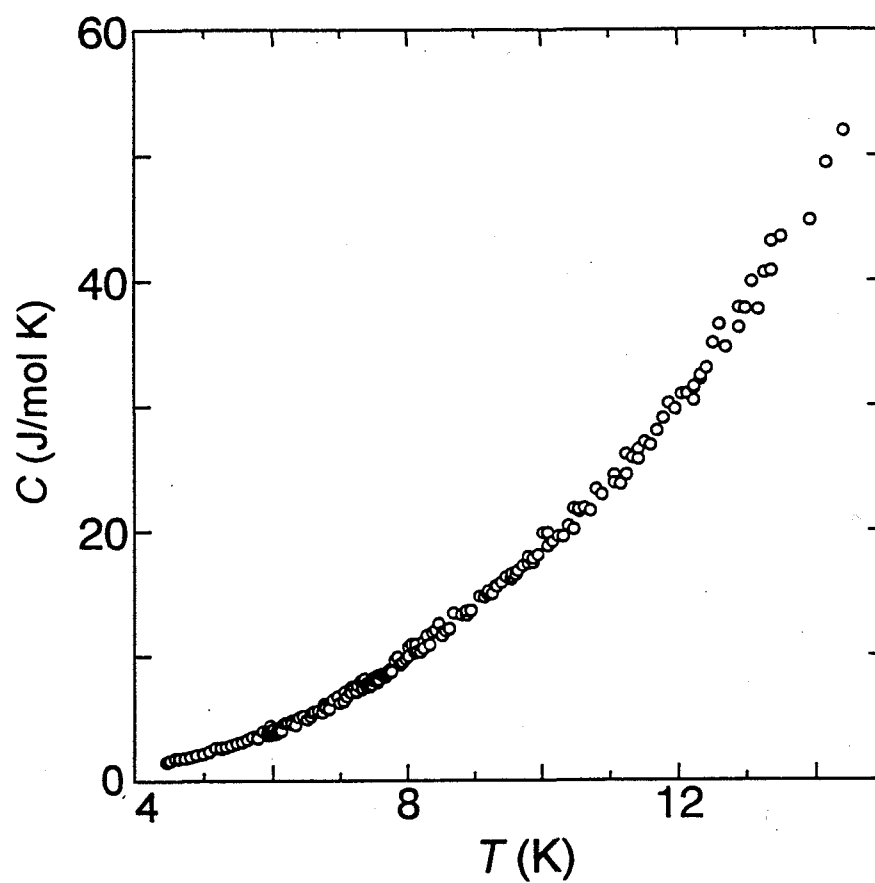


Figure 3.57: Temperature dependence of the heat capacity by the relaxation method, which shows a slight hump around 9 K. The one mol is defined as one unit cell. An antiferromagnetic ordering peak is not observed at  $T_N=7.65$  K.

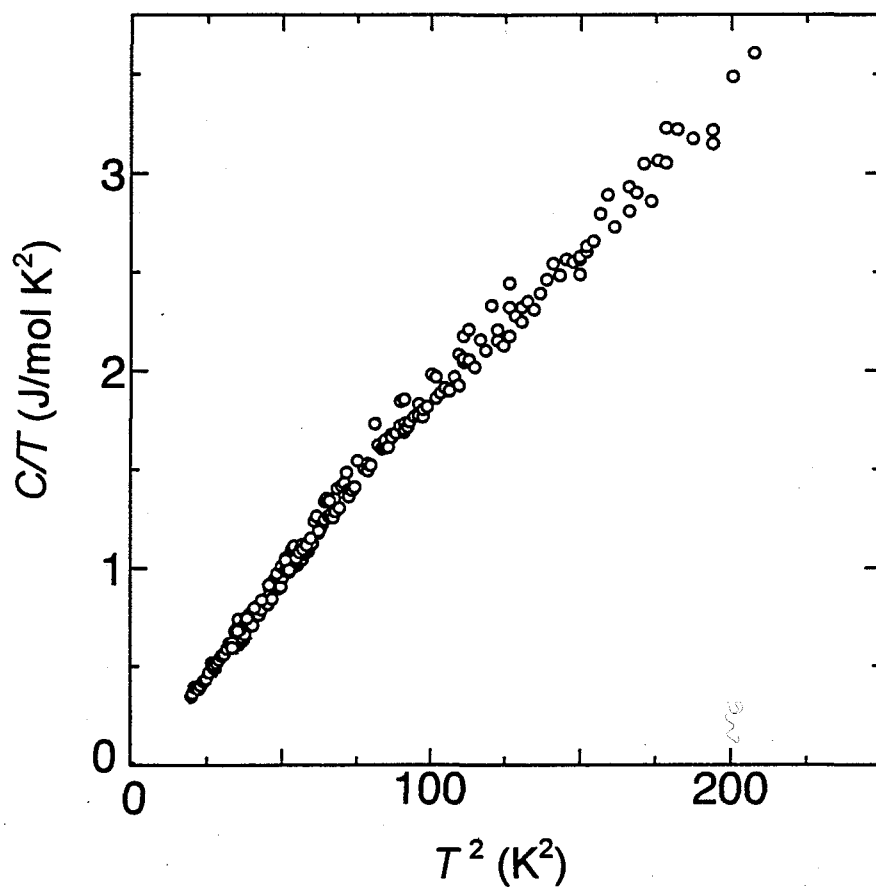


Figure 3.58:  $C/T$  vs  $T^2$  plot of the heat capacity. The linear dependence in the plot below 9 K suggests  $T^3$  dependence of magnetic heat capacity after subtracting the lattice heat capacity having  $T^3$  dependence from the total heat capacity. This feature of the cubic temperature dependence is thought to be the presence of the three-dimensional antiferromagnetic ordering below 9 K on the basis of the spin wave theory.

### 3.4.3 Discussion

#### Origin of structural transition at $T_c$

In this section, we discuss the origin of the phase transition at  $T_c=59$  K using the results of crystal structure, electrical resistivity and magnetic properties. For the consideration of the origin, the experimental findings at the transition are summarized as follow. The resistivity has a discontinuous change at  $T_c$  with the hysteresis and the heat capacity shows the sharp peak with the step of the heat capacity, indicating the first order nature of the transition [92]. From the magnetic susceptibility and EPR measurements, the magnetic properties are described in terms of the magnetic moments on the  $\text{Cu}^{2+}$  ions and the BEDT-TTF cations at the B sites in the high temperature phase. Meanwhile, the spin system in the low temperature phase consists of only the  $\text{Cu}^{2+}$  spins as a results of the disappearance of the BEDT-TTF magnetic moments at  $T_c$ . The change in the magnetic system generates the 50% reduction of the EPR line width accompanied by the change in the  $g$ -values. Namely, the disappearance of the BEDT-TTF magnetic moments brings about the reduction of dipolar field which governs the line width of the EPR signal. Moreover, it is also consistent with the change of  $g$ -value, that is, the  $g$ -values in the low temperature phase are identical to those for the  $\text{Cu}^{2+}$  ion surrounded by the square planar Br ligands. From the point of structural change, the space group changes from  $P2_1/c$  to  $Pc$  at  $T_c$  accompanied by the slight trimerization due to the change from the high temperature phase to the low temperature one. On the basis of the EPR and optical reflectance spectra, the previous papers [14, 92] pointed out the change in the ligand symmetry of the  $\text{CuBr}_4^{2-}$  anions as the structural origin of the phase transition. However, this contradicts the present results of EPR and the X-ray structural analysis [66, 72] in the low temperature phase. Namely, the X-ray analysis indicates that no substantial change of the static Jahn-Teller distortion in the  $\text{CuBr}_4^{2-}$  anion was detected at 20K. Thus, the present experimental findings require the explanation for the disappearance of BEDT-TTF spins at sites B with-

out the change of the ligand symmetry of  $\text{CuBr}_4^{2-}$ . In this respect, we have three kinds of possible explanations for the origin of the transition at  $T_c$ : 1) the transition from paramagnetic to antiferromagnetic insulator state in a Mott insulator; 2) the dimerization of BEDT-TTF cation radicals associated with a spin-Peierls transition; 3) the transition from a Mott insulator to a band insulator.

First, we discuss the possibility of the first explanation. The presence of the localized spins on the BEDT-TTF B molecules evidences that the electronic and the magnetic properties of the BEDT-TTF layer in the high temperature phase is characterized as a Mott insulator where the on-site Coulomb repulsion overwhelms the transfer integral. However, the composition of the present compound gives  $+2/3$  filled band structure, if we neglect the difference between the A and B sites. This is not favorable for ordinary Mott insulators because Mott insulating state requires the half-filled band structure in the one-electron band approximation where the on-site Coulomb repulsion works most effectively. On the other hand, as mentioned in section 3.2, the X-ray analysis proves the presence of the charge separation between  $+1$  (B) and neutral (A), which causes the HOMO level splitting into upper four-fold and lower two-fold sub-levels [14, 65] as shown in Fig. 3.18. As a consequence, the half-filled state is realized in the upper band, which is favorable to the Mott insulator state. In this regard, the behavior at high pressures gives an important information related to the competition between the transfer integral and the on-site Coulomb interaction. Namely, the application of pressure enhances the transfer integral while it does not change the on-site Coulomb interaction effectively. Actually, the remarkable decrease in the resistivity and the appearance of the metal-insulator transition prove the increase of the transfer integrals in comparison with the change of the on-site Coulomb interaction. Here, Figure 3.59 summarizes the temperature-pressure phase diagram obtained from the behavior of resistivity [92] and  $^1\text{H-NMR}$  [89]. In this phase diagram, the high temperature insulator phase I(I) having the localized magnetic moments of BEDT-TTF B molecules borders the low temperature insulator phase I(II) where the magnetic moments disappear. In

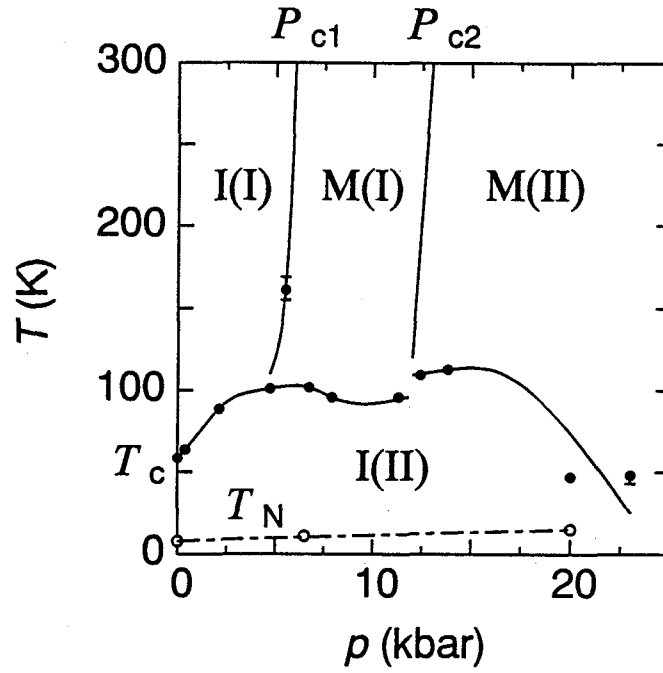


Figure 3.59: Temperature-pressure phase diagram obtained from the electrical properties and  $^1\text{H}$ -NMR [89, 91, 92]. I(I) and I(II) denote the insulator phases, while M(I) and M(II) do the metallic phases. The dash-dotted line indicates the pressure dependence of the antiferromagnetic transition obtained by  $^1\text{H}$ -NMR (Ref. [89, 91]).

the temperature range above the boundary of insulator phase I(II), the application of pressure changes the phase from insulating I(I) to metallic M(I) at  $P_{c1}=7\text{kbar}$ , and finally stabilizes metallic phase M(II) above  $P_{c2}=13\text{kbar}$ . It should be noted that the magnetic susceptibility in phase I(I) becomes reduced with the approach to the phase boundary to M(I), as mentioned in the previous section. In addition, the pressure-temperature phase diagram of  $(\text{BEDT-TTF})_3\text{CuBr}_4$  is reminiscent of that of the typical Mott insulator  $\text{V}_2\text{O}_3$  as shown in Fig. 1.5 [24, 25]. In the phase diagram of  $\text{V}_2\text{O}_3$ , the paramagnetic insulator phase borders the antiferromagnetic insulator phase at the low temperature boundary and the paramagnetic metallic phase at the high pressure boundary. Comparison between the phase diagrams of  $(\text{BEDT-TTF})_3\text{CuBr}_4$  and  $\text{V}_2\text{O}_3$  suggests that the transition from I(I) to M(I) is characterized as the Mott metal-insulator transition which is realized through the competition between the transfer integral and the on-site Coulomb interaction. Thus, the aspect of the Mott transition, the decrease of the magnetic susceptibility

in the I(I) insulator phase in the vicinity of the I(I)-M(I) boundary is considered to be a precursor of the Mott M-I transition. Meanwhile, the disappearance of the localized magnetic moments at the transition from I(I) to I(II) is explained by the transition from the paramagnetic insulator to the antiferromagnetic insulator phase. In this transition, the antiferromagnetic exchange interaction works to couple the magnetic moments with the antiparallel arrangement, resulting in the considerable reduction in the magnetic susceptibility. Moreover, this transition is accompanied by the structural change, similar to the transition from a paramagnetic to an antiferromagnetic state in ordinary Mott insulators. Nevertheless, in an ordinary magnetic system, the antiferromagnetic ordered state is characterized as the appearance of the anisotropy in magnetic susceptibility, which is disagreeable to the present observation. Consequently, it is impossible to explain the origin of the transition with the change from the paramagnetic insulator to antiferromagnetic insulator state in the Mott regime.

Next, we consider a spin-Peierls transition as the possible origin of the phase transition. In the crystal structure as shown in Fig. 3.12, BEDT-TTF donors form the face-to-face stacking structure with the ABBABB sequence in the  $c$ -axis direction, where A molecules are neutral donors and B molecules have a  $\pi$ -hole/molecule with  $S=1/2$ . The transfer integral  $t_{c2}$  between adjacent B molecules is the smallest one in the intrastack direction, while the transfer integrals  $t_{b1}$ ,  $t_{b2}$ ,  $t_{b3}$  have significant values in the side-by-side direction ( $b$ -axis). Taking into account that A molecules are nonmagnetic, the above structural consideration reveals the existence of magnetic linear chains of BEDT-TTF B molecules coupled by the side-by-side interaction with the estimate of the exchange interaction  $J_{B-B} \propto -t_{b2}^2/U$ . Therefore, the one-dimensional structure will favor a spin-Peierls state with the formation of a dimerized structure at low temperatures, resulting in the singlet ground state for B sites. In particular, the absence of the anisotropy in the magnetic susceptibility in the vicinity of  $T_c$  seemingly supports the scenario of the spin-Peierls transition as the disappearance of the magnetic moments at B sites. Actually, the dimeriza-

tion of BEDT-TTF B molecules below  $T_c$  is suggested from the overlap integral calculation based on the X-ray structure analysis [72]. Hence, the development of the dimerization in the B sites enhances the antiferromagnetic exchange interaction between BEDT-TTF spins in a dimer, resulting in the disappearance of the magnetic moments at sites B in the low temperature phase. Moreover, the magnetic gap estimated from the susceptibility below  $T_c$  is considered to correspond to the exchange interaction between the dimerized spins in the spin-Peierls state. In the magnetic susceptibility, the subtraction of the contribution of  $\text{Cu}^{2+}$  spins from the observed value gives the contribution of BEDT-TTF B spins in the vicinity of the transition, where the former contribution is obtained from the fitting curve for the two-dimensional square lattice Heisenberg model as shown in Fig. 3.41. The analysis of the BEDT-TTF contribution just below  $T_c$  based on the singlet-triplet model leads to the minimum value of the intrachain exchange interaction  $J_{\text{B-B}} \sim -220$  K in the dimerized B molecules in the spin-Peierls state for  $T < T_c$ . On the other hand, the exchange energy between the BEDT-TTF molecules in the linear chain above  $T_c$  is roughly estimated at  $J_{\text{B-B}} \sim -100$  K from the Weiss temperature for  $T > T_c$  given by  $\theta \sim 4J_{\text{B-B}}S(S+1)/3k_B$ , where the value is obtained by neglecting  $J_{\text{d-d}}$  and  $J_{\text{B-d}}$ . It is reasonable to explain that the structural transition at  $T_c$  causes ca. 100% enhancement of the exchange interaction, and the above experimental findings give comfortable evidence for the spin-Peierls transition. Nonetheless, the following features of the transition are definitely disagreeable to it. That is, the ordinary spin-Peierls transition is characterized as the second order transition, where the temperature dependence of the magnetic gap is given by the BCS type function [93]. However, the intensity of (0k0) X-ray reflection [66], heat capacity and the magnetic susceptibility at  $T_c$  have the discontinuous behavior at  $T_c$ , suggesting the first order nature of the transition. Further, as mentioned in section 3.2, the X-ray structure analysis [73, 75] indicates the disappearance of the charge disproportionation between BEDT-TTF A and B molecules below  $T_c$ . This observation implies that the BEDT-TTF spin network is not characterized as the one-dimensional mag-

netic chains in the low temperature range. Consequently, the spin-Peierls transition is excluded from the candidate of the origin of the phase transition.

Finally, we discuss the third explanation for the transition at  $T_c$ . As we have mentioned above, it is suggested that the charge distribution between BEDT-TTF A and B molecules is almost uniform with  $+2/3$  charge per BEDT-TTF molecule below  $T_c$ . The disappearance of the charge disproportionation below  $T_c$  is the consistent trend to the change from a Mott insulator to a band insulator because the Mott insulator state in the present compound is strongly related to the charge disproportionation of BEDT-TTF molecules. In this respect, the first order phase transition accompanied by the change of the charge disproportionation in the present compound is reminiscent of the neutral-to-ionic transition observed in mixed-stack donor-acceptor crystal TTF-CA(tetrathiafulvalene-*p*-chloranil) with decreasing the temperature and/or applying the pressure [94, 95]. At the transition, TTF-CA shows discontinuous changes of the molecular ionicity, lattice constants, magnetic susceptibility and conductivity, indicating the first order transition [96, 97]. The simple model suggests that the change of the Madelung energy with decreasing temperature or applying pressure drives the neutral-ionic transition [98]. That is, the compound has the neutral state in the region  $I_D - E_A > V_M$ , while the ionic state in the region  $I_D - E_A < V_M$ , where  $I_D$ ,  $E_A$ ,  $V_M$  are the ionization potential of donor, the electron affinity of acceptor and the Madelung energy of the crystal, respectively. In the donor-acceptor alternate stacking salt (BEDT-TTF)<sub>3</sub>CuBr<sub>4</sub>, the Coulomb interaction between the donors gives an important contribution to the Madelung energy when the charge disproportionation is modified depending on temperature. It is a favorable trend to the dissolution of the disproportionation at the structural transition  $T_c$  with the thermal contraction. That is, the thermal contraction brings about the enhancement of the Coulomb repulsive interaction between the donors at sites B having  $+1$  charges because the charge transfer from cation donors B to neutral donors A reduces the repulsive Coulomb energy. Consequently, the charge re-distribution between the A and B donors toward a uniform one is favored at the



expense of the Coulomb repulsion at  $T_c$ . In addition to this origin, in terms of the magnetic properties, the transition from Mott insulator to the band insulator refer to the magnetic transition from the paramagnetic state above  $T_c$  to the non-magnetic state below  $T_c$ . Here, the difference of the magnetic entropy between the paramagnetic state and the nonmagnetic state is given to be the value of  $4R\ln 2$  in a unit cell which corresponds to the entropy having the magnetic moment on four BEDT-TTF B molecules. Thus, at the transition of  $T_c$ , the magnetic entropy of  $4R\ln 2$  per unit cell is stabilized by the change of the band structure. In conclusion, the transition at  $T_c$  is described by the transition from the Mott insulator to the band insulator accompanying with the stabilization of the magnetic entropy of BEDT-TTF B molecules. However, we do not have appropriate explanation on the metal-insulator transition in the high pressure region, which remains unsolved for the future investigation.

### Feature of magnetic interaction

Now, let us discuss the feature of magnetic interactions of  $(\text{BEDT-TTF})_3\text{CuBr}_4$  on the basis of the magnetic susceptibility, magnetization, EPR, AFMR and DV- $X\alpha$  calculation. The beginning of the discussion devotes to the origin of the strong exchange interactions observed from the susceptibility. The Weiss temperature  $\theta = -100$  K is one or two orders of magnitude as large as that of the other similar organic conductors containing localized  $d$ -electrons such as  $(\text{BEDT-TTF})_2\text{FeCl}_4$  ( $\theta = -6$  K) and  $(\text{BEDT-TTF})\text{FeBr}_4$  ( $\theta = -5$  K) [54]. This suggests that the large Weiss temperature is caused by the presence of the strong antiferromagnetic exchange interaction between the  $\text{BEDT-TTF}^+$  cation layer and the  $\text{Cu}^{2+}$  ion layer. Taking into account that the van der Waals distance is  $3.8\text{\AA}$  for the Br-S atomic contact [14], the shortest distance of  $3.699(3)\text{\AA}$  between the Br atom of  $\text{CuBr}_4$  and the external S atom of BEDT-TTF B molecule is enough short to realize the orbital overlap. Here, the DV- $X\alpha$  calculation implies that the Cu  $3d$  electron extends to the peripheral region of the  $\text{CuBr}_4^{2-}$  anion through the hybridization of the Cu- $3d$

and Br-4p orbitals in the HOMO wave function. This is thought to be a feature in the electronic structure of  $\text{CuBr}_4^{2-}$  different from the other transition metal halide anions. Therefore, the delocalized  $d$ -electrons, which are the origin of magnetic moments of the  $\text{Cu}^{2+}$  ions, can easily interact with the  $\pi$ -electrons delocalized on the BEDT-TTF donors. As a result, it is concluded that the cooperation of the novel electronic structure of  $\text{CuBr}_4^{2-}$  causes the strong exchange interaction between the donor  $\pi$ -electrons and the localized  $d$ -electrons. The existence of the strong  $\pi$ - $d$  interaction is the feature which has never been found in other organic conductors of TTF type having localized  $d$ -electrons.

We move on to the magnetic properties below  $T_c$ , where the magnetic properties are governed only by the localized  $d$ -electrons of  $\text{Cu}^{2+}$  ions. As mentioned in section 3.2, the  $\text{Cu}^{2+}$  spin system is well explained based on the two-dimensional square lattice Heisenberg antiferromagnet model. The estimated exchange interaction energy  $J_{d-d} = -15.7$  K in the susceptibility, which is followed by the result of EPR and  $^1\text{H-NMR}$ , is significantly large although the long distances Cu-Cu(8.724(1) Å) or Br-Br(4.190(1) Å) between the nearest neighbor  $\text{CuBr}_4^{2-}$  anions in the magnetic layer. Thereby, the comparison with the other analogous compounds having  $\text{CuBr}_4^{2-}$  anions reveals the anomalous of the present compound. For instance, in bis(piperidinium)tetrabromocuprate(II) [(pipdH) $_2$ CuBr $_4$ ], the flattened tetrahedral  $\text{CuBr}_4^{2-}$  ions form the dimerized chains [99]. The exchange interaction energy between the dimers is estimated at  $J = -6.64$  K in which the double superexchange paths Cu-Br-Br-Cu are realized with the closest Br-Br distance of 4.10 Å. Further, there is no example of square planar  $\text{CuBr}_4^{2-}$  in the crystals having  $\text{CuBr}_4^{2-}$  anions except (BEDT-TTF) $_3$ CuBr $_4$ , and the anion structures of all the others form the flattened tetrahedral ligands [100]. This suggests that the square planar structure of the  $\text{CuBr}_4^{2-}$  realized in the present compound is caused accidentally by the novel restricted geometry of the surrounding donor packing. Therefore, the difference in the electronic structure caused by the difference in the ligand symmetry between the flattened tetrahedral and the square planar structures gives the difference in

the strengths of the exchange interactions. Consequently, we suggest that the large exchange interaction of the present compound is associated with the extended spin polarization of  $\text{Cu}^{2+}$   $d$ -spins to the ligand Br atoms in  $\text{CuBr}_4^{2-}$ .

Next, we discuss the spin structure in the magnetically ordered state of  $\text{Cu}^{2+}$  spins below  $T_N=7.65$  K using the result of magnetic susceptibility, AFMR and DV-X $\alpha$ . In the antiferromagnetic ordered state, the magnetic anisotropy plays an important role to determine the spin orientation. From the results of the susceptibility and AFMR, it is suggested that the origin of the anisotropy energy is the magnetic dipolar interaction between  $\text{Cu}^{2+}$  spins. In order to investigate the contribution of the dipolar interaction to the magnetic anisotropy, we carry out the calculation for the dipolar energy  $E_d$  using the following equation,

$$E_d = g^2 \mu_B^2 S^2 \sum_{\mu, \nu} \sum_{i, j (i \neq j)} \Phi_{\mu\nu}(r_{ij}) \alpha_\mu \alpha_\nu, \quad (3.48)$$

$$\Phi_{\mu\nu}(r_{ij}) = \frac{1}{r_{ij}^3} \left( \delta_{\mu\nu} - \frac{3x_{ij\mu}x_{ij\nu}}{r_{ij}^2} \right) B(r_i)B(r_j), \quad (3.49)$$

where  $\mu$  and  $\nu$  take  $x$ ,  $y$  and  $z$  for the crystallographic  $a^*$ ,  $b$  and  $c$ -axes, respectively,  $x_{ij\mu}$  and  $x_{ij\nu}$  are the  $\mu$  and  $\nu$  components of the distance  $r_{ij}$  between  $i$  and  $j$  sites for  $i, j = \text{Cu}, \text{Br}$ , also,  $\alpha_\mu$  and  $\alpha_\nu$  are the direction cosines of the spin vectors for the  $\mu$  and  $\nu$  axes, respectively, and then  $\delta_{\mu\nu}$  has the value of 1 ( $\mu=\nu$ ) or 0 ( $\mu \neq \nu$ ).  $B(r_i)$  is the electron occupancy whose value is given from the result of the DV-X $\alpha$  electronic state calculation of the  $\text{CuBr}_4^{2-}$  anions. Here, the magnetic susceptibility indicates that the  $\text{Cu}^{2+}$  spins are oriented antiparallely to the spins of the nearest neighbors in the  $\text{Cu}^{2+}$  layer. However, we can not determine the spin ordered structure in terms of the interlayer interaction between the antiparallel and the parallel alignments. Now, we assume the antiferromagnetic spin arrangement for all the spin sites, taking into account the observed magnetic anisotropy result as mentioned in the magnetic susceptibility and AFMR. The calculation in the antiferromagnetic interlayer interaction gives  $\Phi_{aa} = -5.0 \times 10^{-3}$ ,  $\Phi_{bb} = -3.2 \times 10^{-3}$  and  $\Phi_{cc} = 8.4 \times 10^{-3} \text{ \AA}^{-3}$ , indicating that the easy, intermediate and hard spin axes are oriented parallel to the  $a^*$ ,  $b$  and  $c$ -axes, respectively, while, the experimental results of AFMR and magnetic

susceptibility reveal that the magnetic easy, intermediate and hard-axes lie on the  $b$ ,  $c$  and  $a^*$ -axes. The disagreement is explained by the additional contribution of the anisotropic exchange interaction and/or the extended feature of the  $d$ -electron wave function to BEDT-TTF molecules through the charge transfer interaction.

Finally, we discuss the feature of the antiferromagnetic ordered state below  $T_N$ . From the anisotropy of the magnetic susceptibility, the  $b$ ,  $c$  and  $a^*$ -axes are found to be the easy, intermediate and hard axes, respectively. According to the mean field theory, the perpendicular susceptibility at  $T=0$  is given by  $\chi_{\perp}^0 = Ng_{\text{Cu}}^2 \mu_B^2 / 4z_{\text{Cu}} J_{d-d}$ . Meanwhile, in the low-dimensional Heisenberg antiferromagnets, the quantum spin fluctuation causes the spin reduction which lowers the perpendicular susceptibility below  $T_N$  in comparison with that expected by the mean field theory. From the spin wave theory [101], the perpendicular susceptibility at  $T=0$  is given by

$$\chi_{\perp}(0) = \frac{\chi_{\perp}^0}{1 + 1/2\alpha} \left( 1 - \frac{\Delta S(\alpha)}{S} - \frac{e(\alpha)}{(2 + \alpha)z_{\text{Cu}}S} \right), \quad (3.50)$$

where  $\Delta S(\alpha)$  and  $z$  are the anisotropy dependent spin reduction and the number of nearest neighbors, respectively,  $\alpha = H_A/H_E$  ( $H_A$ :anisotropic field,  $H_E$ :exchange field), and  $e(\alpha)$  is the parameter defined for the Heisenberg exchange energy. Using the magnetic anisotropy value  $\alpha \sim 10^{-4}$ ,  $\Delta S = 0.192$  [102] and  $e(\alpha) \cong e(0) = 0.632$  [101] for the two-dimensional square lattice as a function of  $\alpha$ , we estimate the predicted value  $\chi_{\perp}(0) = 3.07 \times 10^{-3}$  (emu/mol). The observed value of the perpendicular susceptibility for the  $c$ -axis is extrapolated to  $\chi_{\perp}(0) = 4.8 \times 10^{-3}$  (emu/mol) at  $T=0$ K, which is 56% as large as the predicted susceptibility value. Generally, the enhancement in the dimensionality reduces the zero-point reduction [26]. Thus, the difference between the predicted and the observed value is thought to be caused by the presence of the interlayer interaction. However, the interlayer interaction is not realized through the usual superexchange path of  $\sigma$ -bands because the interlayer distance 17 Å of  $\text{Cu}^{2+}$  ions is significantly long. Consequently, the interlayer interaction between  $\text{Cu}^{2+}$  ions is realized by the superexchange of the  $\pi$ -orbitals on BEDT-TTF molecules. This is supported by that the magnetic heat capacity obeys the cubic temperature depen-

dence below 9K obtained by the relaxation method, which evidences the presence of the three-dimensional nature of the antiferromagnetically ordered state. In addition, the reduction value is discrepant to the result of  $^1\text{H}$ -NMR, where the magnitude of the spin values are estimated by the dipole sum calculation from the  $\text{Cu}^{2+}$  ion to the proton site. In the calculation, the delocalization feature of the Cu  $3d$ -electron in the  $\text{CuBr}_4^{2-}$  anion is not taken into account. Thus, the discrepancy is thought to be caused by the point dipole calculation only from the  $\text{Cu}^{2+}$  sites in the  $^1\text{H}$ -NMR analysis. In conclusion, the antiferromagnetic transition is importantly affected by the interlayer interaction between the  $\text{Cu}^{2+}$  layers. In conclusion, the antiferromagnetic ordering between  $\text{Cu}^{2+}$  ions are caused by the interlayer interaction through the  $\pi$ -orbitals on BEDT-TTF molecules.

### 3.5 Summary of (BEDT-TTF)<sub>3</sub>CuBr<sub>4</sub>

In order to clarify the  $\pi$ - $d$  interaction in organic cation radical salts, I have been investigated (BEDT-TTF)<sub>3</sub>CuBr<sub>4</sub> in detail. (BEDT-TTF)<sub>3</sub>CuBr<sub>4</sub> has alternate stacking of two-dimensional conducting sheets of BEDT-TTF donors and two-dimensional magnetic layers of CuBr<sub>4</sub><sup>2-</sup> where the donor sheet consists of two kinds of BEDT-TTF molecules, neutral molecule A and cation radical molecule B with the composition of A/B=1/2. It has the characteristic transitions at  $T_c$ =59 K and  $T_N$ =7.65 K at ambient pressure which are related to the changes in the structures, electronic and magnetic properties, and the remarkable pressure effects in the electronic and magnetic properties. To find out the relation among the crystal structure, electronic and the magnetic properties, I carried out the X-ray analysis at room temperature under ambient and high pressure, electrical resistivity, magnetic susceptibility, EPR, AFMR, heat capacity and DV-X $\alpha$  electronic structure calculation.

Above  $T_c$ , the magnetic susceptibility obeys the Curie-Weiss law with a significantly large antiferromagnetic Weiss temperature  $\theta$ =-100K, which represents the strong magnetic interaction between  $\pi$ -electrons of BEDT-TTF<sup>+</sup> B molecules and localized  $d$ -electron of Cu<sup>2+</sup> ions. Moreover, the single Lorentzian line shape of EPR also proves the existence of the strong  $\pi$ - $d$  interaction, where the interactions is evaluated at  $J_{\pi-d} \gg 0.01$  K. The number of spins estimated from the susceptibility are assigned to two BEDT-TTF B molecules and one Cu<sup>2+</sup> ion having the magnetic moment with  $S=1/2$ . The presence of the localized spins on the BEDT-TTF molecules is considered that the BEDT-TTF layer is described by a Mott insulator realized by the charge separation between BEDT-TTF A and B molecules.

The large discontinuous drop of the susceptibility at  $T_c$  is explained by the disappearance of the magnetic moments on the BEDT-TTF B molecules. Taking into account the dissolution of the charge disproportionation between A and B donor molecules obtained by the low temperature X-ray analysis below  $T_c$ , the disappear-

ance of the magnetic moments at sites B is caused by the transition from a Mott insulator to a band insulator with the first order nature.

The resistivity shows a remarkable decrease with applying the pressure, and the metallic phase is stabilized in the high temperature range of  $T_c$  above 7 kbar. Moreover, the magnetic susceptibility decreases with increasing the pressure in the high temperature Mott insulator phase in the vicinity of the insulator-to-metal boundary at high pressures. These features of the electronic and magnetic properties under pressure suggest that the insulator-to-metal transition at 7 kbar is the Mott metal-insulator transition.

In the low temperature region below  $T_c$ , the magnetic susceptibility is governed by only  $\text{Cu}^{2+}$  spins, and it is well described by the two-dimensional Heisenberg antiferromagnet with the large exchange energy  $J_{d-d} = -15.7$  K which is followed by the results of the critical broadening of EPR and  $^1\text{H}$ -NMR. From the electronic structure calculation of  $\text{CuBr}_4^{2-}$  anion using DV- $X\alpha$  method, the large exchange energy is explained by the widely extension of the localized  $d$ -electron to the Br ligands on the  $\text{CuBr}_4^{2-}$ . The susceptibility shows an antiferromagnetic transition between  $\text{Cu}^{2+}$  ions at  $T_N = 7.65$  K. In the ordered state, the susceptibility and antiferromagnetic resonance find that the magnetic easy, intermediate and hard-axes lie almost on the  $b$ ,  $c$  and  $a^*$ -axes, respectively. From the comparison between the experimental results and the dipole-dipole calculation, the magnetic anisotropy is generated by the dipole-dipole interaction additional to the anisotropic exchange interaction and/or the extended feature of the  $d$ -electron wave function to BEDT-TTF molecules. The presence of the magnetic long range order in the two-dimensional Heisenberg system indicates a important role of the interlayer interaction realized through the  $\pi$ -electrons of BEDT-TTF molecules having itinerant nature.

## **Chapter 4**

### **Solid State Properties of (C<sub>1</sub>TET-TTF)<sub>2</sub>Br**



## 4.1 Introduction

In organic charge transfer complexes composed of TTF derivatives, the  $\pi$ -electron systems form a large variety of electronic structures among superconducting state, charge density wave, spin density wave and Mott insulating state in low-dimensional frame through the competition among the transfer integral, on-site Coulomb interaction and electron-phonon interaction [18]–[21],[103]–[105]. In recent years, these complexes have been found to show interesting features in metallic state around the Mott boundary in relation to superconductivity [9]–[12].

On the contrary to this, the complexes belonging to the Mott insulator regime remain not so well understood, although they are expected to give a novel class of molecule-based low-dimensional magnets. We are interested in the Mott insulating state in the view of the magnetism of the organic charge transfer complexes, because the unpaired electrons delocalized over the molecular  $\pi$ -orbitals on the molecules in the Mott insulating state lead to novel features in their magnetic behavior [106]. Moreover, various types of low-dimensional structures will come to hand on the basis of the modification of the donor molecule arrangements as well as the designing of donor molecules, providing the diversity of magnetic behavior. Consequently, the detailed investigations of organic magnetic insulators will provide new aspects of the magnetism in view of the low-dimensional magnetic systems that have been studied in inorganic compounds through many experimental and theoretical approaches [26, 107]. In the past, several organic Mott insulators such as  $\alpha'$  and  $\beta'$ -(BEDT-TTF)<sub>2</sub>X (X=AuBr<sub>2</sub>, CuCl<sub>2</sub>, IBr<sub>2</sub>, ICl<sub>2</sub> [18]–[22],[103]) have been targeted as low-dimensional antiferromagnets, in all of which a localized magnetic moment with  $S=1/2$  is generated in a BEDT-TTF dimer unit associated with dimerized-donor based crystal structures. On the other hand, a class of organic magnetic insulator (C<sub>1</sub>TET-TTF)<sub>2</sub>Br (C<sub>1</sub>TET-TTF: bis(methylthio)ethylenedithio-tetrathiafulvalene) has a uniform donor arrangement with the absence of dimerized structure that most charge transfer complexes of BEDT-TTF have. Thus, the investigations of this

compound are expected to reveal new interesting features of the magnetic properties among organic magnetic insulators in contrast to ordinary BEDT-TTF salts. Moreover, it is possible to compare the C<sub>1</sub>TET-TTF salt with BEDT-TTF salts in detail in view of the crystal structure, electronic structure and physical properties because the molecular structure of C<sub>1</sub>TET-TTF is very close to that of BEDT-TTF. In the present chapter, we report the crystal structure, the band structure, the electrical resistivity, ESR and the magnetic susceptibility in order to clarify the correlation between the crystal structure and the magnetic properties.

## 4.2 Experimental

Single crystals of (C<sub>1</sub>TET-TTF)<sub>2</sub>Br were prepared by the electrochemical method from C<sub>1</sub>TET-TTF and ((C<sub>2</sub>H<sub>5</sub>)<sub>4</sub>N)<sub>2</sub>CuBr<sub>4</sub> in ethanol under Argon atmosphere at room temperature. In an electrochemical cell, ((C<sub>2</sub>H<sub>5</sub>)<sub>4</sub>N)<sub>2</sub>CuBr<sub>4</sub> was decomposed into Cu<sup>2+</sup> and Br<sup>-</sup>, so that the produced crystal did not contain even a trace of Cu<sup>2+</sup> ions, according to energy-dispersive X-ray (EDX) analysis. After the crystal growth period of two weeks, the black plate or block type single crystals are obtained with typical dimension of 3×1×0.05 mm<sup>3</sup> or 2×1×0.5 mm<sup>3</sup>, respectively. It was found that the crystals with different shapes have the same crystal structure from the X-ray analysis. The found composition is C=28.07, H=2.37 and S=60.25 % from elemental analysis, which is in good agreement with the calculated from the X-ray analysis for (C<sub>1</sub>TET-TTF)<sub>2</sub>Br (C<sub>20</sub>H<sub>20</sub>S<sub>16</sub>Br); C=28.15, H=2.36 and S=60.12 %.

In the X-ray crystal structure analysis, the intensity data were collected from Rigaku four-circle diffractometer AFC-7S with graphite-monochromated Mo *K*α radiation using ω-scan technique ( $2\theta < 55^\circ$ ), then the absorption was corrected. The structure was solved by the direct method (*SHELXS86*) [108] and refined using 3536 reflections by full-matrix least-squares method (*SHELXL93*) [109]. Anisotropic temperature factors were used for all non-hydrogen atoms, and for hydrogen atoms the calculated positions and isotropic temperature factors are adopted. The crystallographic data are listed in Table 4.1.

We calculated the molecular orbitals of the C<sub>1</sub>TET-TTF donor on the basis of the extended Hückel method [110]. The transfer integral  $t$  was estimated from the overlap integral  $s$  using the equation  $t=Es$ , where the  $E$  is the constant value of the order of HOMO energy  $-10$  eV [110]. The band structure was calculated by means of tight binding method. The HOMO level of the donor is considered to be 3/4-filled from the chemical formula.

The electrical resistivity to the  $c$ -axis was measured by four-probe method under ambient pressure in the temperature range 190-300 K. ESR measurements were carried out in the applied field parallel to the  $a^*$ ,  $b$  and  $c$ -axes in the temperature range 3-300 K, using a conventional X-band ESR spectrometer (JEOL JES-TE200) and a helium continuous flow type cryostat (Oxford ESR910) for temperature control. The magnetic field and the microwave frequency were calibrated by a gaussmeter (JEOL NMR field meter ES-FC5) and a frequency counter (Advantest microwave counter TR5212), respectively. A single crystal was mounted on a Teflon rod by silicone grease, and sealed in an ESR quartz tube with thermal exchange gas (He 10 Torr). The temperature dependence of the magnetic susceptibility was measured by a SQUID magnetometer (Quantum Design MPMS-5) in the applied field  $H=10$  kOe parallel to the  $a^*$ ,  $b$  and  $c$ -axes in the temperature range 1.8-400 K. The single crystals, where the crystal axis were collimated, were mounted on a plastic straw with silicone grease. The spin susceptibility was estimated by subtracting the Pascal diamagnetic contribution  $\chi_{\text{dia}}=-4.49\times10^{-4}$  emu/mol (1mol=(C<sub>1</sub>TET-TTF)<sub>2</sub>Br)) from the total susceptibility. In the calculation of the core diamagnetic susceptibility, the contribution of C<sub>1</sub>TET-TTF donor is obtained from the observed value  $\chi=-2.09\times10^{-4}$  emu/mol of neutral C<sub>1</sub>TET-TTF donor at room temperature.

Table 4.1: Crystallographic data of (C<sub>1</sub>TET-TTF)<sub>2</sub>Br.

Chemical Formula	C <sub>20</sub> H <sub>20</sub> S <sub>16</sub> Br
Chemical Formula Weight	853.23
Cell setting	Monoclinic
Space group	<i>P</i> 2 <sub>1</sub> / <i>a</i>
<i>a</i> (Å)	27.71(5)
<i>b</i> (Å)	11.11(2)
<i>c</i> (Å)	5.037(8)
$\beta$ (°)	90.6(1)
<i>V</i> (Å <sup>3</sup> )	1551(4)
<i>Z</i>	2
<i>D<sub>c</sub></i> (Mg·m <sup>-3</sup> )	1.827
Radiation type	Mo <i>K</i> α
Wavelength(Å)	0.71073
Temperature(K)	293
Crystal size (mm <sup>3</sup> )	0.50×0.37×0.33
No. of independent reflections	3537
No. of observed reflections	2394( <i>I</i> > 2σ( <i>I</i> ))
<i>R</i> [ <i>F</i> <sup>2</sup> > 2σ( <i>F</i> <sup>2</sup> )]	0.0685
<i>wR</i> ( <i>F</i> <sup>2</sup> )	0.1988
Weighting scheme	$w = 1/[\sigma^2(F_o^2) + (0.1452P)^2 + 1.7684P]$ , where $P = (F_o^2 + 2F_c^2)/3$

## 4.3 Experimental Results

At the beginning, we present the crystal structure of  $(C_1TET-TTF)_2Br$ .

Table 4.2, Table 4.3 and Table 4.4 summarize the atomic coordinates and the displacement parameters, the anisotropic temperature factors, and the intramolecular distances and bond angles. The molecular structure and the atom indices are shown in Fig. 4.1. Also, the crystal structure is shown in Fig. 4.2. There is one independent donor molecule in a unit cell, while a Br atom is at the position of inversion center. Since all donor molecules are crystallographically equivalent, they are expected to have the same partial charge +0.5 taking into account the donor-to-anion ratio of 2:1. There is the absence of disordered sites of ethylene groups and methylthio groups attached to the TTF moieties, although the thermal motions of methylthio groups are a little large. The intermolecular short S...S contacts within the  $C_1TET-TTF$  layer are shown in Fig. 4.3. The shortest intermolecular S...S contacts are 3.574(6)Å (S3-S8) in the intrastack direction (c-axis) and 3.586(7)Å (S6-S7) in the interstack direction (b-axis), respectively, which are slightly smaller than the sums of the corresponding to the van der Waals radii 3.60Å. As a consequence,  $C_1TET-TTF$  donors form a loosely two-dimensional lattice in the *bc*-plane, where the donor arrangement has zigzag feature with a head-to-tail configuration in the interstack direction. Every  $C_1TET-TTF$  molecule is surrounded by six neighboring donor molecules as shown in Fig. 4.4, resulting in the formation of two-dimensional hexagonal packing structure with the absence of dimerization similar to the  $\theta$ -(BEDT-TTF) $_2X$  salt ( $X=I_3$ ,  $Cu_2(CN)[N(CN)_2]_2$ ) [105, 111]. In view of the symmetry of the structure, the donor molecules of the  $\theta$ -BEDT-TTF salts are known to be located at centrosymmetric sites, in contrast to the present salt. In the present compound, the dihedral angle is estimated at 57.6(2)° between the molecular planes of adjacent donors interrelated by the screw axis symmetry. We note that the asymmetric donor molecules are oriented in the same direction within a column, which is not so common among ordinary asymmetric TTF derivative salts where

donor molecules used to have a head-to-tail configuration in the column except the cases of the present salt and some other salts [112]–[114].

The overlap integrals of the donor HOMO are calculated on the basis of the two-dimensional donor arrangement given in Fig. 4.4, which shows the coexistence of intrastack( $c$ ) and interstack( $b_1$ ,  $b_2$ ) interactions. The estimation provides  $b_1=5.4$ ,  $b_2=4.3$  and  $c=5.8\times 10^{-3}$ , that reveals a two-dimensional character in the energy band caused by small differences in the strengths of the transfer integrals in all the in-plane directions. The magnitude of the overlap integrals are a little small in comparison to usual BEDT-TTF salts with two-dimensional layer, accompanied by the absence of strong S...S contacts. These feature of weak and isotropic overlaps is also observed in  $\theta$ -(BEDT-TTF) $_2$ X salt (X=I $_3$ , Cu $_2$ (CN)[N(CN) $_2$ ] $_2$ ) [105, 111], which is considered as the characteristic of the  $\theta$  or  $\theta$ -like molecular packing structure. Figure 4.5 shows the band structure and the Fermi surfaces calculated by the tight binding method. The band calculation suggests the presence of two-dimensional metallic bands that generate two sets of quasi-one-dimensional Fermi surfaces, though these band widths are narrow ranging about 0.4 eV due to the small overlap integrals. Since the degeneracy in the M-Y dispersion is caused by the crystallographic symmetry, the 3/4-filled nature is intrinsic. On the other side, the first Brillouin zone has the half-filled feature taking into account the Harrison's simplest band construction in the presence of two molecules per unit cell.

Figure 4.6 shows the electrical resistivity, which behaves semiconductive with a single activation energy  $E_a=0.6$  eV in the investigated temperature range 190-300K and indicates the room temperature resistivity value of  $\rho_{rt}=40$   $\Omega$ cm. This observation is in disagreement with the band calculation which suggests metallic nature. This discrepancy will be discussed later. The ESR signal shows the line shape of single Lorentzian type whose  $g$ -values and peak-to-peak line widths are  $g_{a^*}=2.0113$ ,  $g_b=2.0061$ ,  $g_c=2.0055$  and  $\Delta H_{a^*}=15.6$ ,  $\Delta H_b=14.6$ ,  $\Delta H_c=17.6$  G at room temperature in the applied field parallel to the  $a^*$ ,  $b$  and  $c$ -axes, respectively. Taking into account that these  $g$ -values resemble those of BEDT-TTF donors [62] having similar

electronic structure, the unpaired  $\pi$ -electrons observed in the ESR measurements are considered to reside on the  $C_1$ TET-TTF molecules. The temperature dependence of the line width and the  $g$ -value are shown in Fig. 4.7. The line widths show a weak increase below about 100 K with decreasing the temperature and tend to saturate below about 20 K, which suggests the presence of the magnetic short range order effect. They exhibit a broaden-out abruptly below 5 K, indicating the onset of antiferromagnetic ordering in the low-dimensional antiferromagnet. The  $g$ -values show temperature independent behavior above 20 K, and a slight decrease with lowering the temperature below 20 K that is generated by the short range order effect [115], and then finally they increase suddenly with the concomitance of the broaden-out in the line width below 5 K.

Figure 4.8 shows the magnetic susceptibility and the reciprocal susceptibility as a function of temperature in the applied field parallel to the  $c$ -axis. The susceptibility shows the Curie-Weiss behavior in the high temperature range, and then it shows a broad hump of low-dimensional antiferromagnetic short range order around 12 K, that is considered to be related to the weak increase in the line width observed in the same temperature range. In the temperature range 30-290 K, the susceptibility data in the field parallel to the  $a^*$ ,  $b$  and  $c$ -axes are well represented by the sum of a Curie-Weiss term and a temperature independent one after the correction of Pascal diamagnetic contribution;

$$\chi = \frac{C}{T - \theta} + \chi_0.$$

Using this equation, the analysis of the  $c$ -axis data gives the Curie constant  $C=0.454 \pm 0.002$  emu·K/mol, the antiferromagnetic Weiss temperature  $\theta=-17.3 \pm 0.7$  K and the temperature independent diamagnetic susceptibility  $\chi_0=-1.1 \pm 0.1 \times 10^{-4}$  emu/mol, where 1 mol involves one formula unit  $(C_1\text{TET-TTF})_2\text{Br}$ . These values for the  $c$ -axis are in good agreement with those for the  $a^*$  and  $b$ -axes. From the Curie constant, the spin density ( $S=1/2$ ) is estimated at  $N=1.2$  spin/mol using the ESR  $g$ -value; namely, there exists one localized magnetic moment of  $S=1/2$  in two donors. It is noticeable that the susceptibility contains the temperature independent term  $\chi_0$ ,

even after the correction of Pascal diamagnetic contribution  $\chi_{\text{dia}}$ . The magnitude of the  $\chi_0$  amount about 25% of the  $\chi_{\text{dia}}$ . The origin of the  $\chi_0$  is possibly due to the  $\pi$ -electron ring current in the donor molecule. The correction is expected to be affected by the valence state of the donor, namely, I have used the observed core diamagnetic susceptibility of the neutral donor for the evaluation in the charge transfer complex by neglecting the partial valence feature (+0.5) in the actual case. However, the temperature independent term is not solely explained by the correction of the core susceptibility because the enhancement in the core diamagnetism of BEDT-TTF complexes having similar extended  $\pi$ -electronic structure to  $\text{C}_1\text{TET-TTF}$  is only 4% from the corresponding neutral donor [80]. Therefore, the origin of the temperature independent term remains unsolved for  $(\text{C}_1\text{TET-TTF})_2\text{Br}$ .

Figure 4.9 represents the detailed susceptibility behavior in the temperature region below 30 K in the applied field parallel to the  $a^*$ ,  $b$  and  $c$ -axes. The susceptibilities have an antiferromagnetic short range order hump around 12 K. The difference of the susceptibility between the  $a^*$ -axis and the  $b$ ,  $c$ -axes is explained by the difference in the  $g$ -values. Below  $T=3$  K, the susceptibility shows an abrupt increase for the  $a^*$ ,  $b$  and  $c$ -axes. The behavior of the susceptibility and the ESR line width broadening in the low temperature range suggest the appearance of an antiferromagnetic order at  $T_N=3$  K. It is worth noting the absence of magnetic anisotropy below  $T_N$  among the susceptibilities in the field applied parallel to the three independent crystallographic axes. Although a possible explanation for this is the deviation of the easy spin axis from these crystallographic axes, the origin remains unspecified. Figure 4.10 shows the magnetization curves in the field parallel to the  $b$  and  $c$ -axes at 2 K up to 5 T, which indicates a slightly concave with the absence of an apparent spin-flop transition. The behavior of the magnetization appears in the field parallel to  $a^*$ -axis is similar to that with the field parallel to the  $b$  and  $c$ -axis. The concave feature indicates that the large spin reduction in the  $S=1/2$  Heisenberg antiferromagnet with quantum spin fluctuation is suppressed by the external field in the ordered state [116, 117].



Table 4.2: Fractional atomic coordinates and equivalent isotropic displacement parameters of (C<sub>1</sub>TET-TTF)<sub>2</sub>Br (see Fig. 4.1 for the atom indices). Displacement parameter  $U_{eq}$  is defined on the basis of the following equation  $U_{eq}=(1/3)\sum_i\sum_jU_{ij}a_i^*a_j^*\mathbf{a}_i\mathbf{a}_j$ . Displacement parameters for H atoms are fixed on the value of the bonding carbon atoms.

Atom	x	y	z	$U_{eq}/\text{\AA}^2$
Br	0.0000	0.0000	0.0000	0.053
C1	0.2260(2)	0.5777(5)	0.1487(11)	0.031(1)
C2	0.1856(2)	0.5759(6)	-0.0123(12)	0.034(1)
C3	0.2918(2)	0.5219(6)	0.4924(12)	0.034(1)
C4	0.3046(2)	0.6300(5)	0.3982(12)	0.034(1)
C5	0.1066(2)	0.5133(6)	-0.2488(12)	0.036(1)
C6	0.1191(2)	0.6174(6)	-0.3662(11)	0.036(1)
C7	0.3748(3)	0.5185(7)	0.8101(13)	0.045(2)
C8	0.3954(2)	0.5902(7)	0.5858(13)	0.044(2)
C9	0.0458(3)	0.3352(9)	-0.0630(17)	0.071(3)
C10	0.0497(3)	0.7886(7)	-0.4296(16)	0.059(2)
S1	0.23882(6)	0.4585(1)	0.3636(3)	0.037
S2	0.26803(6)	0.6927(2)	0.1493(3)	0.041
S3	0.14457(6)	0.4577(2)	-0.0005(3)	0.040
S4	0.17267(6)	0.6860(2)	-0.2488(3)	0.039
S5	0.32184(7)	0.4315(2)	0.7263(4)	0.050
S6	0.35674(6)	0.7127(2)	0.4796(4)	0.047
S7	0.05374(7)	0.4358(2)	-0.3362(4)	0.052
S8	0.08615(6)	0.6865(2)	-0.6222(3)	0.043
H7A	0.3667(3)	0.5733(7)	0.9529(13)	0.054
H7B	0.3995(3)	0.4642(7)	0.8768(13)	0.054
H8A	0.4009(2)	0.5371(7)	0.4363(13)	0.053
H8B	0.4264(2)	0.6227(7)	0.6411(13)	0.053
H9A	0.0173(3)	0.2878(9)	-0.0921(17)	0.106
H9B	0.0425(3)	0.3807(9)	0.0978(17)	0.106
H9C	0.0733(3)	0.2832(9)	-0.0480(17)	0.106
H10A	0.0291(3)	0.8340(7)	-0.5465(16)	0.088
H10B	0.0703(3)	0.8425(7)	-0.3320(16)	0.088
H10C	0.0303(3)	0.7434(7)	-0.3080(16)	0.088

Table 4.3: Anisotropic temperature factors ( $\text{\AA}^2$ ).

atom	$U_{11}$	$U_{22}$	$U_{33}$	$U_{12}$	$U_{13}$	$U_{23}$
Br	0.0459(6)	0.0508(6)	0.0608(7)	0.0070(4)	-0.0065(5)	-0.0135(5)
C1	0.034(3)	0.031(3)	0.029(3)	0.004(2)	-0.001(2)	0.002(2)
C2	0.036(3)	0.033(3)	0.033(3)	0.006(2)	0.002(2)	0.000(2)
C3	0.038(3)	0.034(3)	0.030(3)	0.003(3)	-0.001(2)	-0.002(2)
C4	0.034(3)	0.028(3)	0.039(3)	0.003(2)	-0.001(2)	-0.001(2)
C5	0.037(3)	0.036(3)	0.034(3)	0.006(3)	-0.004(2)	-0.002(2)
C6	0.041(3)	0.038(3)	0.028(3)	0.009(3)	-0.003(2)	0.002(2)
C7	0.043(4)	0.057(4)	0.034(3)	0.001(3)	-0.010(3)	-0.001(3)
C8	0.035(3)	0.059(4)	0.039(3)	-0.001(3)	-0.007(3)	-0.005(3)
C9	0.069(5)	0.081(6)	0.062(5)	-0.037(5)	0.012(4)	0.006(5)
C10	0.071(5)	0.046(4)	0.059(5)	0.024(4)	0.007(4)	0.002(3)
S1	0.0400(8)	0.0305(7)	0.0415(8)	-0.0035(6)	-0.0062(7)	0.0052(6)
S2	0.0398(9)	0.0369(8)	0.0471(9)	-0.0022(7)	-0.0036(7)	0.0120(7)
S3	0.0433(9)	0.0336(8)	0.0431(9)	-0.0026(6)	-0.0076(7)	0.0061(6)
S4	0.0418(9)	0.0388(8)	0.0360(8)	-0.0003(7)	-0.0019(6)	0.0066(6)
S5	0.0554(11)	0.0388(9)	0.0542(10)	-0.0036(8)	-0.0175(8)	0.0133(8)
S6	0.0421(9)	0.0347(9)	0.0638(11)	-0.0054(7)	-0.0071(8)	0.0013(7)
S7	0.0492(10)	0.0503(11)	0.0550(11)	-0.0068(8)	-0.0133(8)	0.0016(8)
S8	0.0497(10)	0.0477(9)	0.0328(8)	0.0111(8)	-0.0025(7)	0.0026(7)

Table 4.4: Bond lengths and angles of C<sub>1</sub>TET-TTF (see Fig. 4.1 for the atom indices).

Bond length (Å)			
C1-C2	1.377(9)	C5-C6	1.346(9)
C1-S2	1.728(7)	C5-S3	1.740(7)
C1-S1	1.745(6)	C5-S7	1.751(7)
C2-S3	1.737(7)	C6-S8	1.750(7)
C2-S4	1.742(7)	C6-S4	1.765(7)
C3-C4	1.340(9)	C7-C8	1.501(10)
C3-S1	1.748(7)	C7-S5	1.804(8)
C3-S5	1.752(7)	C8-S6	1.810(8)
C4-S2	1.748(7)	C9-S7	1.788(9)
C4-S6	1.758(7)	C10-S8	1.808(8)
Bond angle (°)			
C2-C1-S2	123.8(5)	S3-C5-S7	120.3(4)
C2-C1-S1	120.9(5)	C5-C6-S8	124.4(5)
S2-C1-S1	115.3(4)	C5-C6-S4	116.4(5)
C1-C2-S3	121.3(5)	S8-C6-S4	119.2(4)
C1-C2-S4	123.5(5)	C8-C7-S5	115.1(5)
S3-C2-S4	115.1(4)	C7-C8-S6	113.1(5)
C4-C3-S1	117.0(5)	C1-S1-C3	95.1(3)
C4-C3-S5	128.8(5)	C1-S2-C4	95.3(3)
S1-C3-S5	114.2(4)	C2-S3-C5	95.7(3)
C3-C4-S2	117.2(5)	C2-S4-C6	95.3(3)
C3-C4-S6	127.2(5)	C3-S5-C7	103.3(3)
S2-C4-S6	115.4(4)	C4-S6-C8	99.2(3)
C6-C5-S3	117.6(5)	C5-S7-C9	102.9(4)
C6-C5-S7	122.1(5)	C6-S8-C10	99.8(4)

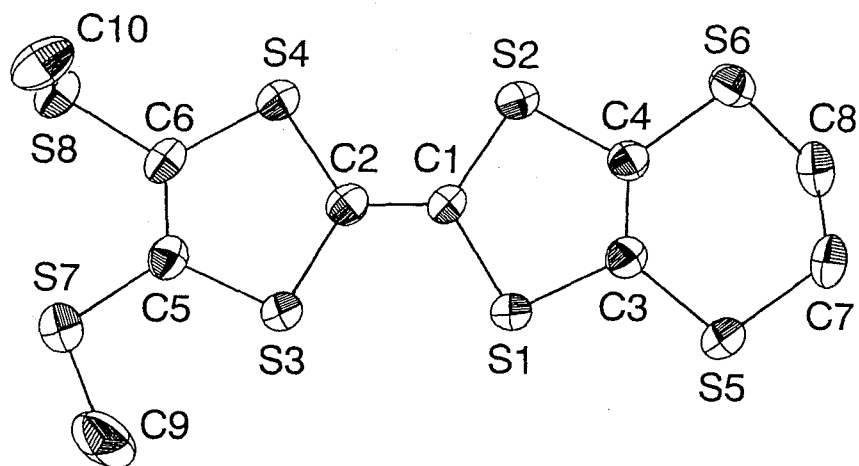


Figure 4.1: Molecular structure of  $C_1$ TET-TTF drawn by ORTEP [48, 71].

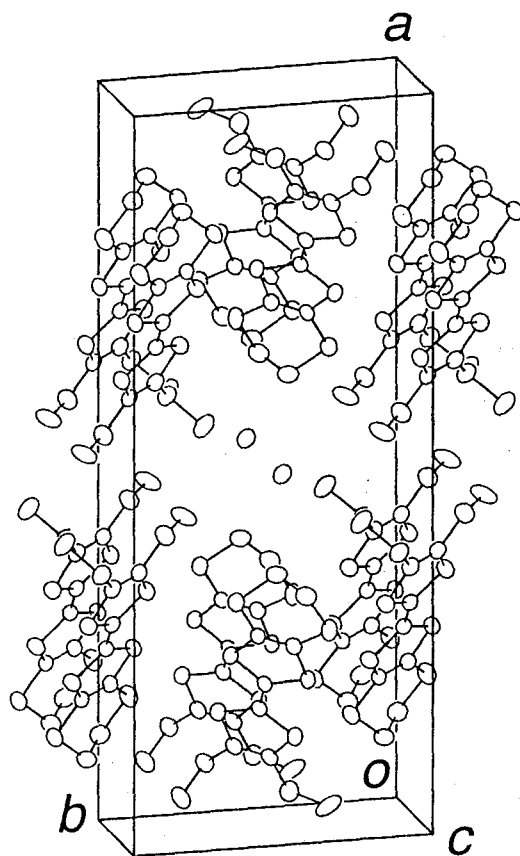


Figure 4.2: Crystal structure of  $(C_1\text{TET-TTF})_2\text{Br}$ , where the donor molecule have the alternating stacking along the  $a$ -axis [48].

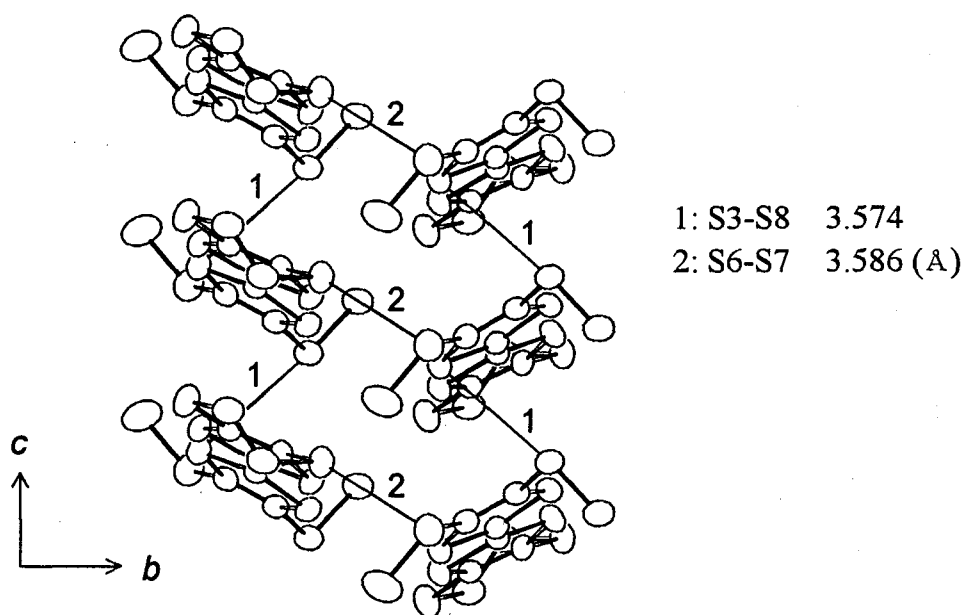


Figure 4.3: Intermolecular S...S distance of  $(C_1TET-TTF)_2Br$  within the corresponding to the van der Waals radii.

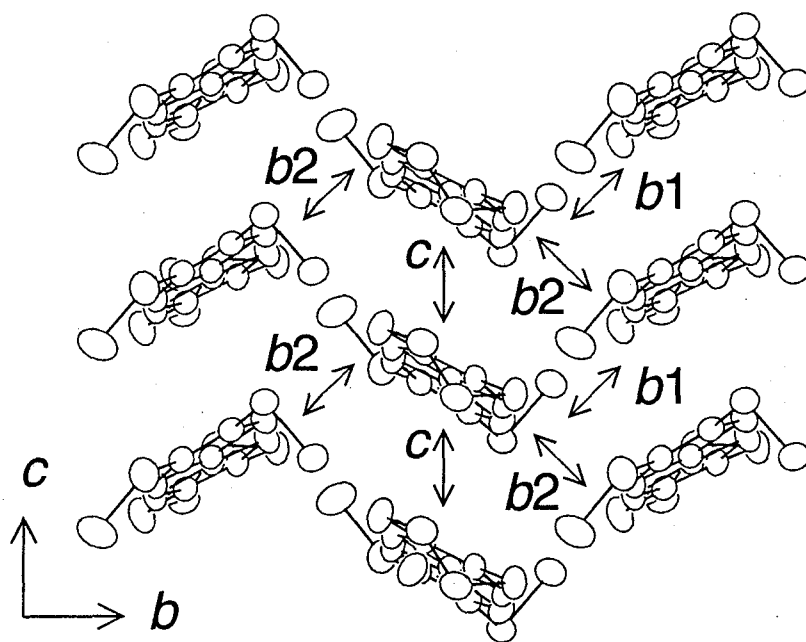


Figure 4.4: The arrangement of  $C_1TET-TTF$  donors projected on the  $bc$ -plane. The calculated overlap integrals are  $b_1=5.4$ ,  $b_2=4.3$  and  $c=5.8 \times 10^{-3}$  [48].

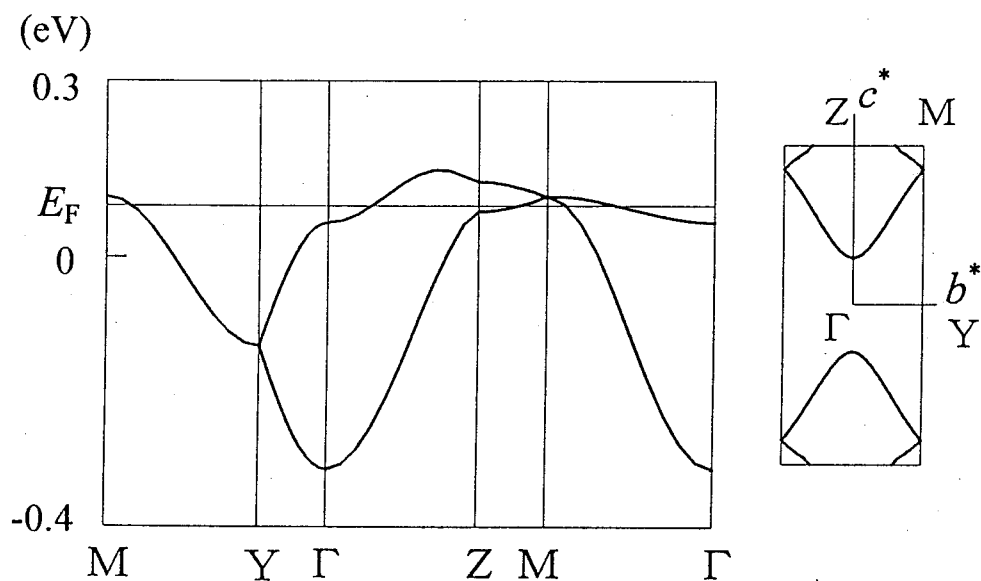


Figure 4.5: Band structure and Fermi surfaces of  $(C_1TET-TTF)_2Br$ . The energy scale is given on the basis of the donor HOMO energy ( $-10$  eV) [48].

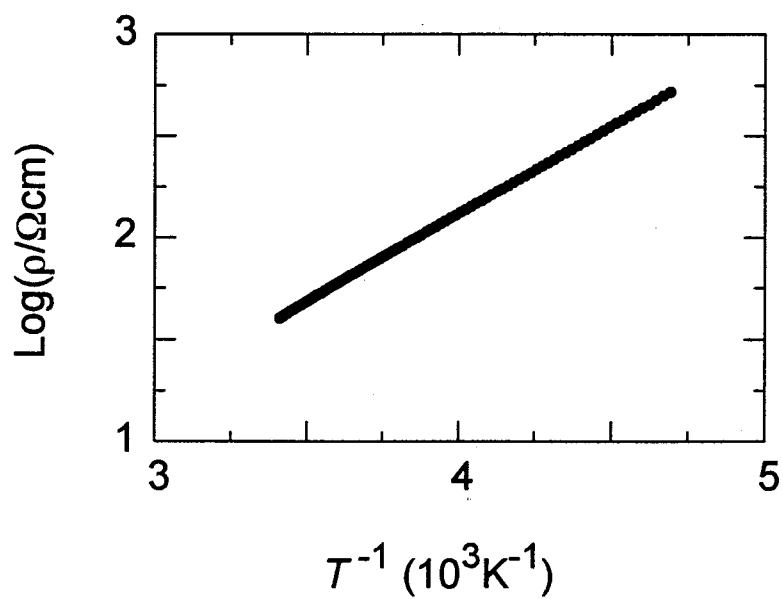


Figure 4.6: Temperature dependence of the electrical resistivity, which is the semi-conductive behavior with a single activation energy of  $E_a=0.6$  eV.

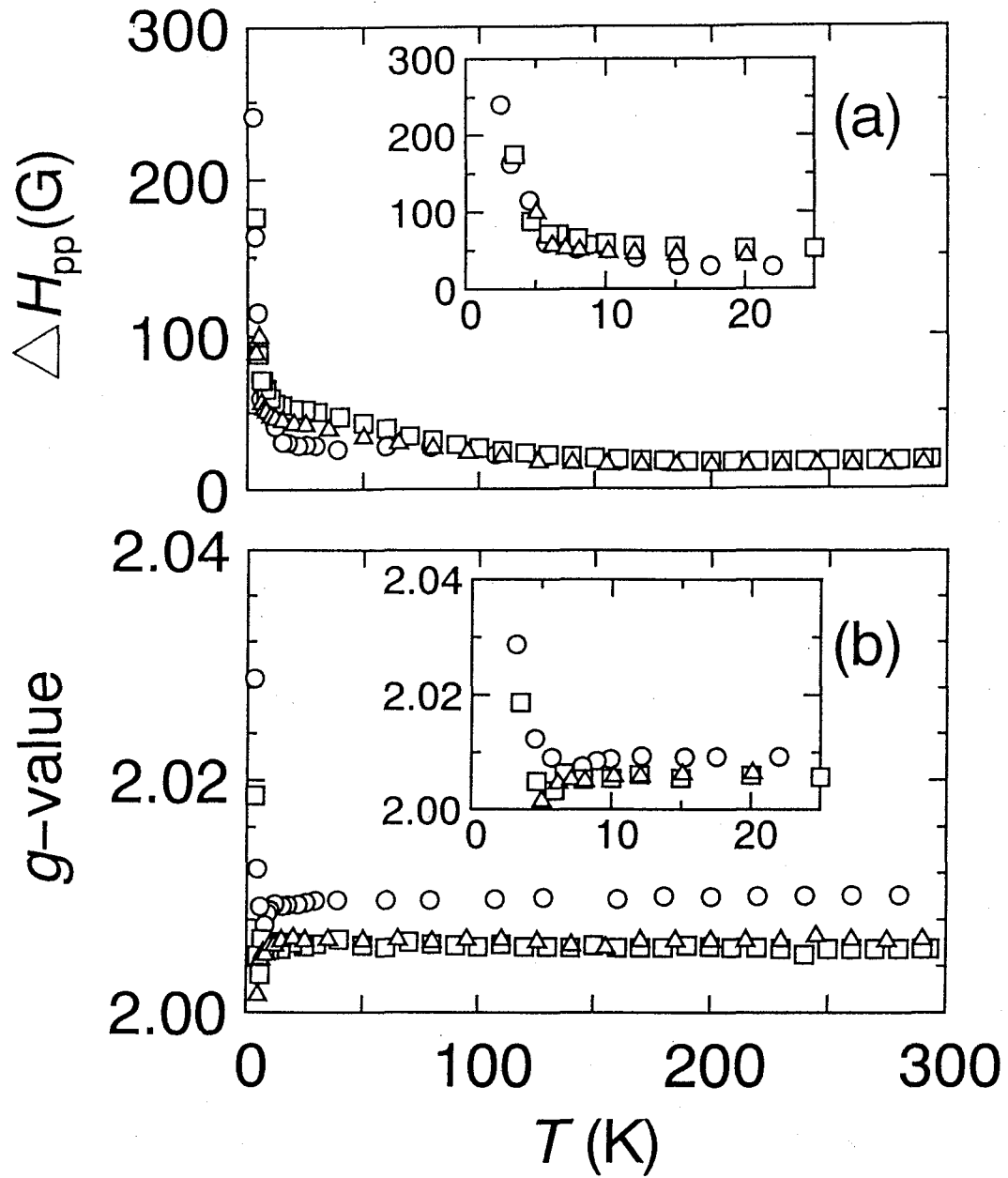


Figure 4.7: Temperature dependence of ESR line widths (a) and  $g$ -values (b) in the applied field parallel to the  $a^*$ ( $\circ$ ),  $b$ ( $\Delta$ ) and  $c$ ( $\square$ )-axes. The insets show the detailed behavior in the low temperature range, suggesting the presence of an anti-ferromagnetic ordering at  $T_N=3$  K [48].

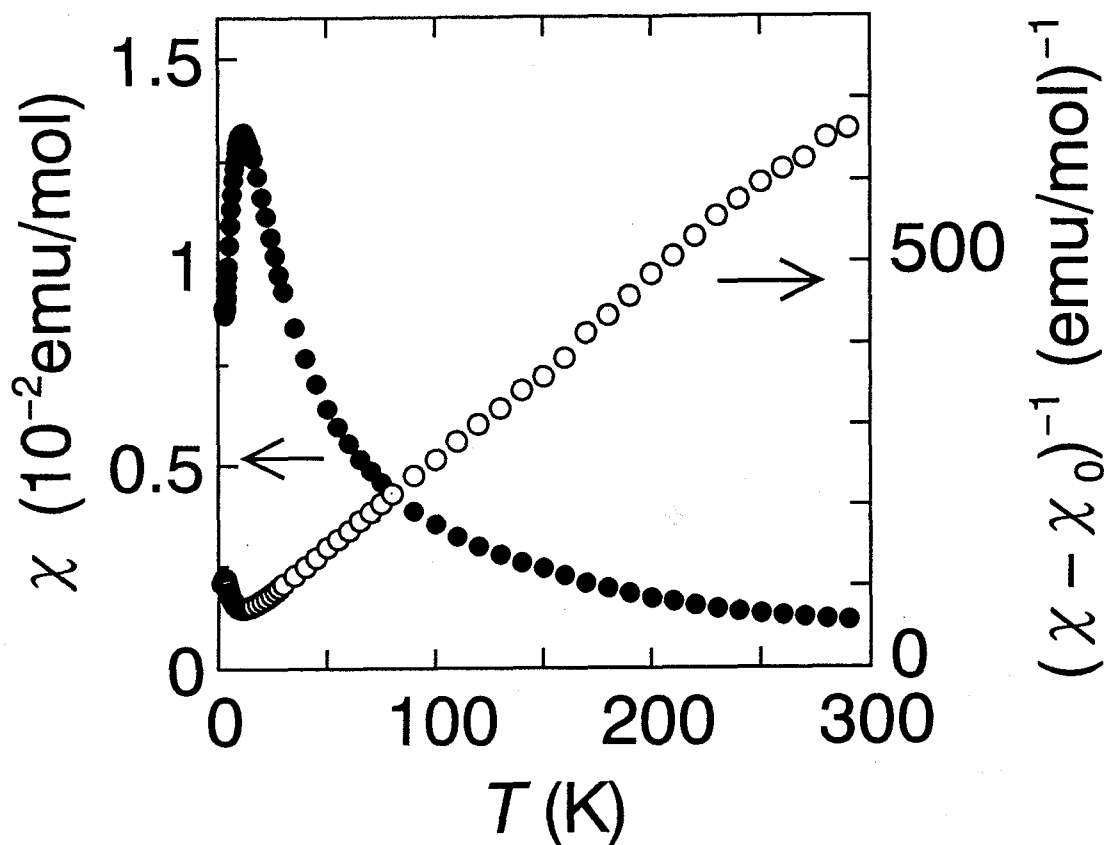


Figure 4.8: Temperature dependence of magnetic susceptibility and reciprocal susceptibility in the field of  $H=10$  kOe applied parallel to the  $c$ -axis.  $\chi_0=-1.1\times 10^{-4}$  emu/mol denotes the temperature independent term in the susceptibility. The mole unit corresponds to the formula unit of  $(C_1TET-TTF)_2Br$ . The best fitting with a single Curie-Weiss contribution gives the spin density  $N=1.2$  spin/mol and the Weiss temperature  $\theta=-17.3$  K [48].



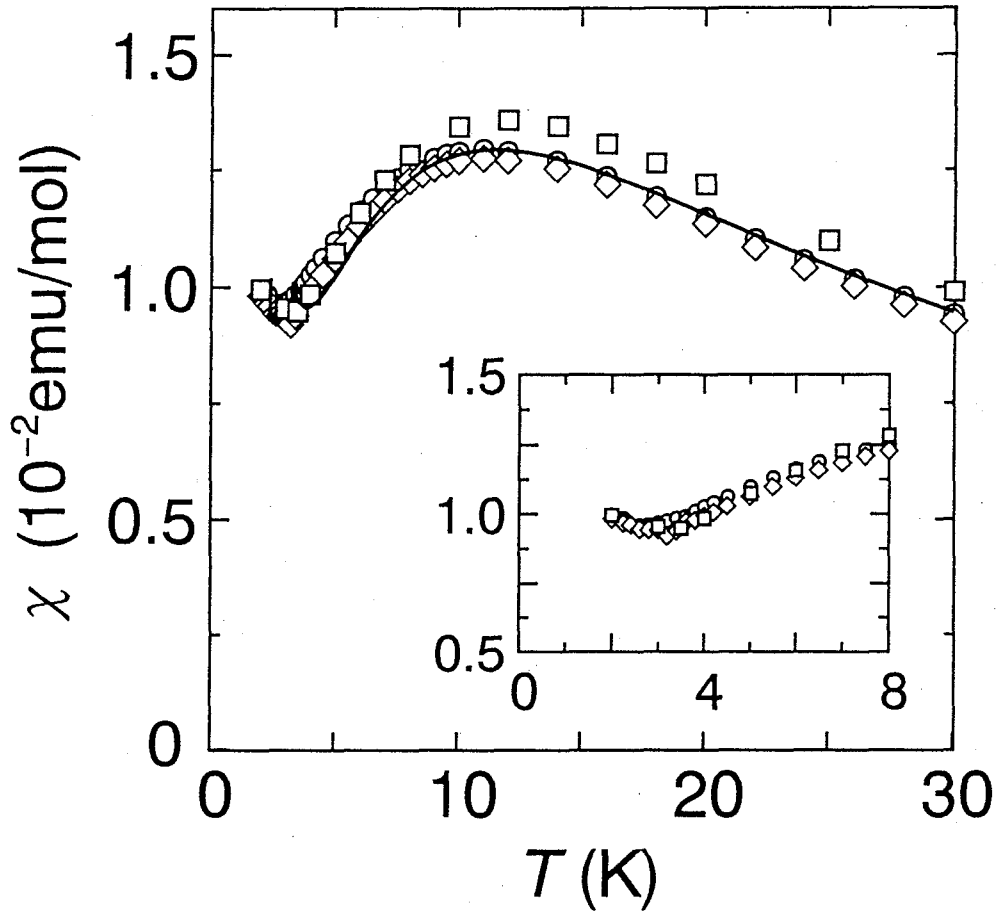


Figure 4.9: Temperature dependence of magnetic susceptibility at low temperatures below 30 K in the applied field of  $H=10$  kOe parallel to the  $a^*$ ( $\square$ ),  $b$ ( $\diamond$ ) and  $c$ ( $\circ$ )-axes. The solid line denotes the theoretical fitting for the two-dimensional square lattice Heisenberg antiferromagnet model [88] in the temperature range 8-290 K, where 0.5 spin with  $S=1/2$  is allotted to one  $C_1$ TET-TTF donor according to the charge distribution. The exchange interaction is estimated at  $J=-6.1$  K. An antiferromagnetic transition is observed at  $T_N=3$  K. The inset shows the detailed behavior around the antiferromagnetic transition [48].

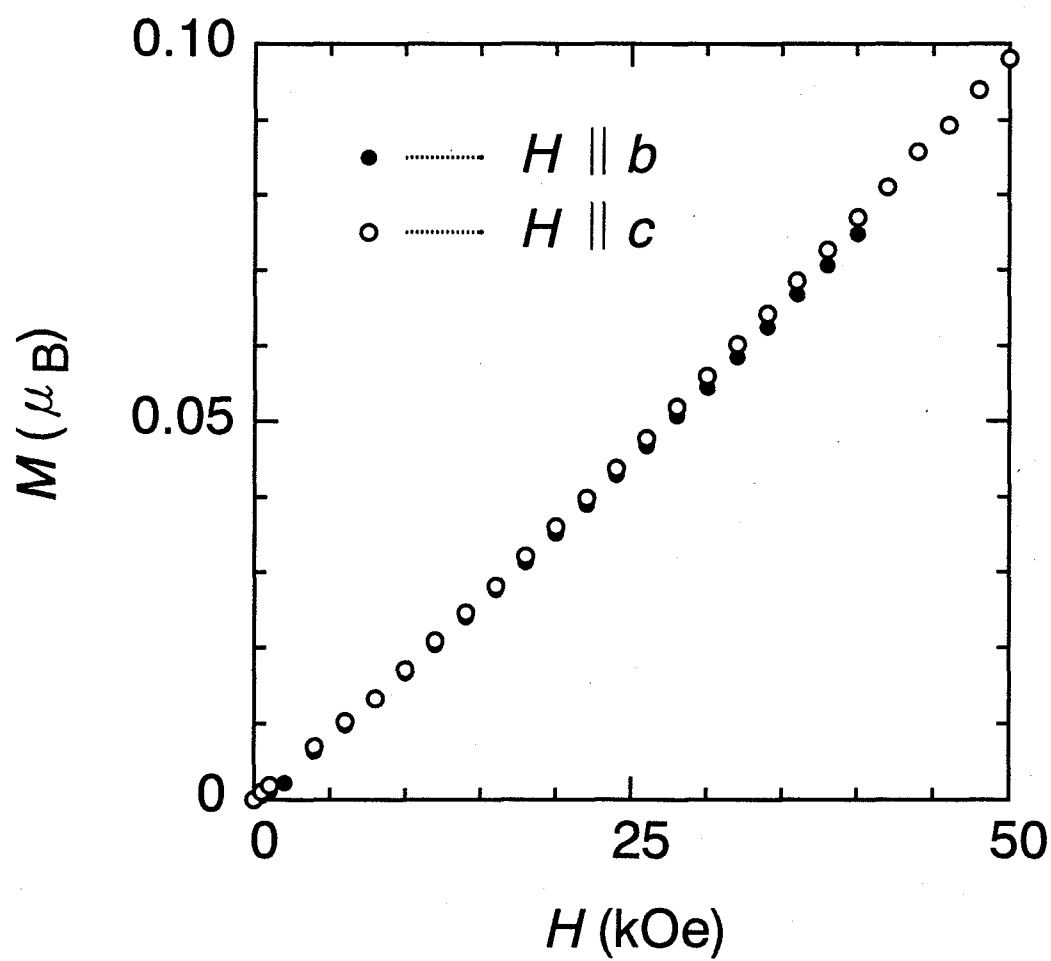


Figure 4.10: Magnetization curves in applied field parallel to the  $b$  and  $c$ -axes at 2 K up to 5 T, which show a slightly concave without an apparent spin-flop transition.

## 4.4 Discussion

The semiconductive nature with large activation energy and the presence of localized magnetic moments on C<sub>1</sub>TET-TTF donors evidence features of Mott insulator generated by the competition between the on-site Coulomb interaction and the transfer integral. Comparison to the reported BEDT-TTF-based Mott insulators [18]–[22],[103] provides a good suggestion on the electronic structure of the present compound. For instance,  $\alpha'$  and  $\beta'$ -ET<sub>2</sub>X type Mott insulators have intrinsic half-filled bands, which are realized by the band splitting due to the strong dimerization of donor molecules. In these compounds, the competition between the interdimer transfer integral and the effective on-site Coulomb interaction  $U_{\text{eff}}$ , the latter of which is given by the intradimer transfer integral, generates the Mott insulating state, where the magnetic moment is well localized around the region confined in the dimerized unit of BEDT-TTF molecules. The effective on-site Coulomb interaction  $U_{\text{eff}}$  defined as the on-site Coulomb energy in a dimer unit is given by

$$U_{\text{eff}} = \frac{U - \sqrt{U^2 + 4t_{\text{intra}}^2}}{2} + 2|t_{\text{intra}}| \sim 2|t_{\text{intra}}|, \text{ (for } U \gg |t_{\text{intra}}|), \quad (4.1)$$

where  $U$  is the on-site Coulomb energy of the individual donor and  $t_{\text{intra}}$  is the intradimer transfer integral. On the contrary, the present compound has the 3/4-filled band structure due to the uniform donor stacking, indicating that this compound is not likely to the ordinary Mott insulator, although the band structure of this compound has the half-filled nature in the first Brillouin zone as shown in Fig. 4.5. In this sense, the picture of the donor-dimer-based Mott insulating state is failed here, suggesting that the region, where a localized moment exists, is extended widely in a unit cell. Consequently, the features of the electron localization are considered to be situated far from those of Mott insulator state realized in the ordinary BEDT-TTF complexes and are just around the Mott boundary in this compound. Moreover, it is possible that this less localized nature affects the magnetic behavior in (C<sub>1</sub>TET-TTF)<sub>2</sub>Br.

Now, we discuss the magnetic structure and the exchange interaction mechanism in details. Taking into account that all donor molecules are crystallographically equivalent, all the donor molecules are equally charged due to the charge transfer to anions. Here, it is likely to assume that 0.5 spin with  $S=1/2$  exists on a donor molecule within the consideration of the X-ray average structure, although the underlying physics behind it remains to be clarified in the future. The antiferromagnetic exchange interaction  $J \propto -t^2/U$  between the donor molecules is described in terms of the transfer integral  $t$  and the on-site Coulomb interaction  $U$ . Thus, the above consideration leads to the estimation of the exchange interactions  $J_1 \propto -t_{b1}^2/U \sim -t_c^2/U$  and  $J_2 \propto -t_{b2}^2/U$  for magnetic neighbors in the different three directions in the  $bc$ -plane, where the ratio of the exchange interactions is given to be  $J_2/J_1 \sim 0.5$  from the extended Hückel electronic structure calculation discussed before. From the information on the structure and the band calculation, as shown in Fig. 4.11, the predominant exchange interactions  $J_1$  form a distorted square magnetic lattice, while  $J_2$  causes the frustration in the spin arrangement. Therefore, the exchange interaction network is described in terms of a triangular lattice with two kinds of antiferromagnetic exchange interactions  $J_1$  and  $J_2$ , where the magnetic moments in the distorted square lattice formed by the stronger interactions  $J_1$  are coupled to each other through the weaker interactions  $J_2$ .

In the case of  $J_1=J_2$ , the magnetic system is described as a two-dimensional regular triangular lattice antiferromagnet, which provides interesting models for classical and quantum spins [118, 119]. Namely, in the two-dimensional regular "triangular" lattice, the next nearest neighbor of a magnetic site is the nearest neighbor of the magnetic site, where the antiferromagnetic interaction causes a novel spin arrangement with frustration feature. Meanwhile, in the present case having  $J_1 > J_2$ , the magnetic lattice is expected to be the distorted triangular one. It is possible to compare this compound with  $\text{CuCl}_2$ -graphite intercalation compounds (GIC), where  $\text{Cu}^{2+}$  magnetic moments form an  $S=1/2$  two-dimensional distorted triangular lattice Heisenberg antiferromagnet [120]. The susceptibility of  $\text{CuCl}_2$ -GIC has a magnetic

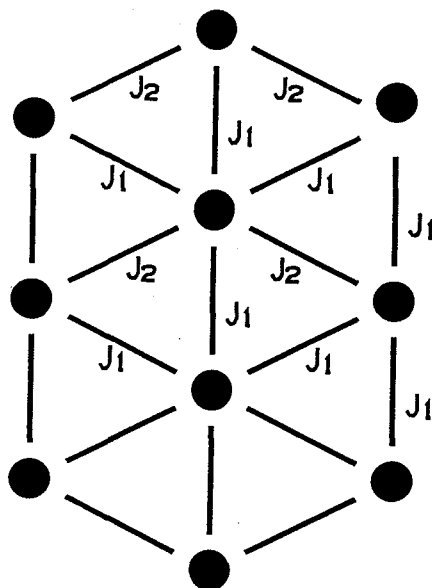


Figure 4.11: Schematic representation of the triangular magnetic lattice for the  $C_1$ TET-TTF layer with antiferromagnetic interactions  $J_1$  and  $J_2$ .

short range order hump characteristic of low-dimensional antiferromagnet around 60 K and no magnetic phase transition above 0.5 K, which is explained by the spin frustration in the  $S=1/2$  triangular lattice Heisenberg antiferromagnet.

Here, we examine the presence of the spin frustration in view of the estimation of the exchange interaction in this compound. To my knowledge, there is no theoretical prediction for the susceptibility of the two-dimensional distorted triangular Heisenberg antiferromagnet. Thus, the susceptibility with a hump is analyzed by means of the two-dimensional square lattice antiferromagnetic Heisenberg model [88] with predominant exchange constant  $J_1$ . The susceptibility is well described by the two-dimensional square lattice Heisenberg antiferromagnet model with the exchange energy of  $J_1 = -6.1$  K as shown in Fig. 4.9. It is worth reminding that the estimated exchange interaction is one order of magnitude small in comparison with the exchange interactions of  $\alpha'$ ,  $\beta'$ -(BEDT-TTF) $_2$ X and  $\theta$ -(BEDT-TTF) $_2$ Cu $_2$ (CN)[N(CN) $_2$ ] $_2$  salts. Actually, the transfer integral between the adjacent dimers in  $\alpha'$  and  $\beta'$ -(BEDT-TTF) $_2$ X salts, which have a two-dimensional square antiferromagnetic lattice with

dimerized donors having  $S=1/2$  [19]–[21], is in the same range to the transfer integrals of the present compound in spite of the large difference in the magnitudes of the exchange interactions. Furthermore, in  $\theta$ -(BEDT-TTF)<sub>2</sub>Cu<sub>2</sub>(CN)[N(CN)<sub>2</sub>]<sub>2</sub> which has the similar distorted triangular antiferromagnetic lattice [111] to the present compound, the transfer integral is also in the same range. In this case, the ratio of the exchange interactions estimated at  $J_2/J_1=0.1$  is considerably smaller than that in the present compound, suggesting that the predominance of  $J_1$  makes spin frustration considerably depressed. Consequently, the difference in the exchange interactions between the present compound and the above BEDT-TTF salts is supposed to be associated with the frustrated spin arrangement through the competition between the antiferromagnetic interactions  $J_1$  and  $J_2$ . In other words, the competition between antiferromagnetic  $J_1$  and  $J_2$  is considered to strengthen the features of spin frustration in (C<sub>1</sub>TET-TTF)<sub>2</sub>Br, resulting in the reduction of the apparent value of the estimated exchange interaction. It is also worth pointing out the importance of the novel electronic structure for the novel magnetic features, that is, the less localized nature in the electronic structure, discussed before in relation to the peculiar features realized in Mott boundary, is suggested to cause the reduction in the strengths of exchange interactions in comparison with the ordinary organic magnetic insulators having well localized magnetic moments on the donor molecules.

## 4.5 Summary

We investigate the crystal structure and physical properties of organic antiferromagnet  $(\text{C}_1\text{TET-TTF})_2\text{Br}$  in order to contribute to the developments of magnetic organic molecular conductors. In  $(\text{C}_1\text{TET-TTF})_2\text{Br}$ , the donor molecules form two-dimensional  $\theta$ -type donor arrangements with the absence of donor dimerization that the ordinary BEDT-TTF complexes behaving as Mott insulators have. The resistivity behaves semiconductive with a single activation energy  $E_a=0.6$  eV, which is in disagreement with the band calculation. ESR and the magnetic susceptibility prove the presence of localized magnetic moments  $S=1/2$  on donor molecules, whose concentration is given to be the assumption of 0.5 spin/donor. These findings appreciably evidence the features of Mott insulating state in this compound, although the absence of donor dimerization suggests that the magnetic moments are less localized. The temperature dependence of ESR line width shows a broaden-out abruptly below 5 K. The susceptibility shows the Curie-Weiss behavior having the antiferromagnetic Weiss temperature  $\theta=-17.3$  K in the high temperature range, it shows a broad hump of low-dimensional antiferromagnetic short range order around 12 K, and finally suggests the presence of antiferromagnetic long range ordering below  $T_N=3$  K. The consideration based on the calculation of the transfer integral reveals the feature of an  $S=1/2$  two-dimensional distorted triangular Heisenberg antiferromagnetic lattice with exchange interactions  $J_1$  and  $J_2$  having different strengths ( $J_1>J_2$ ). The fitting to the model of a square lattice Heisenberg antiferromagnet gives the estimate of exchange interaction  $J_1\approx-6$  K by neglecting  $J_2$ , which is considerably small in comparison with the similar systems belonging to BEDT-TTF complexes. This demonstrates the important role played by the spin frustration in the triangular antiferromagnetic arrangement formed through the competition of two antiferromagnetic interactions with different strengths. The less localized electronic state realized in the 3/4-filled band structure is also considered to be responsible for the novel features of magnetism.

## **Chapter 5**

### **General Conclusion**



Organic charge transfer complexes are eminently suitable for the development of molecular magnets. In these complexes,  $\pi$ -electrons system gives a large variety of magnetic interactions in the low-dimensional electronic structures with the competition between the transfer integral and the on-site Coulomb interaction. In the large on-site Coulomb interaction, the systems form the low-dimensional magnet composed by the  $\pi$ -electrons on the organic molecules. In the case, with the competition between the transfer integral and the on-site Coulomb interaction, the systems become itinerant magnets with the coexistence of electron transport and magnetism. In the case of the transfer integral overwhelming the on-site Coulomb interaction, the systems give a metallic state. To the above system, I introduce magnetic anions consisting of 3d transition metal halides, where the interaction between the  $\pi$ -electrons on organic molecules and the localized  $d$ -electrons of the anions is expected to provide novel magnetic interactions through the  $\pi$ - $d$  interaction. On the basis of these stand points of organic cation radical salts, we have developed magnetic organic systems using various TTF or TTP-types organic donors. Among these salts, we have obtained two interesting systems classified into different two categories (BEDT-TTF)<sub>3</sub>CuBr<sub>4</sub> and (C<sub>1</sub>TET-TTF)<sub>2</sub>Br. In the former, the presence of  $\pi$ - $d$  interaction gives novel electronic properties related to the coexistence of the electron transport and magnetism. Meanwhile, the latter shows the feature of a low-dimensional quantum spin system composed by the  $\pi$ -electron magnetic moments. Here, we summarize the essence of the results in the present thesis.

In Chapter 2, I present my trial on the development of organic metal magnets having the  $\pi$ - $d$  interaction on the basis of the cation radical salts with a various TTF or TTP-type donors. I employed the cation radical donor BEDO-TTF(BO), C<sub>1</sub>TET-TTF, BMDT-TTF, EDT-TTF, EOPT, EOOT, BDT-TTP, TMEO-TTP, TEMT-TTP and CPTM-TTP as organic conduction parts and 3-d transition metal halides as the counter anions for the localized magnetic moments. The obtained crystals were characterized by means of EDX for elemental analysis, X-ray crystal structure analysis, electrical resistivities, EPR and magnetic susceptibilities. The

important results for the obtained crystals are summarized below. The resistivity measurements found some metallic salts  $\text{BO}_{3.8}\text{CoCl}_6$  and  $\text{BO}_4\text{MnCl}_4$  or the semi-conductive behavior salts  $(\text{EDT-TTF})_3\text{CuCl}_4$  and  $(\text{TMET-TTP})_4\text{FeCl}_4$  with the low activation energy. However, EPR measurements and magnetic susceptibilities suggest the absence of strong exchange interactions for most of obtained crystals. Since X-ray crystal structure analysis were unsuccessful due to the poor qualities of the crystals, it is difficult that we discuss the detailed solid state properties.

In Chapter 3, I investigated  $(\text{BEDT-TTF})_3\text{CuBr}_4$  systematically in view of the  $\pi$ - $d$  interaction in organic cation radical salts, resulting in the clarification of novel electronic structure related to the coexistence of electronic transport and magnetism.  $(\text{BEDT-TTF})_3\text{CuBr}_4$  has alternate stacking of two-dimensional conducting sheets of BEDT-TTF donors and two-dimensional magnetic layers of  $\text{CuBr}_4^{2-}$  where the donor sheet consists of two kinds of BEDT-TTF molecules, neutral molecule A and cation radical molecule B with the composition of  $A/B=1/2$ . It has two phase transitions at  $T_c=59$  K and  $T_N=7.65$  K at ambient pressure, and shows the remarkable decrease in the electronic resistivity under pressure. Above  $T_c$ , the magnetic susceptibility obeys the Curie-Weiss law with the large antiferromagnetic Weiss temperature  $\theta=-100$ K. The large Weiss temperature proves the existence of the strong  $\pi$ - $d$  interaction between the BEDT-TTF conducting sheet and the  $\text{Cu}^{2+}$  magnetic sheet in the high temperature phase above  $T_c$ . The observed spins correspond to two magnetic moments on BEDT-TTF B molecules and one  $\text{Cu}^{2+}$  spin. The existence of the magnetic moments on BEDT-TTF molecules suggests that the BEDT-TTF layer is described by a Mott insulator above  $T_c$  realized by the charge separation of BEDT-TTF A and B molecules. At  $T_c$ , the large discontinuous drop of the susceptibility is caused by the disappearance of the magnetic moments on the BEDT-TTF B molecules. Taking into account that the low-temperature X-ray analysis shows the dissolution of the charge disproportionation between A and B donor molecules below  $T_c$ , the disappearance of the magnetic moments at sites B suggests that the transition is caused by the transition from a Mott insulator to a band insulator with

the first order nature. The resistivity shows a remarkable decrease with applying the pressure, and the metallic phase is stabilized in the high temperature range above  $T_c$  above 7 kbar. Further, the magnetic susceptibility decreases with increasing the pressure in the high temperature Mott insulator phase in the vicinity of the insulator-to-metal boundary at high pressures. These feature of the electronic and magnetic properties under pressure proves that the insulator-to-metal transition at 7 kbar is characterized as the Mott metal-insulator transition. In the low temperature region below  $T_c$ , the magnetic susceptibility is governed by the two-dimensional Heisenberg antiferromagnetic layer of  $\text{Cu}^{2+}$  spins with the large exchange energy  $J_{d-d} = -15.7$  K, and it undergoes an antiferromagnetic transition at  $T_N = 7.65$  K. The large exchange interaction between  $\text{Cu}^{2+}$  ions is caused by the widely extended of the localized  $d$ -electrons to the Br ligands on  $\text{CuBr}_4^{2-}$  anion. The presence of the magnetic long range order suggests a important role of the interlayer interaction mediated by the  $\pi$ -electrons of BEDT-TTF molecules having itinerant nature.

In Chapter 4, I investigate the crystal structure and physical properties of organic antiferromagnet  $(\text{C}_1\text{TET-TTF})_2\text{Br}$  as a low-dimensional quantum spin system comprising magnetic moments of  $\pi$ -electrons on the donor molecules. The donor molecules consist of two-dimensional  $\theta$ -type donor arrangements without the donor dimerization that the ordinary BEDT-TTF complexes behaving as Mott insulators have. The resistivity behaves the semiconductive type with a single activation energy  $E_a = 0.6$  eV, which is in disagreement with the band calculation of extended Hückel method. ESR and the magnetic susceptibility prove the presence of localized magnetic moments  $S = 1/2$  on donor molecules, whose concentration is given to be the assumption of 0.5 spin/donor. These findings appreciably evidence the feature of Mott insulating state in this compound, although the absence of donor dimerization suggests that the magnetic moments are less localized. The temperature dependence of ESR line width shows a broaden-out abruptly below 5 K. The susceptibility shows the Curie-Weiss behavior with the antiferromagnetic Weiss temperature  $\theta = -17.3$  K in the high temperature range. It shows a broad hump characteristic

of the low-dimensional antiferromagnetic short-range-order effect around 12 K, and finally suggests the presence of antiferromagnetic long-range-order below  $T_N=3$  K. The consideration based on the calculation of the transfer integral reveals the feature of an  $S=1/2$  two-dimensional distorted triangular Heisenberg antiferromagnetic lattice with exchange interactions  $J_1$  and  $J_2$  having different strengths ( $J_1>J_2$ ). The fitting to the model of a square lattice Heisenberg antiferromagnet gives the exchange interaction  $J_1\approx-6$  K by neglecting  $J_2$ , which is considerably small in comparison with the similar systems belonging to BEDT-TTF complexes. This demonstrates the important role played by the spin frustration in the triangular antiferromagnetic arrangement formed through competition of two antiferromagnetic interactions with different strengths. The less localized electronic state realized in the 3/4-filled band structure is also considered to be responsible for the novel features of magnetism.

I describe the future scope of the investigation in my thesis. As discussed above, I have investigated the solid state properties of organic cation radical salts (BEDT-TTF)<sub>3</sub>CuBr<sub>4</sub> and (C<sub>1</sub>TET-TTF)<sub>2</sub>Br, and developed new organic metal magnets with  $\pi$ - $d$  interaction. Nevertheless, we remain to solve the problems for their compounds. Thus, I will carry out the measurements to solve the problems as described below.

In (BEDT-TTF)<sub>3</sub>CuBr<sub>4</sub>, the present band calculation on the basis of the extend Hückel method can not explain the solid state properties. Namely, the magnetic susceptibility indicates that the present compound is described by Mott insulator which requires the half-filled band structure within the one-electron approximation, while, the present band calculation shows the narrow band gap state at the Fermi energy, suggesting the band insulator. Consequently, we will need to calculate the band structure using more sophisticated calculation method in order to solve the disagreement between the experimental findings and the band calculation.

Next, I will measure the temperature and the pressure dependence of optical reflectance spectra. As discussed in Chapter 3, the phase transition at  $T_c$  is caused

by the dissolution of the charge separation between BEDT-TTF A and B molecules. However, the valence state of BEDT-TTF molecules are estimated by the bond lengths from the X-ray structure analysis, which does not provide the detailed temperature dependence of the valence state of BEDT-TTF molecules precisely. Moreover, we do not have the information of the charge distribution under pressure. Marsden et al. indicates the charge separation between BEDT-TTF molecules from C-S stretching mode in the measurement of the optical spectra [14] at room temperature. Thus, we will be able to estimate the detailed temperature dependence and the pressure dependence using the optical spectra, which provide the favorable information for the consideration of the band structure under pressure.

Thirdly, I will carry out the high pressure resistivity above 25 kbar. In the present thesis, we do not find out the apparent instability in the metallic electronic state associated by the  $\pi$ - $d$  interaction. However, the pressure-temperature phase diagram suggests the possibility of the metallic state in the low temperature above 25 kbar. As a consequence, I will measure the electrical resistivity above 25 kbar to find out the feature of metallic electronic instability caused by the  $\pi$ - $d$  interaction.

In  $(C_1TET-TTF)_2Br$ , I am interested in the high pressure resistivity measurements. As discussed in Chapter 4, the present compound has a less localized nature of the magnetic moments on the organic donor molecules. However, the electronic transport shows the semiconductive behavior with a large activation energy. Here, the application of the pressure increases the transfer integrals between the donor molecules, resulting in reduction of the charge localization. Thus, the resistivity measurement under high pressure can be used to investigate the origin of the localization.

Next, I will measure the magnetic heat capacity in the low temperature range to investigate the origin of the antiferromagnetic transition. As shown in Chapter 4, the EPR line width is broadened out at 3 K, which suggests the magnetic long range order at 3 K. However, the magnetic susceptibility shows a slight anomaly and have no magnetic anisotropy below  $T_N=3$  K which is away from the ordinary

antiferromagnetic ordering state. The magnetic heat capacity provides the information to consider the magnetic properties in detail. Consequently, I will carry out the magnetic heat capacity measurement to find out the detailed feature of the magnetic transition.

In the development of the organic cation radical salts having the strong  $\pi$ - $d$  interactions, the crystal structure determinations were unsuccessful for almost all the obtained compounds because of the poor qualities of the obtained samples. Thus, I will try to synthesize samples having better qualities and determine the crystal structures, which make the detailed discussion possible for the magnetic interaction in the obtained compounds.

# Bibliography

- [1] H. N. McCoy and W. C. Moore: *J. Am. Chem. Soc.* **33** (1911) 272.
- [2] H. J. Kraus: *J. Am. Chem. Soc.* **34** (1913) 1732.
- [3] H. Akamatsu, H. Inokuchi and Y. Matsunaga: *Nature* **173** (1954) 168.
- [4] J. Ferraris, D. O. Cowan, V. J. Walatka and J. H. Perlstein: *J. Am. Chem. Soc.* **95** (1973) 948.
- [5] K. Bechgaard, C. S. Jacobsen, K. Mortensen, M. J. Pedersen and N. Thorup: *Solid State Commun.* **33** (1980) 1119.
- [6] H. Urayama, H. Yamochi, G. Saito, K. Nozawa, T. Sugano, M. Kinoshita, S. Saito, K. Oshima, K. Kawamoto and J. Tanaka: *Chem. Lett.* (1988) 55.
- [7] A. M. Kini, U. Geiser, H. H. Wang, K. D. Carlson, J. M. Williams, W. K. Kwok, K. G. Vandervoort, J. E. Thompson, D. L. Jung and M. H. Whangbo: *Inorg. Chem.* **29** (1990) 3262.
- [8] J. M. Williams, A. M. Kini, H. H. Wang, K. D. Carlson, V. Geiser, L. K. Montgomery, G. J. Pyrka, D. M. Warktis, J. E. Schirber, D. L. Overmyer, D. Jung and M. H. Whangbo: *Inorg. Chem.* **29** (1990) 3262.
- [9] J. E. Schirber, D. L. Overmyer, K. D. Carlson, J. M. Williams, A. M. Kini, H. Han Wang, H. A. Charlier, B. J. Love, D. M. Watkins and G. A. Yaconi, *Phys. Rev. B* **44** (1991) 4666.
- [10] U. Welp, S. Fleshler, W. K. Kwok, G. W. Cratree, K. D. Carlson, H. H. Wang, V. Geiser, J. M. Williams and V. M. Hitsman, *Phys. Rev. Lett.* **69** (1992) 840.
- [11] Yu. V. Sushko, H. Ito, T. Ishiguro, S. Horiuchi and G. Saito, *Solid State Commun.* **87** (1993) 997.

- [12] K. Miyagawa, A. Kawamoto, Y. Nakazawa and K. Kanoda, *Synth. Met.* **70** (1995) 969.
- [13] J. Yamaura, K. Suzuki, Y. Kaizu, T. Enoki, K. Murata and G. Saito: *J. Phys. Soc. Jpn.* **65** (1996) 2645.
- [14] J. R. Marsden, M. L. Allan, R. H. Friend, M. Kurmoo, D. Kanazawa, P. Day, G. Bravic, D. Chasseau, L. Ducasse and W. Hayes: *Phys. Rev. B* **50** (1994) 2118.
- [15] H. Kobayashi, H. Tomita, T. Naito, A. Kobayashi, F. Sakai, T. Watanabe and P. Cassoux: *J. Am. Chem. Soc.* **118** (1996) 368.
- [16] R. Kato, H. Kobayashi, A. Kobayashi, T. Mori and H. Inokuchi: *Chem. Lett.* (1987) 1579.
- [17] T. Mori, H. Inokuchi, A. Kobayashi, R. Kato and H. Kobayashi: *Phys. Rev.* **38** (1988) 5913.
- [18] M. A. Beno, M. A. Firestone, P. C. W. Leung, L. M. Sowa, H. H. Wang, J. M. Williams and M.-H. Whangbo: *Solid State Commun.* **57** (1993) 735.
- [19] S. D. Obertelli, R. H. Friend, D. R. Talham, M. Kurmoo and P. Day: *J. Phys. Condens. Matter* **1** (1989) 5671.
- [20] N. Yoneyama, A. Miyazaki, T. Enoki and G. Saito: to be published in *Synth. Met.* (1997).
- [21] M. Tokumoto, H. Anzai and T. Ishiguro: *Synth. Met.* **19** (1987) 215.
- [22] H. Kobayashi, R. Kato, A. Kobayashi, G. Saito, M. Tokumoto, H. Anzai and T. Ishiguro: *Chem. Lett.* (1986) 89.
- [23] N. F. Mott: *Metal-Insulator Transitions* (Taylor & Francis, 1990)
- [24] D. B. McWhan and J. P. Remeika: *Phys. Rev. B* **2** (1970) 3734.
- [25] D. B. McWhan, J. P. Remeika, T. M. Rice, W. F. Brinkman, J. P. Maita and A. Menth: *Phys. Rev. Lett.* **27** (1971) 941.
- [26] L. J. de Jongh and A. R. Miedema: *Advances in Physics* **23** (1974) 1.
- [27] A. W. Graham, M. Kurmoo and P. Day: *J. Chem. Soc. Chem. Commun.* (1995) 2061.



- [28] M. Kurmoo, A. W. Graham, P. Day, S. J. Coles, M. B. Hursthouse, J. L. Caulfield, J. Singleton, F. L. Pratt, W. Hayes, L. Ducasse and P. Guionneau: *J. Am. Chem. Soc.* **117** (1995) 12209.
- [29] W. A. Fertig, D. C. Johnston, L. E. DeLong, R. W. McCallum, M. B. Maple and B. T. Matthias: *Phys. Rev. Lett.* **38** (1977) 987.
- [30] M. Ishikawa,  $\phi$ . Fischer and J. Muller: *J. de Physique* **39** (1978) C6-1379.
- [31] A. Kobayashi, T. Uchida, H. Tomita, T. Naito and H. Kobayashi: *Chem. Lett.* (1993) 2179.
- [32] H. Kobayashi, H. Tomita, T. Naito, A. Kobayashi, F. Sakai, T. Watanabe and P. Cassoux: *J. Am. Chem. Soc.* **118** (1996) 368.
- [33] M. Tokumoto, T. Naito, H. Kobayashi, A. Kobayashi, V. N. Laukhin, L. Brossard and P. Cassoux: to be published in *Synth. Met.* (1997).
- [34] H. Sawa, M. Tamura, S. Aonuma, R. Kato, M. Kinoshita and H. Kobayashi: *J. Phys. Soc. Jpn.* **62** (1993) 2224.
- [35] H. Kobayashi, A. Miyamoto, R. Kato, F. Sakai, A. Kobayashi, Y. Yamakita, Y. Furukawa, M. Tasumi and T. Watanabe: *Phys. Rev. B* **47** (1993) 3500.
- [36] R. Kato, H. Kobayashi, A. Kobayashi: *J. Am. Chem. Soc.* **111** (1989) 5224.
- [37] Y. Misaki, T. Matsui, K. Kawakami, H. Nishikawa, T. Yamabe and M. Shiro: *Chem. Lett.* (1993) 1337.
- [38] Y. Misaki, H. Nishikawa, T. Yamabe, T. Mori, H. Inokuchi, H. Mori and S. Tanaka: *Chem. Lett.* (1993) 729.
- [39] B. Garreau, D. de Montanzon, D. Cassoux, J.-P. Legros, J.-M. Fabre, K. Saoud, S. Chakroune: *New. J. Chem.* **19** (1995) 161.
- [40] Y. Misaki, H. Nishikawa, T. Yamabe, T. Mori, H. Inokuchi, H. Mori and S. Tanaka: *Chem. Lett.* (1993) 733.
- [41] Y. Misaki, H. Nishikawa, T. Yamabe, T. Mori, H. Inokuchi, H. Mori and S. Tanaka: *Chem. Lett.* (1993) 2085.
- [42] T. Mori, H. Inokuchi, A. M. Kini and J. M. Williams: *Chem Lett.* (1990) 1279.

- [43] H. Tatemitsu, E. Nishikawa, Y. Sakata and S. Misumi: J. Chem.Soc. , Chem. Chommun. (1985) 106.
- [44] Y. Misaki, K. Kawakami, H. Fujiwara, T. Yamabe, T. Mori, H. Mori and S. Tanaka: Chem. Lett. (1995) 1125.
- [45] R. Kato, A. Kobayashi, Y. Sasaki and H. Kobayashi: Chem. Lett. (1984) 993.
- [46] R. Kato, H. Kobayashi, A. Kobayashi and Y. Sasaki: Chem. Lett. (1984) 1693.
- [47] R. Kato, H. Kobayashi and A. Kobayashi: Chem. Lett. (1986) 2013.
- [48] J. Yamaura, A. Miyazaki, T. Enoki and G. Saito: Phys. Rev. B**55** (1997) 3649.
- [49] M. M. Schieber: Experimental Magnetochemistry , ed. E. P. Wohlfarth (North-Holland, 1967).
- [50] T. Enoki, M. Enomoto, M. Enomoto, K. Yamaguchi, N. Yoneyama, J. Yamaura, A. Miyazaki and G. Saito: Mol. Cryst. Liq. Cryst. **285** (1996) 19.
- [51] I. Tomomatsu: Master Thesis, Prof. Enoki's Group, Faculty of Science, Tokyo Institute of Technology, Tokyo, 1990.
- [52] T. Mallah, C. Hollis, S. Bott, M. Kurmoo, P. Day, M. Allan and R. Friend: J. Chem. Soc. Dalton Trans. (1990) 859.
- [53] T. Mori and H. Inokuchi: Bull. Chem. Soc. Jpn. **61** (1988) 591.
- [54] P. Day, M. Kurmoo, T. Mallah, I. R. Marsden, R. H. Friend, F. L. Pratt, W. Hayes, D. Chasseau, J. Gaultier, G. Bravic and L. Ducasse: J. Am. Chem. Soc. **114** (1992) 10722.
- [55] H. Yamochi, S. Horiuchi, G. Saito, M. Kusunoki, K. Sakaguchi, T. Kikuchi and S. Sato: Synth. Met. **55-57** (1993) 2096.
- [56] T. Haseda: J. Phys. Soc. Jpn. **15** (1960) 483.
- [57] D. J. Breed: Physica **37** (1967) 35.
- [58] H. Yamochi, T. Nakamura, G. Saito, T. Kikuchi, S. Sato, K. Nozawa, M. Kinoshita, T. Sugano and F. Wudl: Synth. Met. **41-43** (1991) 1741.
- [59] J. Bissey, R. Berger, P. Beziade, N. Chanh, T. Maris, R. Zouari and A. Daoud: Solid State Commun. **97** (1996) 669.

- [60] V. Fernandez, M. Moran, M. T. Gutierrez-Rios, C. Foces-Foces and F. H. Cano: *Inorg. Chim. Acta* **128** (1987) 239.
- [61] C. Chow, K. Chang and R. D. Willett: *J. Chem. Phys.* **59** (1973) 2629.
- [62] T. Sugano, G. Saito and M. Kinoshita: *Phys. Rev. B* **34** (1986) 117.
- [63] T. Enoki, J. Yamaura, N. Sugiyasu, K. Suzuki and G. Saito: *Mol. Cryst. Liq. Cryst.* **233** (1993) 325.
- [64] T. Enoki, I. Tomomatu, Y. Nakano, K. Suzuki and G. Saito: *The Physics and Chemistry of Organic Superconductors*, ed. G. Saito and S. Kagoshima (Springer, Verlag, 1990) p. 294.
- [65] T. Mori, F. Sakai, G. Saito and H. Inokuchi: *Chem. Letters.* (1987) 927.
- [66] M. Watanabe, Y. Nogami, K. Oshima, J. Yamaura, T. Enoki and G. Saito: *Solid State Commun.* **100** (1996) 755.
- [67] P. Guionneau, G. Bravic, J. Gaultier, D. Chasseau, M. Kurmoo, D. Kanazawa and P. Day: *Acta Cryst. C* **50** (1994) 1894.
- [68] O. Shimomura, K. Takemura, H. Fujihisa, Y. Fujii, Y. Ohishi, T. Kikegawa, Y. Amemiya and T. Matsushita: *Rev. Sci. Instrum.* **63** (1992) 967.
- [69] H. Kobayashi, A. Kobayashi, Y. Sasaki, G. Saito and H. Inokuchi: *Chem. Lett.* (1984) 183.
- [70] P. Guionneau, C. J. Kepert, D. Chasseau, M. R. Truter and P. Day: to be published in *Synth. Met.* (1997).
- [71] C. K. Johnson, "ORTEP-II, Report ORNL-5138," Oak Ridge National Laboratory, Tennessee, USA (1976).
- [72] M. Watanabe, Y. Nogami, K. Oshima, J. Yamaura, T. Enoki and G. Saito: to be published in *Synth. Met.* (1997).
- [73] M. Watanabe, Y. Nogami, K. Oshima, J. Yamaura, T. Enoki and G. Saito: in preparation for publication.
- [74] Y. Watanabe, H. Sato, T. Sasaki and N. Toyota: *J. Phys. Soc. Jpn.* **60** (1991) 3608.

- [75] D.Chasseau, P. Guionneau, J. Gaultier, Y. Barrans, L. Ducasse, C. J. Kepert, P. Day and M. Kurmoo: to be published in Synth. Met. (1997).
- [76] G. Grimvall: Thermophysical properties of materials, ed. E. P. Wohlfarth (North-Holland, 1986) Vol. XVIII.
- [77] E. S. Itskevich: Cryogenics Dec. (1964) 365.
- [78] H. Takahashi and Y. Okayama: J. High Press. Instrument **30** (1992) 44.
- [79] I. Giaever and K. Megerle: Phys. Rev. Lett. **21** (1968) 96.
- [80] M. Kobayashi, T. Enoki, K. Imaeda, H. Inokuchi and G. Saito: Phys. Rev. B **36** (1987) 1457.
- [81] D. Kohnlein: Zeitschrift fur Physik **208** (1968) 142.
- [82] Ch. Butzlaff: *QUANTUMSTATES* (QUANTUM DESIGN and QUANTUM MAGNETICS, 1994) winter.
- [83] K. Yoshida: Prog. Theor.. Phys. **7** (1952) 425.
- [84] T. Nagamiya: Prog. Theor.. Phys. **11** (1954) 309.
- [85] T. Nagamiya, K. Yoshida, R. Kubo: Adv. Phys. **4** (1955) 1.
- [86] R. Bachmann, F. J. DiSalvo, Jr., T. H. Gebalee, R. L. Greene, R. E. Howard, C. N. King, H. C. Kitsch, K. N. Lee, R. E. Schwall, H.-U. Thomas and R. B. Zubeck: Rev. Sci. Instrum. **43** (1972) 205.
- [87] K. Nakazawa: Dr. Thesis, Faculty of Science, Tokyo Institute of Technology, Tokyo, 1993.
- [88] M. E. Lines: J. Phys. Chem. Solids **31** (1970) 101.
- [89] R. Tsuchiya, S. Yoshizaki, T. Nakamura, T. Takahashi, J. Yamaura, K. Suzuki, T. Enoki and G. Saito: Synthetic Metals **70** (1995) 967.
- [90] T. G. Castner and M. S. Seehra: Phys. Rev. B **47** (1993) 578.
- [91] S. Yoshizaki, R. Tsuchiya, T. Nakamura, T. Takahashi, J. Yamaura, K. Suzuki, T. Enoki, G. Saito and K. Murata: unpublished
- [92] K. Suzuki, J. Yamaura, N. Sugiyasu, T. Enoki and G. Saito: Synthetic Metals **55-57** (1993) 2191.

- [93] D. E. Moncton, R. J. Birgeneau, L. V. Interrante and F. Wudl: Phys. Rev. Lett. **39** (1977) 507.
- [94] J. B. Torrance, J. E. Vazquez, J. J. Mayerle and V. Y. Lee: Phys. Rev. Lett. **46** (1981) 253.
- [95] J. B. Torrance, A. Girlando, J. J. Mayerle, J. I. Crowley, V. Y. Lee, P. Batail and S. J. LaPlaca: Phys. Rev. Lett. **47** (1981) 1747.
- [96] Y. Tokura, H. Okamoto, T. Koda, T. Mitani and G. Saito: Solid State Commun. **57** (1986) 607.
- [97] T. Mitani, G. Saito, Y. Tokura and T. Koda: Phys. Rev. Lett. **53** (1984) 842.
- [98] R. M. Metzger and J. B. Torrance: J. Am. Chem. Soc. **107** (1985) 117.
- [99] B. R. Patyal, B. L. Scott and R. D. Willett: Phys. Rev. B **41** (1990) 1657.
- [100] K. Waizumi, H. Masuda, H. Einaga and N. Fukushima: Chem. Lett. (1993) 1145.
- [101] F. Keffer: *Encyclopedia of Physics*, ed. H. P. J. WIJN (Springer, Verlag, 1966) Vol. **XVIII/2**, p. 124.
- [102] J. H. P. Colpa, E. G. Sieverts and R. H. Van Der Linde: Physica **51** (1971) 573.
- [103] T. Enoki, M. Enomoto, M. Enomoto, K. Yamaguchi, N. Yoneyama, J. Yamaura, A. Miyazaki and G. Saito, Mol. Cryst. Liq. Cryst. **285** (1996) 19.
- [104] A. Miyazaki, K. Yamaguchi, T. Enoki and G. Saito, to be published in Synth. Met (1997).
- [105] H. Kobayashi, R. Keizo, A. Kobayashi, Y. Nishio, K. Kajita and W. Sasaki, Chem. Lett. (1986) 833.
- [106] H. M. McConnell, J. Chem. Phys. **39** (1963) 1910.
- [107] *Magnetic Properties of Layered Transition Metal Compounds*, ed. L. J. de Jongh (Kluwer Academic, Boston, 1990).
- [108] G. M. Sheldrick, "SHELXS86, Program for the Solution of Crystal Structures," Univ. of Göttingen, Germany (1985).

- [109] G. M. Sheldrick, "*SHELXL93, Program for the Refinement of Crystal Structures*," Univ. of Göttingen, Germany (1993).
- [110] T. Mori, A. Kobayashi, Y. Sasaki, H. Kobayashi, G. Saito and H. Inokuchi, Bull. Chem. Soc. Jpn. **57** (1984) 627.
- [111] T. Komatsu, H. Sato, T. Nakamura, N. Matsukawa, H. Yamochi, G. Saito, M. Kusunoki, K. Sakaguchi and S. Kagoshima, Bull. Chem. Soc. Jpn. **68** (1995) 2223.
- [112] A. Otsuka, H. Yamochi, G. Saito, T. Sugano, M. Kinoshita, S. Sato, K. Honda, K. Ohfuchi and M. Konno, Synth. Met. **41-43** (1991) 1699.
- [113] T. Nakamura, G. Saito, T. Inukai, T. Sugano, M. Kinoshita and M. Konno: Solid State Commun. **75** (1990) 583.
- [114] H. Mori, I. Hirabayashi, S. Tanaka, T. Mori, Y. Maruyama and H. Inokuchi: Solid State Commun. **88** (1993) 411.
- [115] K. Nagata and Y. Tazuke, J. Phys. Soc. Jpn. **32** (1972) 337.
- [116] J. C. Bonner and M. E. Fisher, Phys. Rev. **135A** (1964) 640.
- [117] H. Nishimori and S. Miyashita, J. Phys. Soc. Jpn. **55** (1986) 4448.
- [118] H. Kawamura and S. Miyashita, J. Phys. Soc. Jpn. **53** (1984) 9.
- [119] P. W. Anderson, Mat. Res. Bull. **8** (1973) 153.
- [120] M. Suzuki, I. Suzuki, C. Burr, D. G. Wiesler, N. Rosov and K. Koga, Phys. Rev. B **50** (1994) 9188.